A MODEL OF THE GREENLAND ICE SHEET DEGLACIATION

Benoit Lecavalier

Thesis submitted to the
Faculty of Graduate and Postdoctoral Studies
in partial fulfilment of the requirements
for the Master of Science degree in Physics

Department of Physics
Faculty of Science
University of Ottawa

ABSTRACT

The goal of this thesis is to improve our understanding of the Greenland ice sheet (GrIS) and how it responds to climate change. This was achieved using ice core records to infer elevation changes of the GrIS during the Holocene (11.7 ka BP to Present). The inferred elevation changes show the response of the ice sheet interior to the Holocene Thermal Maximum (HTM; 9-5 ka BP) when temperatures across Greenland were warmer than present. These ice-core derived thinning curves act as a new set of key constraints on the deglacial history of the GrIS. Furthermore, a calibration was conducted on a three-dimensional thermomechanical ice sheet, glacial isostatic adjustment, and relative sea-level model of GrIS evolution during the most recent deglaciation (21 ka BP to present). The model was data-constrained to a variety of proxy records from paleoclimate archives and present-day observations of ice thickness and extent.

DECLARATION

The following is a declaration made by the lead author of the research article on the "Revised estimates of Greenland ice sheet thinning histories based on ice-core records", which was published in the Journal of Quaternary Science Reviews and is Section 2 of this thesis. I conducted all the numerical modelling for this study, which involved the calibration of a GIA model for the Canadian Arctic by constraining it to RSL to determine vertical land motion spatially and temporally. I applied these findings and improved the methodologies needed to derive more accurate elevation histories for the Greenland ice sheet. This was performed using ice-core records, which I also used to derive temperature reconstructions at the periphery of the ice sheet. I wrote the manuscript independently, although I did receive comments from my research advisor (Glenn Milne). This research entailed the initiation of international collaborations. While my advisor supplied the models, newly established collaborators at National Resources Canada (NRCan) (David Fisher) and Niels Bohr Institute in Denmark (Bo Vinther) provided insight and feedback on my proposed methodologies based on their expertise in ice-core research. Arthur Dyke, also at NRCan, provided copious RSL data to constrain our model and finally, my collaborator in Norway (Matthew Simpson) provided a recent reconstruction of the Greenland ice sheet to input within our GIA model of sea-level change. The published results are relevant to multiple disciplines, from glaciology and Greenland field geology, to ice sheet, sea-level and climate modelling. We therefore selected a journal which has high visibility within these disciplines (5-year impact factor 5.04). Furthermore, in September 2013 the article was cited in the United Nations (UNEP & WMO) established Intergovernmental Panel on Climate Change (IPCC) fifth assessment report (AR5 WG1).

The research article on "A model of Greenland ice sheet deglaciation based on observations of ice extent and relative sea-level", was recently submitted into the Journal of Quaternary Science Reviews and is Secton 3 of this thesis. I conducted all the numerical modelling for this study, which involved the calibration of a glaciological, GIA and RSL model for the GrIS over the deglaciation. The manuscript was written independently, although similarly to the previous publication I did receive comments from my research advisor. This research established international collaborations across multiple disciplines. My advisor supplied the GIA and RSL model, while my colleague Philippe Huybrechts (Vrije Universiteit Brussel, Belgium) provided the three-dimensional thermomechanical ice sheet model. Model developments on the climate forcing component of the ice sheet model were performed in collaboration with Leanne Wake (University of Northumbria, UK). Based on weather station observations, she concluded a revised positive degree day algorithm which we implemented. I benchmarked the model and conducted several sensitivity analyses to validate the theoretical behaviour of the developments. Lev Tarasov from Memorial University provided a collection of North American ice sheet models which I amalgamated to our global ice model to study the implications to Greenland RSL. Newly established collaborators in Denmark: Nicolaj Larsen, Kristian Kjeldsen and Svend Funder (Aarhus University; University of Copenhagen) have provided ice extent and RSL data along with feedback on the resulting ice sheet reconstructions based on their expertise in Greenland field geology. Similarly, Antony Long and Sarah Woodroffe from Durham University (UK) along with Arthur Dyke (NRCan) have provided large compilations of RSL data to constrain our models. Finally, my collaborator Matthew Simpson (Norwegian Mapping Authority), who conducted the previous Huy2 model study that I build upon, has contributed through guidance and feedback on my proposed methodology. On a similar basis as the Greenland thinning curves research paper being submitted to the Journal of Quaternary Science Reviews, the Huy3 study was justifiably submitted to this same journal.

FORWARD

Throughout my Master of Science program I had the opportunity to attend several conferences and workshops where I presented the research contained within this thesis. Furthermore, I took part of two summerschools where I was taught on the newest developments in my research field. I established over a dozen successful international and national collaborations with internationally renowned researchers based in the UK, Belgium, Denmark, Norway, USA, and Canada. Finally, the core of this thesis consists of two publications, both of which I am first author. In addition to these two projects I was also involved in a number of other studies which have materialized into complementing publications.

Conferences & Workshops:

- *Milne, G.A.*,* ***Lecavalier, B.S.****, Kjeldsen, K.K.,* Kjær, K., Wolstencroft, M.,*Wake, L., Simpson, M.J.R., Korsgaard, N.J.,* Bjørk, A., Khan, A. (2013) Uncertainty in Greenland glacial isostatic adjustment. American Geophysical Union Fall meeting, San Francisco, USA. abstract submitted.
- *Buizert, C.*, Gkinis, V., Severinghaus, J.P., He, F.,* ***Lecavalier, B.S.****, Carlson, A.,White, J.W.C., Vinther, B., Brook, E.J.* (2013) Greenland temperature response to climate forcing during the last deglaciation. American Geophysical Union Fall meeting, San Francisco, USA. abstract submitted.
- ***Lecavalier, B.S.****, Milne, G.A.,Wake, L., Simpson, M.J.R., Kjeldsen, K.K., Funder, S., Woodroffe, S., Long, A., Huybrechts, P., Tarasov, L., Dyke, A.* (2013) Calibrating a model of the Greenland ice sheet from the last glacial maximum to present. International Geodesy Symposium, Ilullisat, Greenland . Oral presentation.
- ***Lecavalier, B.S.****, Wake, L., Milne, G.A., Marshall, S., Simpson, M.J.R., Huybrechts, P.* (2013) Sensitivity of the Greenland ice sheet to the Holocene thermal maximum. PAGES Open Science Meeting, Goa, India. Oral presentation.
- ***Lecavalier, B. S.****, Milne, G. A., Vinther, B. M., Fisher, D. A., Dyke, A. S., Simpson, M. J. R., Tarasov, L.* (2012) Revised estimates of Greenland ice sheet thinning histories based on ice-core records. PALSEA, Wisconsin, USA. Poster presentation.
- *Wake, L.*, Marshall, S., Milne, G.,* ***Lecavalier, B. S.****, Bayou, N., Huybrechts, P., Hanna, E.* (2012) Linking surface energy balance calculations and temperature index models of surface melt: Revision of the positive degree day (PDD) methodology for the Greenland ice sheet. European Geophysical Union Assembly, Vienna. Poster presentation.
- ***Lecavalier, B. S.****, Milne, G. A., Vinther, B. M., Fisher, D. A., Dyke, A. S., Simpson, M. J. R.* (2011) The influence of land uplift on the isotopic temperature record from the Agassiz ice cap: implications for the Holocene thinning of the Greenland ice sheet. American Geophysical Union Fall meeting, San Francisco, USA. Poster presentation.

Summerschools:

- **Lecavalier, B.S.**, Milne, G. A., Simpson, M. J. R., Wake, L., Huybrechts, P., Kjeldsen, K. K., Funder, S., Tarasov, L., Long, A. J., Woodroffe, S. A.,Larsen, N.K., Dyke, A. (2013) A model of Greenland ice sheet deglaciation based on observations of ice extent and relative sea-level. ACDC summer school, Nyksund, Norway. Oral presentation.
- **Lecavalier, B. S.***, (2011) Reconstructing the evolution of an ice sheet. Karthaus summer school, Karthaus, Italy. Oral presentation.

Articles Published:

- ***Lecavalier, B. S.***, *Milne, G. A., Vinther, B. M., Fisher, D. A., Dyke, A. S., Simpson, M. J. R. (2013)* Revised Estimates of Greenland ice sheet thinning histories based on ice-core records. **Quaternary Science Reviews**. 63: 73-82.
- *Woodroffe, S. A., Long, A. J.,* ***Lecavalier, B.S.****, Milne, G. A., Bryant, C. L.* (2013) Using relative sea-level data to constrain the deglacial history of southern Greenland. **Quaternary Science Reviews**. JQSR-D-13-00050R1, In Press.
- ***Lecavalier, B.S.****, Milne, G. A., Simpson, M. J. R., Wake, L., Huybrechts, P., Kjeldsen, K. K., Funder, S., Tarasov, L., Long, A. J., Woodroffe, S. A.,Larsen, N.K., Dyke, A.* (Submitted) A model of Greenland ice sheet deglaciation based on observations of ice extent and relative sea-level. **Quaternary Science Reviews**.

ACKNOWLEDGEMENTS

I would like to start by thanking my supervisor Glenn Milne who has been an exceptional and inspiring role model throughout my studies. I thank you for providing me a chance to prove myself along with the opportunity to establish myself in an active, dynamic, and fascinating field of research. Even with your busy schedule you have made time to guide me through my research and have always been available to answer my questions. I am looking forward to continuing our work together in the future. I wish the best for you and your family. Furthermore, I would like to thank my numerous collaborators. You have provided encouragement and feedback, code and data, inspiring discussions and enthusiasm. You have received me in your countries and exercised patience with my questions.

To my friends and colleagues, thanks for keeping me grounded through it all and for the company. Finally, I would like to thank my parents, Pierre and Julie for the continuous support. You have always been there to discuss everything and anything from science, philosophy, economics and politics. You have instigated and instilled my scientific curiosity for which I will be forever grateful for.

TABLE OF CONTENTS

A Model of the Greenland Ice Sheet Deglaciation 1
Abstract 2
Declaration 2
Forward 5
Acknowledgements 7
Table of Contents 8
List of Figures 10
List of Symbols 15
List of Key Mathematical Terms 16
1. Introduction 17
  1.1 Ice and Climate 17
    1.1.1 Ice Ages on Earth 22
    1.1.2 The Greenland Ice Sheet in the Past, Present and Future 26
    1.1.3 Motivation and Outline of Thesis 29
  1.2 Model Description 33
    1.2.1 Glacial Isostatic Adjustment and Relative Sea Level Model 33
    1.2.2 Three-Dimensional Thermomechanical Ice Sheet Model 44
  1.3 Data 54
2. Revised Estimates of Greenland Ice Sheet Thinning Histories based on Ice-Core Records 60
  2.1 Abstract 60
  2.2 Introduction 62
    2.2.1 Holocene Thinning of the Greenland Ice Sheet 62
    2.2.2 Interpreting δ18o from the Renland and Agassiz ice caps 65
  2.3 Methodology 68
    2.3.1 Agassiz and Renland Land Uplift Correction 68
    2.3.2 Holocene Temperature and Thinning Reconstructions 69
  2.4. Results and Discussion 71
    2.4.1 GIA Correction 71
    2.4.2 AR Temperature Records 76
    2.4.3 Revised Holocene Thinning Curves 77
    2.4.4 Comparison of Thinning Curves to Output from Numerical Ice Models 79
  2.5 Conclusion 83

2.6 Reference 84
3. A Model of Greenland Ice Sheet Deglaciation based on Observations of Ice Extent and Relative Sea Level 87
3.1 Abstract 87
3.2 Introduction 88
3.3 Data 92
3.3.1 Ice Extent during Deglaciation 94
3.3.2 Relative Sea Level and Marine Limit 97
3.3.3 Holocene Thinning Curves 99
3.4 Model Description 99
3.4.1 Ice Sheet Model 102
3.4.2 Glacial Isostatic Adjustment and Relative Sea Level Model 103
3.5 Modelling Results 105
3.5.1 Introduction 105
3.5.2 Huy3 Calibration 115
3.5.3 Ice Sheet Interior 140
3.6 Discussion 143
3.6.1 GrIS Evolution 143
3.6.2 Data-Model Misfit 147
3.7 Conclusion 152
3.8 References 155
3.9 Supplementary Material 167
4. Conclusions 178
4.1 Overview 178
4.2 GrIS Deglaciation 179
4.3 Future Work 181
4.3.1 Present-Day Vertical Land Motion 181
4.3.2 Model Weaknesses 183
5. References 184

LIST OF FIGURES

1.1 The present state of the global cryosphere. This does not include the areal distribution of seasonal snow cover, river and lake ice, and atmospheric ice crystals. The bulk of the ice in the cryosphere (>98%) is stored within the Antarctic and Greenland ice sheet (~56.2 and ~7.1 m equivalent mean sea-level, respectively) (UNEP/GRID-Arendal Global Outlook for Ice and Snow, 2007).

1.2 A temperature proxy record obtained from globally distributed deep ocean cores, starting in the Cenozoic Era (a), expanded from the Pliocene onward (b) and in the last half million years (c). The blue bars indicate the presence of modern ice sheets, the darker blue bands represent periods of full size ice sheets. (From Hansen & Sato 2011)

1.3 The Vostok palaeoclimate CO_2 (parts per million by volume), Temperature, CH_4 (parts per billion by volume) and $\delta^{18}O$ records (parts per thousand) and solar variations at 65°N due to Milankovitch cycles (top to bottom) [Petit et al., 1999].

1.4 Some of the many processes that affect relative sea level (RSL) [Milne, 2008].

1.5 Characteristic timescales of mantle deformation processes for a Maxwell viscoelastic Earth where the Maxwell time is expressed as: $\tau_M = \frac{\eta}{\mu}$ (Yuen et al. 1982).

1.6 The diagram shows an exaggerated case (A) of an ice sheet gravitationally attracting surrounding ocean water producing a deeper water column and (B) consequently as the ice sheet melts, the relaxation of the ocean and subsequent solid Earth deformation [Milne, 2008].

1.7 A shift from t to t^+ of the rotation pole relative to the Earth produces a global scale deformation where blue areas experience a sea-level rise while white areas a sea-level fall. Notice that this deformation can be conveniently represented by the Y_2^1 spherical harmonic (From Mound and Mitrovica 1998).

1.8 The cross section of a valley glacier experiencing gravitationally driven deformation. The pathlines are shown to be transporting elements of ice to a region of lower gravitational potential. The mass balance of a body of ice is dictated by the climate forcing, where generally speaking high altitudes undergo net accumulation while ablation occurs in lower warmer terrain. The basal topography, composition, and temperature constrain the velocity profile of the ice. A history of past climate and of geothermal heat at the base provides the necessary boundary conditions to understand the temperature evolution of the ice.

2.1 (a) The location and names of the relevant ice cores discussed in this study. (b) The synchronized $\delta^{18}O$ records for all the sites shown in (a); both raw and smoothed (Gaussian filtered) signals are shown.

2.2 The distribution of sites (black circles and 12 numbered sites) across the Canadian Arctic and Greenland which had sufficient sea level proxy information to constrain our glacial isostatic adjustment (GIA) model.

2.3 Relative sea-level observations and predictions at the 12 sites which are of greatest relevance to the GIA/RSL model. The red (down facing) and blue triangles (pointing up) represent an upper and lower bound on sea level, respectively. The sea-level curve on each graph was generated using ICE-5G as the ice model and an optimal Earth model with lithosphere thickness of 71 km, upper mantle viscosity of 3×10^{20} Pa·s, and lower mantle viscosity of 10^{21} Pa·s.

2.4 (a) The spatial variability in GIA-induced uplift of Ellesmere Island at 10 ka BP using the optimal Earth model. The plot shows the location of the Agassiz ice cap core locations (A87 and A84, both at the dome) along with the two sites at which uplift was predicted (A,B). (b) Top frame shows predicted uplift curves generated using the optimal Earth model at the two locations (A, B; orange, blue, respectively) shown in (a). Also shown is the uplift curve adopted by Vinther et al. (2009) (black). Bottom frame shows the Renland original uplift correction applied in Vinther et al. (2009) (black) along with the uplift curve generated using the optimal model (red) from Simpson et al. (2009) (see text for details).

2.5 The Agassiz (site A and B acceptable range; blue) and Renland (red) gaussian filtered $\delta^{18}O$ records corrected for land uplift. For Agassiz, the curves predicted at the two chosen locations were applied: site A (top) and site B (bottom). A $\delta^{18}O$ profile is interpolated/extrapolated across Greenland using the uplift-corrected and height synchronized Agassiz and Renland curves.

2.6 Temperature reconstruction at the Agassiz (dark blue) and Renland (dark red) ice caps are obtained by correcting the uplift corrected $\delta^{18}O$ from AR (Fig.2.5), for changes in the ocean's $\delta^{18}O$ content and applying the $^{o}C/\delta^{18}O$ slope of $2.1\pm0.2^{o}C/\delta^{18}O$. The original temperature reconstruction for the whole Greenland region from the Vinther et al. analysis is shown in black. The 1-σ uncertainty is shown by the lighter coloured bands and dashed black lines.

2.7 Ice elevation curves at four Greenland ice core locations (Fig. 2.1a). The original results of Vinther et al. (2009) are displayed (solid black line) along with the 1-σ uncertainty (dashed black line). The newly derived curves define a range of values associated with the two different uplift curves for Agassiz (site A & B in Fig. 2.2a); this range is indicated (darker coloured band) along with the estimated 1-σ uncertainty (lighter coloured band).

2.8 (a) Comparison of the newly derived thinning curve (black; uncertainty bounds indicated by grey lines) at the GRIP drill site with output from three-dimensional thermomechanical models of the GrIS (orange, Huybrechts (2002); blue, Lhomme et al. (2005); green, Greve (2005); purple, Tarasov & Peltier (2003); red, Simpson et al. (2009)).

2.9 Comparison of the Huy2 Greenland ice model (solid black) used in this study with the new Holocene thinning curves. The dashed black line is the predicted ice surface elevation change when the land height signal is computed using the isostasy treatment in the ice model. The solid black line is the predicted elevation change when the land height signal is computed using a more sophisticated treatment of isostasy (in terms of the loading and the Earth deformation). See text for details.

3.1 (a) The locations and names of RSL and ice-core data sites discussed and applied in this study. The circles indicate the location of sea-level index point data while triangles refer to limiting data. A list of RSL data site locations and the corresponding source literature used to compile the data base used in this study is found in Table 2. (b) A map showing the location of individual ML observations that supplement the RSL observations shown in (a); these observations are particularly useful where RSL data is sparse.

3.2 A flow diagram describing the modelling methodology of this study. Firstly, a glaciological model simulates the evolution of the GrIS (Huybrechts and de Wolde, 1999; Huybrechts, 2002). The Greenland ice model is then combined with a background global ice model lacking a Greenland component (ICE-5G - GrB; Peltier, 2004). A sensitivity analysis on the global ice model was also conducted by swapping the ICE-5G North American ice complex with a high variance set from Tarasov et al. (2012). The global ice and Earth model were adopted in the GIA and RSL model to produce predictions of RSL and glacial rebound which are compared to observations. Optimal Earth model parameters were determined using a χ^2 analysis and an F-test.

3.3 The chronology of lateral ice extent for the Huy2 model (16 ka BP – pink; 14 ka BP – dark blue; 12 ka BP – light blue; 10 ka BP – yellow; 9 ka BP – orange; 6 ka BP – red; 4 ka BP – green; present-day - black).

3.4 RSL predictions for the Huy2 and GrB ice models with their respective optimal Earth model(s). The Huy2 model predictions are generated using its two optimal Earth model where the black curves denotes the optimal viscosity structure obtained using the entire regional RSL data set (120 km lithosphere, upper mantle viscosity of $0.5\text{x}10^{21}$Pas, and lower mantle viscosity of 10^{21} Pas) and the dashed black curve represents the alternate viscosity structure obtained by considering data from the East coast only (120 km lithosphere, upper mantle viscosity of $0.3\text{x}10^{21}$Pas, and lower mantle viscosity of $50\text{x}10^{21}$ Pas). In contrast, the Greenland ice model of ICE5G (GrB; Tarasov & Peltier, 2002) is applied with the VM2 Earth model to produce RSL predictions (grey curves). Sea-level index points are shown as crosses with both time and height error bars. Lower limiting dates are denoted by grey upward pointing triangles, while upper limiting dates are shown by white downward pointing triangles. The black horizontal line highlights present-day sea-level. The grey dashed horizontal line represents the marine limit which marks the highest point reached by sea-level during ice-free conditions at each location. Data locations are shown in Fig. 3.1a (site 1-8, 9-16, 17-24, 25-32, 33-40, 41-44 constitute Fig. 3.4 a,b,c,d,e, and f, respectively).

3.5 The three LGM ice mask extents which are discussed in this study: the original Huy2 LGM extent (red), the Funder extent (green) (Funder et al., 2011), and the revised Huy3 LGM ice mask (blue).

3.6 The GRIP temperature record prescribed in the model is represented by the black curve alongside the Huy2 revised HTM temperature forcing (upper bound of dark grey envelop). The Huy3 model HTM was parameterized within the grey envelop with an optimal imposed HTM scaling shown in light grey. The following climatic events are annotated: Bolling-Allerod (BA), Younger Dryas (YD), and Holocene Thermal Maximum (HTM).

3.7 The chronology of lateral ice extent for the Huy3 model (16 ka BP – pink; 14 ka BP – dark blue; 12 ka BP – light blue; 10 ka BP – yellow; 9 ka BP – orange; 6 ka BP – red; 4 ka BP – green; present-day - black).

3.8 The left panes show the glaciologically self-consistent Tarasov et al. (2012) optimal NAIC model while the right panes show the ICE-5G NAIC component (Peltier, 2004). The two panes at the top, middle and bottom represent the 16, 12, and 8 ka BP time slices, respectively. In all panes, the Greenland component shown is the Huy3 model. There are clearly significant differences in the grid resolution, ice volume, thickness, and chronology between the two reconstructions.

3.9 A spatial plot of RSL predictions from non-Greenland ice at 16 ka BP from the (a) ICE-5G model and (b) ICE-5G with the NAIC component from the optimal Tarasov et al. (2012) reconstruction. (c) The difference between the RSL contribution from ICE-5G and the Tarasov et al. (2012) optimal model is shown to illustrate the propagating impact on Greenland RSL predictions considering uncertainties in the NAIC.

3.10 The χ^2 result for the Huy3 model with each frame shows results for a fixed value of lithospheric thickness (120 km (top), 96 km (middle), 71 km (bottom). The optimal fit was achieved with a lithospheric thickness of 120 km, upper mantle viscosity of $0.5\text{x}10^{21}$ Pas and lower mantle viscosity of $2\text{x}10^{21}$ Pas. A subset of best-fitting models (95% confidence) is listed in Table 3.3.

3.11 RSL predictions generated by the Huy2 reconstruction with the optimal Earth model (black curves) and alternate eastern Earth model (dashed black curves). The Huy3 RSL predictions were generated using the optimal Earth model (LT120, UMV0.5, LMV2; see Figure 11) and are shown by the dark grey curves with the light grey envelop representing the range in RSL predicted using Earth structures within the 95% confidence interval of the χ^2 analysis (Table 3.3). Sea-level index points are shown as crosses with both time and height error bars. Lower limiting dates are denoted by grey upward pointing triangles, while upper limiting dates are shown by white downward pointing triangles. The black horizontal line highlights present day sea-level. The grey dashed horizontal line represents the marine limit which marks the highest point reached by sea-level during ice-free conditions at each locality (site 1-8, 9-16, 17-24, 25-32, 33-40, 41-44 constitute Fig. 3.4 a,b,c,d,e, and f, respectively).

3.12 The Huy3 present-day (a) surface velocity, (b) ice thickness, and (c) the observed (Bamber et al., 2001) minus modelled (Huy3) ice thickness in metres.

3.12 The ice-core derived thinning curves compared to the Huy3 model predictions (dashed black curves) at GRIP, NGRIP, DYE-3, and Camp Century. The predictions consist of ice thinning at each core site along with vertical land motion due to glacial isostatic adjustment using the optimal Earth model (LT120, UMV0.5, LMV2). The subset of optimum Earth models that partner the Huy3 ice model (Table 3.3) were also used but make very little difference to the model curves (grey band). Results for the Huy2 ice model and its partnering Earth model (LT120, UMV0.5, LMV1) are shown by the solid black curves.

3.14 The Huy3 model predictions (blue curves) for ice sheet volume (top) and areal extent (bottom) compared to the Huy2 predictions (black curves).

3.15 Huy3 ice thickness for the time slices: (a) 16 ka BP, (b) 12 ka BP, (c) 8 ka BP, and (d) 4 ka BP.

3.16 Spatial plots of RSL predictions (in metres) from the Huy3 reconstruction using the optimal Earth model for the time slices: (a) 16 ka BP, (b) 12 ka BP, (c) 8 ka BP, and (d) 4 ka BP.

3.17 Present-day uplift rates as predicted by the Huy3 reconstruction and its optimal Earth model. The Earth structure uncertainty (upper and lower bound) on present-day uplift rates was generated using the 95% confidence interval of the χ^2 analysis and shown in Figure S7.

3.S1 (a) The distribution of marine limit observations along northeast Greenland which can indirectly constrain the LGM ice extent by bounding the amplitude of sea-level change. The marine limit is shown by the grey horizontal line in (b) along with the optimal RSL predictions from the Huy2 model (black curve), the Funder et al. (2011) LGM extent (dashed black curve), and the O'Cofaigh et al. (2012) revised extent (dotted black curve). These results are based on the optimum Earth model for Huy2 (LT120, UMV0.5, LMV1).

3.S2 (a) The distribution of ML observations along northwest Greenland which can indirectly constrain the LGM ice extent by bounding the amplitude of sea-level change. The marine limit is shown by the grey horizontal lines in (b) along with the optimal RSL predictions from the Huy2 model (black curve), the Funder et al. (2011) LGM extent (dashed black curve), and the O'Cofaigh et al. (2012) revised extent (dotted black curve).

3.S3 Predictions of ice sheet volume (top) and area (bottom) for the original Huy2 model with its DDF tuning of minus 30% (black curves) and with zero scaling (dashed black curves) which produces a massive volume and extent deficit. The revised PDD algorithm incorporated in this study is shown by the dotted curves which reached PD geometries without the unphysical tuning of the DDFs.

3.S4 The sea-level forcing is dealt with using parametric equations to define at what depth ice can remain grounded. In Simpson et al. (2009), a total of three different SLFs were investigated that resulted in early (dashed curve), intermediate (black line), and late (dotted curve) retreat histories. In this study we not only vary this parameterization spatially across Greenland but also sample a continuous range of parametric equations (grey envelop) which share the same characteristic quadratic form as those used by Simpson et al. (2009).

3.S5 RSL predictions generated by the Huy2 reconstruction with its optimal Earth model (black curves) and alternate Eastern Earth model (dashed black curves). The Huy3 RSL predictions are also shown based on its optimal Earth model (LT120, UMV0.5, LMV2; dark grey curves) and the light grey envelop around these results represents the range in predictions when a series of alternate NAIC components from a high-variance subset were adopted within the non-Greenland ice model (Tarasov et al., 2012). The dark grey dashed curve represents the Huy3 model predictions as in the non-dashed counterpart except with the original ICE-5G NAIC component in place. Sea-level index points are shown as crosses with both time and height error bars. Lower limiting dates are denoted by grey upward pointing triangles, while upper limiting dates are shown by white downward pointing triangles. The black horizontal line highlights present day sea-level. The grey dashed horizontal line represents the marine limit which marks the highest point reached by sea-level during ice-free conditions at each location (site 1-8, 9-16, 17-24, 25-32, 33-40, 41-44 constitute Fig. 3.4 a,b,c,d,e, and f, respectively).

3.S6 The (a) upper and (b) lower bound present-day uplift rates given uncertainties in Earth structure generated using the 95% confidence interval of the χ^2 analysis and the Huy3 ice model reconstruction.

4.1 From top to bottom we have the GRIP temperature record prescribed in the glaciological model as represented by the black curve alongside the envelop of parameterization for the HTM temperature forcing (dark grey envelop). The Huy3 model GRIP temperatures were parameterized with an optimal imposed HTM scaling shown by the light grey curve. The following climatic events are annotated: Bolling-Allerod (BA, 14 ka BP), Younger Dryas (YD, 11.5 ka BP), and Holocene Thermal Maximum (HTM, 9-5 ka BP). The Huy3 model predictions for ice sheet volume and extent are illustrated in the middle and bottom frame by the black curve.

4.2 (a) The Huy3 Greenland reconstruction with its optimal Earth model is applied to generate present-day uplift rates across Greenland due to past changes in the ocean and ice loading. Uncertainties in the Earth structure are considered with the Huy3 model to calculate explicit asymmetric error bars which results in (b) upper and (b) lower bound predictions for present-day uplift rates.

LIST OF SYMBOLS

Acronyms and definitions
AIS: Antarctic ice sheet
AR: Agassiz and Renland
BP: before present
DDFs: degree day factors
Ga: billion years
GIA: glacial isostatic adjustment
GrB: Tarasov & Peltier (2002) Greenland reconstruction in ICE-5G
GREEN1: Flemming & Lambeck (2004) Greenland reconstruction
GrIS: Greenland ice sheet
HTM: Holocene Thermal Maximum
Huy1: Huybrechts (2002) Greenland reconstruction
Huy2: Simpson et al. (2009) Greenland reconstruction
Huy3: Greenland reconstruction for this study
IESL: ice-equivalent sea-level
IRD: ice rafted debris
ka: thousand years
LGM: Last Glacial Maximum
LMV: lower mantle viscosity
LT: lithospheric thickness
Ma: million years
ML(s): marine limit(s)
NAIC: North American ice complex
PDD: positive degree day
PD: present-day
RSL: relative sea-level
SLF(s): sea-level forcing(s)
UMV: upper mantle viscosity

LIST OF KEY MATHEMATICAL TERMS

Q: energy flux [$W \cdot m^{-2}$]
e: strain [dimensionless]
τ: stress [Pa]
μ and λ: elastic Lamé parameters [Pa]
η: viscosity [Pa·s]
t: time [s]
ρ: density [$kg \cdot m^{-3}$]
φ: gravitational potential [$m^2 \cdot s^{-2}$]
G: gravitational constant [$m^3 \cdot kg^{-1} \cdot s^{-2}$]
$\vec{u}$: displacement field [m]
δ_{ij}: Kronecker delta
a: surface [m]
$u(a, \gamma, t)$: radial displacement [m]
$v(a, \gamma, t)$: tangential displacement [m]
$\varphi_1(a, \gamma, t)$: geopotential perturbation [$m^2 \cdot s^{-2}$]
$P_l(\cos(\gamma))$: Legendre polynomials
$\delta(t)$: Dirac delta function [s^{-1}]
$h_l^L(t)$: radial displacement love number
$l_l^L(t)$: tangential displacement love number
$k_l^L(t)$: rearrangement of matter love number
$\Upsilon^L(\gamma, t)$: gravitational potential Green's function
$\Gamma^L(\gamma, t)$: radial displacement Green's function
$L(\theta, \psi, t)$: impulse load [$kg \cdot m^{-2}$]
$G(\theta, \psi, t)$: geoid perturbation [m]
$R(\theta, \psi, t)$: surface perturbation [m]
$\xi(t)$: height shift of the geoid [m]
$S(\theta, \psi, t)$: relative sea-level [m]
f: gravitational body force [$N \cdot m^{-3}$]
H: ice thickness [m]
h: bedrock elevation [m]
τ_*: effective stress [Pa]
A(T*): flow law coefficient [$m^3 \cdot s^5 \cdot kg^{-3}$]
m: empirical flow law parameters
a: empirical flow law parameters [$Pa^{-3} \cdot s^{-1}$]
R: gas constant [$J \cdot mol^{-1} \cdot K^{-1}$]
Q: creep activation energy [$J \cdot mol^{-1}$]
T^*: absolute temperature [K]
T: temperature [K]
$\vec{v}(x, y, z)$: velocity field [$m \cdot s^{-1}$]
M: mass balance [$m \cdot s^{-1}$]
S: basal melt rate [$m \cdot s^{-1}$]
k: thermal conductivity [$J \cdot m^{-1} \cdot K^{-1} \cdot s^{-1}$]
c: heat capacity [$J \cdot kg^{-1} \cdot K^{-1}$]
Φ: internal frictional heating [$J \cdot m^{-3} \cdot s^{-1}$]
γ_g: geothermal heat flux [$W \cdot m^{-2}$]
L: latent heat [$J \cdot kg^{-1}$]

1. INTRODUCTION

1.1 ICE AND CLIMATE

The temperature at the Earth's surface fluctuates around the triple point of water, defined as the point where liquid water, ice and water vapour coexist in thermodynamic equilibrium at 273.16K (atmospheric pressure). At present, half of the Earth's land mass experiences temperatures below this triple point at some time in the year, which promotes the formation of ice. This defines the classification of the cryosphere, which encompasses all that is frozen water in the Earth system, such as ice sheets, ice caps, glaciers, sea ice, seasonal snow and permafrost (see Fig. 1.1). Since the Earth's temperature fluctuates around the freezing point, the cryosphere is highly sensitive to regional temperatures, making it one of the strongest coupled feedback systems on Earth [Brown & Mote, 2009; Flanner et al., 2011].

The thermodynamic characteristics of ice govern the exchanges of energy between the cryosphere, ocean, and atmosphere. The properties of ice also govern its sensitivity to climate change and cryospheric feedbacks. Specifically, the high specific enthalpy of water is remarkably resistive to phase changes. Water and ice also have large specific heat capacities which provide them with a tremendous amount of thermal inertia. The low thermal conductivity of ice is another property which differentiates ice from other surface features on Earth. Thermal conductivity plays a crucial role in heat transfer, especially thermal diffusion of atmospheric heat into deeper ice layers. This makes snow and ice an excellent natural insulator. This is to say, that a cold snow pack is quite resilient to the melt season, since warming the snow pack to $0^{O}C$ requires time for thermal diffusion into the snow and a great deal of energy, and the latent energy required to melt the snow is tremendous relative to the energy needed to induces changes in temperature. This all works in favour of inhibiting melt water formation and run off. Ice sheets are therefore a large energy sink which act as an indirect measure of climate change but also play a crucial role in climate change due to their influence on global energy balance [van Angelen et al., 2012].

Figure 1.1 The present state of the global cryosphere. This does not include the areal distribution of seasonal snow cover, river and lake ice, and atmospheric ice crystals. The bulk of the ice in the cryosphere (>98%) is stored within the Antarctic and Greenland ice sheets (~56.2 and ~7.1 m equivalent mean sea-level, respectively) [figure from UNEP/GRID-Arendal Global Outlook for Ice and Snow, 2007].

Net incoming radiation from the sun primarily drives temperatures on Earth, however, solar variability remains relatively static on annual to million year time-scales [Budyko, 1969, Muscheler & Heikkila, 2011]. This suggests that highly rapid and dynamic changes within the Earth system drive high frequency climate variability, such as changes in global albedo driven by seasonal/centennial/millennial scale advance and retreat of the cryosphere. The role of the cryosphere in the climate system is intricate but it is defined by the high albedo of ice and snow [Flanner et al., 2011]. Albedo is defined as the ratio of reflected to incoming radiation which is intrinsically wavelength dependent. Snow and ice both backscatter shortwave radiation, while they absorb a higher proportion of long wavelength radiation such as near-infrared [Wiscombe & Warren, 1980]. The influence of the cryosphere on planetary surface albedo and energy balance drastically affects fluxes of heat and moisture between the atmosphere, ocean, and Earth surface. This thermodynamic interplay affects the patterns of circulation in the ocean and atmosphere, which illustrates how the cryosphere modulates the climate and vice versa.

The reflection of solar radiation from ice back into the atmosphere reduces the heat absorbed at the surface. For a given time interval different energy transfer processes take place; the net energy exchange dictates the thermodynamic response of the ice. Energy exchange is often described as surface and internal energy balance. As discussed in Cuffey & Paterson (2010), the surface balance is defined as the energy flux between the ice surface and the atmosphere while internal balance refers to internal energy conservation within the ice. The net energy flux (Q_n) has units of watts per square metre and is defined as:

$$Q_n = Q_l + Q_s + Q_g + Q_p + Q_r + Q_h + Q_e \tag{1.1}$$

where Q_l is the net energy flux for long-wavelength radiation which is expressed as incoming longwave radiation minus outgoing longwave radiation (product of longwave albedo and incoming longwave radiation; $Q_{l,out} = \alpha_l \cdot Q_{l,in}$). Longwave radiation is centred on the infrared part of the electromagnetic spectrum, affiliated with thermal and terrestrial radiation. Even though the sun emits less long wavelength radiation relative to short, it still plays a pivotal role in regulating ice sheets. Longwave radiation is absorbed, re-emitted and scattered by greenhouse gases in the atmosphere such as water vapour, methane, carbon dioxide and chlorofluorocarbons. Incoming longwave radiation is far from constant because of variability in such greenhouse gases in the troposphere. Similarly, Q_s is the net shortwave radiation and is expressed identically to net longwave radiation however, for incoming/outgoing shortwave radiation. Incoming shortwave radiation is absorbed and scattered by ice and mainly drives snow and ice melt. The incoming radiation at the Earth's surface is known as insolation and varies spatially and temporally; these dependences arise due to changes in the angle of incidence through changes in the Earth's orbit around the Sun [Hays et al., 1976; Raymo & Huybers, 2008]. The subsurface energy flux is Q_g and is associated with the conduction of heat into the ice from radiation transfer. This flow of energy from the surface to the underlying snow/ice occurs through the penetration of shortwave radiation and thermal diffusion, which helps warm the subsurface. Q_p and Q_r express sensible heat advected by precipitation of snow and/or water at the surface and surface runoff. The heat fluxes affiliated with sensible and latent heat are Q_h and Q_e respectively, which deal with the snow/ice surface and the atmosphere ice boundary layer. The turbulent eddy motions at the near-surface interface and friction dissipates momentum into the upper snow layer which results in an energy flux. The net energy flux conveys whether there is a net surplus (> 0) or deficit (< 0) of energy in the surface layers.

Automatic weather stations can measure many of these energy fluxes at the surface; however, several fluxes have to be modelled using the data from these stations, such as internal energy balance [Box & Steffen, 2012]. Internal energy fluxes are assessed by modeling the internal evolution of the ice temperature. This is performed by numerically solving for vertical heat conduction using the following boundary conditions: the geothermal heat flux at the bedrock and ice surface temperature. The thermal conductivity of ice attenuates the surface temperature signal, filtering out high frequency temperature variations. The timescale of the temperature response of ice to climate change depends on the ice properties. As discussed above, ice is a great insulator, therefore, deeper ice has yet to respond to present temperatures due to the extensive time lag induced through thermal diffusion [Dahl-Jensen et al., 1998]. The ice which is located deeper within the ice column of an ice sheet has yet to respond to present conditions, the ice is just now responding to past climate because of the slow conductance of heat through ice. This illustrates how an ice sheet holds extensive information on past climate and the millennial-scale response time of ice sheets to climate change. Automatic weather stations have primarily been used extensively on valley glaciers and ice sheets in the past several decades; therefore, a compromise is generally used for most studies which extend back before a time of direct measurement of temperature, radiation fluxes, humidity, and turbulent energy fluxes over ice bodies. This generally summarizes the thermodynamics required to understand the internal temperature evolution and surface melt of an ice sheet. This allows us to extract valuable information from the major ice sheets, such as temperature histories to ice sheet behaviour to past climate. The material properties of ice define the heat exchange between the atmosphere and ocean with the cryosphere, which is paramount for understanding the climate system.

When the atmospheric conditions allow for snow accumulation to exceed ablation over several decades, the nucleation of an ice mass occurs under the weight of the overlying snow. Since ice behaves as a nonlinear visco-plastic fluid, a large enough ice mass will flow under its own weight because of internal gravitational stresses [Glen, 1955; Cuffey & Paterson, 2010]. There is a large variety of ice masses on Earth that are primarily classified by their topographic setting, such as valley glacier. A high elevation plateau with favorable conditions could result in the formation of an icefield which conforms to the topography. The distinguishing feature of an ice cap however, is that it overwhelms the underlying topography and its geometry is a product of ice flow. These ice formations are found in both hemispheres at high latitudes such as in the Canadian High Arctic. The largest ice masses in the world are continental-scale ice caps such as the Antarctic and Greenland ice sheets. These ice sheets are massive topographic features that rival major mountain chains; they influence atmospheric and ocean circulation, they store a massive volume of water affecting sea-level, and effect planetary albedo. Some important ice sheet features include ice streams and ice shelves, these dynamic features help with ice sheet drainage. Ice streams are fast flowing channels of ice with velocities significantly exceeding average regional velocities, while ice shelves are thick floating platforms of ice which directly interact with the ocean. For example, ice streams can be primarily understood through three main mechanisms; internal creep deformation as a result of gravitational stresses, the ice-bed interface being at the pressure melting point leading to decoupling of the boundary, and the deformation of subglacial sediments [Cuffey & Paterson, 2010]. These processes will be discussed in section 1.2.2 when elaborating on the theory behind simulating ice sheet behaviour and evolution.

1.1.1 ICE AGES ON EARTH

For the greater part of Earth's history, the planet has been ice-free even at high latitudes [Frakes et al., 1992; Ramstein et al., 2004b; Amiot et al., 2006]. More recently however, there have been periods of glaciation where ice sheets expanded over continents, ice caps lay scattered across Polar Regions, and mountain glaciers flowed down-valley carving the landscape. The present consensus states that there have been at least four major noteworthy ice ages [Ramstein, 2011]. From this point forth, all dates are shown in calibrated years unless stated otherwise.

The first well established severe ice age other than the present one, termed the Huronian, was originally identified by studying the layering of glacial and non-glacial sediment deposits at Lake Huron [Kasting, 2005]. This was one of the longest and most severe ice age in geologic history; it initiated 2.4 billion calibrated years (Ga) before present (BP) and terminated 2.1 Ga BP, and was suspected to have been triggered by the oxygen catastrophe, wherein the biologically induced appearance of O_2 in the atmosphere oxidized atmospheric methane, thus depleting this major greenhouse gas [Catling & Claire, 2005; Bertrand, 2005]. This biological crisis provoked the largest extinction event in Earth's history [Dorado et al., 2010]. The most severe ice age of the last billion years was the Cryogenian which occurred from 850 to 630 million years (Ma) BP [Hoffman et al., 1998; Hoffman & Schrag, 2002]. Similarly to the Huronian ice age, some believe the glacial ice sheets reached the equator producing a "snowball Earth" [Hoffman & Schrag, 2002; Ramstein 2004a], which remains a controversial topic today. During the ice age of the Cryogenian period, ice covered all major continents, inhibiting silicate weathering and photosynthesis which are dominant CO_2 sinks. Therefore, the increase of atmospheric CO_2 during the Cryogenian period is thought to have abruptly terminated this ice age [Kirschvink, 1992]. Approximately 360 Ma ago, evolution of land plants led to an immense increase in vegetation, which increased atmospheric O_2 and reduced CO_2 levels. This change in atmospheric composition resulted in the Karoo ice age (360 Ma BP) which ended approximately 260 Ma BP [Beerling & Berner, 2000; Donnadieu et al., 2006]. The present-day Antarctic ice sheet (AIS) began to substantially grow 35 Ma ago as atmospheric

CO_2 decreased [DeConto & Pollard, 2003; Pagani et al., 2005], however, it was not until 3-2.58 Ma BP, when ice sheets drastically advanced over large portions of continents in the northern hemisphere [Bintanja & van de Wal, 2008; Lunt et al., 2008; Koenig et al., 2011], that the current Pliocene-Quarternary ice age is termed to have officially begun,.

During an ice age, there are climatically cool and warm periods of glacial advance (glacial period) and glacial retreat (interglacial period). These cycles are strongly correlated with solar forcing as described by the Milankovitch theory which states that variations in eccentricity, axial tilt, and precession of the Earth's orbit determine insolation patterns on Earth [Hays et al., 1976; Raymo & Huybers, 2008]. These insolation patterns act in unison with many feedback mechanisms to describe the long-term trends of glacial/interglacial cycles. Recently, the paleoclimate records from deep-ocean and ice cores have confirmed the Milankovitch theory to a higher degree of confidence [e.g. Raymo & Huybers, 2008]. Data derived from deep-ocean sediment cores as shown in Figure 1.2 illustrate the use of $\delta^{18}O$ (^{18}O parts per thousand with respect to ^{16}O; see Section 1.3 for details) as a temperature and ice volume proxy record as the fractionation of ^{16}O and ^{18}O is primarily dominated by changes in temperature and ice volume [Dansgaard, 1961; Hansen & Sato 2012]. As explained in Section 1.3, water molecules with the isotope of ^{16}O preferentially evaporated and vapour molecules with ^{18}O are preferentially precipitated as the moisture travels towards Polar Regions.Generally speaking there is a strong correlation between $\delta^{18}O$ and temperature [Dansgaard, 1961; Johnsen & White, 1989; Johnsen et al., 2001]. As the ^{16}O enriched moisture travels and precipitates over an ice sheet, the ocean becomes enriched with ^{18}O as the ice sheet grows, which accounts for the relationship between marine $\delta^{18}O$ and global ice volume.

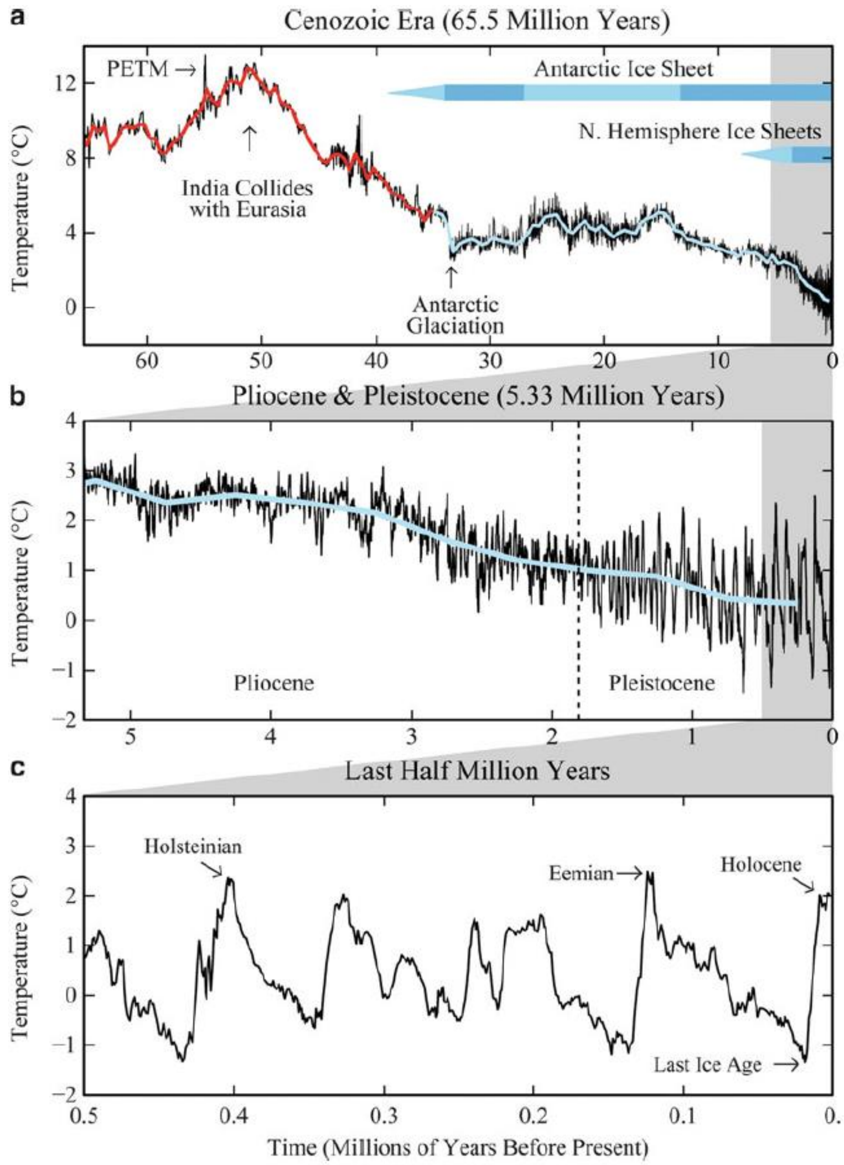

Figure 1.2 A temperature proxy record obtained from globally distributed deep ocean cores, (a) starting in the Cenozoic Era, (b) expanded from the Pliocene onward and (c) in the last half million years. The horizontal blue bars indicate the presence of modern ice sheets, the darker blue bands represent periods of full size ice sheets [From Hansen & Sato 2012].

Similar to marine sediment cores, ice cores taken from ice sheets contain a large range of proxy data. Once snow turns into ice, air bubbles are trapped within the ice. These bubbles contain valuable paleoclimate data such as a CO_2 and CH_4 concentrations of ancient atmospheres [Petit et al., 1999]. The Vostok ice core drilled in Antarctica contains one of the longest of such time series, extending 420 thousand years (ka) BP. A temperature reconstruction based on the Vostok $\delta^{18}O$ record is shown in Figure

1.3 along with a methane and carbon dioxide record which is presented in comparison to solar variation (insolation) at 65°N based on the Milankovitch theory [Imbrie et al., 1992]. High $\delta^{18}O$ values illustrate periods of high global ice volume, such as the last glacial maximum (LGM) at 21 ka BP with an excess of ~120 - 135 metres of ice-equivalent sea-level [Clark & Mix, 2002]. The last interglacial, termed the Eemian period, occurred at ~125 ka BP, which corresponds analogously to present-day interglacial conditions, low $\delta^{18}O$ values and high temperatures. However, during the Eemian period, ice sheets were significantly smaller and global mean sea level was ~6 to 9 m higher than today [Kopp et al., 2013]. Notice in Figure 1.3, the 100 ka cycle associated with Quaternary glaciation. The Eemian period (interglacial) clearly illustrates such a cycle with a slow and gradual build-up of ice volume (Dansgaard-Oeschger events) which culminated in the LGM (glacial). It was subsequently followed by a rapid

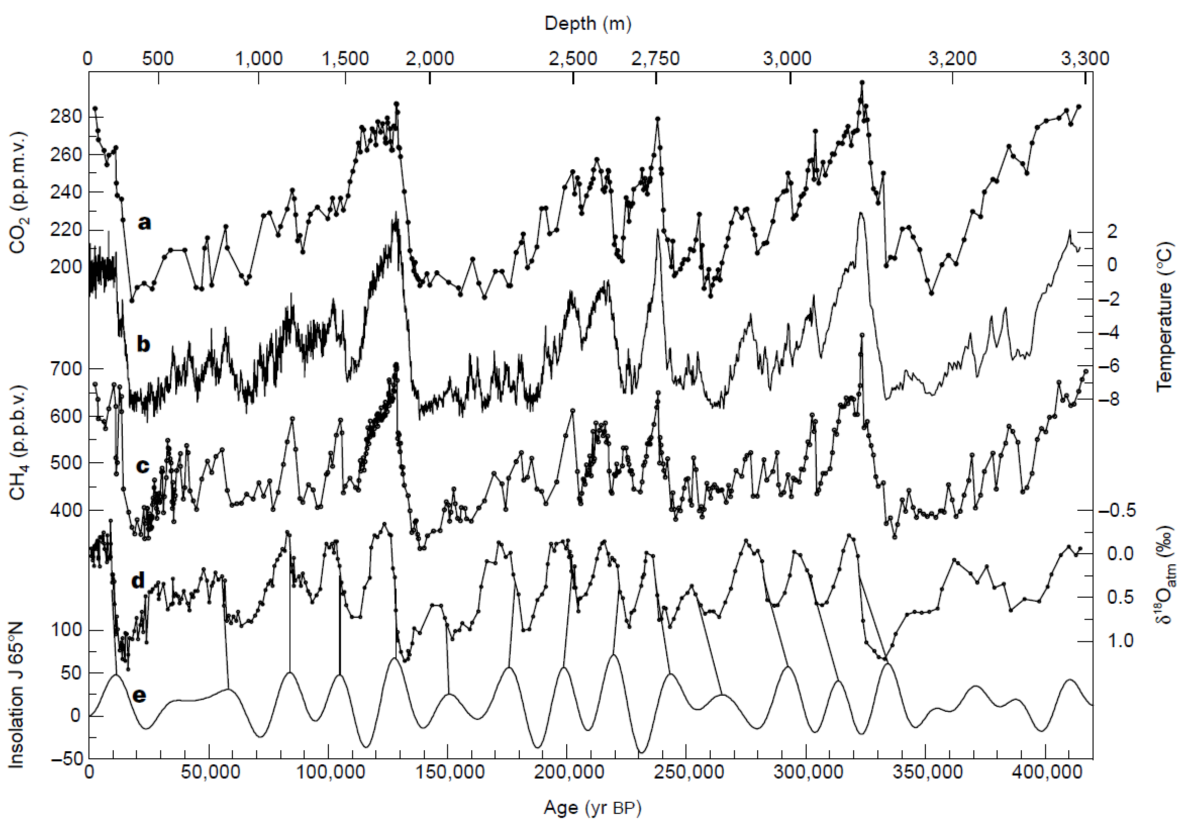

Figure 1.3 The Vostok palaeoclimate (a) CO_2 (parts per million by volume), (b) Temperature, (c) CH_4 (parts per billion by volume) and (d) $\delta^{18}O$ records (parts per thousand) and (e) solar variations at 65°N due to Milankovitch cycles (top to bottom) [Petit et al., 1999].

retreat/collapse of major ice sheets to present-day volumes (interglacial). Over this 21 ka period, some ice sheets collapsed, such as the North American ice sheets (NAIC) and Fennoscandian ice sheets, while the Greenland ice sheet (GrIS), Antarctic ice sheets (AIS), and mountain glaciers predominantly retreated in response to entering interglacial conditions [Clark & Mix, 2002; Peltier & Fairbanks, 2006]. At approximately 11 ka BP (early Holocene), the Earth transitioned from a glacial to an interglacial period [Adams et al. 1999]. This thesis focuses on the behaviour and evolution of the GrIS from the LGM to present, especially how it has retreated and re-advanced in response to sea-level and climate change.

Climate change operates on a wide range of time scales. Over the last several millions years as shown in Figure 1.2, we observe secular trends in the data most likely affiliated to processes which operate on tectonic time-scales. This involves the redistribution of continents to Polar Regions, and the converging of plates to form mountain ranges which influences atmosphere-ocean circulation and the calcium carbonate ($CaCO_3$) weathering thermostat (Carbon burial) [Sleep and Zahnle, 2001]. On millennial time-scales the climate system seems to respond to orbital changes as shown in Figure 1.3. It is important to understand the growth and decay of major ice sheets on millennial time-scales since at present, ice sheets are still responding to these changes in conjunction to contemporary climate change.

1.1.2 THE GREENLAND ICE SHEET IN THE PAST, PRESENT AND FUTURE

The mass balance of the GrIS is a quantity that indicates whether the ice sheet is gaining or losing mass by means of accumulation and ablation processes. Accumulation occurs primarily through meteoric snowfall while ablation occurs through melting and calving of icebergs. Melting mostly occurs at the ice-atmosphere and ice-ocean interface while calving is a process by which slabs of ice mechanically fracture off at the ice margin. The net mass balance is the difference between accumulation and ablation. This value varies spatially and a region where the net mass balance is zero is defined as in a state of equilibrium. Several years of positive mass balance produces a new ice layer after snow compaction, which dynamically flows under its own weight. The ice is transported to areas with negative mass balance where lower precipitation and/or warmer climate fails to sustain the ice. This body of ice perpetually attempts to achieve a steady state condition, however, the long response time of a glacier or ice sheet prevents this from occurring since the time scale of weather dynamics are far too short. Most of the world's bodies of ice have been out of equilibrium since the climatic conditions of the little ice age (~0.2 ka BP). Many glaciers and ice caps are located in places that once supported ice growth but today have a significant negative net mass balance [Meier et al., 2007] which is believed to be the case for the GrIS [Shepherd et al., 2012]. However, positive net mass balance across Greenland dominated for thousands of years which ultimately resulted in today's ice sheet.

Extensive glaciation across Greenland began around 3 million years ago [Lunt et al., 2008; Koenig et al., 2011]. The interior of Greenland started accumulating snow which underwent compaction and formed ice. As the GrIS thickened it flowed outward due to gravitationally driven internal deformation and basal sliding. The margins of the ice sheet thickened and extended past the equilibrium line where the mass balance is negative due to greater loss by surface melting and calving at outlet glaciers compared to mass gain by snowfall. Since the GrIS established itself, the climate has fluctuated drastically on Earth, resulting in varying precipitation and temperature patterns over Greenland. The ice sheet has passed through numerous glacial cycles where it has experienced enormous fluctuations in ice volume and extent. During the last interglacial, the Eemian period, the climate was $8 \pm 4\ ^{o}C$ warmer over the GrIS [Dahl-Jensen et al., 2013], and the GrIS was a fraction of its present size: ~2 to 3 metres of ice-equivalent sea-level smaller [Letreguilly et al., 1991; Ritz et al., 1997; Cuffey & Marshall, 2000; Stone et al., 2013]. From the Eemian interglacial to the glacial period, the GrIS advanced until it reached its LGM volume and extent at 19 ka BP [Funder et al., 2011]. During the LGM, global sea-level was ~120m lower which allowed the GrIS to extend out on the continental shelf; the ice sheet was thought to have an excess volume of 2-3 m ice-equivalent sea-level relative to present [Clark & Mix, 2002]. However, model reconstructions have suggested larger LGM ice volumes of 4 m ice-equivalent sea-level [Simpson et al., 2009].

The present-day GrIS covers an area of 1.71 million km^2 and contains enough ice to raise global mean sea-level by ~7 metres [Bamber et al., 2001]. The interior of an ice sheet is usually a polar desert, however the division and categorization of an ice sheet is usually based on geography and ice dynamics. For example, some ice masses adjacent to major ice sheets are dynamically independent and so are classified differently, such as the Renland ice cap in eastern Greenland. The GrIS at present is primarily land based with numerous tide-water glaciers around its periphery which undergo iceberg calving. It is currently losing mass: ~50% of this mass loss is through surface melting, while the rest is through iceberg calving [Wake et al., 2009]. The interior is thought to be near balance while the margins have experienced rapid mass loss in recent decades [Lemke et al., 2007; Shepherd et al., 2012].

Recent studies suggest accelerated mass loss of the GrIS which is partly associated with increased ice flow around major outlet glaciers and partly due to increased surface melting. During the past few years, the ablation area has increased extensively; this culminated with over 98.6% of the surface ice having dramatically thawed in June 2012 [Nghiem et al., 2012]. A mounting body of evidence indicates that the GrIS is in an overall negative state of mass balance. A recent review of geodetic observations has concluded that the GrIS is losing mass at an accelerating rate [Shepherd et al., 2012]. However the time span of these observations is relatively short on a geological time-scale, therefore there are those who argue that these changes are not a result of a sustained response to the persistent warming of modern climate but are a continued response to past changes.

What is the future of the GrIS? A look back at the early Holocene offers some insight given that temperatures across Greenland were marginally higher than today's temperatures. Reconstructions of the GrIS during this period have suggested geometries significantly smaller than the present one [Tarasov & Peltier, 2002; Flemming & Lambeck, 2004; Simpson et al., 2009]. This approach will be discussed in more details in Section 3. Studies have investigated the future evolution of the GrIS by varying greenhouse gas emission scenarios and have concluded that it will contribute 1 to 12 cm of ice-equivalent sea-level by the end of the century [Meehl et al., 2007]. This is at most 1.7% of the present ice volume within the next 87 years, making this a period of dramatic change for the ice sheet. The current warming trend is expected to continue and so ice sheets are expected to play a bigger role in global sea-level rates in the 21st century compared to the 20th century. It is important, however, to be critical of these future projections, since glaciological models tend to lack processes driving high frequency changes, such as rapid increases in ice stream velocities and unstable ground line retreats. Some studies have with relative success modelled individual Greenland outlet glaciers which capture some of these poorly understood processes [Nick et al., 2009; Vaaughan and Arthern, 2007; Alley et al., 2005]. However, they have yet to be nested into whole Greenland models to investigate the larger-scale ramifications. Studies of this sort have suggested much quicker dynamics around the margins and proposed sea-level contributions up to 54 cm by the end of the century from Greenland alone [Meehl et al., 2007]. This value is significantly higher than previously discussed and portrays the modelling challenges and uncertainties in our understanding. Recent studies have also looked into the longer term response of the ice sheet and found that most of it would disappear if, relative to preindustrial values, carbon dioxide levels have a sustained increase of 4 fold or temperatures surpass 4.5 ± 0.9 ºC [Gregory & Huybrechts, 2006; Charbit et al., 2008; Ridley et al., 2010]. Preindustrial levels of CO_2 inferred from ice cores are 260-270 ppmv and in 2013, we reached 400ppmv, while global mean temperatures are approximately 1 ºC above preindustrial levels [Hansen & Sato, 2012]. Climate models forecast a global increase in temperature of 2.1 to 4.7 ºC by the end of the century [Andrews et al., 2012]. Therefore, we have reason to further our understanding of the GrIS. It isn't simply critical to the climate system; it is responding aggressively to climate change and ultimately has a direct impact on sea-level and security in coastal areas.

1.1.3 MOTIVATION AND OUTLINE OF THESIS

The motivation for this work is to understand how the GrIS reacted to past sea-level and climate change. The physical properties of ice render ice sheets one of the slowest responding components of the climate system. As the ice sheets are still responding to past climate change from several millennia ago, it is necessary to consider this when interpreting the state of the present-day (PD) ice sheet and its response to contemporary warming.

Geodetic satellite observations track ice surface and gravitational changes across Greenland to assess contemporary mass balance of the ice sheets [Shepherd et al., 2012]. Prior to extracting mass loss from the ice sheet using geodetic observations, it is necessary to correct their record for the vertical motion of the bedrock caused by the visco-elastic relaxation of the Earth due to past ice sheet changes [e.g. King et al., 2012]. The isostatic response of the solid Earth to past changes in ice and ocean load are understood using GIA models, however uncertainties in the deglacial ice chronology and Earth structure directly affects our knowledge of present-day uplift rates. Quantifying these uncertainties and model weaknesses are crucial to increase the degree of confidence on our assessment of present-day mass balance of the ice sheets.

During the Holocene thermal maximum (HTM; 9-5 ka BP), the temperatures across Greenland were marginally higher than they are at present and the GrIS retreated past its present-day margin which resulted in a deficit ice volume relative to present [Tarasov et al., 2002; Flemming & Lambeck, 2004; Kaufman et al., 2004; Simpson et al., 2009]. Given that present Greenland temperatures are approaching those experienced during the HTM, the response of the GrIS to this past climate forcing is an analogue that can be used to inform and assess estimates of future mass balance.

An ice sheet, GIA, and RSL model was constrained to reconstruct the evolution of the GrIS over the deglaciation. The calibration builds upon the work conducted by Simpson et al. (2009) by considering a more extensive data set and extending different aspects of the model in an attempt to address data-model misfits. The remaining discrepancies highlight model weaknesses due to missing physics, poorly represented sub-grid processes, and uncertain boundary conditions which suggests avenues of future research and development.

This thesis consists of two projects, both of which improve our current understanding of the GrIS. The research involves numerically modelling the interaction between the solid Earth, ice sheets, and sea-level as the system responds to climate change. This is performed through the calibration of a glaciological, glacial isostatic adjustment (GIA) and relative sea-level (RSL) model.

The first project (Section 2) revisits a study recently published in Nature by Vinther et al., (2009). The original study used two ice-cores from the Renland and Agassiz ice cap (near the GrIS) to isolate elevation fluctuations for a number of Greenland ice-cores. The results describe the thinning of the GrIS in response to climate change during a time when temperatures across Greenland were marginally warmer than today's temperatures. As the present GrIS is experiencing accelerated mass loss, our work highlights the behaviour of the ice sheet during a time of analogous climatic conditions. We improve upon the Vinther et al. study by deriving more accurate uplift corrections for the Renland and Agassiz ice-core records using a GIA model calibrated to sea-level observations near the relevant ice-core sites. The two $\delta^{18}O$ records from Agassiz and Renland deviated from one another; therefore, a profile was derived to account for the deviations to isolate elevation variations across the Greenland ice-cores. This work yields an additional set of key constraints for reconstructing ice sheet evolution. Additionally, a more extensive uncertainty assessment was performed which concluded in much larger error bars than previously thought. Finally, we identified short-comings in the Vinther et al. (2009) study where the impact of the Innuitian ice sheet on Ellesmere island drastically influences the measured $\delta^{18}O$ values recorded at the Agassiz ice cap during the Early Holocene. These new found revelations lead to a breakdown of the original methodology and assumptions during the Early Holocene, having significant consequences on the final results of the original study published in Nature.

The second project (Section 3) and main component of this thesis focuses on reconstructing the evolution of the GrIS over the deglaciation (LGM to present). This work builds on the deglaciation model published by Simpson et al. (2009). In our case, the glaciological model was modified through its ensemble parameters to explore the uncertainty in the ice-physics, the climate forcing, and ice-ocean interaction. A chosen set of ensemble parameters defines an ice sheet reconstruction. Hundreds of reconstructions were generated and prescribed within our GIA and RSL model where we sampled a range of Earth structures. The model predictions for all the reconstructions were compared to observations to assess the model quality. The data-constrained methodology involves comparing the model to RSL observations, ice extent data, and newly derived ice-core thinning curves. Additionally, model developments are performed to the climate and sea-level forcing components to improve the physical behaviour of the ice sheet and maximize the fit to observations. The data applied constrains the model to identify a set of optimal model parameters along with an optimal reconstruction of the GrIS termed the Huy3 model. The Huy3 model predictions are explored for uncertainties with regards to Earth structure and non-local ice to evaluate the level of confidence in our reconstruction. In Section 3 we suggest avenues for improving pre-existing methods to better constrain and understand the system, decrease data-model misfits and explore sources for remaining discrepancies.

The models adopted in this work are described in section 1.2, along with some introductory derivations of the fundamental physical concepts the models are based on. In section 1.3, the data applied to constrain the models are discussed.

1.2 MODEL DESCRIPTION

The following sections 1.2.1 and 1.2.2 host a review of the physical principles underlying the evolution of ice sheets given prescribed climatic conditions and their interaction with the solid Earth and the resulting sea-level change. We explore the geophysics behind the visco-elastic relaxation of the Earth upon the unloading of ice and the consequent sea-level response and finally the thermomechanical (thermodynamic and mechanical) evolution of a body of ice. We highlight poorly constrained and key model parameters; those that are predominantly parameterized in our study to produce accurate crustal uplift predictions and ice sheet reconstructions. We end by mentioning the numerical schemes applied at solving this system of equations.

1.2.1 GLACIAL ISOSTATIC ADJUSTMENT AND RELATIVE SEA LEVEL MODEL

It is necessary to define some geophysical concepts prior to introducing some theory. First, relative sea level (RSL) is defined as the height of the ocean surface relative to the solid Earth. Therefore any process that perturbs the vertical position of the solid Earth, or the ocean surface, will contribute to sea-level change. The processes that result in RSL change operate over various timescales; from days (e.g. due to ocean tides) to millennia (e.g. due to deformations of the solid Earth caused by changes in the distribution of grounded ice; see Figure 1.4).

There are many mechanisms that deform the solid Earth and depending on the time scale of the forcing, the Earth reacts elastically and/or viscously. An elastic rheology can be expressed as:

$$e_s = \frac{\tau_s(t)}{2\mu} \tag{1.2}$$

where e_s is the shear strain, $\tau_s(t)$ is the applied shear stress, and μ is the elastic rigidity modulus. For an elastic rheology the applied stress results in an instantaneous strain response, therefore, an elastic model could be used to simulate the Earth’s response to a seismic event, such as an earthquake. On the other hand, the mantle which is found below the crust and has a thickness of approximately 2800 km has a

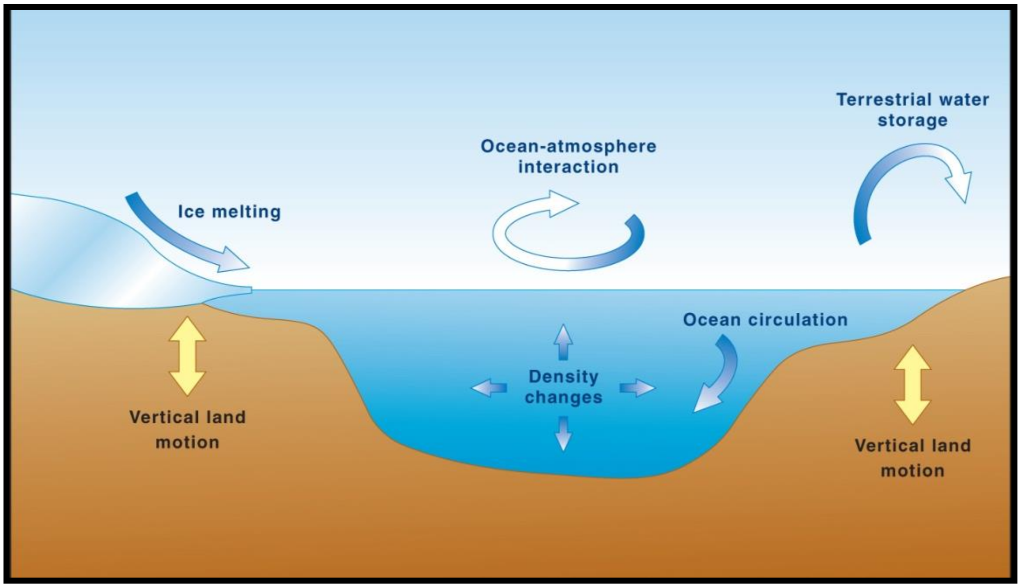

Figure 1.4 Some of the many processes that affect relative sea level (RSL) [Milne, 2008].

viscosity (η) in the range of approximately 10^{22} Pa·s and so if there were a large mass placed on the surface of the Earth there would be an immediate elastic response. However, over a longer timescale, say a few thousand years, the mantle material will flow to account for this new surface mass and for this reason, viscous models are commonly applied to simulate the response of the Earth to buoyancy stresses in the mantle. A viscous rheology is expressed as:

$$\frac{de_s}{dt} = \frac{\tau_s(t)}{2\eta} \tag{1.3}$$

and one can see that stress is proportional to the rate of strain. Since we are interested in anything that perturbs the solid Earth in an attempt to model sea level, a spherical visco-elastic Earth model is applied. This Maxwellian rheology can be generalized as:

$$e_s = \frac{\tau_s(t)}{2\mu} + \int_{to}^{t1} \frac{\tau_s(t)}{2\eta} dt \tag{1.4}$$

which is constituted of an instantaneous elastic response and a rate dependent viscous component (see Figure 1.5).

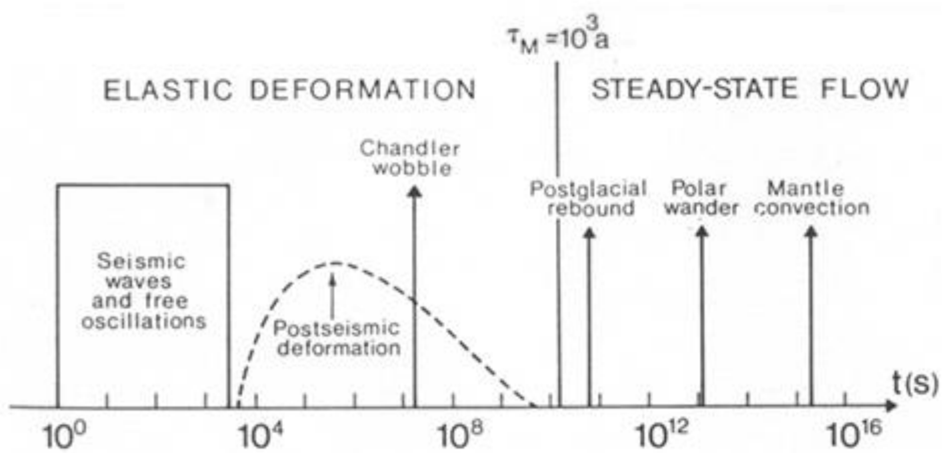

Figure 1.5 Characteristic timescales of mantle deformation processes for a Maxwell viscoelastic Earth where the Maxwell time is expressed as: $\tau_M = \frac{\eta}{\mu}$ [Yuen et al. 1982].

The ocean surface lies on an equipotential surface of the Earth's gravitational field, termed the *geoid*. The Earth's gravitational field is changing and the dominant mechanism on timescales of thousands of years is the growth and ablation of major ice sheets due to internal and external redistribution of mass. Imagine the onset of glaciation, when a large ice sheet grows over a few thousand years. Since mass is conserved within the Earth system, the addition of such a load must result in a global drop in mean sea-level, which can be expressed as the ocean surface going from one equipotential surface to another of a lower potential. Also, the presence of this new ice sheet increases the local gravitational field. This produces a rise in sea-level in ocean areas near the ice sheet since the local equipotential surface that the ocean surface rests on has been deflected upward. The new presence of a deeper water column is essentially redistribution of surface mass and, in conjunction with the original ice sheet, produces a solid Earth deformation. The deformation associated with ocean loading is termed hydroisostasy, while the deformation associated with the ice load is termed glacioisostasy (see Figure 1.6).

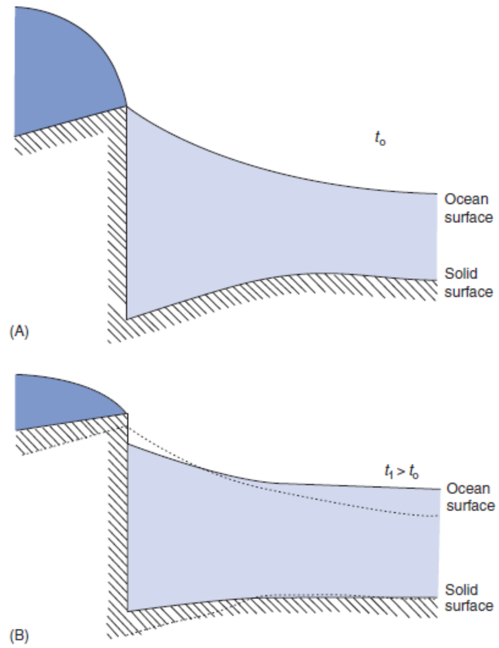

Figure 1.6 The diagram shows an exaggerated case (A) of an ice sheet gravitationally attracting surrounding ocean water producing a deeper water column and (B) consequently as the ice sheet melts, the relaxation of the ocean and subsequent solid Earth deformation [Milne, 2008].

The surface mass redistribution and subsequent solid Earth deformation, due to the growth and ablation of major ice sheets, perturbs the Earth's inertia tensor producing a change in the rate of Earth rotation and the orientation of the Earth's spin axis. This perturbation to the Earth's inertia tensor produces a global-scale deformation of the physical Earth due to the shift in the rotational potential (see Figure 1.7). This contribution to vertical land motion is small relative to other processes but it is included in the model used in Section 2 and 3. All these mechanisms work together with many others to generate a time evolution of the ocean surface and solid Earth which produces the spatio-temporal evolution of RSL.

An important remark to make is that places where large ice sheets once existed during the last glacial maximum (LGM) are undergoing significant glacial isostatic adjustment (GIA). This is due to the relatively high viscosity of mantle material, which limits the rate at which the solid Earth can reach isostatic equilibrium after the removal of ice. Therefore, sea-level proxies collected near places experiencing GIA are going to be sensitive to the Earth's viscosity structure.

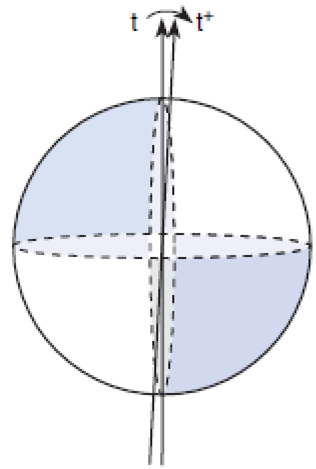

Figure 1.7 A shift from t to t[+] of the rotation pole relative to the Earth produces a global scale deformation where blue areas experience a sea-level rise while white areas a sea-level fall. Notice that this deformation can be conveniently represented by the Y_2^1 spherical harmonic (From Mound and Mitrovica 1998).

Evaluating how the Earth's gravitational field is perturbed by the presence of an ice mass and its corresponding solid Earth deformation is essential in developing the theory behind the sea-level equation. By understanding that an idealized forcing, such as one instantaneous in time and point-like in space can easily be extended for a generalized load, the response of a spherically symmetric visco-elastic Earth model to this idealised forcing is described below. Furthermore, the Earth model is in an equilibrium state prior to an impulse load and so when the body is perturbed, a small displacement out of equilibrium occurs, and the response satisfies the momentum equation (Navier-Stokes) which has been linearized:

$$\vec{\nabla}\bar{\bar{T}}_1 + \vec{\nabla}(\vec{u}\vec{\nabla})\bar{\bar{T}}_0 - \rho_1\vec{\nabla}\varphi_0 - \rho_0\vec{\nabla}\varphi_1 = 0 \tag{1.5}$$

where $\bar{\bar{T}}_i$, ρ_i, and φ_i are the stress tensor, density and the gravitational potential respectively as a function of r, the radius, and the index i is either 0 or 1 – the equilibrium and the perturbation state to their respective fields. The vector $\vec{u}$ is the load induced vector displacement field. For matter to be conserved within the system, the continuity equation must be simultaneously satisfied with equation (1.5). The continuity equation simply relates ρ_0 to ρ_1 via the divergence of the displacement field:

$$\rho_1 = -(\vec{\nabla}\vec{\mathrm{u}})\rho_0. \tag{1.6}$$

We must also satisfy the mass redistribution and its influence on the potential field φ_1 according to Poisson's equation:

$$\nabla^2\varphi_1 = 4\pi G\rho_1 = -4\pi G(\vec{\nabla}\vec{\mathrm{u}})\,\rho_0 \tag{1.7}$$

where G is the gravitational constant [$m^3 \cdot kg^{-1} \cdot s^{-2}$]. Solutions of the momentum equation (1.5) are looked for in the form of the observables φ_1 and $\vec{\mathrm{u}}$, and to do so requires the substitution of equation (1.6) into the momentum equation (1.5) and to express the deviatoric stress field, $\bar{\bar{T}}_1$, in terms of the displacement field, $\vec{\mathrm{u}}$. To do so, the constitutive equation for a visco-elastic rheology is applied which has the form:

$$\dot{\tau}_{ij} + \frac{\mu}{\eta}\left(\tau_{ij} - \frac{1}{3}\tau_{rr}\delta_{ij}\right) = 2\mu\dot{e}_{ij} + \lambda\dot{e}_{rr}\delta_{ij} \tag{1.8}$$

where μ and λ are the elastic Lamé parameters, τ_{ij} is the ij^{th} component of the stress tensor $\bar{\bar{T}}_1$, $\dot{e}_{ij}$ is the ij^{th} component of the strain rate tensor, and δ_{ij} the Kronecker delta. Using the correspondence principle, the Laplace transform of equation (1.8) is determined to yield:

$$\tilde{\tau}_{ij} = \lambda(s)\tilde{e}_{rr}\delta_{ij} + 2\mu(s)\tilde{e}_{ij} \tag{1.9}$$

$$\lambda(s) = \lambda + \frac{\frac{2}{3}\mu(\frac{\mu}{\eta})}{s+\frac{\mu}{\eta}} \quad \text{and} \quad \mu(s) = \frac{\mu s}{s+\frac{\mu}{\eta}}\,. \tag{1.10}$$

The tilde (~) denotes implicit dependence on the Laplace transform variable s. This new expression for the Laplace transformed elements of the stress tensor is then solved similarly to that of a Hookean elastic solid. Solving the elastic problem over a range and inverting the transform back to the time domain yields an expression for the stress tensor $\bar{\bar{T}}_1$ in terms of the displacement field. Therefore, substituting expression (1.9) and equation (1.6) into a Laplace transformed equation (1.5) allows us to finally solve the momentum equation (1.5) for perturbations to the displacement field and the gravitational potential. Simultaneously, solving the Laplace transform of the Poisson equation ensures that the solutions are gravitationally self-consistent. The solutions for the visco-elastic problem are expressed as an infinite series of Legendre polynomials:

$$u(a,\gamma,t) = \sum_{l=0}^{\infty} u_l(a,t) P_l(\cos(\gamma)) \tag{1.11}$$

$$v(a,\gamma,t) = \sum_{l=0}^{\infty} v_l(a,t) P_l(\cos(\gamma)) \tag{1.12}$$

$$\varphi_1(a,\gamma,t) = \sum_{l=0}^{\infty} \varphi_{1,l}(a,t) P_l(\cos(\gamma)) \tag{1.13}$$

where the radial and tangential components of the induced displacement field are $u(a,\gamma,t)$ and $v(a,\gamma,t)$ respectively, and $\varphi_1(a,\gamma,t)$ is the perturbation to the geopotential on the surface $r = a$. The Legendre polynomials are given as $P_l(\cos(\gamma))$ where γ is the great circle angle between the impulse load point and the observation point. Their coefficients are expressed as:

$$u_l(a,t) = u_l^E \delta(t) + \sum_{k=1}^{K} \delta u_{l,k}^{NE} exp(-s_k^l t) \tag{1.14}$$

$$v_l(a,t) = v_l^E \delta(t) + \sum_{k=1}^{K} \delta v_{l,k}^{NE} exp(-s_k^l t) \tag{1.15}$$

$$\varphi_{1,l}(a,t) = \varphi_{1,l}^E \delta(t) + \sum_{k=1}^{K} \delta \varphi_{1,l,k}^{NE} exp(-s_k^l t) \tag{1.16}$$

where $\delta(t)$ is the Dirac delta function which represents the instantaneous elastic response with its associated elastic component u_l^E, v_l^E, and $\varphi_{1,l}^E$. The non-elastic components $\delta u_{l,k}^{NE}$, $\delta v_{l,k}^{NE}$ and $\delta \varphi_{1,l,k}^{NE}$ are characterized by the exponential decay time s_k^l. For computational convenience, instead of using

$u(a,\gamma,t)$, $v(a,\gamma,t)$ and $\varphi_1(a,\gamma,t)$ to predict GIA observables we convert them into dimensionless numbers, the visco-elastic load Love numbers. The perturbation to the geopotential and displacement field relate to the Love numbers as such:

$$\begin{bmatrix} h_l^L(t) \\ l_l^L(t) \\ k_l^L(t) \end{bmatrix} = \left(\frac{g}{\varphi_{2,l}(a)}\right) \begin{bmatrix} u_l(a,t) \\ v_l(a,t) \\ \dfrac{-\varphi_{1,l}(a,t)}{g} \end{bmatrix}. \tag{1.17}$$

The Love numbers $k_l^L(t)$ physically represent the new arrangement of matter within the Earth, $h_l^L(t)$ the radial displacement of the solid surface, while $l_l^L(t)$ the tangential displacement. The Earth's surface gravitational acceleration is denoted by g, and $\varphi_{2,l}(a)$ is the l^{th} component in the Legendre expansion of the perturbation to the surface gravity field caused by the direct attraction of the surface load. The following expressions are obtained:

$$h_l^L(t) = h_l^{L,E}(t)\delta(t) + \sum_{k=1}^{K} r_k^{l,L} exp(-s_k^l t) \tag{1.18}$$

$$l_l^L(t) = l_l^{L,E}(t)\delta(t) + \sum_{k=1}^{K} \hat{r}_k^{l,L} exp(-s_k^l t) \tag{1.19}$$

$$k_l^L(t) = k_l^{L,E}(t)\delta(t) + \sum_{k=1}^{K} \check{r}_k^{l,L} exp(-s_k^l t) \tag{1.20}$$

The Love numbers can be decomposed into two separate time-dependent expressions, one immediate elastic component associated with the delta function and the other as the weighted exponential decay.

Sea-level change prediction requires the calculation of the perturbation to the Earth's gravitational potential and the radial displacement of the solid surface. The load induced responses for these quantities are:

$$\Upsilon^{\mathrm{L}}(\gamma,t) = \frac{ag}{M_e}\sum_{l=0}^{\infty}\left(\delta(t) + k_l^L\right) P_l(cos(\gamma)) \tag{1.21}$$

$$\Gamma^{\mathrm{L}}(\gamma,t) = \frac{a}{M_e}\sum_{l=0}^{\infty} h_l^L\, P_l(\cos(\gamma)) \tag{1.22}$$

These two equations are known as the gravitational potential and radial displacement Green's functions for a surface, respectively, where M_e represents the mass of the Earth. Notice how the gravitational potential Green's function depends on the k_l^L, which is the rearrangement of matter within the Earth and the radial displacement Green's function depends on h_l^L, which is the radial displacement of the Earth surface.

To transform the solution from an impulse load which is point-like in space and time into a generalized load, $L(\theta,\psi,t)$ with units of mass per unit area, where θ and ψ are co-latitude and east longitude, the calculation of the space-time convolution of the general load function with the relevant Green's function yields the following expression:

$$G(\theta,\psi,t) = \frac{a^2}{g}\int_{-\infty}^{t}\iint_{\Omega} L(\theta',\psi',t')\Upsilon^{\mathrm{L}}(\gamma,t-t')d\Omega' dt' + \xi(t) \tag{1.23}$$

$$R(\theta,\psi,t) = a^2\int_{-\infty}^{t}\iint_{\Omega} L(\theta',\psi',t')\Gamma^{\mathrm{L}}(\gamma,t-t')d\Omega' dt' \tag{1.24}$$

The expression $G(\theta,\psi,t)$ and $R(\theta,\psi,t)$ are respectively the load induced perturbation to the geoid and to the solid Earth, where Ω is the spatial integration over the unit sphere. By imposing conservation of mass within the system, the load-induced deformation produces a shift in the volume of the ocean which is essentially a height shift of the geoid, represented by $\xi(t)$.

From the definition of relative sea-level change, $S(\theta,\psi,t)$, can be expressed as:

$$S(\theta,\psi,t) = C(\theta,\psi,t)[G(\theta,\psi,t) - R(\theta,\psi,t)] \tag{1.25}$$

where $G(\theta,\psi,t)$ is the ocean surface (geoid), $R(\theta,\psi,t)$, the solid earth and the function $C(\theta,\psi,t)$ is the ocean Heaviside function which is expressed as:

$$C(\theta,\psi,t) = \begin{cases} 1, & \textit{located in the ocean} \\ 0, & \textit{located on land} \end{cases} \tag{1.26}$$

It is important to note that there is a time dependence on the ocean function; the model accounts for migrating shorelines [Milne, 1998; Mitrovica and Milne, 2003], since as sea-level changes so do the contour of continents. Substituting equation (1.23) and (1.24) into (1.25) yields an expression for GIA-induced sea-level change on a non-rotating visco-elastic Earth:

$$S(\theta,\psi,t) = C(\theta,\psi,t)[\int_{-\infty}^{t} \iint_{\Omega} a^2 L(\theta',\psi',t') \left\{ \frac{\Upsilon^{L}(\gamma,t-t')}{g} - \Gamma^{L}(\gamma,t-t') \right\} d\Omega' dt' + \xi(t)]. \tag{1.27}$$

This fundamental expression is termed the sea-level equation. The Love numbers depend on the elastic and density structure of the Earth which can be taken from seismic constraints [Dziewonski & Anderson, 1981]. Moreover, while the elastic response is instantaneous, the viscous response depends on time since the system flows slowly. Therefore to incorporate a viscous component to the model we require a time dependant component which depends on the ice load history.

The load $L(\theta,\psi,t)$ is composed of an ice component $I(\theta,\psi,t)$, and an ocean component, $S(\theta,\psi,t)$, from the subsequent ocean redistribution due to the ice load, which is expressed as:

$$L(\theta,\psi,t) = \rho_I I(\theta,\psi,t) + \rho_W S(\theta,\psi,t) \tag{1.28}$$

where ρ_I and ρ_W are the density of ice and water respectively. With a substitution of equation (1.28) into (1.27) our expression for the sea-level equation becomes:

$$S(\theta,\psi,t) = a^2 C(\theta,\psi,t)\left[\int_{-\infty}^{t}\iint_{\Omega} \rho_I I(\theta',\psi',t')\left\{\frac{\Upsilon^{\mathrm{L}}(\gamma,t-t')}{\mathrm{g}} - \Gamma^{\mathrm{L}}(\gamma,t-t')\right\} d\Omega' dt' + \right. \tag{1.29}$$
$$\left. \int_{-\infty}^{t}\iint_{\Omega} \rho_W S(\theta',\psi',t')\left\{\frac{\Upsilon^{\mathrm{L}}(\gamma,t-t')}{\mathrm{g}} - \Gamma^{\mathrm{L}}(\gamma,t-t')\right\} d\Omega' dt' + \xi(t)\right].$$

Take notice on how the sea-level is now an integral function of sea-level. Therefore accurate solutions are obtained using an iterative method; specifically a pseudo-spectral iterative numerical algorithm is applied in solving the sea-level equation [Kendall et al., 2005].

Since the original theory of the sea-level equation developed by Farrell and Clark (1976), there have been many extensions to their work, such as including global deformation due to a shift in rotational potential [Milne & Mitrovica, 1998], to the inclusion of migrating shorelines [Milne, 1998, Mitrovica & Milne, 2003] which are processes included in our GIA and RSL model.

There are two primary inputs to modeling sea level using the sea-level equation: an ice load history, which is the evolution of ice sheets through time where a continuously changing load is broken down into a series of ice loads $L_i(\theta,\psi,t)$ and Heaviside functions $H(t-t_i)$ applied at a time t_i, and an Earth model which is the rheological properties of the Earth's interior which simulate the deformation associated with the surface load and rotational potential. As mentioned earlier, a spherically symmetric visco-elastic rotating Earth model is adopted to calculate relative sea-level change for which an elastic and density structure is given by Preliminary Reference Earth Model (PREM) [Dziewonski & Anderson, 1981], and a tri-layer approach is used for the viscosity profile: lithosphere, upper mantle, and lower mantle. The lithosphere is treated elastically, having a relatively high viscosity and so we only vary its thickness (LT), while the upper-lower mantle boundary is chosen at a depth of 1800km, where a viscosity is chosen for both upper and lower cells (UMV, LMV).

Part of the problem in solving the sea-level equation is the quantity being solved for is a key component of the load which drives the system. The viscosity structure is a parameter inferred by modeling GIA and is still debated and being researched today. The accuracy of the viscosity structure will depend on the accuracy of the ice model which is why in this study we solve both systems and study parameter trade-offs.

There are different ways to generate a realistic ice model. One could use geomorphological data sets, such as moraines, to map out ice extent in combination with GIA data to infer an ice thickness [e.g. Peltier, 2004], or one could produce an ice reconstruction from a glaciological self-consistent ice sheet model which uses input data from climate change, sea-level, topography, and basal conditions [e.g. Huybrechts, 2002]. Both of these methods produce an ice load history to input into our model each with their own strengths and weaknesses. Since one can obtain a best fit between observation and model output with a particular ice model and earth structure, we find there are many solutions that give a reasonable fit to observations. Therefore we have to address the issue of non-uniqueness by either performing sensitivity studies to determine parameter trade-off between ice loading and viscosity models or one could utilize a subset of data which is relatively insensitive to either the viscosity model or ice model to constrain one or the other. In this thesis we combine both approaches to reconstruct the evolution of the Greenland ice sheet while simultaneously calibrating in series a GIA and RSL model to identify internally self-consistent model parameters.

1.2.2 THREE-DIMENSIONAL THERMOMECHANICAL ICE SHEET MODEL

The physical principles underlying the evolution of ice sheets are given by the mechanical and thermodynamic properties of ice. A simple illustration of a glacier (Figure 1.8) will be used as reference to highlight concepts. As stated in Section 1.1 ice deforms under its own weight, transporting ice from the interior to the margins where the ice sheet is more susceptible to mass loss. The ice flows over bedrock that is occasionally sediment covered. The variable topography channels ice flow or impedes it. Additionally geothermal heat from the bedrock can modify basal conditions by introducing meltwater which can facilitate ice transport through lubrication. The ice interacts with the ocean and atmosphere by means of energy exchange affecting mass balance of the ice sheet through surface melting and calving of icebergs.

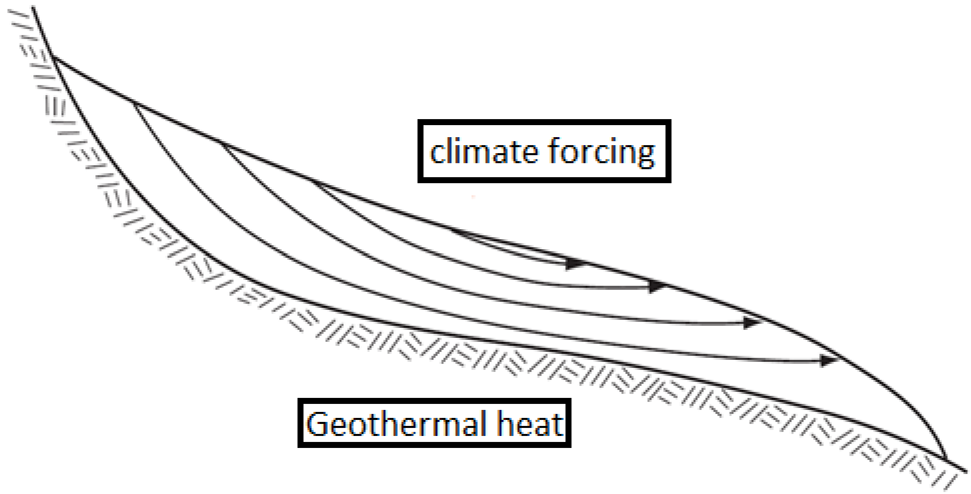

Figure 1.8 The cross section of a valley glacier experiencing gravitationally driven deformation. The pathlines are shown to be transporting elements of ice to a region of lower gravitational potential. The mass balance of a body of ice is dictated by the climate forcing, where generally speaking high altitudes undergo net accumulation while ablation occurs in lower warmer terrain. The basal topography, composition, and temperature constrain the velocity profile of the ice. A history of past climate and of geothermal heat at the base provides the necessary boundary conditions to understand the temperature evolution of the ice.

We begin by developing the mechanical theory of ice from Newton's second law for a continuum. The Navier-Stokes equation encapsulates conservation of momentum and relates stresses to body forces. Ice undergoes gravitationally driven deformation and given that this force is continuously acting on it, we assume the ice is in a steady state (no acceleration):

$$\sum_{i=x,y,z} \partial_i \tau_{ji} + f_i = 0 \tag{1.30}$$

where τ_{ji} are elements of the stress tensor and f_i is the body force, in this instance f_i is the gravitational force. The expression expands out to the following in Cartesian coordinates:

$$\frac{\partial \tau_{xx}}{\partial x} + \frac{\partial \tau_{xy}}{\partial y} + \frac{\partial \tau_{xz}}{\partial z} = 0 \tag{1.31}$$

$$\frac{\partial \tau_{yx}}{\partial x} + \frac{\partial \tau_{yy}}{\partial y} + \frac{\partial \tau_{yz}}{\partial z} = 0 \tag{1.32}$$

$$\frac{\partial \tau_{zx}}{\partial x} + \frac{\partial \tau_{zy}}{\partial y} + \frac{\partial \tau_{zz}}{\partial z} = \rho g \tag{1.33}$$

where g is the acceleration due to gravity (9.81 m/s^2) and ρ is the density of ice (910 kg/m^3). For large bodies of ice (i.e. ice sheets) you can assume the bedrock and surface slopes are relatively small which implies normal stress deviators can be neglected since hydrostatic equilibrium dominates (longitudinal stress = hydrostatic stress) [shallow ice approximate; Nye, 1969].

$$\frac{\partial \tau_{zz}}{\partial z} \gg \frac{\partial \tau_{xz}}{\partial x} + \frac{\partial \tau_{yz}}{\partial y}\,. \tag{1.34}$$

This assumption fails marginally in several instances. For instance this occurs when there is too much basal sliding at the margins due to large slopes [Weertman, 1961]; moreover, high frequency irregularities in the bedrock causes similar inaccuracies [Budd, 1970]. This implies the approximation has issues resolving a fine grid due to rapidly varying slopes; however it remains very applicable for large ice sheets [Oerlemans, 1981; Tarasov & Peltier, 2002; Whitehouse et al., 2012]. Furthermore, to fully solve the system without this approximate is extremely computationally expensive and would render a large-ensemble data-constrained millennial-scale ice sheet calibration impossible.

We define a deviatoric stress tensor $\tau_{ij}{}'$ as the stress tensor minus the hydrostatic component with:

$$\tau'_{xx} = 0 = \tau'_{yy} = \tau'_{zz} \tag{1.35}$$

$$\tau_{xx} = \tau_{yy} = \tau_{zz} \tag{1.36}$$

$$\tau'_{ij} = \tau_{ij} - \delta_{ij}\frac{1}{3}\tau_{kk} \tag{1.37}$$

where δ_{ij} is the kronecker delta and i,j,k = x,y,z. Additionally, the ice sheet does not suffer shear stress at its sides ($\tau_{yx} = \tau_{xy} = 0$) since deformations by shear are under its own weight which is parallel to the geoid. Therefore, the non-zero shear stress components are τ_{xz} and τ_{yz} which reduces the equations of motion to the following:

$$\frac{\partial \tau_{xx}}{\partial x} + \frac{\partial \tau_{xz}}{\partial z} = 0 \tag{1.38}$$

$$\frac{\partial \tau_{yy}}{\partial y} + \frac{\partial \tau_{yz}}{\partial z} = 0 \tag{1.39}$$

$$\frac{\partial \tau_{zz}}{\partial z} = \rho g \tag{1.40}$$

The ice thickness and bedrock elevation is denoted by H(x,y) and h(x,y) respectively, while neglecting atmospheric pressure you can integrate equation (1.40) from the surface z = H + h to a height z yielding an expression for the normal stress components.

$$\tau_{zz} = \rho g(z - H - h) = -\rho g(H + h - z) = \tau_{xx} = \tau_{yy}. \tag{1.41}$$

Equation (1.38) and (1.39) are similarly integrated (e.g. $\tau_{xz} = -(H + h - z)\frac{\partial \tau_{xx}}{\partial x}$) and substituting equation (1.41) yield shear stress:

$$\tau_{xz} = -\rho g(H + h - z)\frac{\partial (H + h)}{\partial x} \tag{1.42}$$

$$\tau_{yz} = -\rho g(H + h - z)\frac{\partial (H + h)}{\partial y} \tag{1.43}$$

Now that we have obtained the relevant stress equations we require a constitutive equation which relates the stress to the strain in the goal of deriving a velocity field. The constitutive creep equation for polycrystalline ice was first described by Glen (1955) using a non-linear plastic flow law [Cuffey & Paterson, 2010]:

$$\dot{\varepsilon}_{ij} = A(T^*)\tau_*^{n-1}\tau_{ij} \tag{1.44}$$

where $\dot{\varepsilon}_{ij}$ is the strain rate, $\tau_* = \sqrt{\tau_{xz}^2 + \tau_{yz}^2}$ is the effective stress, n is the flow law exponent often chosen to be 3, and A(T*) is a flow law coefficient. The flow law exponent and coefficient remains a source of uncertainty as they depend on numerous poorly constrained regional factors of the ice [Cuffey & Paterson, 2010]. For example, the flow law coefficient depends on the temperature of the ice, crystal size, orientation, impurities, presence of meltwater, among other things. Here we only consider temperature dependence since this remains a dominating parameter and we are interested in the thermo-mechanical properties of the ice. An approximation for the flow law coefficient is proposed by laboratory experiments and is termed the Arrhenius relationship:

$$A(T^*) = m \cdot a \cdot e^{-\frac{Q}{RT^*}}. \tag{1.45}$$

The constants 'm' is initialize as 3.5 [dimensionless] and tuned through time to modify flow and 'a' which is also an empirically determined tuning parameters, R is the gas constant (8.314 J/mol·K), and Q is the creep activation energy. T* is the absolute temperature corrected for pressure melting:

$$T^* = T + 8.7 \cdot 10^{-4}(H + h - z). \tag{1.46}$$

The activation energy and parameter 'a' are determined empirically and depend on the temperature regime of the ice:

$$\begin{gathered} a = 1.14 \cdot 10^{-5} Pa^{-3} yr^{-1}, Q = 60\ KJ \cdot mol^{-1}\ when\, T^* < 263.15K \\ a = 5.47 \cdot 10^{10} Pa^{-3} yr^{-1}, Q = 139\ KJ \cdot mol^{-1}\ when\, T^* \geq 263.15K \end{gathered} \tag{1.47}$$

Finally, we relate the strain rate (rate of deformation) to the displacement field:

$$\dot{\varepsilon}_{xz} = \frac{1}{2}\left(\frac{\partial v_x}{\partial z} + \frac{\partial v_z}{\partial x}\right) = A(T^*)\tau_*^{n-1}\tau_{xz} \tag{1.48}$$

$$\dot{\varepsilon}_{yz} = \frac{1}{2}\left(\frac{\partial v_y}{\partial z} + \frac{\partial v_z}{\partial y}\right) = A(T^*)\tau_*^{n-1}\tau_{yz} \tag{1.49}$$

where $v_i = \frac{\partial i}{\partial t}$ is the velocity in the i^th^ direction. From these expressions a 3D velocity vector $\vec{v}(x, y, z)$ [m/yr] is obtained knowing that vertical gradients in velocity are much greater than horizontal ones:

$$\frac{\partial v_z}{\partial x} \ll \frac{\partial v_x}{\partial z}, \quad \frac{\partial v_z}{\partial y} \ll \frac{\partial v_y}{\partial z}. \tag{1.50}$$

After some brief manipulation using equation (1.48), (1.50), and (1.42) one obtains:

$$\frac{1}{2}\frac{\partial v_x}{\partial z} = -A(T^*)\rho g(H + h - z)\frac{\partial(H + h)}{\partial x}\ \tau_*^{n-1} \tag{1.51}$$

$$\tau_* = \rho g(H + h - z)[\nabla(H + h) \cdot \nabla(H + h)]^{\frac{1}{2}} \tag{1.52}$$

$$\frac{\partial v_x}{\partial z} = -2\, A(T^*)[\rho g(H + h - z)]^n \frac{\partial(H + h)}{\partial x}[\nabla(H + h) \cdot \nabla(H + h)]^{\frac{n-1}{2}} \tag{1.53}$$

$$\frac{\partial v_y}{\partial z} = -2\, A(T^*)[\rho g(H + h - z)]^n \frac{\partial(H + h)}{\partial y}[\nabla(H + h) \cdot \nabla(H + h)]^{\frac{n-1}{2}} \tag{1.54}$$

which is integrated for the velocity from the bedrock to a height 'z' in the ice yields.

$$v_x(z) - v_x(h) = -2\,(\rho g)^n[\nabla(H + h) \cdot \nabla(H + h)]^{\frac{n-1}{2}} \frac{\partial(H+h)}{\partial x} \cdot \int_h^z A(T^*)(H + h - z)^n dz. \tag{1.55}$$

Similarly, the velocity component v_y is obtained from equation (1.49), (1.50), and (1.43) to yield the velocity field of the ice.

$$\vec{v}(z) - \vec{v}(h) = -2\,(\rho g)^n[\nabla(H + h) \cdot \nabla(H + h)]^{\frac{n-1}{2}}\nabla(H + h) \cdot \int_h^z A(T^*)(H + h - z)^n dz. \tag{1.56}$$

At the base of the ice sheet you have the boundary condition $\vec{v}(h)$ which represents the basal sliding velocity. This depends on basal conditions such as whether the bedrock is covered in sediments which facilitates the flow of ice. Furthermore, whether it is warm or cold-based ice implies the potential introduction of meltwater which can saturate the sediment pores that decouples the base of the ice from the bedrock.

Recall A(T*) is a function of temperature; therefore, the velocity depends on temperature of the ice. This implies we have to solve for the temperature distribution in the ice to properly generate a velocity field. Integrating equation (1.56) from the base of the ice to the surface generates the depth averaged horizontal velocity.

$$\vec{\bar{v}}H = -2\,(\rho g)^n[\nabla(H+h)\cdot\nabla(H+h)]^{\frac{n-1}{2}}\nabla(H+h)\cdot\int_h^{H+h}\int_h^z A(T^*)(H+h-z)^n\,dzdz. \tag{1.57}$$

Substituting this expression in the vertically integrated continuity equation, sets up the time-dependent evolution of the ice sheet:

$$\frac{\partial H}{\partial t} = \nabla\left(\vec{\bar{v}}H\right) + M - S \tag{1.58}$$

where M is the mass balance and S is the basal melting rate. Interestingly, the flux divergence term can be written as $-\nabla \mathrm{D}\cdot\nabla(H+h)$ where D could be interpreted as a nonlinear diffusion coefficient. Finally, we apply the expression for conservation of mass of the system:

$$\nabla\cdot\vec{v} = 0 = \frac{\partial v_x}{\partial x} + \frac{\partial v_y}{\partial y} + \frac{\partial v_z}{\partial z} \tag{1.59}$$

$$0 = \dot{\varepsilon}_{xx} + \dot{\varepsilon}_{yy} + \dot{\varepsilon}_{zz} \tag{1.60}$$

which yields the vertical velocity component of the ice:

$$v_z(z) - v_z(h) = -\int_h^z \nabla\cdot\vec{v}(x,y)\,dz \tag{1.61}$$

while obeying kinematic boundary conditions at the bedrock and ice surface.

$$v_z(h) = \frac{\partial h}{\partial t} + \vec{v}(h)\cdot\nabla \mathrm{h} \tag{1.62}$$

$$v_z(H+h) = \frac{\partial(H+h)}{\partial t} + \vec{v}(H+h)\cdot\nabla(\mathrm{H}+\mathrm{h}) - \mathrm{M} + \mathrm{S}. \tag{1.63}$$

With equation (1.56) and (1.61) the three dimensional velocity field is fully described. However, the temperature distribution within the ice has to be solved for simultaneously to evaluate the proper mechanical evolution of an ice sheet.

To adjust the flow law parameter A(T*) we need to know the temperature distribution in the ice. This is performed by evaluating the dominant heat transfer mechanisms within the ice. As discussed in Section 1.1, the thermodynamics of ice are encapsulated within equation (1.64) with the first term on the right hand side is the diffusion component, the second is the advective and the third term is the internally generated deformational friction term.

$$\frac{\partial T}{\partial t} = \frac{k}{\rho c_p}\nabla^2 T - \vec{v}\cdot\nabla T + \frac{\Phi}{\rho c_p}. \tag{1.64}$$

The variable T is the temperature, t is time, k is the thermal conductivity (6.62x10^7 J/m·K·yr), ρ is the density of ice, c_p is the heat capacity of ice (2009 J/kg·K), $\vec{v}$ is the ice velocity, and finally Φ is the internal frictional heating [J/m^3·yr]. Vertical gradients in temperature are much greater than horizontal ones which implies $\nabla^2 T \approx \frac{\partial^2 T}{\partial z^2}$. The internal heating rate per unit volume is expressed by:

$$\Phi = \sum_{i,j} \dot{\varepsilon}_{ij}\, \tau_{ij}. \tag{1.65}$$

As previously stated, we assume longitudinal strain rates are small relative to horizontal shear strain rates, which simplifies the expression to:

$$\Phi \cong 2\dot{\varepsilon}_{xz}\tau_{xz} + 2\dot{\varepsilon}_{yz}\tau_{yz} = -\rho g(H+h-z)\frac{\partial\vec{v}}{\partial z}\nabla(H+h). \tag{1.66}$$

We apply boundary conditions at the surface and base of the ice sheet. The surface boundary condition consists of the mean annual temperature which remains one of the largest source of uncertainty in ice sheet modelling due to the poorly constrained temporal and spatial evolution of climate over millennias.

We apply ice-core temperature records to constrain the prescribed temperature field, however the records are few and far between resulting is many assumptions being made. The boundary condition at the base is the heat gain from sliding friction and geothermal heat flux which is also another poorly constrained parameter since we know little about the conditions at the base of the ice sheet.

$$\left[\frac{\partial T}{\partial z}\right]_b = \gamma_g + \frac{\tau_b \vec{v}(h)}{k}. \tag{1.67}$$

The variable γ_g is the geothermal heat flux at the base which varies spatially, τ_b is the basal shear stress, and $\vec{v}(h)$ is the basal sliding velocity. Phase changes at the base of the ice are incorporated when basal temperatures are at the pressure melting point or when basal melt water is present. The basal melt rate is expressed as:

$$S = \frac{k}{\rho L}\left\{\left[\frac{\partial T}{\partial z}\right]_c - \left[\frac{\partial T}{\partial z}\right]_b\right\} \tag{1.68}$$

where the first right hand term is the basal temperature gradient after correcting for pressure melting while L is the specific latent heat of fusion (3.35×10^5 J/kg).

With equation (1.64) we can fully solve for the temperature distribution in the ice. However, the temperature profile in the ice depends on the stress, strain and velocity of the ice, conversely the velocity of the ice depends on the temperature distribution of the ice. One can see the need to simultaneously solve this system of equations numerically to fully understand the thermodynamic and mechanical properties of the ice through time. To solve this system of nonlinear parabolic differential equations, the numerical methods applied are those of a finite difference scheme [Huybrechts, 1986].

Now that we can confidently solve for the thermomechanical properties of an ice sheet, we can explore the necessary climate and sea-level forcing that result in its evolution. Prescribed climatic conditions are derived across the ice sheet from an ice-core from the summit of the GrIS (GRIP). Other ice-cores are applied as guidance to infer the extrapolated profile across Greenland. However the temperature and precipitation patterns prescribed in the model are poorly constrained and remain a significant source of uncertainty. To account for this, the climate forcing acts as a key tuning parameter (see Section 3). Due to the millennial-scale nature of this study, the model incorporates a positive degree day (PDD) algorithm to deal with mass balance. Based on weather station observations, a PDD scheme correlates the number of days with a positive degree to melt and runoff [Cuffey & Paterson, 2010]. As described in greater detail in Section 3, the PDD algorithm incorporates processes such as saturation of the snowpack by melt water, among other things. Additionally, model developments to the climate forcing were conducted for this study which is described in Section 3.5.2.2. The sea-level forcing is defined at the ice-ocean interface where marine-based ice calves icebergs into the ocean. Given that there lacks a proper ice calving law and that these (sub-grid) processes are not fully understood, the glaciological model adopts a series of parametric equations to simulate ice flux past the grounding line (see Section 3.5.2.3). Given that a mean (eustatic) sea-level history is prescribed in the model as described in Section 1.3, model developments were conducted to take into consideration the spatial variability in past sea-level. This is performed by regionally parameterizing the sea-level forcing to best capture the ice extent and sea-level observations.

There are other poorly constrained boundary conditions which contribute to the overall model uncertainty as mentioned in Section 1.3. Moreover, a number of additional key model parameters were varied over the course of this project, including extensive sensitivity analyses to investigate parameter trade-off and issues of non-uniqueness.

1.3 DATA

This project involves working with large quantities of field observations. The observations applied range from ice-cores, marine cores, and lake cores to weather station data and ice-penetrating radar surveys. The data serves a variety of applications: from (i) model boundary conditions and/or prescribed inputs, (ii) direct constraint to model output, and (iii) poorly constrained and/or qualitative supporting observational evidence. A summary of the observations is going to be described below to provide the necessary introductory context for Sections 2 and 3.

Ice-core records are obtained by drilling through a body of ice such as an ice cap or ice sheet and provide a continuous column of ice. A body of ice forms through positive mass balance, where annual layer of snow superimpose and undergo compaction. As the density of snow increases, it becomes firn and subsequently transitions into ice which is defined as the point that the ice seals bubbles off from the atmosphere trapping atmospheric properties in the ice. A column of ice therefore consists of a record of past atmospheric composition (e.g. CO_2, CH_4). The isotopic composition of the water constituting the ice preserves additional characteristics pertaining to past climate. The Earth is considered a closed system which implies that the relative isotopic abundance of water molecules is globally fixed through time. The most abundant isotopes of hydrogen and oxygen are ^{1}H and ^{16}O (99.985% and 99.757%, respectively) with their less abundant stable isotopic counterpart ^{2}H and ^{18}O (0.015% and 0.021%, respectively). Generally speaking, isotopically light water molecules preferentially evaporate and as the moisture is transported poleward isotopically heavy molecules preferentially precipitate. Consequently, snowfall is rich in isotopically light water making ice sheets a major sink for light water molecules. The fractionation of hydrogen and oxygen isotopes preserves similar physical characteristics of the climate system therefore are treated as a comparable proxy. For this reason we focus the remainder of the discourse on oxygen fractionation which is expressed as:

$$\delta^{18}O = \left[\frac{\left({}^{18}O/{}^{16}O\right)_{sample} - \left({}^{18}O/{}^{16}O\right)_{standard}}{\left({}^{18}O/{}^{16}O\right)_{standard}}\right] \cdot 1000\ {}^{o}/_{oo} \tag{1.69}$$

where the standard value is the present-day standard mean ocean water. Many other processes affect the fractionation process of $\delta^{18}O$ and the values represent different proxies depending on whether the record is derived from a marine core or an ice-core. The $\delta^{18}O$ values obtained from ice cores are influenced by air temperature, location of the moisture source, the pathways by which the moisture is transported, elevation and precipitation (Dansgaard, 1961, Vinther et al., 2009). To first order ice-core $\delta^{18}O$ values represent past ice volumes and surface air temperatures. The temperature along the length of the borehole which contained the ice-core is measured to reveal the temperature of the surround ice with depth. A Monte Carlo inverse modelling method is applied to calibrate the $\delta^{18}O$ record with the borehole temperature profiles by numerically solving the differential equation for heat conduction (Section 1.2.2) [Dahl-Jensen et al., 1998; Dahl-Jensen et al., 2013]. A parameterisation which best defines the relationship between $\delta^{18}O$ and temperature is obtained by identifying the proper temperature history which best reproduces the borehole temperature profile. Temperature reconstructions from ice-cores $\delta^{18}O$ records enlighten the past climate and act as a crucial driving boundary condition in contemporary glaciological models. The sparse geographic distribution of ice-cores across Greenland which capture the deglaciation implies that many assumptions on the past climate are still necessary in generating a temperature profile. Furthermore, considering that little is known on past precipitation patterns, the climate forcing remains one of the largest sources of uncertainty in any deglacial ice sheet model.

To freely simulate the evolution of an ice sheet model, a climate and sea-level history is required. A climate history is generated using ice-core temperature reconstructions while a sea-level history is derived from marine sediment cores. In the marine sediments are fossil remains from benthic foraminifera which excrete calcium carbonate ($CaCO_3$) shells which are measured for $\delta^{18}O$. Contrary to ice-cores, marine core $\delta^{18}O$ values reflect deep water temperatures from where the shells were formed and global ice volume. An effectively global distribution of marine records is applied to derive a global ice volume history from marine shells $\delta^{18}O$ records which is converted to a global mean sea-level history (Imbrie et al., 1984). Now that we have described the necessary prescribed forcings to simulate the glacial system we require a few remaining boundary conditions, I will now specifically highlight the bedrock (basal) topography. Airborne ice-penetrating radar flights have passed over large portions of the GrIS. Radio-echo sounding methods simply propagate electromagnetic waves through the ice and measure arrival times of the reflected waves to derive ice thickness. Airborne sweeps across Greenland can then yield bedrock topography beneath the ice [Bamber et al., 2001]. Moreover, a present-day geometry and volume for the ice sheet are obtained from the procedurally interpolated thickness profiles which act as one of the most powerful direct constraints on our GrIS reconstruction. It should be noted that the present-day bedrock topography is not necessarily that of the LGM considering processes such as glacial flow-induced sediment transport mechanisms. This is however the assumption we apply in our model and it remains another poorly constrained boundary condition which ultimately contributes to the overall uncertainties.

The key boundary conditions prescribed in the glaciological model have now been described in the preceding paragraph. Thus we now explore geological and geomorphological observations that enlighten the past chronology of the ice sheet. Around the periphery of the Greenland land mass are continental shelves beneath relatively shallow seas which were generally exposed during glacial periods. At the LGM the GrIS extended far out onto the continental shelf. As it retreated it marked the landscape leaving behind geomorphological evidence. The ice sheet at its maximum extent formed terminal moraines which are asymmetric ridge-like features created by the accumulation of unconsolidated glacial debris at the ice margin [e.g. Winkelmann et al., 2010; O'Cofaigh et al., 2012]. As the ice sheet sporadically retreated it left comparable features termed recessional moraines (land-based and marine). Occasionally these geomorphological features are dated to provide greater constraint on the extent of the ice and timing of retreat. Sub-marine moraines scattered across the continental shelf are identified using acoustic mapping of the seafloor and are rarely dated due to a number of challenges affiliated with marine coring. In addition to geomorphological features, geological evidence of ice sheet behaviour is often recorded in marine cores [e.g. Andrews et al., 1998]. As the ice sheet retreats rapidly it sheds countless icebergs into the sea. These icebergs host sediments of various sizes and when the iceberg melts, they deposit anomalously large sediments on the seafloor. Marine cores identify sections with spikes in ice rafted-debris (IRD) and they are indicative of rapid ice wastage. Additionally, the IRD can be traced back to a source region which qualitatively proposes a margin which was actively retreating. The LGM extent based on terminal moraines acts as a direct constraint in the glaciological model, while other geomorphological and geological evidence is applied to qualitatively constrain and/or validate the modelled reconstructions.

The weight of an ice sheet has the ability to deform the solid Earth. As the ice and ocean load change through time the Earth responds in a visco-elastic fashion. As described in Section 1.2.1, the elastic response is instantaneous as the strain is directly proportional to the stress, conversely the viscous response depends on time ($\sigma \sim \dot{\varepsilon}$) with the full steady state response for a fixed loading taking several thousand years. The response of the Earth to the redistribution of mass on its surface and interior depends entirely on the internal structure of the Earth. Specifically, the elastic behaviour of the Earth is defined by the density structure as inferred by Dziewonski and Anderson (1981). Dziewonski and Anderson applied data from a global seismic survey to obtain the travel time of countless seismic waves propagating through the Earth. The velocity of a seismic wave from an Earthquake or controlled explosion is directly related to the density structure; given the travel time we can solve the inverse problem to obtain a profile for density structure. Dziewonski and Anderson (1981) applied an approximately globally distributed dataset which implies a global average density profile. Our Earth model is spherically symmetric therefore, a global average density structure to predict elastic deformations is most appropriate. In comparison, the viscous relaxation of the Earth evidently depends on the viscosity structure. The viscosity structure however, is not inferred by seismic surveys and remains poorly constrained [Mitrovica, 1996;

Mitrovica & Forte, 1997] and acts as a primary tuning parameter in our GIA model when calibrating to sea-level observations.

For this thesis we are interested in millennial scale sea-level changes on the order of tens of metres since it acts as a primary constraint in our models. In the Canadian Arctic and Greenland, past sea levels have been reconstructed using a variety of indicators: isolation basins, raised beaches and deltas, marine shells, drift wood, perched boulders, whale bones and microfossils.

The sea-level index points used in this thesis with the highest precision are those from isolation basins [e.g. Long et al., 2011, Woodroffe et al., 2013]. Sea-level generally lowered around the periphery of Greenland due to GIA, producing a staircase of basins and raised beaches. These basins are natural depressions which have throughout time been either connected or isolated from the sea. The three processes associated with basins useful for RSL studies are: the fully marine phase when the basin is in continuous mixture with the ocean, brackish-water phase when the basin moves up and is exposed to both marine and freshwater (tidal range), and the freshwater phase when the basin is isolated from the ocean. By analysis of the micro fossils (foraminifera) and sediment stratigraphy preserved in these basins from lake cores, the moment of isolation from the sea can be identified in time and given basin location relative to the present sea-level a height is assessed, which defines RSL for the site. However, the lack of spatial homogeneity of such field studies, especially in the high Arctic, forces the use of less precise sea-level proxies to improve the spatial distribution of data.

The remaining sea-level proxies such as marine shells (molluscs), drift wood and whale bones have less of an indicative meaning, providing a limiting constraint on sea-level rather than an absolute value with a given height and time. The molluscs habitat the seashore below the sea surface therefore act as a lower bound for sea-level, while drift wood and whale bones are transported inland by the highest tide which renders them proxies for a sea-level upper bound. The height of the proxies relative to sea-level is measured and radiocarbon dated for time. This places an upper or lower bound on past RSL; however the temporal and spatial uncertainty is very large. Another sea-level proxy is the marine limit, often defined by the lower limit of perched boulders above wave-washed bedrock which identifies the highest point sea-level reached at a given site during ice free conditions. The marine limit acts to bound the amplitude of sea-level change which constrains the isostatic response due to the unloading of ice.

These observations are applied in conjunction to model the dynamics of ice sheets in response to climate change, their interaction with the solid Earth, and their sea-level contribution. Additionally, the field observations allow for a quantitative and robust assessment of our model results which discriminates between model ensemble parameters.

2. REVISED ESTIMATES OF GREENLAND ICE SHEET THINNING HISTORIES BASED ON ICE-CORE RECORDS

Quaternary Science Reviews 63 (2013) 73-82

Benoit Lecavalier[1], Glenn A. Milne[1,2], Bo M. Vinther[3], David A. Fisher[2,4], Arthur S. Dyke[4], Matthew J.R. Simpson[5]

[1] *Department of Physics, University of Ottawa, Canada*
[2] *Department of Earth Sciences, University of Ottawa, Canada*
[3] *Centre for Ice and Climate, Niels Bohr Institute, University of Copenhagen, Denmark*
[4] *Geological Survey of Canada, NRCan, Ottawa, Canada*
[5] *Norwegian Mapping Authority, Hønefoss, Norway*

2.1 ABSTRACT

Ice core records were recently used to infer elevation changes of the Greenland ice sheet throughout the Holocene. The inferred elevation changes show a significantly greater elevation reduction than those output from numerical models, bringing into question the accuracy of the model-based reconstructions and, to some extent, the estimated elevation histories. A key component of the ice core analysis involved removing the influence of vertical surface motion on the δ^{18}O signal measured from the Agassiz and Renland ice caps. We re-visit the original analysis with the intent to determine if the use of more accurate land uplift curves can account for some of the above noted discrepancy. To improve on the original analysis, we apply a geophysical model of glacial isostatic adjustment calibrated to sea-level records from the Queen Elizabeth Islands and Greenland to calculate the influence of land height changes on the δ^{18}O signal from the two ice cores. This procedure is complicated by the fact that δ^{18}O contained in Agassiz ice is influenced by land height changes distant from the ice cap and so selecting a single location at which to compute the land height signal is not possible. Uncertainty in this selection is further complicated by the possible influence of Innuitian ice during the early Holocene (12-8 ka BP). Our results indicate that a more accurate treatment of the uplift correction leads to elevation histories that are shifted down relative to the original curves at GRIP, NGRIP, DYE-3 and Camp Century. In addition, compared

to the original analysis, the 1-σ uncertainty is considerably larger at GRIP and NGRIP. These changes reduce the data-model discrepancy reported by Vinther et al. (2009) at GRIP. A more accurate treatment of isostasy and surface loading also acts to improve the data-model fits such that the residuals at all four sites for the period 8 ka BP to present are significantly reduced compared to the original analysis. Prior to 8 ka BP, the possible influence of Innuitian ice on the inferred elevation histories prevents a meaningful comparison.

2.2 INTRODUCTION

2.2.1 HOLOCENE THINNING OF THE GREENLAND ICE SHEET

Vinther et al. (2009) applied a novel procedure to determine ice surface elevation curves of the Greenland ice sheet (GrIS) at four ice core locations (GRIP, NGRIP, DYE-3 and Camp Century; see Fig. 2.1a). These observationally-constrained curves depict a Holocene thinning history that is considerably more rapid and of greater amplitude than that indicated from the output of numerical ice models. The discrepancy is large, several hundred metres at some core sites, and brings into question the accuracy of both the ice models and the thinning curves. This paper revisits two aspects of the Vinther et al. (2009) (shortened to Vinther et al. in the following) analysis in order to assess their impact on the resulting thinning curves and whether it can account for some of the discrepancy mentioned above.

In the original Vinther et al. analysis, the thinning curves were derived by considering the climate records in two ice caps, Agassiz and Renland (henceforth AR), situated on either side of Greenland (Fig. 2.1a). After estimating and removing the contribution of vertical land motion to the AR $\delta^{18}O$ records, the elevation-corrected $\delta^{18}O$ records were applied to infer a homogeneous $\delta^{18}O$ field for the entire region. As discussed below, the AR ice caps have topographical constraints that limit their former vertical extent (thickness) (Fisher et al., 1995; Johnsen et al., 1992). Consequently, no elevation correction for thickness changes of either ice cap was applied in the Vinther et al. analysis.

A synchronized stratigraphical timescale for the Holocene (GICC05) of DYE-3, GRIP, NGRIP, Camp Century, Renland and Agassiz was made by matching prominent volcanic reference horizons in electrical conductivity measurements (Vinther et al., 2006; Vinther et al., 2008) and gaussian filtered to capture millennium scale variations (Fig. 2.1b). By removing the uplift-corrected AR $\delta^{18}O$ records from the $\delta^{18}O$ records at Camp Century, DYE-3, GRIP and NGRIP, changes in ice surface elevation were isolated at these sites. The two aspects of the original analysis investigated in this paper are (i) the accuracy of the elevation corrections applied at the AR ice caps and (ii) the resulting inference and application of a $\delta^{18}O$ profile for the entire region.

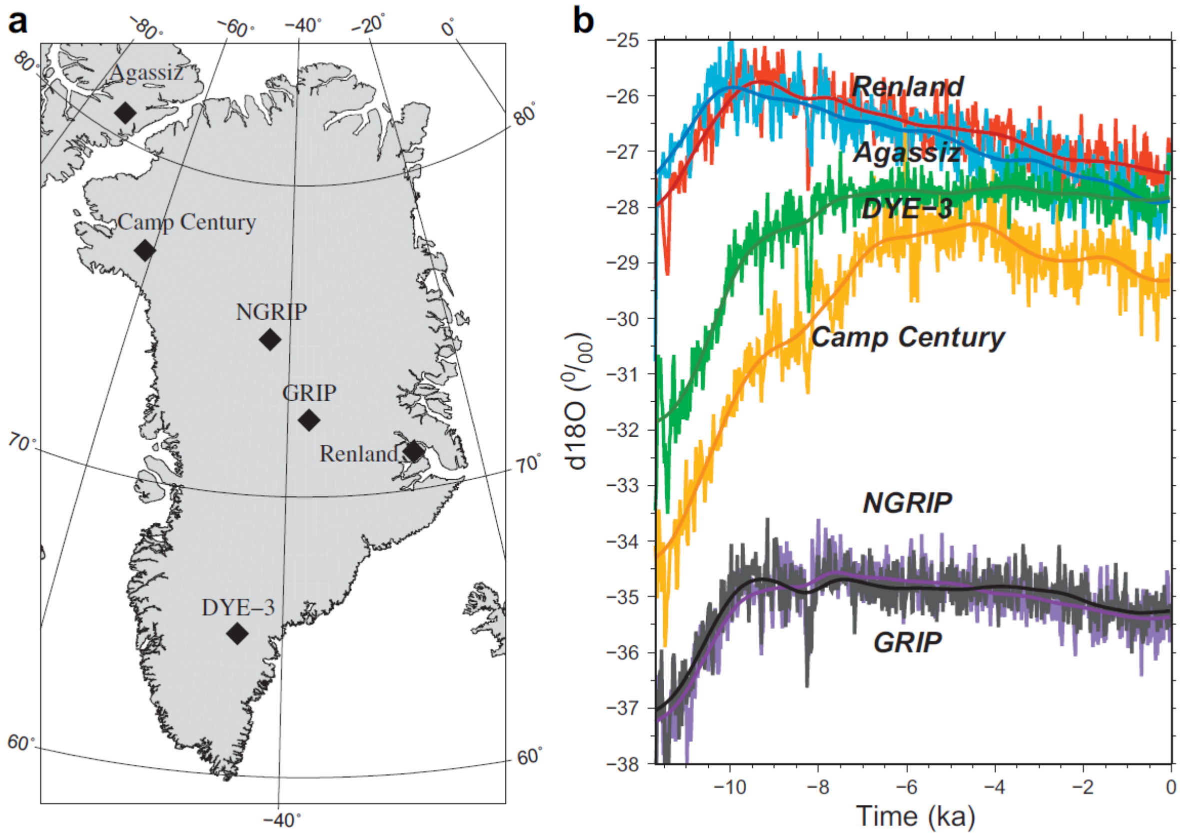

Figure 2.1 (a) The location and names of the relevant ice cores discussed in this study. (b) The synchronized $\delta^{18}O$ records for all the sites shown in (a); both raw and smoothed (Gaussian filtered) signals are shown.

The main contribution of this study is to assess the accuracy of the land uplift correction applied in the original Vinther et al. analysis and determine the impact of this on the estimated thinning curves. The post glacial uplift estimated for AR in Vinther et al. was conducted using observations of past changes in relative sea level (RSL) in nearby fiords. The Agassiz bedrock elevation history is based on a set of data dating back to 9.5 ka before present (BP; relative to AD 2000) and extrapolated to 11.7 ka BP using the observed exponential decay time for RSL change (Dyke & Peltier, 2000). Similarly, the uplift estimated for Renland was obtained using past changes in sea level in nearby fiords (Funder, 1978). Using RSL as a proxy for vertical land motion will lead to some degree of error due to the contribution from vertical motion of the sea surface. We improve upon this method here by modelling RSL observations from Ellesmere and Devon Islands and north-west Greenland (Fig. 2.2) to calibrate a glacial isostatic adjustment (GIA) sea-level model for this region. The calibrated model is then applied to determine land uplift histories at the appropriate locations (not necessarily at the ice core sites – see Section 2.2.2).

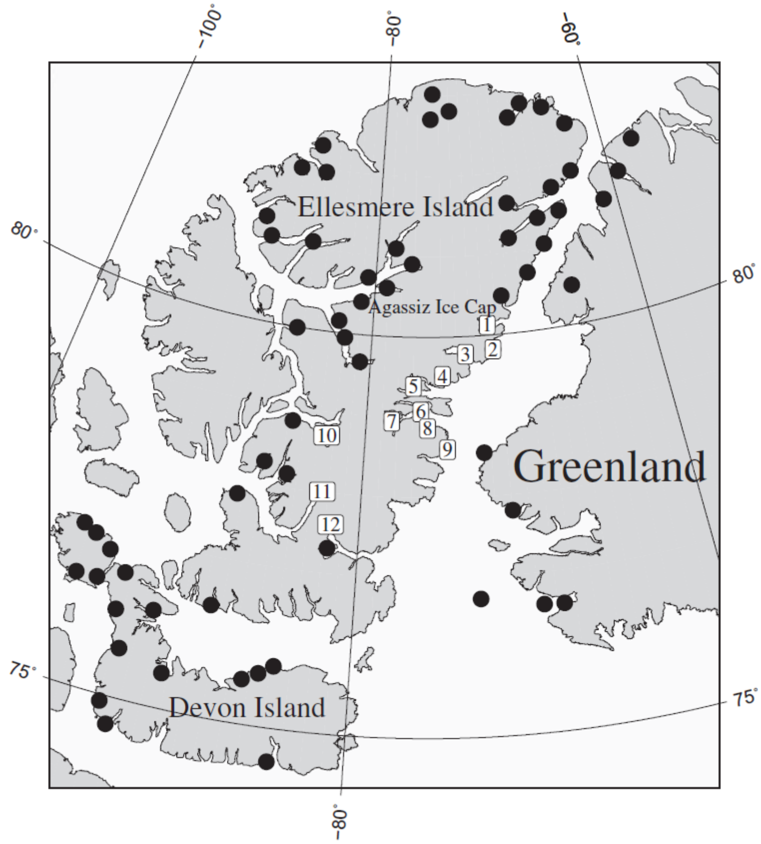

Figure 2.2 The distribution of sites (black circles and 12 numbered sites) across the Canadian Arctic and Greenland which had sufficient sea level proxy information to constrain our glacial isostatic adjustment (GIA) model.

The second contribution of this study relates to the temperature reconstruction from the individual AR $\delta^{18}O$ records and the spatially varying $\delta^{18}O$ history generated across Greenland. The revised land uplift corrections result in a substantial difference between the $\delta^{18}O$ records inferred from the AR cores. Therefore, instead of averaging this to create a homogeneous $\delta^{18}O$ profile for the region (which would result in large error bars on the inferred thinning curves), we use the differences between the AR records to infer a spatial gradient in $\delta^{18}O$ and apply this non-homogeneous signal to estimate thinning curves at the Greenland ice core sites.

As stated above, the over-arching aim of this work is to assess whether these extensions of the original Vinther et al. analysis can account for at least some of the discrepancy between the inferred and modelled Holocene thinning of the GrIS.

2.2.2 INTERPRETING δ18O FROM THE RENLAND AND AGASSIZ ICE CAPS

A key aspect of the Vinther et al. study is the estimation of temperature from observations of $\delta^{18}O$ in AR ice. The $\delta^{18}O$ values obtained from ice cores are affected by air temperature, location of the moisture source, the pathways by which the moisture is transported, and precipitation (Dansgaard, 1961). Understanding which of these processes are primary versus secondary drivers of $\delta^{18}O$ changes is crucial for assessing the accuracy of the inferred elevation histories. It has been observed that numerous northern hemisphere $\delta^{18}O$ records from ice cores extending back through and beyond the Holocene are described to first order by two effects that relate to changes in air temperature: an altitude effect (-0.6‰ per 100 m) and a latitude effect (-0.54 ‰ per degree N) (Dansgaard, 1961; Johnsen et al., 1989). It is through the former that elevation of the ice surface, in this case dominated by GIA, influences the adiabatic cooling of the local air mass in which precipitation induced fractionation occurs and ultimately influences the $\delta^{18}O$ signal. It is also noteworthy that the AR $\delta^{18}O$ records are surprisingly similar considering the distance between the sites (Koerner, 1978; Funder, 1979).

The Renland ice cap is located on a high plateau with steep descents down to the Scoresbysund Fjord and the surrounding terrain, thereby limiting the lateral extent of the ice cap. From considering the equilibrium profile of an ice cap, this constraint on the lateral extent of the base limits the maximum thickness that the ice cap can achieve over millennium timescales. Although Renland can thin beyond this maximum equilibrium thickness, there is strong evidence that it has not done so during the Holocene. The present maximum extent of Renland associated with relatively warm air temperature and high precipitation is most likely indicative of its extent during the Holocene when, in general, temperatures were relatively high. Because this part of the GrIS receives some of the highest accumulation rates, it makes it difficult to argue for a significant thinning of the ice cap during the Holocene. Indeed, conceptual models of the recent glacial-interglacial transition, with increased warming and accumulation resulted in no more than 30 m of change to Renland's thickness (Vialov, 1958; Johnsen et al., 1992). Furthermore, the continuous stratigraphy of the Renland ice core, including basal Eemian ice, indicates very long survival (Johnsen et al. 1992). We therefore think it is reasonable to assume that the Renland $\delta^{18}O$ record is not significantly influenced by altitude variation through changes in ice thickness.

The Agassiz ice cap is found on the central part of Ellesmere Island (Fig. 2.2), where two ice cores (84/87) were drilled on a local dome. The dome is located at the point of highest bedrock elevation which has resulted in the formation of a Raymond bump in the layering of the ice cap (Vinther et al., 2008). Ice flow between Agassiz boreholes in connection with wind scouring effects has been modelled and the results illustrate the relative stability of the ice cap over the Holocene (Fisher et al., 1995). The melt records from the Agassiz ice cores display the response of the ice cap to the Holocene thermal maximum (HTM) and suggest thinning of the ice cap on the order of 100 m at that time (Fisher et al., 1995). However, we note that changes in thickness of the ice cap do not affect the $\delta^{18}O$ content of Agassiz ice; there is no evidence of local altitude effects (e.g. from Agassiz ice thickness changes) on the observed $\delta^{18}O$ (Fisher, 1992; Koerner, 1979; Koerner & Fisher, 1990). The air masses that precipitate onto the Agassiz ice cap primarily originate in Baffin Bay. These are first elevated along the eastern shores of Ellesmere Island and since there is no inland topography capable of forcing the air masses higher, the $\delta^{18}O$ from Agassiz ice is more sensitive to elevation changes along this shoreline (Fisher, 1990). This pattern of air mass elevation and isotopic fractionation has several important implications: (1) Agassiz thickness changes on the order of 100 m are of no consequence to a Vinther et al. type analysis, the elevation correction associated with land uplift should not be calculated at the drill sites, but rather at a location along the coastline of Ellesmere Island and (2) the position at which the correction should be estimated will change throughout the Holocene due the influence of Innuitian ice on the topography of southern Ellesmere Island. Thinning of Innuitian ice will, in fact, dominate over isostatic land uplift during the early Holocene. This component of the Agassiz elevation correction, which was overlooked in the original analysis, will add considerably to the uncertainty in the estimated thinning curves for the early Holocene. As discussed in Section 2.3, these issues complicate the task of arriving at a well-constrained elevation correction for the Agassiz $\delta^{18}O$ record prior to 8 ka BP.

2.3 METHODOLOGY

2.3.1 AGASSIZ AND RENLAND LAND UPLIFT CORRECTION

As described above, we used a GIA model to remove the land uplift contribution to the AR $\delta^{18}O$ data. We calibrated the model using RSL data from Arctic Canada and Greenland. Our GIA model computes Earth deformation, gravity and sea-level changes resulting from the interaction between ice sheets and the solid Earth (e.g. Farrell & Clark 1976; Milne & Mitrovica 1998; Mitrovica & Milne 2003). The model uses two primary inputs, an ice model and an Earth model. Two ice models were used: ICE-5G (Peltier, 2004) and a revised version of ICE-5G with the Greenland component removed (referred to as GrB; Tarasov & Peltier, 2002) and replaced by a more recent reconstruction of this ice sheet (referred to as Huy2; Simpson et al, 2009). A spherically symmetric viscoelastic rotating Earth model was adopted with the elastic and density structure given by the seismic Preliminary Reference Earth Model (Dziewonski & Anderson, 1981), and the viscous structure more crudely defined into three shells: lithosphere, upper mantle, and lower mantle. The lithosphere was assigned a relatively high viscosity to simulate an elastic outer shell with a thickness that was varied when seeking an optimal model fit to the RSL data. The upper-lower mantle boundary was defined at a depth of 670 km and the viscosity in these two regions used as free parameters when modelling the RSL data (e.g. Simpson et al., 2009).

RSL data from Ellesmere, Devon Islands and Greenland were used to determine optimal Earth model parameters (lithospheric thickness, upper and lower mantle viscosity) for each ice model. A total of 171 Earth viscosity models were considered in seeking an optimal data-model fit. The RSL data are generally of low precision as the reconstructions are based on, for the most part, shells, whale bones and drift wood (e.g. Dyke & Peltier, 2000). This type of evidence permits only upper and lower limits to be placed on RSL (see Fig. 2.3). The results of the Earth model calibration exercise are given in Section 2.4.1, along with the revised uplift corrections.

2.3.2 HOLOCENE TEMPERATURE AND THINNING RECONSTRUCTIONS

The reconstruction of Holocene surface air temperatures from the AR $\delta^{18}O$ records requires corrections for both uplift and changes in $\delta^{18}O$ content of sea water (Waelbroeck et al., 2002). A forward modelling method is used to calibrate the AR corrected $\delta^{18}O$ records with the borehole temperature profiles from GRIP, NGRIP, DYE-3 and Camp Century by numerically solving the differential equation for heat conduction in moving ice yielding a $^{o}C/\delta^{18}O$ slope of 2.1±0.2 (Johnsen & Dansgaard, 1992; Johnsen, 1977; Gundestrup et al., 1993; Dahl-Jensen & Johnsen, 1986; Dahl-Jensen et al., 1998; Dahl-Jensen et al., 2003; Vinther et al., 2009).

In the Vinther et al. study, based on the original uplift corrections on the AR ice caps, the two $\delta^{18}O$ records were strikingly similar, therefore, the records were averaged to ultimately yield a single temperature reconstruction for the entire region. Using the $\delta^{18}O$ signal for the region, variations in ice elevation at each Greenland core site was isolated and subsequently corrected for upstream effects at NGRIP, DYE-3, and Camp Century, yielding the Holocene thinning curves (Reeh et al., 1985; Buchardt & Dahl-Jensen, 2007; Vinther et al., 2009). An important consequence in adopting a single $\delta^{18}O$ record is that the residual between the uplift-corrected AR $\delta^{18}O$ records translates into an uncertainty in the estimated thinning curves (of amplitude ±25m in the original analysis).

When applying more accurate uplift curves (see below) it was found that the AR $\delta^{18}O$ records diverged from one another by a greater amount than in the original study (Vinther et al., 2009; Fig. 5), especially after reducing the AR records to the same height to remove the elevation difference between AR. This $\delta^{18}O$ discrepancy translates into an uncertainty in the final thinning curves that would be much greater than that obtained in the original analysis. As a consequence, rather than average the AR records, we have extended the original study to account for a spatial gradient in the $\delta^{18}O$ between the ice cores and thus reduce the uncertainty resulting from the AR $\delta^{18}O$ discrepancy. The difference in the uplift-corrected height synchronized $\delta^{18}O$ records from the AR cores were applied to generate a linear $\delta^{18}O$ profile from

Renland to Agassiz, along with a temperature reconstruction at the Renland and Agassiz cores. A site specific $\delta^{18}O$ record is deduced at GRIP, NGRIP, DYE-3 and Camp Century by interpolating/extrapolating the Renland to Agassiz $\delta^{18}O$ records. Based on these site specific $\delta^{18}O$ records, new thinning curves are derived.

2.4. RESULTS AND DISCUSSION

2.4.1 GIA CORRECTION

RSL predictions for a subset of sites are shown in Fig. 2.3a and b (numbered sites in Fig. 2.2); the model fits are shown at these particular sites since it is along this section of Ellesmere (east coast, south of the Agassiz ice cap) that the vertical land motion correction is to be applied. Red and blue data points indicate upper and lower bounds (limiting dates) for sea-level, respectively. The elevation of the variety of sea-level indicators collected in the Arctic was measured using an altimeter and have an estimated uncertainty of ±1m for markers below 20m in elevation and ±5% for indicators above 20m (Dyke & Peltier, 2000; Blake, 1999). The curves were computed using the ICE-5G ice model and an Earth model which produced the best fit for Ellesmere Island RSL data; lithosphere thickness of 71 km, upper mantle viscosity of 0.3×10^{21} Pa·s, and lower mantle viscosity of 10^{21} Pa·s. We also considered observations from north-west Greenland and Devon Island and the optimal Earth models obtained for these regions are compatible (within the 95% confidence range) with those inferred from Ellesmere Island. This suggests that there are no large gradients in Earth structure that influences the GIA signal in the region and so the use of a 1D Earth model is appropriate. Using the Huy2 model within ICE-5G, the optimal Earth model parameters obtained using the Greenland data were also compatible with those inferred using the original ICE-5G ice model. This indicates that our viscosity inference for Agassiz is not strongly affected by the adopted Greenland ice model component (i.e. Huy2 vs GrB).

The data-model fits shown in Fig. 2.3 (a, b) are generally of high quality, with the predicted curve bisecting the limiting dates as required. There are two sites (9 & 12) where the data-model residual is substantial (more than ~10 m) as the modelled curve is too low. This could relate to inaccuracies in the adopted ice loading model or limitations in the Earth model (e.g. the assumption of 1-D structure). Regardless of the source of the residual at these two sites, a key point is that the locations chosen to compute the uplift corrections for the Agassiz δ^{18}O record are in the vicinity of sites 3 and 7, where the model fits are compatible with the data to within uncertainty (compare Figs 2.2 and 2.4a).

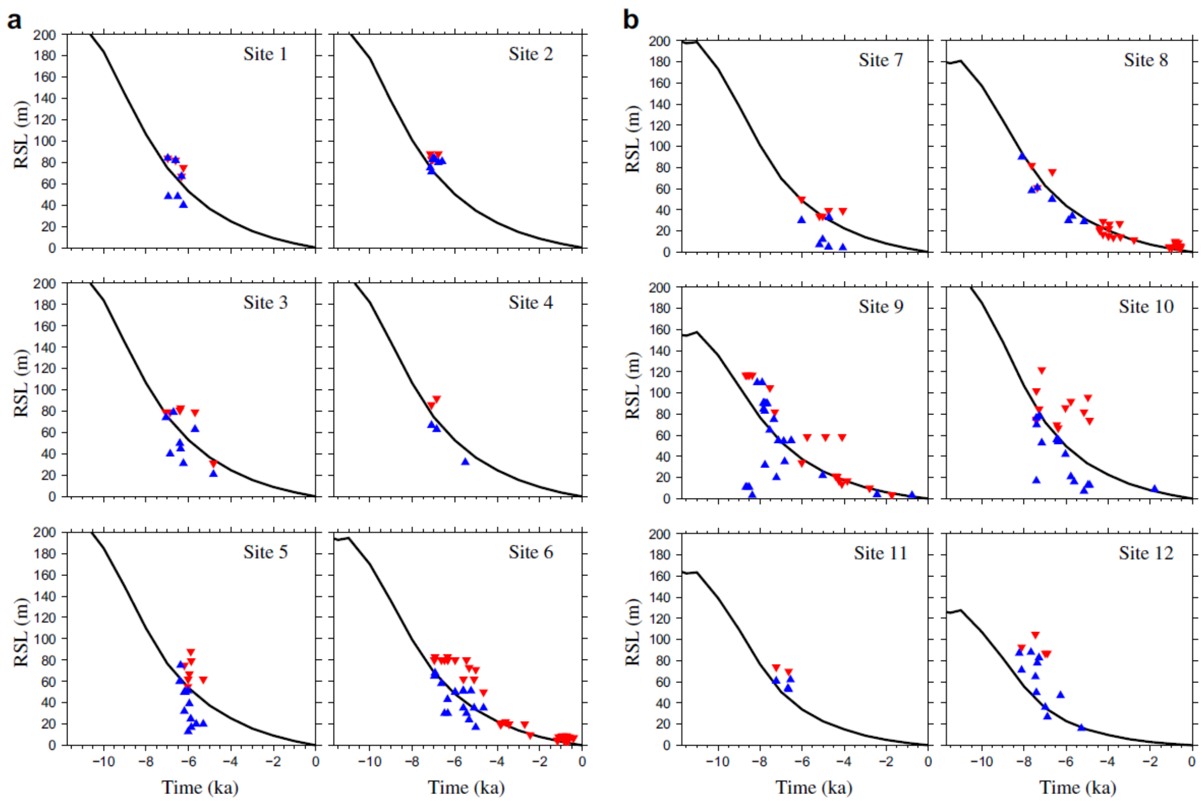

Figure 2.3 Relative sea-level observations and predictions at the 12 sites which are of greatest relevance to the GIA/RSL model. The red (down facing) and blue triangles (pointing up) represent an upper and lower bound on sea level, respectively. The sea-level curve on each graph was generated using ICE-5G as the ice model and an optimal Earth model with lithosphere thickness of 71 km, upper mantle viscosity of 3 x 10^{20} Pa·s, and lower mantle viscosity of 10^{21} Pa·s.

As outlined above, choosing a location to apply the uplift correction for the Agassiz cores is difficult, since the moisture pathways are not well constrained in space and time. The limitations of high resolution atmospheric modeling over timescales of thousands of years do not permit the use of this approach to identify the most common pathways by which the air mass was carried from Baffin Bay to the Agassiz ice cap during the Holocene. As a result, we focus here on placing a bound on the range of uplift curves that can be applied to the Agassiz ice core data. This range can then be used to define an uncertainty on the GIA-induced land uplift signal in the Agassiz ice cap δ^{18}O record. As shown in Figure 2.4a, there is considerable spatial variability in the predicted amplitude of land uplift along the east coast of Ellesmere

Island. Two sites (A & B, Fig. 2.4a) were chosen to evaluate the uplift correction for Agassiz as they correspond to topographic highs that bound the most likely pathways over which moisture could have been transported before precipitating over the Agassiz ice cap, while taking into account changes in sea-ice cover through time (England et al., 2006; England et al., 2008). Uplift at site B was likely the dominant control on Agassiz $\delta^{18}O$ during the early to mid-Holocene after the Innuitian ice sheet thinned enough to expose the underlying high terrain and when greater sea ice cover would have resulted in more southerly moisture pathways. The predicted uplift curves for sites A and B are shown in Fig. 2.4b along with the curve used by Vinther et al. (2009). We note that there are differences of up to ~100 m between the revised curves and that estimated in the original analysis.

Using RSL data from east Greenland, Simpson et al. (2009) found an optimal Earth model (to partner their Huy2 ice model) with a lithospheric thickness of 120 km and upper and lower mantle viscosities of 0.3×10^{21} Pa·s and 5.0×10^{22} Pa·s, respectively. This Earth model provided the best fit to the data at their sites 11-17 (see their Figures 1 and 16 of Simpson et al., 2009). We adopted the Simpson et al. ice model (ICE-5G revised to contain Huy2) and this Earth model to generate a land uplift curve at the location of the Renland ice core (Fig. 2.4b). This new uplift curve is similar to that adopted in the original Vinther et al. analysis.

The results in Fig. 2.4b indicate that the total amplitude of the uplift-correction for the Agassiz $\delta^{18}O$ record can range from ~-220 m (Site A) to ~-150 m (Site B). In order to determine the influence of this range on the estimated ice elevation curves at the GrIS ice core sites, we follow the general procedure adopted by Vinther et al. but use the two end member Agassiz uplift curves to incorporate the uncertainty introduced by this issue. As discussed above, neither $\delta^{18}O$ records from Agassiz nor Renland are believed to have experienced significant changes in $\delta^{18}O$ as a result of changes in ice thickness over the Holocene. Therefore, once their respective $\delta^{18}O$ records are corrected for changes in land elevation (see Fig.2.5) and other processes (see Section 2.2.2), the resulting time series represents a proxy for surface air temperature changes at each locality (Vinther et al., 2009).

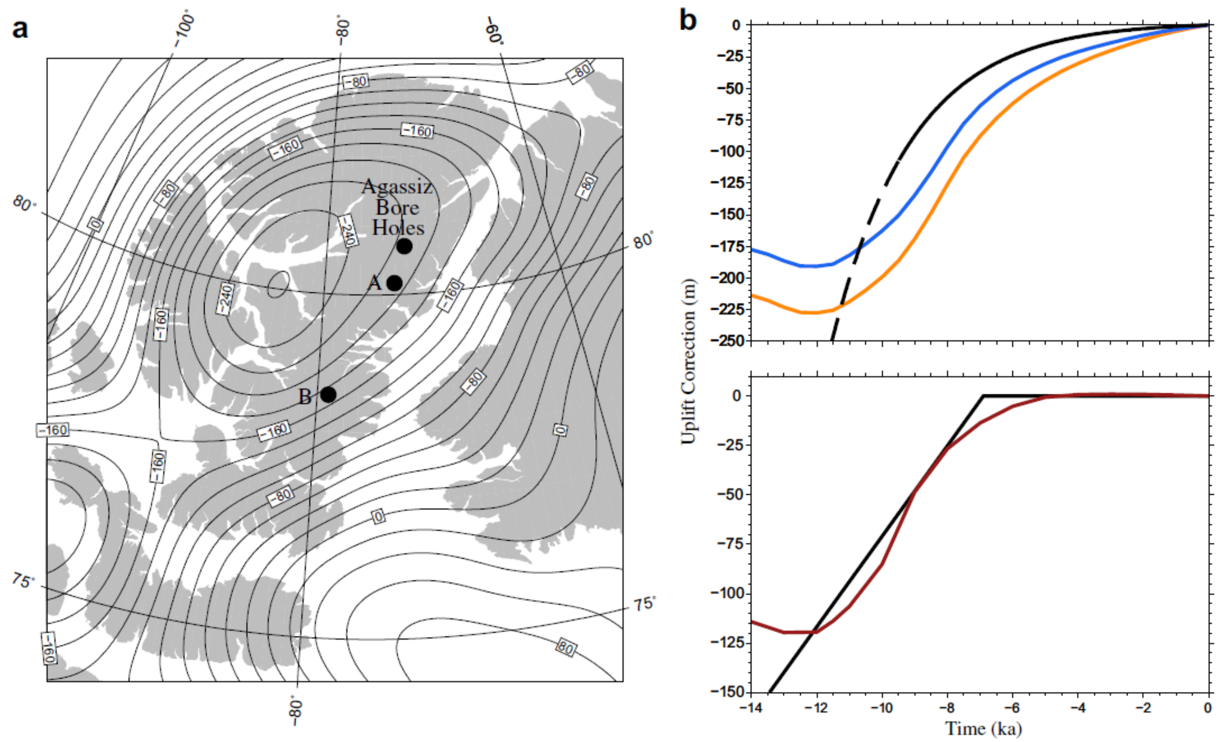

Figure 2.4 (a) The spatial variability in GIA-induced uplift (metres) of Ellesmere Island at 10 ka BP using the optimal Earth model. The plot shows the location of the Agassiz ice cap core locations (A87 and A84, both at the dome) along with the two sites at which uplift was predicted (A,B). (b) Top frame shows predicted uplift curves generated using the optimal Earth model at the two locations (A, B; orange, blue, respectively) shown in (a). Also shown is the uplift curve adopted by Vinther et al. (2009) (black). Bottom frame shows the Renland original uplift correction applied in Vinther et al. (2009) (black) along with the uplift curve generated using the optimal model (red) from Simpson et al. (2009) (see text for details).

During the early Holocene, the Innuitian ice sheet was quite extensive in southern Ellesmere Island. As a consequence, it likely affected the predominant moisture pathways and, therefore, the correction to be applied to the Agassiz $\delta^{18}O$ record. Quantifying the effect of this ice is not straightforward, however. It might have shifted the location where the elevation correction is to be applied and also increased the elevation to which the air moisture was elevated to. Based on field evidence (England et al., 2006; England et al., 2008), the Innuitian ice sheet reduced significantly in vertical extent along the south east coast of Ellesmere Island until approximately 8 ka BP. In the ICE-5G reconstruction, ice thickness in southern Ellesmere reaches present-day values around 8 ka BP. Therefore, the influence of the ice was likely only significant during the early Holocene (and certainly prior to 8 ka BP). We raise this issue only

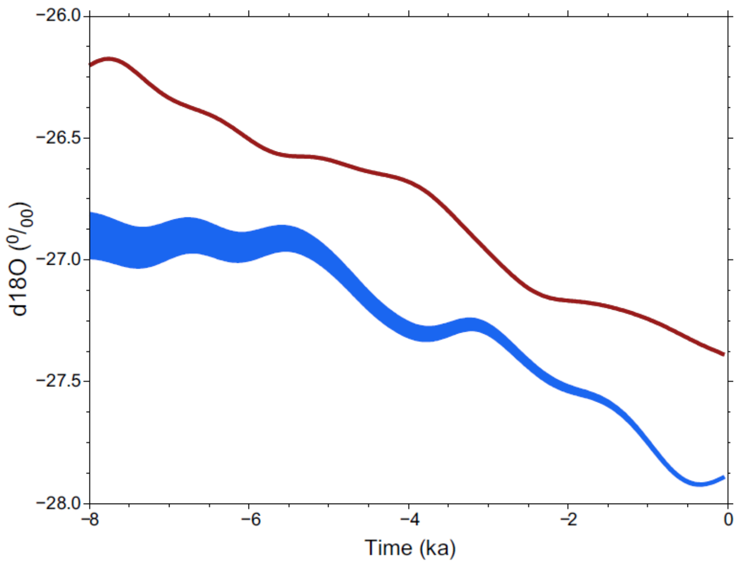

Figure 2.5 The Agassiz (site A and B acceptable range; blue) and Renland (red) gaussian filtered $\delta^{18}O$ records corrected for land uplift. For Agassiz, the curves predicted at the two chosen locations were applied: site A (top) and site B (bottom). A $\delta^{18}O$ profile is interpolated/extrapolated across Greenland using the uplift-corrected and height synchronized Agassiz and Renland curves.

to make the point that the elevation corrections for Agassiz ice (Fig. 2.4b) might require revision for the period prior to 8 ka BP. Quantifying this revision requires the application of high resolution atmospheric modelling as well as accurate reconstructions of ice extent in this region. This work is beyond the scope of this study. Qualitatively the addition of the Innuitian ice to existing topography will, however, result in an increased topographic barrier or/and a longer moisture pathway. Both effects are likely to cause further depletion of $\delta^{18}O$ in precipitation at the Agassiz drill site, thus dominating the effect over the uplift curves presented in Fig. 2.4b during the early Holocene. The resulting impact of the Innuitian ice sheet on the thinning curves will likely be a greater thinning rate at GRIP, NGRIP, and Camp Century and a decreased rate at DYE-3, which would act, in general, to increase the discrepancy between the thinning curves and model reconstructions noted in the original analysis. However, incorporating the influence of this effect into the analysis will result in a large amplification of the uncertainty in the early part (12 ka to 8 ka) of the estimated thinning curves.

2.4.2 AR TEMPERATURE RECORDS

A temperature reconstruction is conducted on both the AR records. Since the $\delta^{18}O$ records from these ice caps haven't been drastically influenced by changes in ice thickness (especially during the late Holocene), once the vertical land motion correction is applied, a relatively untainted mid to late Holocene temperature reconstruction at high latitudes is obtained (Fig. 2.6). These temperature records relate the temperature history for an absolute height (ice cap surface) relative to sea-level through time. The Agassiz temperature record could be used to assess the accuracy of the uplift correction applied if interpreted with

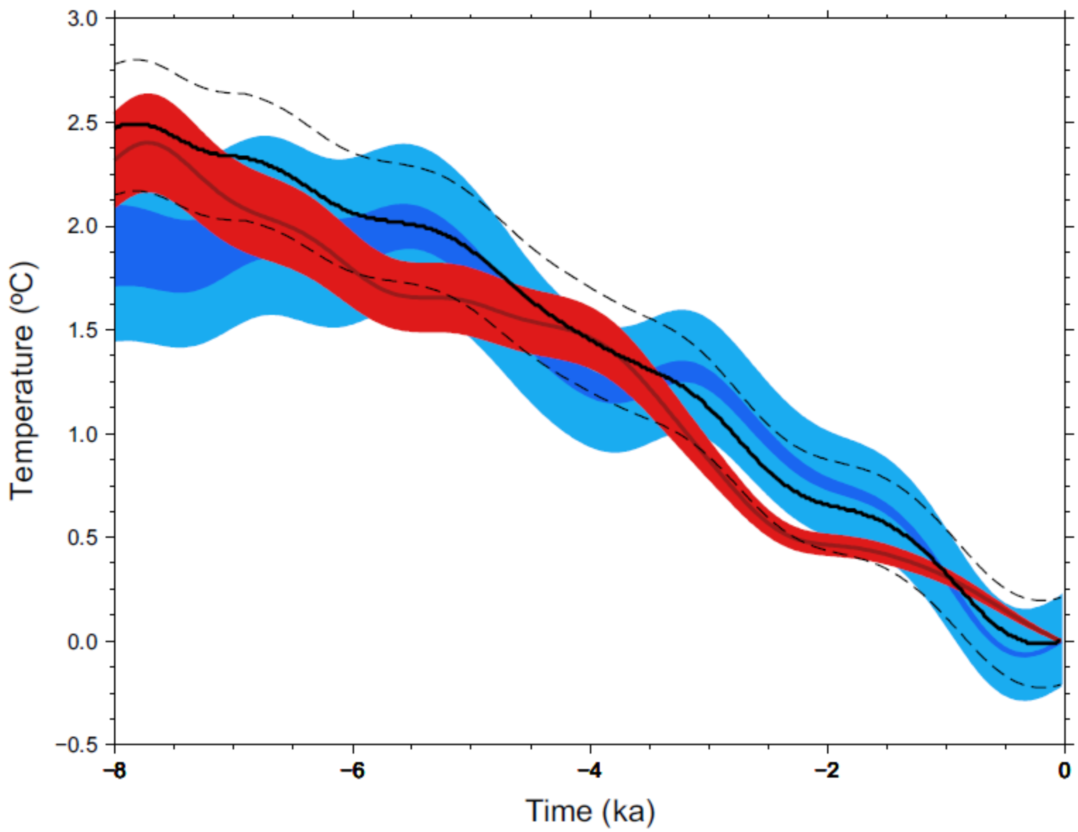

Figure 2.6 Temperature reconstruction at the Agassiz (dark blue) and Renland (dark red) ice caps are obtained by correcting the uplift corrected $\delta^{18}O$ from AR (Fig.2.5), for changes in the ocean's $\delta^{18}O$ content and applying the $^{o}C/\delta^{18}O$ slope of $2.1\pm0.2^{o}C/\delta^{18}O$. The original temperature reconstruction for the whole Greenland region from the Vinther et al. analysis is shown in black. The 1-σ uncertainty is shown by the lighter coloured bands and dashed black lines.

the Agassiz melt record (Fisher et al., 1995), since both records should agree on the timing of the HTM. The AR temperature record has further applications in reconstructions of the Greenland ice sheet through glaciological modelling studies. Most numerical ice sheet models of Greenland use the GRIP temperature record to force the ice sheet by extrapolating the record over Greenland (e.g. Huybrechts, 2002), however, there are few temperature reconstructions from the ice margin that can be used to validate the accuracy of the extrapolation scheme.

2.4.3 REVISED HOLOCENE THINNING CURVES

As discussed above, a spatially variable (linear) $\delta^{18}O$ profile is applied since the AR uplift corrected records differ by a significant amount (Fig. 2.5), especially after height synchronization. Following the method outlined in Section 2.3.2, site specific $\delta^{18}O$ profiles are calculated for GRIP, NGRIP, DYE-3 and Camp Century based on the uplift-corrected AR records. In Figure 2.7, the revised ice surface elevation curves (coloured) are shown with those from the original Vinther et al. analysis (black). In general, the new uplift corrections result in a decreased overall amplitude to the thinning curves with similar characteristics and introduce uncertainty - one that increases with time (max of ±26 m) - due to the lack of a specific location at which to apply the Agassiz uplift correction. The revised thinning curves remain within the 1-sigma uncertainty of the original analysis. The differences between the old and new thinning curves reflect the relative importance of the AR records on each site, the records applied to correct them and their interpretation. The $\delta^{18}O$ profile has the greatest impact on the DYE-3 thinning curves since the new extrapolated site specific $\delta^{18}O$ record emphasizes and amplifies differences in the AR corrected $\delta^{18}O$ record (see Fig. 2.1a).

As stated above, rather than average the AR records, we calculate a (linear) spatial gradient in $\delta^{18}O$ between the AR $\delta^{18}O$ records. To determine the uncertainty associated with this procedure, we compare the gradient estimated from the uplift-corrected and elevation synchronised (using -0.6‰ per 100 m) AR $\delta^{18}O$ records to that estimated from Greenland ice cores, -0.54‰ per degree North (Johnsen et al., 1989). Since the thinning curves are obtained with the use of these empirical latitudinal and elevational relationships, it is appropriate to quantify the accuracy of our results based on their consistency with these relationships.

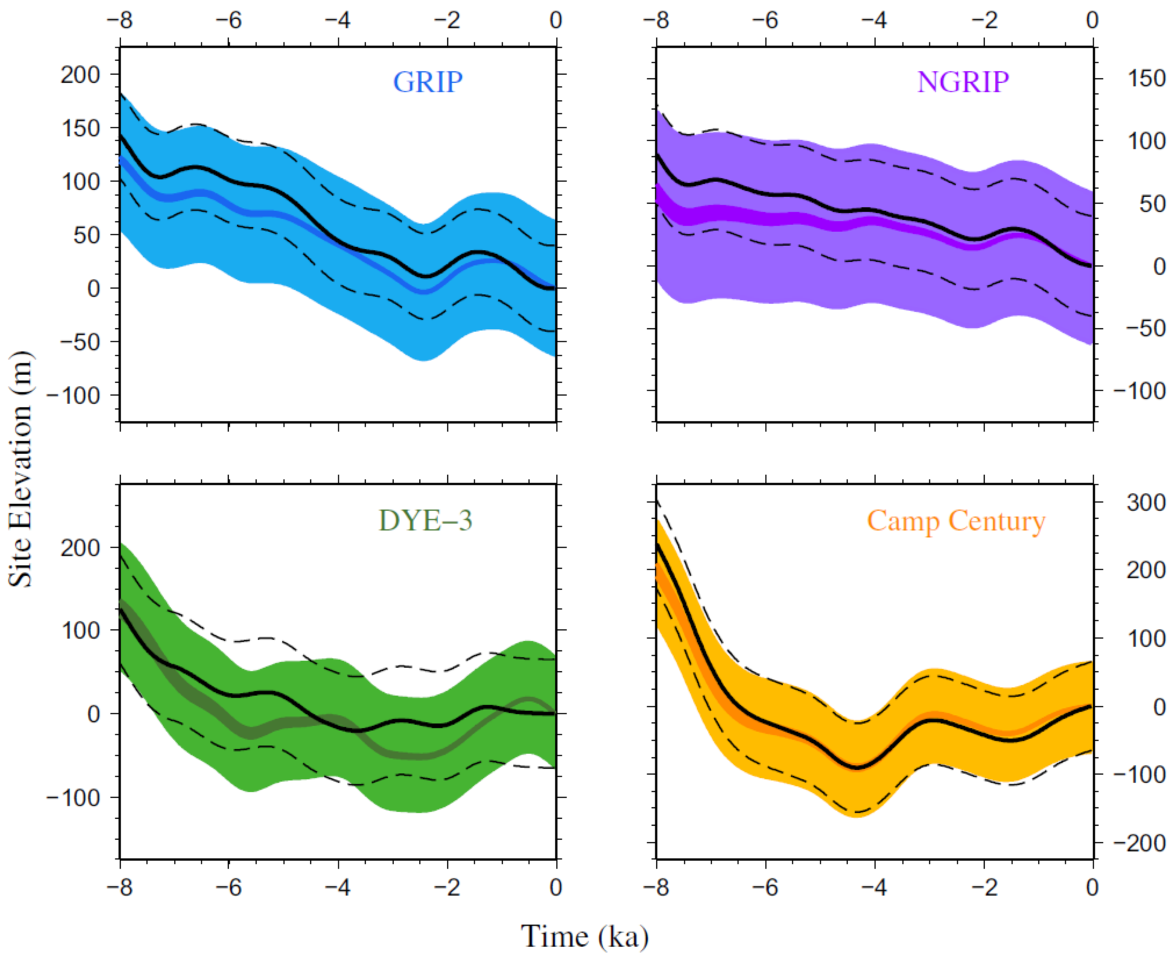

Figure 2.7 Ice elevation curves at four Greenland ice core locations (Fig. 2.1a). The original results of Vinther et al. (2009) are displayed (solid black line) along with the 1-σ uncertainty (dashed black line). The newly derived curves define a range of values associated with the two different uplift curves for Agassiz (site A & B in Fig. 2.2a); this range is indicated (darker coloured band) along with the estimated 1-σ uncertainty (lighter coloured band).

An additional error is introduced by the two Agassiz ice cores, 87 and 84, producing a further uncertainty of ±16 m at all sites. The error associated with DYE-3 and Camp Century is larger due to contributions from less precise $\delta^{18}O$ measurements in core layers at these locations producing an additional error of ±25 m. Combining these error sources quadratically leads to the total maximum 1-σ uncertainty (lighter coloured shading in Fig. 2.7) respectively being ± 62, 62, 67, and 67 m for GRIP, NGRIP, DYE-3, and Camp Century. These uncertainty ranges are somewhat larger than those for the original curves and result in a poorer signal to noise ratio, particularly for the period 8 ka BP to present.

With respect to the ice-core analysis and the resulting elevation histories, interpreting the $\delta^{18}O$ variations as elevation changes at GRIP, NGRIP, DYE-3 and Camp Century is an aspect of the study that should be refined as more studies investigate $\delta^{18}O$ differences amongst northern hemisphere ice cores. The relatively simplistic empirical relationships employed in this study (linear dependence of ‰ $\delta^{18}O$ with latitude and altitude) does not capture the complexities of $\delta^{18}O$ variability across the region and so further studies to quantify these relationships would improve the accuracy of the inferred thinning curves. Also, if total gas content of the NGRIP was measured, we could validate the thinning history at the NGRIP site (Vinther at al., 2009). The above analysis could be improved through obtaining better constraints on dominant moisture sources and pathways for precipitation on the Agassiz ice cap. This is particularly important for the early portion of the curve (12-8 ka BP) when the largest changes likely occurred and the influence of Innuitian ice could have been significant.

2.4.4 COMPARISON OF THINNING CURVES TO OUTPUT FROM NUMERICAL ICE MODELS

The Holocene thinning curves are a unique observational constraint that can be compared to output from numerical ice sheet models. To date, this type of information has only been available through identifying and dating geomorphological features such as trim lines that are generally found in proximity to the ice margin. Figure 2.8 shows the new thinning curve at the present summit of the GrIS (GRIP) as well as output from 3D numerical ice sheet models (Huybrechts, 2002; Lhomme et al., 2005; Greve 2005; Tarasov & Peltier, 2003; Simpson et al., 2009). The model fits are improved relative to the original thinning curve and several models capture the thinning for the period 8 ka BP to present. Results from the Lhomme et al. (2005), Huybrechts (2002) and Simpson et al. (2009) models are closest to the estimated thinning curve. We note that the Huy2 model is an extended version of the Huybrechts (2002) model, calibrated to fit both a regional RSL data set and field constraints on ice extent. However, there still exists discrepancy during the early Holocene (12 to 8 ka BP), although this section of the curve could change significantly. All models result in a considerable elevation increase during the early Holocene, except for the Huy2 reconstruction which shows a relatively stable ice surface throughout the Holocene (Figure 2.8).

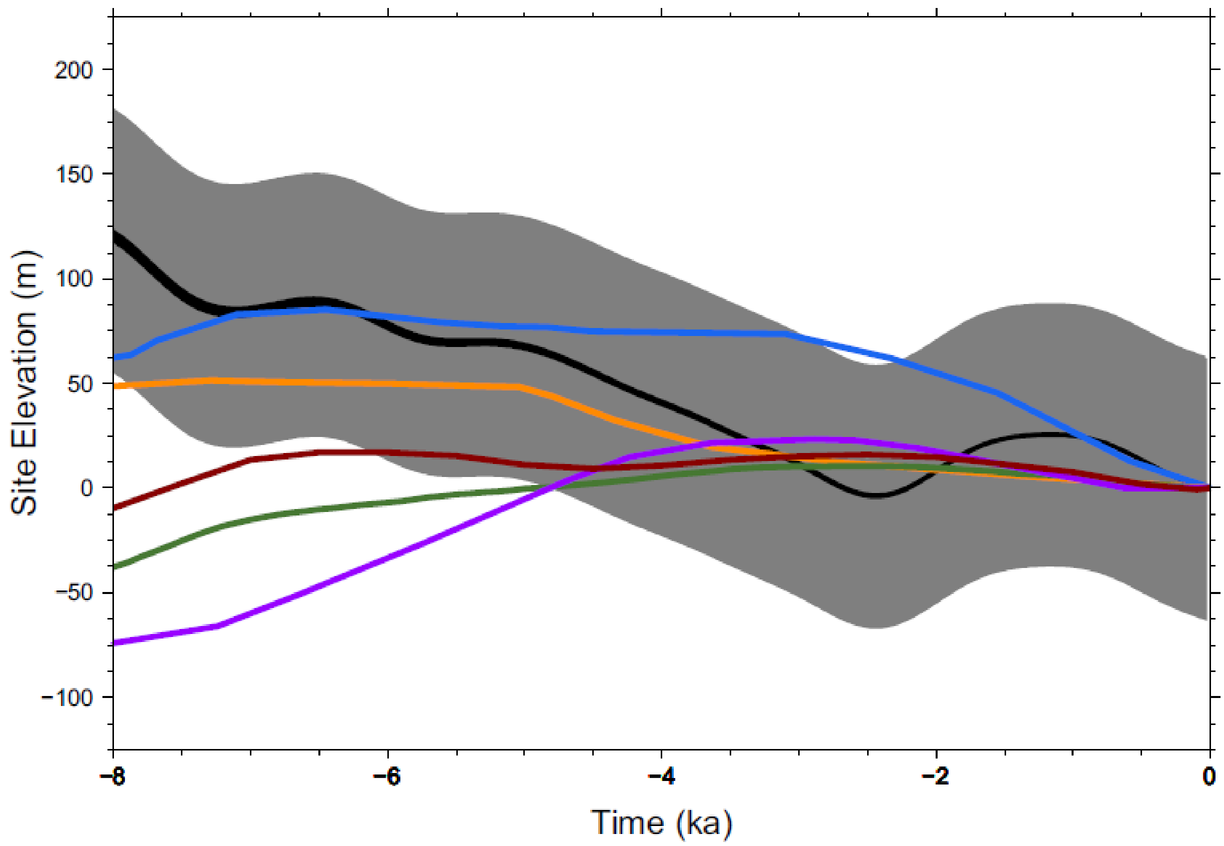

Figure 2.8 (a) Comparison of the newly derived thinning curve (black; uncertainty bounds indicated by grey lines) at the GRIP drill site with output from three-dimensional thermomechanical models of the GrIS (orange, Huybrechts (2002); blue, Lhomme et al. (2005); green, Greve (2005); purple, Tarasov & Peltier (2003); red, Simpson et al. (2009)).

The model misfits illustrated in Fig. 2.8 bring into question the accuracy of the current generation of deglacial GrIS reconstructions obtained from numerical ice models. It is important to determine the sources of the discrepancy, which likely include both the ice models (in terms of the processes simulated, model parameterisation, and numerical accuracy) and data employed to constrain model input (e.g. climate) and output (e.g. ice extent). This task requires multiple lines of investigation using numerical ice sheet models with increasing degrees of sophistication to incorporate effects such as grounding line migration, longitudinal stresses, ice-ocean heat exchange (e.g. Pollard and DeConto, 2009). Given that a key aspect of the current study is modelling vertical land motion, we briefly consider limitations in this aspect of the calculation in computing the contribution of vertical land motion to the modelled ice surface elevation changes in Fig. 2.8. The treatment of isostasy in an ice model will affect both the output of ice extent through time (e.g. Le Meur and Huybrechts, 1996; Van de Berg et al., 2008) as well as computations of vertical land motion for a given ice load distribution history. It is the latter that we consider here.

In Fig. 2.9 we show ice surface elevation curves at all four core sites for the Huy2 ice model. Two model curves are shown that are based on the same ice model reconstruction but adopt different treatments of isostasy and loading functions in the land height change component of the surface elevation changes. The dashed black line is based on a treatment of isostasy that is commonly employed in numerical ice sheet models (essentially, elastic plate flexure that incorporates viscous mantle flow by introducing a single response or relaxation time; see, for example, Le Meur and Huybrechts, 1996). In this case, the loading model comprises the Greenland ice sheet reconstruction and a eustatic ocean load. The solid black line is based on more complex Earth and loading models commonly applied in GIA analyses. The Earth model is a spherically symmetric, self-gravitating, Maxwell body and includes both elastic and non-elastic response components, with the latter defined by a spectrum of decay times and amplitudes that vary for different wavelengths of deformation (e.g. Peltier, 1974; Le Meur and Huybrechts, 1996). The loading model includes a gravitationally-self consistent ocean load (Farrell and Clark, 1976; Mitrovica and Milne, 2003) and a global reconstruction of ice loading changes (ICE-5G minus GrB) in addition to the Greenland ice component (Huy2). Inspection of Fig. 2.9 shows that the more realistic model results in an increased surface lowering at all core sites. This difference is dominated by the loading influence of non-Greenland ice (largely North American ice) leading to land subsidence of 30-40 m throughout the Holocene. While the application of this more realistic loading and Earth deformation model certainly acts to improve the fit at each site, there remains significant discrepancy at the sites closest to the margin

(Camp Century and DYE-3). Those at Camp Century could be related to enhanced pre-Holocene thickening at this site due to the confluence of the Greenland and Innuitian ice sheets, while those at Dye-3 could be related to the high amplitude and short wavelength terrain in this area which are not well captured in the Huy2 ice model.

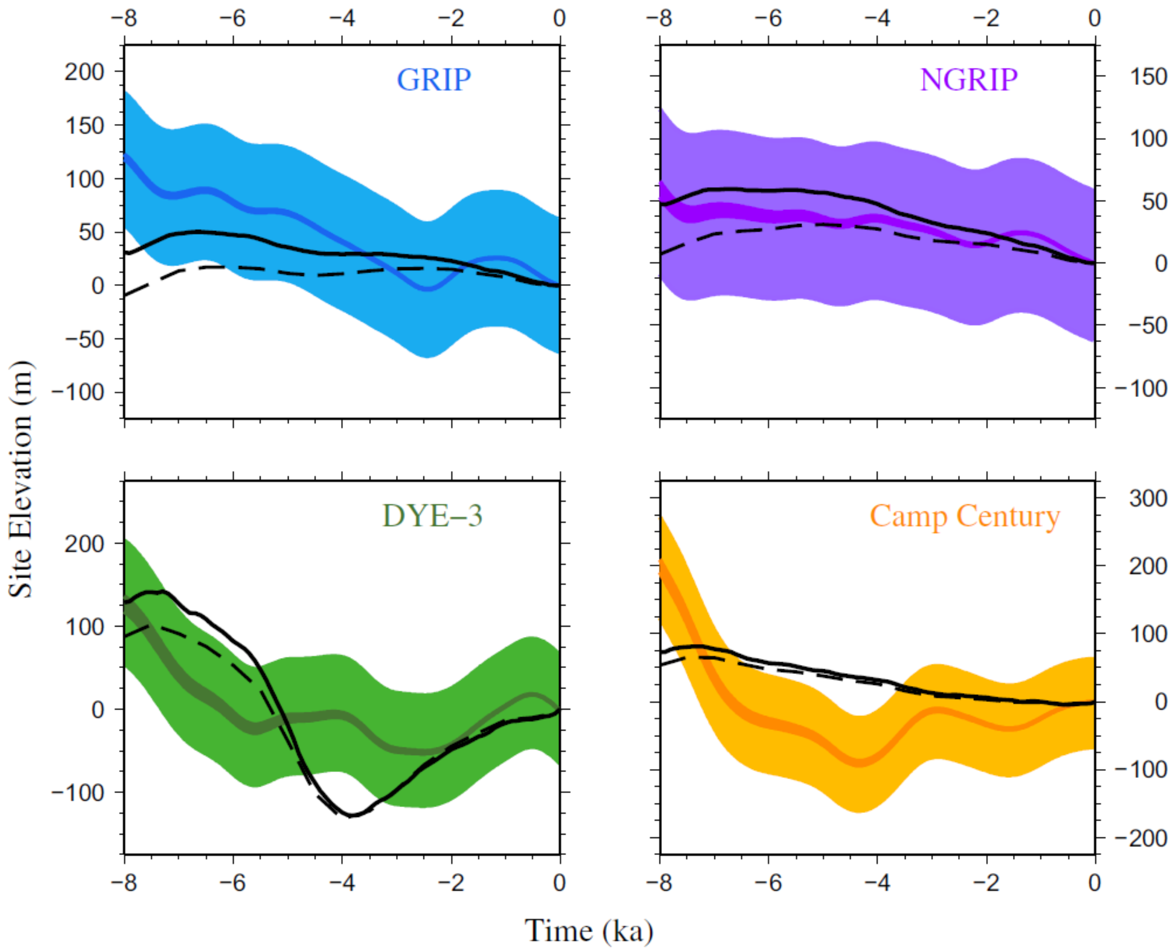

Figure 2.9 Comparison of the Huy2 Greenland ice model (solid black) used in this study with the new Holocene thinning curves. The dashed black line is the predicted ice surface elevation change when the land height signal is computed using the isostasy treatment in the ice model. The solid black line is the predicted elevation change when the land height signal is computed using a more sophisticated treatment of isostasy (in terms of the loading and the Earth deformation). See text for details.

2.5 CONCLUSION

We revisited the analysis of Vinther et al. (2009) to determine if the use of more accurate land uplift corrections for the $\delta^{18}O$ records from the AR ice caps would result in a significant difference to the inferred ice surface thinning histories at Greenland ice core sites. The primary motivation of this exercise was to determine if changing this aspect of the original analysis could account for the large discrepancy between the original thinning curves and output from numerical ice models. We applied uplift histories that were computed using a GIA model calibrated to sea-level observations from Arctic Canada and Greenland. Removing the land height signal from the Agassiz $\delta^{18}O$ record is complicated by the fact that the specific locality to apply this correction is not accurately known. This is due to uncertainty in the moisture pathways and the possible influence of Innuitian ice prior to ~8 ka BP (the latter issue is not quantified in this analysis). The new thinning curves for the period 8 ka BP to present are shifted down relative to the original curves at GRIP, NGRIP, DYE-3 and Camp Century. In addition, compared to the original analysis, the 1-σ uncertainty is considerably larger at GRIP and NGRIP. These changes reduce the data-model discrepancy reported by Vinther et al. (2009) at the Greenland core sites. A more accurate treatment of isostasy and surface loading also acts to improve the data-model fits such that the residuals at all sites for the period 8 ka BP to present are significantly reduced compared to the original analysis. Prior to 8 ka BP, the possible influence of Innuitian ice on the inferred elevation histories prevents a meaningful comparison. Incorporating this component into the analysis is a prime target for future investigation.

2.6 REFERENCE

Blake, W. Jr.. 1999. Glaciated landscapes along Smith Sound, Ellesmere Island, Canada and Greenland. Annals of Glaciology 28, 40-46.

Buchardt, S.L., Dahl-Jensen, D., 2007. Estimating the basal melt rate at NorthGRIP using a Monte Carlo technique: International Symposium on Earth and Planetary Ice-Volcano Interactions, Jun 19-23, 2006 Univ Iceland, Inst Earth Sci, Reykjavik, Iceland. Annals of Glaciology, 45, 137-142.

Dahl-Jensen, D., Johnsen, S.J., 1986. Palaeotemperatures still exist in the Greenland ice-sheet. Nature, 320, 250-252.

Dahl-Jensen, D., Mosegaard, K.E., Gundestrup, N.S., Clow, G.D., Johnsen, S.J., Hansen, A.W., Balling, N., 1998. Past temperatures directly from the Greenland ice sheet. Science, 282, 268-271.

Dahl-Jensen, D., Gundestrup, N.S., Gogineni, S., Miller, H., 2003. Basal melt at NorthGRIP modeled from borehole, ice-core and radio-echo sounder observations. Ann. Glaciology, 37, 207-212.

Dansgaard, W., 1961. The isotopic composition of natural waters. Meddelelser om Grønland. 165, 2.

Dyke, A.S., Peltier, W.R., 2000. Forms, response times and variability of relative sea-level curves, glaciated North America. Geomorphology 32, 315-333.

Dziewonski, A.M., Anderson, D.L., 1981. Preliminary reference Earth model. Physics of the Earth and Planetary Interiors 25, 297.

England, J., Atkinson, N., Bednarski, J., Dyke, A.S., Hodgson, D.A., Ó Cofaigh, C., 2006. The Innuitian Ice Sheet: configuration, dynamics and chronology. Quaternary Science Review 25, 689-703.

England J.H., Lakeman, T.R., Lemmen, D.S., Bednarski, J.M., Steward, T.G., Evans, D.J.A., 2008. A millennial-scale record of Arctic Ocean sea ice variability and the demise of the Ellesmere Island ice shelves. Geophysical Research Letters 35, L19502.

Farrell, W.E., Clark, J.A., 1976. On postglacial sea level. Geophysical Journal. Royal Astronomical Society 46, 647-667.

Fisher, D.A., 1990. A zonally-averaged stable-isotope model coupled to a regional variable-elevation stable-isotope model. Annals of Glaciology 14,65-71.

Fisher, D.A., Koerner, R.M., Reeh, N., 1995. Holocene climatic records from Agassiz ice cap, Ellesmere Island, NWT, Canada , Sage 5, 19-24.

Fisher, D.A., 1992. Stable isotope simulations using a regional stable isotope model coupled to a zonally averaged global model. Cold Regions Science and Techonology 21, 61-77.

Funder, S., 1978. Holocene stratigraphy and vegetation history in the Scoresby Sund area, east Greenland, Grønl. Geologiske Undersoekels Bulletin. 129.

Greve, R., 2005. Relation of measured basal temperatures and the spatial distribution of the geothermal heat flux for the Greenland ice sheet. Annals of Glaciology 42, 424-432.

Gundestrup, N.S., Dahl-Jensen, D., Johnsen, S.J., Rossi, A., 1993. Bore-hole survey at dome GRIP 1991. Cold Regions Science and Technology, 21, 399-402.

Johnsen, S., Dahl-Jensen, D., Dansgaard, W., Gundestrup, N.S., 1995. Greenland palaeotemperatures derived from GRIP bore hole temperature and ice core isotope profiles. Tellus B, 47(5), 624-629.

Johnsen, S.J., Clausen, H.B., Dansgaard, W., Gundestrup, N.S., Hansson, M., Jonsson, P., Steffensen, J.P., Sveinbjörnsdottir, A.E., 1992. A deep ice core from east Greenland. Meddelelser om Grønland 29, 3–29.

Johnsen, S.J., White, J.W.C., 1989. The origin of Arctic precipitation under present and glacial conditions, Tellus, 41B, 452-468.

Johnsen, 1977. Stable isotope profiles compared with temperature profiles in firn with historical temperature records, in proc. Symp. On Iso-topes and Impurities in Snow and Ice, I.U.G.G. XVI, General Assembly, Grenoble, 1975, 388-392.

Huybrechts, P., 2002. Sea-level change at the LGM from ice-dynamics reconstructions of the Greenland and Antarctic ice sheets during the glacial cycles. Quaternary Science Review 21, 203-231.

Koerner, R.M., 1979. Accumulation, ablation, and oxygen isotope variations on the Queen Elizabeth Islands ice caps, Canada. Journal of Glaciology 22, 86, 25-41.

Koerner, R.M. and Fisher, D.A., 1990. A record of Holocene summer climate froma Canadian high Arctic ice core. Nature, 343(6259),630-631.

Le Meur, E., Huybrechts, P., 1996. A Comparison of different ways of dealing with isostasy: examples from modeling the Antarctic ice sheet during the last glacial cycle. Annals of Glaciology, 23, 309-317.

Lhomme, N., Clarke, G.K.C, Marshall, S.J., 2005. Tracer transport in the Greenland Ice Sheet: constraints on ice cores and glacial history. Quaternary Science Review 24, 173-194.

Meehl, G.A., T. F. Stocker, and Contributing Authors including P. Huybrechts (2007): Global Climate Projections, in: Solomon, S., D. Qin, M. Manning, Z. Chen, M. Marquis, K.B. Averyt, M. Tignor and H. L. Miller (eds.): Climate Change 2007: The Physical Science Basis: Contribution of Working Group I to the Fourth Assessment Report of the Intergovernmental Panel on Climate Change, Cambridge University Press, 747-845.

Milne, G.A., Mitrovica, J.X., 1998. Postglacial sea-level change on a rotating Earth. Geophysical Journal International 133, 1-19.

Mitrovica, J.X., Milne, G.A., 2003. On post-glacial sea level. Geophysical Journal International 154, 253-267.

Reeh, N., Johnsen, S.J., Dahl-Jensen, D., 1985. Dating the DYE-3 deep ice core by flow model calculations. Am. Geophys. Un. Geophys. Monogr 33, 57-65.

Peltier, W.R., 1974. The impulse response of a Maxwell Earth. Reviews of Geophysics and Space Physics 12: 649-69.

Peltier, W.R., 2004. Global glacial isostasy and the surface of the ice-age Earth: The ICE-5G (VM2) model and GRACE. Annual Review of Earth and Planetary Sciences 32:111-49.

Pollard, D., Deconto, R., 2009. Modelling West Antarctic ice sheet growth and collapse through the past five million years. Nature 458(7236), 329-332.

Simpson, M.J.R., Milne, G.A., Huybrechts, P., Long, A.J., 2009. Calibrating a glaciological model of the Greenland ice sheet from the last glacial maximum to present-day using field observations of relative sea level and ice extent. Quaternary Science Reviews 28, 1630-1656.

Tarasov, L., and Peltier, W.R., 2002. Greenland glacial history and local geodynamic consequences. Geophysical Journal International 150(1), 198-229.

Tarasov, L., Dyke, A.S., Neal, R.M., Peltier, W.R., 2012. A data-calibrated distribution of deglacial chronologies for the North American ice complex from glaciological modeling. Earth and Planetary Science Letters 315-316, 30-40.

Vialov, 1958. Regularities of glacial ice shields movement and the theory of glaciers, Int. Ass. Hydrol. Sci. Pub., 47, 266-275

Vinther, B.M., Buchardt, S.L., Clausen, H.B., Dahl-Jensen, D., Johnsen, S., Fisher, D.A., Koerner, R.M., Raynaud, D., Lipenkov, V., Andersen, K.K., Blunier, T., Rasmussen, S.O., Steffensen, J.P., Svensson, A.M., 2009. Holocene thinning of the Greenland ice sheet. Nature 461,385-388.

Van de Berg, J., Van de Wal, R.S.W., Milne, G.A., Oerlemans, J., 2008. Effect of isostasy on dynamical ice sheet modeling: A case study for Eurasia. J. Geophys. Res., 113, B05412.

Vinther, B.M., Clausen, H.B., Fisher, D.A., Koerner, R.M., Johnsen, S.J., Andersen, K.K., Dahl-Jensen, D., Rasmussen, S.O., Steffensen, J.P., Svensson, A.M., 2008. Synchronizing ice cores from the Renland and Agassiz ice caps to the Greenland Ice Core Chronology. J. Geophys. Res., 113, D08115.

Vinther, B.M., Clausen, H.B., Johnsen, S.J., Rasmussen, S.O., Andersen, K.K., Buchardt, S.L., Dahl-Jensen, D., Seierstad, I.K., Siggaard-Andersen, M.-L., Steffensen, J.P., Svensson, A., Olsen J., Heinemeier J., 2006. A synchronized dating of three Greenland ice cores throughout the Holocene. J. Geophys. Res., 111, D13102.

Waelbroeck, C., Labeyrie, L., Michel, E., Duplessy, J.C., McManus, J.F., Lambeck, K., Balbon, E., Labracherie, M., 2002. Sea-level and deep water temperature changes derived from benthic foraminifera isotopic records. Quaternary Science Reviews 21, 295-305.

3. A MODEL OF GREENLAND ICE SHEET DEGLACIATION BASED ON OBSERVATIONS OF ICE EXTENT AND RELATIVE SEA LEVEL

Quaternary Science Reviews (submitted November; 2013)

Benoit Lecavalier[1], Glenn A. Milne[1,2], Matthew J.R. Simpson[3], Leanne Wake[4], Philippe Huybrechts[5], Kristian K. Kjeldsen[6], Svend Funder[6], Lev Tarasov[9], Antony J. Long[7], Sarah Woodroffe[7], Arthur Dyke[10], Nicolaj K. Larsen[8]

[1] Department of Physics , University of Ottawa, Canada
[2] Department of Earth Sciences, University of Ottawa, Canada
[3]Norwegian Mapping Authority, Hønefoss, Norway
[4]University of Northumbria, UK
[5]Vrije Universiteit Brussel, Belgium
[6] Centre for GeoGenetics, Natural History Museum of Denmark, University of Copenhagen, Denmark
[7] Department of Geography, Durham University, UK
[8]Department of Geoscience, Aarhus University, Denmark
[9]Department of Physical Oceanography, Memorial University, Canada
[10] Geological survey of Canada, NRCan, Canada

3.1 ABSTRACT

An ice sheet model was constrained to reconstruct the evolution of the Greenland ice sheet (GrIS) from the last glacial maximum to present to improve our understanding of the GrIS response to climate change. The study involved calibrating a glaciological model in series with a glacial isostatic adjustment and relative sea-level (RSL) model. The model calibration builds upon the work of Simpson et al. (2009) through four main extensions: (1) a larger constraint database consisting of RSL and ice extent data; model improvements to the (2) climate and (3) sea-level forcing components; (4) accounting for uncertainties in non-Greenland ice in our model predictions. The research was conducted to address data-model misfits and to quantify inherent model uncertainties with the Earth structure and non-Greenland ice. Our new model (termed Huy3) fits the majority of observations and is characterised by a number of defining features. During the last glacial maximum, the ice sheet had an excess of 4.5 m ice-equivalent SL (IESL), which reached a maximum volume of 5.0 m IESL at 16.5 ka BP. Retreat of ice from the continental shelf progressed at different rates and timings in different sectors. Southwest and Southeast Greenland began to retreat from the shelf by ~16 to 14 ka BP, thus responding to the Bolling-Allerod

warm event (14 ka BP); subsequently ice in the the Southern tip of Greenland readvanced during the Younger Dryas cold event. North Greenland retreated rapidly from the continental shelf upon the climatic recovery out of the Younger Dryas to present-day (PD) interglacial conditions. Upon entering the Holocene (11.7 ka BP), the ice sheet soon became land-based. During the Holocene thermal maximum (HTM; 9-5 ka BP), temperatures across Greenland were marginally higher than those at present and the Greenland ice sheet margin retreated past its PD southwest position by 40 to 60 km at 4 ka BP which produced a deficit volume of 0.17 m IESL relative to present. In response to the HTM, our optimal model reconstruction lost mass at a maximum rate of 103.7 Gt/a, which is 27% less than that inferred for the period 1992 to 2011 (Shepherd et al., 2012). Our results suggest that remaining model-data discrepancies are affiliated with missing physics and sub-grid processes of the glaciological model and uncertainties in lateral Earth structure and non-Greenland ice (particularly the North American component). Finally, applying the Huy3 Greenland reconstruction with our optimal Earth model we generate PD uplift rates across Greenland due to past changes in the ocean and ice loads with explicit error bars due to uncertainties in the Earth structure. PD uplift rates due to past changes are spatially variable and range from 4 to -7 mm/a (including Earth model uncertainty); therefore, to interpret geodetic observations it is crucial to correct for this signal.

3.2 INTRODUCTION

Between 26.5 and 19 ka before present (BP) global ice volume reached and maintained a maximum value resulting in global mean sea-level being 130 m below present (Clark et al., 2009). During this period, known as the last glacial maximum (LGM), there was large-scale glaciation across North America and Eurasia as well as more extensive ice in Greenland and Antarctica (compared to present). During the subsequent deglaciation and transition to a warmer interglacial climate the large North American and Eurasian ice complexes perished, glaciers and ice caps reduced in size and withered away, and the Antarctic and Greenland ice sheets underwent significant mass loss. This dramatic change in the distribution of global ice has left its mark on the landscape and in the surface geology such as recessional moraines which provide a direct means of reconstructing ice extent chronology (e.g. Dyke and Prest, 1987). Also, the water mass transfer from continents to oceans leads to a global-scale visco-elastic response of the Earth (e.g. Peltier and Andrews, 1976; Clark et al., 1978) with rapid land uplift still observed at present where large ice sheets once existed (e.g. Milne et al., 2001).The vertical land motion in previously glaciated areas results in raised marine deposits or erosional features which provide valuable indirect information on past changes in local and regional ice extent (e.g. Lambeck et al., 1998). In more recent years, information from ice core records has also been used to place constraints on past ice thickness changes (Vinther et al., 2009). In this study, we apply a range of direct and indirect observations of ice extent and sea-level to reconstruct the Greenland ice sheet (GrIS) during its most recent deglaciation.

The rapid change in relative sea-level (RSL) and climate following the LGM had dramatic consequences for the evolution of the GrIS. A great deal of field observations suggest that the LGM ice sheet extended across large portions of the continental shelf and, in some areas, extending as far as the shelf break (e.g. O'Cofaigh et al., 2012, Larsen et al., 2010). This maximum extent for the GrIS has often been affiliated with an increase in volume of 2-3 m ice equivalent sea-level (IESL) relative to present (Clark & Mix, 2002). During the subsequent deglaciation, the GrIS retreated predominantly through the calving of its marine-based ice in a series of successive retreats as sealevels rose (Kuijpers et al., 2007).

By approximately 10ka BP, the ice sheet was mainly land-based with the exception of some outlet glaciers (e.g. Funder et al., 2011), after which time, deglaciation of the ice sheet reached a slower pace and was dominated by surface melt. However, there was a period during the Holocene from about 9 to 5 ka BP when temperatures across Greenland were warmer than present; often defined as the Holocene Thermal Maximum (HTM) (Kaufman et al., 2004). It has been suggested that, in some areas, the ice sheet retreated past its present-day (PD) margin in response to the HTM, attaining a post-LGM volume minimum around 4 ka BP (Simpson et al., 2009) which was followed by climate deterioration and consequent so-called neoglacial readvance (Kelly, 1980). Due to the readvance of ice, all direct geomorphological evidence pertaining to the minimum configuration was overridden. Thus, inferences of the minimum configuration of the ice sheet can only be obtained through indirect observations such as RSL and ice-core records.

The main motivation of this research is to more accurately understand the response of the ice sheet to past climate change with the goal of better predicting how it will behave to future changes. Considering that the GrIS retreated past its PD margin during the warmer climate of the HTM, it is important to assess the potential sea-level contribution of the GrIS to analogously warm conditions. The necessity of understanding the current state of the ice sheet is becoming increasingly evident. Recently, in July 2012, satellite observations reported unprecedented melt events over 98.6% of the GrIS surface (Nghiem et al., 2012). Furthermore, the GrIS is still responding to millennial-scale climate change which must be carefully accessed to better predict future behaviour (Simpson et al., 2011). Recently satellite altimetry, interferometry, and gravimetry data sets have been applied to estimate the mass balance of the GrIS (Shepherd et al., 2012). It was shown that the GrIS was losing mass at an accelerated rate with a total loss of 142±49 Gt/yr between the year 1992 to 2011. However, only with a longer record of satellite observations will we be able to determine if the accelerating ice loss from the GrIS is due to a sustained response to recent warming. However, prior to extracting mass loss from the ice sheet using geodetic satellite data sets, it is necessary to correct their record for the vertical motion of the solid Earth due to past ice sheet changes. Considering uncertainties in the ice chronology and Earth structure directly affects our understanding of PD uplift rates. To interpret contemporary mass changes of the ice sheets requires a proper understanding of past changes.

There are several distinct approaches which have been used in the past to reconstruct GrIS deglaciation (Huybrechts, 2002; Tarasov & Peltier 2002; Flemming & Lambeck, 2004; Peltier, 2004; Simpson et al., 2009) which all have their associated advantages and disadvantages. This includes the lack of glaciological self-consistency (Peltier, 2004) to small set of constraints (Huybrechts, 2002). This study builds upon the work conducted by Simpson et al., 2009 (henceforth referenced as the Simpson study) where we reconstruct the behaviour of the GrIS from the LGM to present. The approach they adopted to reconstruct the deglacial history of the GrIS employed a three-dimensional ice sheet model forced by a set of prescribed climatic conditions (e.g. Huybrechts, 2002). Output from the glaciological model was tested directly against ice extent observations and indirectly by comparing observations to RSL predictions - computed using the ice history as input to a glacial isostatic adjustment (GIA) model of sea-level change (Kendall et al., 2005).

In this study, we build upon the work of Simpson et al. (2009) by initially adopting their model reconstruction of GrIS evolution (termed Huy2) and improving it in several respects. The Huy2 reconstruction was achieved by simultaneously calibrating a 3-D thermomechanical ice sheet in series with a GIA model of sea-level change to a collection of field observations of RSL and ice extent. Our improved reconstruction adopts the same general approach but with four main extensions. The database includes additional RSL and ice extent constraints which are detailed in Section 3.3. Key additions are an up-to-date Greenland-wide marine limit data base (K. Kjeldsen & S. Funder, personal communication) and ice-core derived thinning curves (from GRIP, NGRIP, Dye-3, and Camp Century) which constrain elevation changes of the ice surface for the period 8 ka BP to present (Vinther et al., 2009; Lecavalier et al., 2013). Two other extensions relate to developments that improved the accuracy of the adopted ice model; these were (1) advances to the parameterization of the positive degree day algorithm for computing surface mass balance changes (Wake et al., 2013) and (2) considering spatial variability in the sea-level forcing (SLF) to better match the observed marine retreat chronology. The final key extension involves assessing the RSL contribution around Greenland due to explicit uncertainties in the North American ice complex (NAIC). In addition to these advances, this study involves several sensitivity analyses on a number of key model parameters and inputs to investigate the level of non-uniqueness and to produce a reconstruction of the GrIS which minimized data-model discrepancies.

The article structure is a follows: Section 3.3 covers the pertinent datasets; Section 3.4 provides an overview of the models applied; Section 3.5 presents the modelling results and sequentially introduces the main extensions of this study resulting in the Huy3 model; finally Section 3.6 discusses the ramifications of the Huy3 model. To enhance the clarity of the text a list of abbreviations is located in Table 3.1.

BP	before present
DDFs	degree day factors
IESL	ice equivalent sea-level
GIA	glacial isostatic adjustment
GrB	Tarasov & Peltier (2002) Greenland reconstruction in ICE-5G
GREEN1	Flemming & Lambeck (2004) Greenland reconstruction
GrIS	Greenland ice sheet
HTM	Holocene Thermal Maximum
Huy1	Huybrechts (2002) Greenland reconstruction
Huy2	Simpson et al. (2009) Greenland reconstruction
Huy3	Greenland reconstruction for this study
LGM	Last Glacial Maximum
LMV	lower mantle viscosity
LT	lithospheric thickness
NAIC	North American ice complex
ML(s)	marine limit(s)
PDD	positive degree day
PD	present-day
RSL	relative sea-level
SLF(s)	sea-level forcing(s)
UMV	upper mantle viscosity

Table 3.1 Abbreviations used in the text.

3.3 DATA

In this study we consider a broad range of field observations to constrain a subset of key selected model parameters. There are four primary sets of constraints: (1) evidence of past ice extent based on terminal and recessional moraines, marine sediment cores, exposure dating and threshold lakes; (2) field evidence that constrains past changes in relative sea level; (3) ice-core derived thinning curves at the GRIP, NGRIP, DYE-3 and Camp Century site which constrain the surface elevation of the ice sheet as

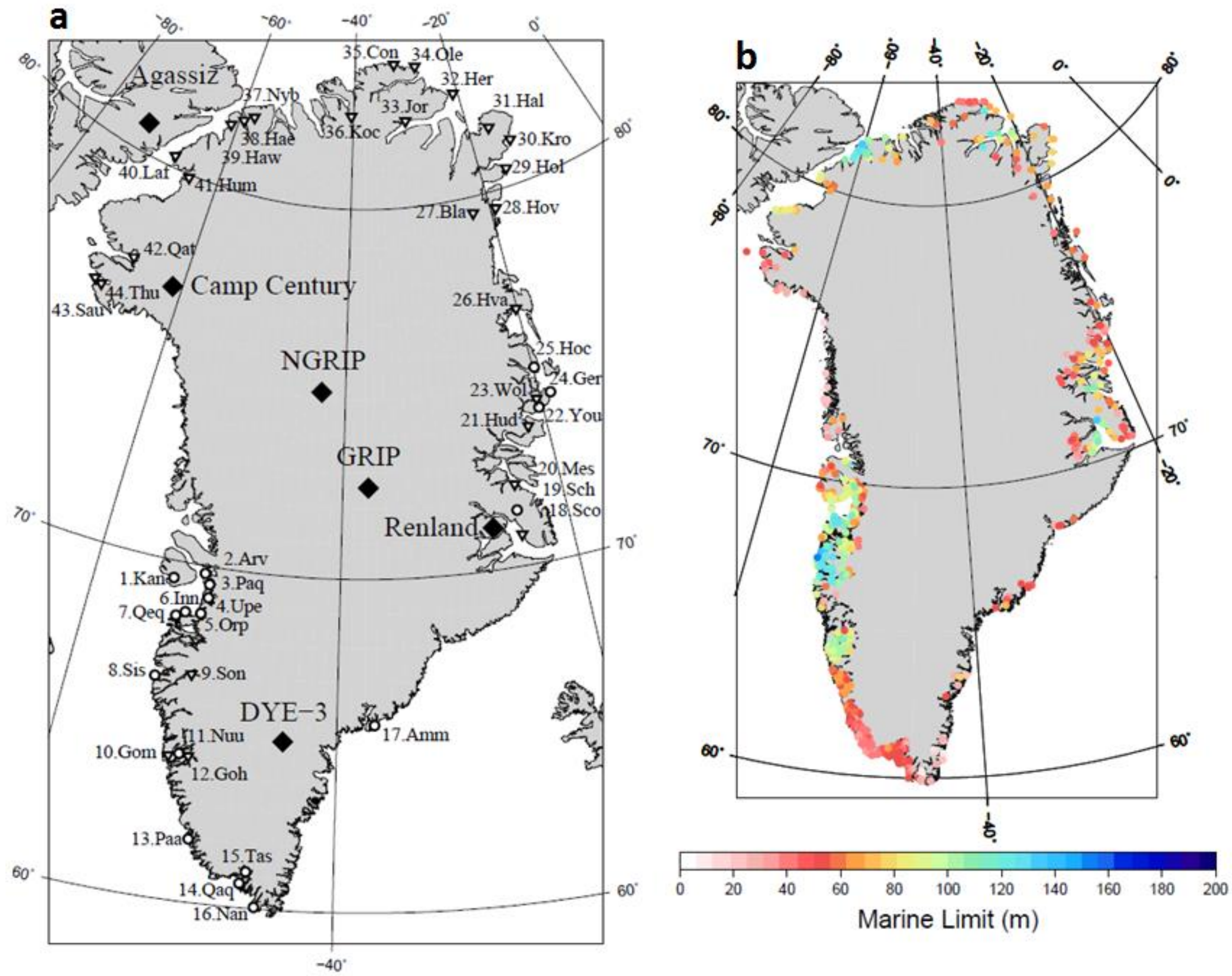

Figure 3.1 (a) The locations and names of RSL and ice-core data sites discussed and applied in this study. The circles indicate the location of sea-level index point data while triangles refer to limiting data. A list of RSL data site locations and the corresponding source literature used to compile the data base used in this study is found in Table 2. (b) A map showing the location of individual ML observations that supplement the RSL observations shown in (a); these observations are particularly useful where RSL data is sparse.

controlled by ice thinning and vertical motion of the solid Earth; (4) the PD configuration of the ice sheet such as ice thickness, elevation and surface velocities. To provide relevant background to Sections 3.5

and 3.6, we review the most relevant aspects of these observational constraints in the following sub-sections. The locations and source references of the ice-core sites and sea-level data are shown in Figure 3.1. Henceforth, all dates given are listed in calibrated years unless stated otherwise.

3.3.1 ICE EXTENT DURING DEGLACIATION

Geological and geomorphological field evidence provides valuable information that constrains the past lateral extent of the GrIS; here we focus only on constraints used to infer margin positions from the LGM through to the late Holocene (Funder et al., 2011; Funder & Hansen, 1996; Funder, 1989). During the LGM, North West Greenland ice was dynamically connected to the Innuitian ice sheet on Ellesmere Island. Marine ice in Nares Strait was fed by ice streams from both ice sheets and did not recede until ~12.5 ka BP (Blake, 1999, England, 1999). It was not until 11.2 ka BP that ice streams sustaining marine based ice in the Strait retreated to their respective fjord mouths leading to a saddle collapse by ~10 ka BP (Kelly and Bennike, 1992; Zreda et al., 1999). In contrast North Greenland had ice extending far onto the mid-outer continental shelf which was buttressed against stationary multiyear sea ice in the Arctic Ocean (Moller et al., 2010). Optically stimulated luminescence dating of glaciolacustrine sediments along with exposure dates showed that ice extending out onto the shelf started degrading sometime between 16 to 10.3 ka BP before the final breakup of marine based ice in this region by 10.1 ka BP (Larsen et al., 2010). North East Greenland has a wide and shallow continental shelf which is covered in glacial landforms such as submarine moraines (Evans et al., 2009; Winkelmann et al., 2010). These features are affiliated with an LGM mid-shelf extent as a plausible lower bound extent with an initial retreat at 10 ka BP (Landvik, 1994; Hjort, 1997; Wilken & Mienert, 2006; Evans et al., 2009; Winkelmann et al., 2010). The marine sedimentary record near Kejser Franz Joseph Fjord on the East Greenland coast suggests glaciation of the continental shelf; a mid-shelf moraine defines a plausible LGM extent for the region (Evans et al., 2002) while mass-wasting deposits from submarine channels suggest grounded ice reaching the outer continental shelf (O'Cofaigh et al., 2004). Deglaciation of the region commenced after 15.3 ^{14}C ka BP with the mid-shelf free of grounded ice by 13 ka BP which coincides with a significant drop in sedimentation in the submarine channel. The inner shelf was most likely free of ice by 9.1 ^{14}C ka BP (Evans et al., 2002; O'Cofaigh et al., 2004).

It has been proposed that ice extent in Scoresby Sund during the LGM was out to Kap Brewster (Hakansson et al., 2007b; Hakansson et al., 2009). Sedimentary cores from the Scoresby Sund region identify a maximum in ice-rafted debris deposition on the continental slope between 22 and 14 ka BP which coincides with the retreat of ice from its LGM extent (Stein et al., 1996; Funder et al., 1998). Between 12 to 10 ka BP, the outer fjord basins appear to be free of glaciers (Funder et al., 1998). The South East margin of the ice sheet during the LGM extended to the shelf edge as indicated by terminal moraines (Sommerhoff 1981; Andrews, 2008; Dowdeswell et al., 2010). The ice margin at Kangerlussuaq reached the shelf edge by 21 ka BP and began to retreat shortly after 17 ka BP (Andrews et al., 1997; Andrews et al., 1998; Jennings et al., 2006; Andrews, 2008). During the LGM, ice south of Helheim glacier reached the shelf break and maximum values of coarse-grained ice-rafted debris occurred during the period between 19 and 15 ka BP which coincides with rapid ice retreat from the shelf after 16 ka BP (Nam et al., 1995; Kuijpers et al., 2003). Southern Greenland has a narrow continental shelf and ice reached the shelf break during the LGM; the initial retreat occurred at 15 ka BP, with exposure dates suggesting that the ice-margin quickly reached its present position by 10 ka BP (Bennike et al., 2002; Sparrenbom et al., 2006a,b). Along the west Greenland continental shelf, sub-marine moraine-belts are distributed intermittently which suggest an LGM margin out to the shelf break (Roberts et al., 2009; O'Cofaigh et al., 2012). Ice streams which extended out onto the shelf persisted into the early Holocene but had receded by 10.2 ka BP causing ice free conditions in the embayment of Disko Bugt (Ingolfsson et al., 1990; Lloyd et al., 2005).

As indicated by the observations summarised above, the initial retreat of the GrIS from its maximum extent varies in space and time. This likely reflects changes in a variety of controlling processes and boundary conditions - such as rising sea-level and ocean temperatures, shelf bathymetry, sea ice extent - and also the use of different proxies which have different sensitivities to margin position. In general, grounded ice retreated from the shelf during the period 17 to 11.5 ka BP, such as the Scoresby Sund ice free timing of 12.4 ka BP (Hall et al., 2010) and the main retreat phase of Southern Greenland between 14 to 12 ka BP (Bennike et al., 2002). The Younger Dryas event (YD; 12.8 to 11.7 ka BP Steffensen et al., 2008) caused a mild re-advance of the ice margin in some regions (Hall et al., 2010) but no signal in many others (Jennings et al., 2006; Sparrenbom et al., 2006b; Kuijpers et al., 2003). Following the YD stadial, Holocene interglacial climate set in over the ice sheet with a temperature increase on the order of 10 degrees Celsius (Steffensen et al., 2008; Walker et al., 2009) which led to a predominantly land based ice sheet (Funder & Hansen 1996; Bennike & Bjorch, 2002; Jennings et al., 2006; Sparrenbom et al., 2006b; Hall et al., 2008; Long et al., 2008a; Wagner et al., 2010; Larsen et al., 2010). During the Early Holocene the ice sheet continued to deglaciate but at a slower pace since the ocean influence was much reduced and retreat was driven by surface melt and calving of fjord glaciers (Funder et al., 2004; Funder & Hansen, 1996). From 11 to 8 ka BP, large land-areas were uncovered by the ice sheet in West Greenland (Weidick & Bennike, 2007; Long et al., 2006).

Threshold lake data from around the periphery of the GrIS has been used to date the onset of ice free conditions (Briner et al., 2010; Larsen et al., 2013). These data have also been used to interpret the timing at which the PD margin is reached and the minimum configuration of the ice sheet. Furthermore, they have been applied to infer that the GrIS margin was advancing in North Greenland between 9.6 to 6.3 ka BP (Moller et al., 2010). This is believed to have been caused by an increase in atmospheric moisture content due to greater heat transport in the North Atlantic. The GrIS is thought to have reached a minimum configuration in response to the HTM as documented by C^{14}-dates from historical moraines or surfaced organic material by movement along shear planes (Bennike & Weidick, 2001; Weidick et al., 2004; Weidick & Bennike, 2007). Following the HTM and the subsequent response of the ice sheet, evidence suggests there was a neoglacial regrowth of the GrIS in the South West sector which culminated in a maximum extent during the Little Ice Age. A wide range of proxies with differing sensitivities recorded a cooling trend across Greenland after approximately 5 to 3 ka BP which documented the spatially variable regrowth of the ice sheet (Seidenkrantz et al., 2008; Jakobsen et al., 2008; Klug et al., 2009; Norgaard-Pedersen & Mikkelsen, 2009; Kelly & Lowell, 2009; Ren et al., 2009; Bennike et al., 2010; Schmidt et al., 2010).

3.3.2 RELATIVE SEA LEVEL AND MARINE LIMIT

For this modelling study we are interested in millennial scale sea-level changes on the order of tens of meters. In Greenland, past sea levels have been reconstructed using a variety of indicators: isolation basins, raised beaches and deltas, marine shells, drift wood, perched boulders, and whale bones. Figure 3.1 illustrates the locations of the RSL observations used in this study and Table 3.2 lists the related source references.

Region	Site	Site name	Source reference
West	1	Kangerlusuaq (Kan)	Long et al., 2011; Bennike, 1995
	2	Arveprinsen (Arv)	Long et al., 1999
	3	Pakitsoq (Paq)	Long et al., 2006
	4	Upernivik (Upe)	Long et al., 2006
	5	Orpisook (Orp)	Long & Roberts, 2002
	6	Innaarsuit (Inn)	Long et al., 2003
	7	Qeqertarsiatsuaq (Qeq)	Long & Roberts, 2003
Southwest	8	Sisimiut (Sis)	Bennike et al., 2011; Long et al., 2008
	9	Sondre (Son)	van Tatenhove & van der Meer, 1996; Ten Brink, 1974; Weidick, 1972
	10	Godmouth (Gom)	Berglund, 2003; Fredskild, 1983; Weidick, 1976
	11	Nuuk (Nuu)	Fredskild, 1983
	12	Godhead (Goh)	McGovern et al., 1996; Fredskild, 1983; Weidick, 1976; Fredskild, 1972
	13	Paamiut (Paa)	Woodroffe et al., 2013
South	14	Qaqortoq (Qaq)	Sparrenbom et al., 2006b
	15	Tasiusaq (Tas)	Fredh, 2008; Randsalu, 2007
	16	Nanortalik (Nan)	Bennike et al., 2002; Sparrenbom et al., 2006b
Southeast	17	Ammassalik (Amm)	Long et al., 2008

East	18	Scoresby Sund (Sco)	Funder & Hansen, 1996
	19	Schuchert (Sch)	Hall et al., 2010
	20	Mesters Vig (Mes)	Trautman & Willis, 1963; Washburn & Stuiver, 1962
	21	Hudson (Hud)	Hjort, 1981; Hjort, 1979; Hjort & Funder, 1974
	22	Young Sound (You)	Pedersen et al 2011
	23	Wollaston (Wol)	Christiansen et al., 2002; Hjort, 1979
	24	Germania (Ger)	Bennike & Wagner; 2012
	25	Hochstetter (Hoc)	Bjorck et al., 1994
Northeast	26	Hvalroso (Hva)	Landvik, 1994
	27	Blaso (Bla)	Bennike & Weidick, 2001
	28	Hovgaard (Hov)	Bennike & Weidick, 2001
	29	Holm Land (Hol)	Funder et al., 2011
	30	Kronprins (Kro)	Funder et al., 2011; Hjort, 1997
	31	Ingebord Halvo (Hal)	Funder et al., 2011
North	32	Herlufsholm (Her)	Funder et al., 2011
	33	Jorgen (Jor)	Funder & Abrahamsen, 1988
	34	Ole Chiewitz (Ole)	Funder et al., 2011
	35	Constable (Con)	Funder et al., 2011
	36	JPKoch (Koc)	Landvik et al., 2001; Kelly & Bennike, 1992
Northwest	37	Nyboe (Nyb)	Kelly & Bennike, 1992; England, 1985
	38	HallEast (Hae)	Kelly & Bennike, 1992; England, 1985
	39	HallWest (Haw)	Kelly & Bennike, 1992; England, 1985
	40	Lafayette (Laf)	Bennike, 2002
	41	Humboldt (Hum)	Bennike, 2002
	42	Qeqertat (Qeq)	Fredskild, 1985
	43	Saunders (Sau)	Funder, 1990
	44	Thule (Thu)	Kelly et al., 1999; Funder, 1990

Table 3.2 The RSL observations applied in this study and their source references. These observations are used to constrain our GIA and RSL model and their locations are marked in Fig. 3.1.

The sea-level observations used in this study with the highest precision are those from isolation basins (Long et al., 2011). Studies of isolation basins have only been conducted for a little over 20 years in Greenland, which yields approximately 122 relevant data points for this study (e.g. Long et al., 2011; Bennike et al., 2011; Woodroffe et al., 2013). In comparison, the Simpson et al. (2009) study incorporated only 73 isolation basin sea-level index points. However, the lack of spatial homogeneity of such RSL field studies, especially in the high Arctic, forces the use of less precise sea-level proxies to improve the spatial distribution of data. The remaining sea-level proxies applied (360 data points) consist of marine shells (molluscs), drift wood and whale bones that have a less precise relationship to mean sea level and thus provide only a limiting constraint. That is, they place an upper or lower bound on RSL for a given time and location; however the temporal and height uncertainty can be very large (over ±1 ka and ±1 m, respectively). The marine limit (ML) for a given location defines an upper limit of RSL which constrains the isostatic response due to the unloading of ice. The ML is often defined by the lower limit of perched boulders above wave-washed bedrock which identifies the highest point sea-level reached at a given site during ice free conditions. Lakes that lack a marine phase have also been used to define the ML in some locations (e.g. Woodroffe et al., 2013). A total of 629 ML observations have been compiled which captures the Greenland coast quite homogeneously as shown in Figure 3.1b with characteristic dome features of high ML values (Weidick, 1976; Funder, 1989; Funder and Hansen, 1996; K. Kjeldsen & S. Funder, personal communication). This data is quite valuable in regions where other RSL observations are lacking, particularly in northwest and southeast Greenland as illustrated in Figure 3.1a.

3.3.3 HOLOCENE THINNING CURVES

Vinther et al. (2009) applied a novel procedure to determine ice surface elevation curves at four GrIS ice core locations (GRIP, NGRIP, DYE-3 and Camp Century; see Fig. 3.1a). These data-constrained curves depict a Holocene thinning history that is considerably more rapid and of greater amplitude than that indicated from numerical ice models. Recently, this analysis was revisited by Lecavalier et al. (2013) who concluded that the ice-core derived thinning curves have much larger uncertainties than previously thought, particularly prior to 8 ka BP due to the influence of the Innuitian ice sheet. However, regardless of these limitations, we include these constraints (see Section 3.5.3) given that they provide the only information on past ice thickness changes in the interior of the ice sheet.

3.4 MODEL DESCRIPTION

The key model components and set-up applied in this study, as adopted from Simpson et al. (2009), are shown in Figure 3.2. The calibration is initialized with a 3-D thermomechanical ice sheet model which freely simulates the evolution of the GrIS and is compared to lateral extent data and the PD ice sheet geometry. The Greenland ice model is then amalgamated to a global ice model to act as a primary input to the GIA & RSL model. In conjunction with a global ice model, an Earth model is prescribed to the GIA & RSL model to produce sea-level and vertical land motion predictions. A sweep of key model parameters samples the range of model predictions which are compared to observations. Finally a statistical analysis yields optimal model parameters which minimize the misfit between model predictions and observations. It should be stated that the thermomechanical ice sheet model and GIA model operate independently in series.

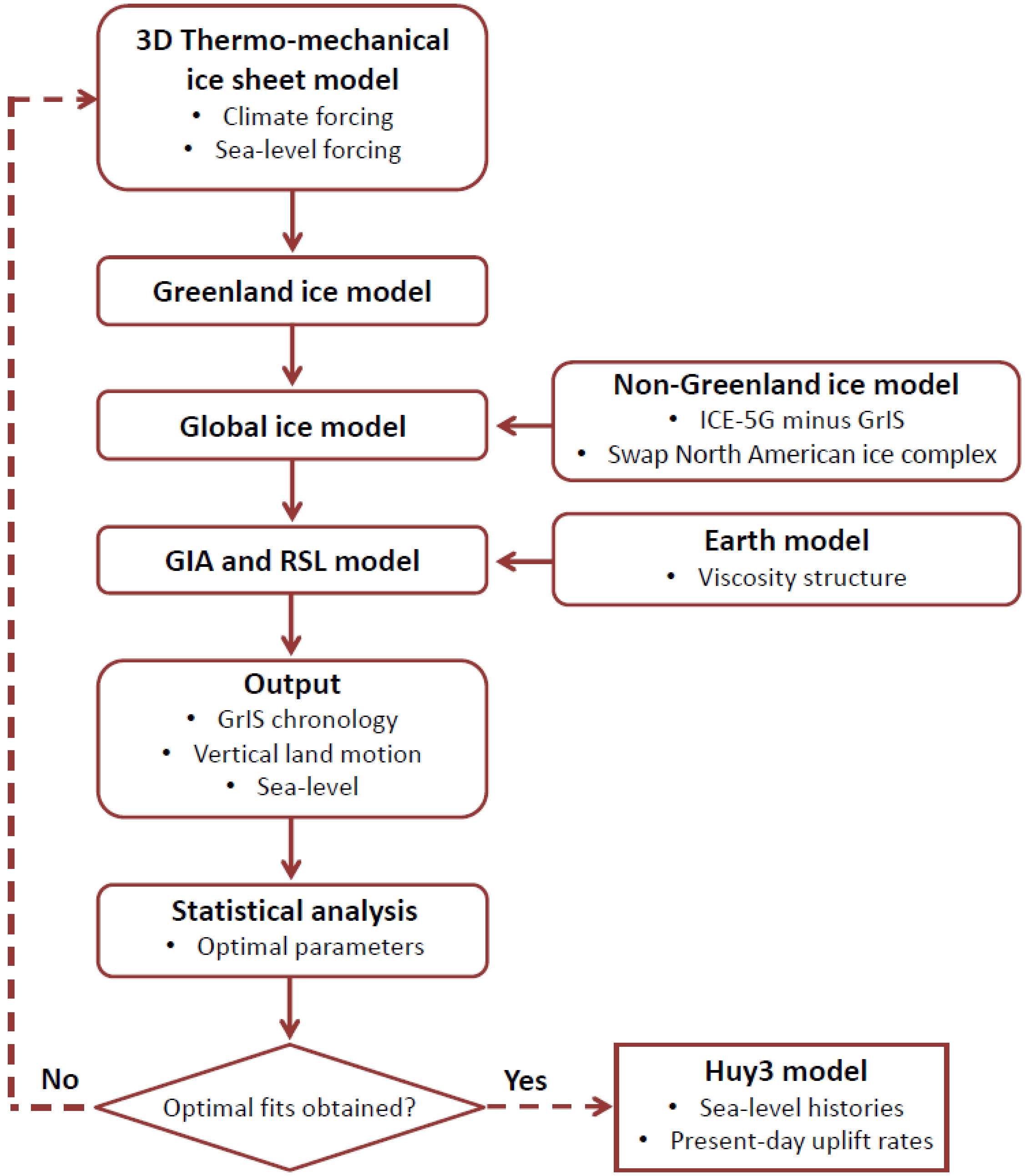

Figure 3.2 A flow diagram describing the modelling methodology of this study. Firstly, a glaciological model simulates the evolution of the GrIS (Huybrechts and de Wolde, 1999; Huybrechts, 2002). The Greenland ice model is then combined with a background global ice model lacking a Greenland component (ICE-5G - GrB; Peltier, 2004). A sensitivity analysis on the global ice model was also conducted by swapping the ICE-5G North American ice complex with a high variance set from Tarasov et al. (2012). The global ice and Earth model were adopted in the GIA and RSL model to produce predictions of RSL and glacial rebound which are compared to observations. Optimal Earth model parameters were determined using a χ^2 analysis and an F-test. Sensitivity analyses were conducted to adequately explore the parameter space which resulted in the comparison of 250,000 sets of model predictions to our constraint database before identifying optimal model parameters.

3.4.1 ICE SHEET MODEL

The glaciological model simulates the evolution of the GrIS in response to changes in past climate and sea-level over the last two glacial cycles. The model is described in detail in Huybrechts and de Wolde, (1999) and Huybrechts, (2002) and so only a brief overview of the most relevant aspects relating to ice dynamics, isostasy and mass balance are provided here. The model consists of 31 vertical layers and has a lateral resolution of 20 by 20 km which is represented by 83 by 141 horizontal grid cells for the entire region. Given the scale of the ice sheet and time-scale of study, the ice dynamics are modelled using the shallow ice approximation (Hutter, 1983). Gravitationally-driven non-linear plastic flow represented using Glen's flow law governs internal deformation (Glenn 1955), while the parameterisation of basal sliding defines the flow over the bedrock. Longitudinal stresses are ignored and grounding-line dynamics are not modelled but expressed as parametric equations within the SLF component of the model. These parametric equations are tuned to fit geological and geomorphological evidence (see Section 3.5.2.3) which correlates sea level to ice flux past the grounding line through an empirical formulation which defines a maximum grounding depth. This marine ice parameterisation reproduces to first-order large-scale ice margin changes (Zweck and Huybrechts, 2003, 2005). The isostatic component of the ice model is different from the one employed in the glacial isostatic adjustment and relative sea-level model; it is based on a more simplistic elastic lithosphere overlying a relaxed asthenosphere with a single decay time of 3 ka; these parameters were not varied in this study. The mass balance of the ice model is defined as snowfall accumulation minus meltwater runoff and calving of icebergs. Due to the relatively long timescale of the modelling analysis and the inherent parametric uncertainties in the energy balance methodology over millennial timescales, the surface runoff is calculated using a positive degree day algorithm (e.g. Braithwaite, 1995). The surface air temperature is derived from the GRIP ice core $\delta^{18}O$ record which is applied to generate a Gaussian distribution for monthly temperatures (see Section 3.5.2.2). These derived temperatures are then correlated to the number of positive degrees days to produce melt rates which uses the recalibrated runoff model of Janssens and

Huybrechts (2000). The glaciological model outputs the Greenland component needed for the subsequent GIA & RSL computations.

3.4.2 GLACIAL ISOSTATIC ADJUSTMENT AND RELATIVE SEA LEVEL MODEL

Our GIA model computes Earth deformation, gravity and sea-level changes resulting from the interaction between ice sheets and the solid Earth (e.g. Farrell & Clark 1976; Milne & Mitrovica 1998; Mitrovica & Milne 2003, Kendall et al., 2005). The model uses two primary inputs, a global ice model and an Earth model. The background global ice loading model used is ICE-5G (Peltier, 2004). The ice model is revised by removing the original Greenland component (GrB; Tarasov & Peltier, 2002) and replaced with our own reconstructions as noted in the previous section. As demonstrated in previous studies, RSL changes in Greenland are significantly influenced by the deglaciation of North American ice (Fleming and Lambeck, 2004; Simpson et al. 2009). We therefore replace the North American component of ICE-5G by glaciological reconstructions of these ice complexes (Tarasov et al., 2012) to assess the degree of this sensitivity and its ramifications for arriving at an improved model of GrIS deglaciation.

The Earth model adopted is typical in GIA modelling studies (Peltier, 1974), with a spherically symmetric geometry and Maxwell visco-elastic rheology. The elastic and density structure given by the seismic Preliminary Reference Earth Model (Dziewonski & Anderson, 1981), and the viscous structure is more crudely defined into three shells: lithosphere, upper mantle, and lower mantle. The lithosphere was assigned a relatively high viscosity to simulate an elastic outer shell with a thickness that was varied when seeking an optimal model fit to the RSL data. The upper-lower mantle boundary was defined at a depth of 670 km and the viscosity in these two regions was also varied to optimise model fits to the RSL data (e.g. Simpson et al., 2009). A total of 216 Earth viscosity models were considered in seeking an optimal data-model fit for each ice model reconstruction. The results of the Earth model calibration exercise are given in Section 3.5.2.5.

The GIA and RSL model output includes the influence of ocean loading due to sea-level changes by solving the sea-level equation as presented in Mitrovica & Milne (2003) using the Kendall et al. (2005) algorithm. Furthermore, the results include GIA-induced perturbations in Earth rotation due to a shift in the Earth's rotational inertia tensor based on the revised theory in Mitrovica et al. (2005).

3.5 MODELLING RESULTS

3.5.1 INTRODUCTION

Since we build upon the Huy2 model of Simpson et al. (2009), we begin by comparing predictions from this model to our newly established constraint database in order to identify key weaknesses to target in developing an improved model. We present in Figure 3.4 the sea-level predictions produced from our GIA and RSL model using the Huy2 reconstruction joined to ICE5G with the Earth model identified as providing optimal fits to the RSL data base considered in Simpson et al. (2009). This Earth model consists of a 120 km lithosphere (LT120), upper mantle viscosity of 0.5×10^{21} Pa·s (UMV0.5), and lower mantle viscosity of 10^{21} Pa·s (LMV1). The optimal Earth model was determined by minimizing the data-model misfit using a statistical χ^2 analysis. The Huy2 model is biased towards fitting data on the west Greenland coast due to the high number and precision of RSL data found there. Furthermore the χ^2 results suggested a different optimal Earth structure for the West and East coasts (LT120, UMV0.5, LMV1 and LT120, UMV0.3, LMV50 respectively). The existence and influence of lateral Earth structure was attributed as one of the major unknowns and model weaknesses which could have profound consequences on the accuracy of the ice chronology. Marine-based ice retreated from its maximum LGM shelf extent more or less simultaneously in all regions in the Huy2 model (Fig. 3.3); however observations of ice extent suggest an earlier retreat on the East coast relative to the West. As suggested in Simpson et al., the improvements in data-model fits by adopting different viscosity parameters for the east coast might also be achieved by revising the ice chronology such that there is asynchronous retreat on the east and west coasts. This is an issue we explore below (see Section 3.5.2.3).

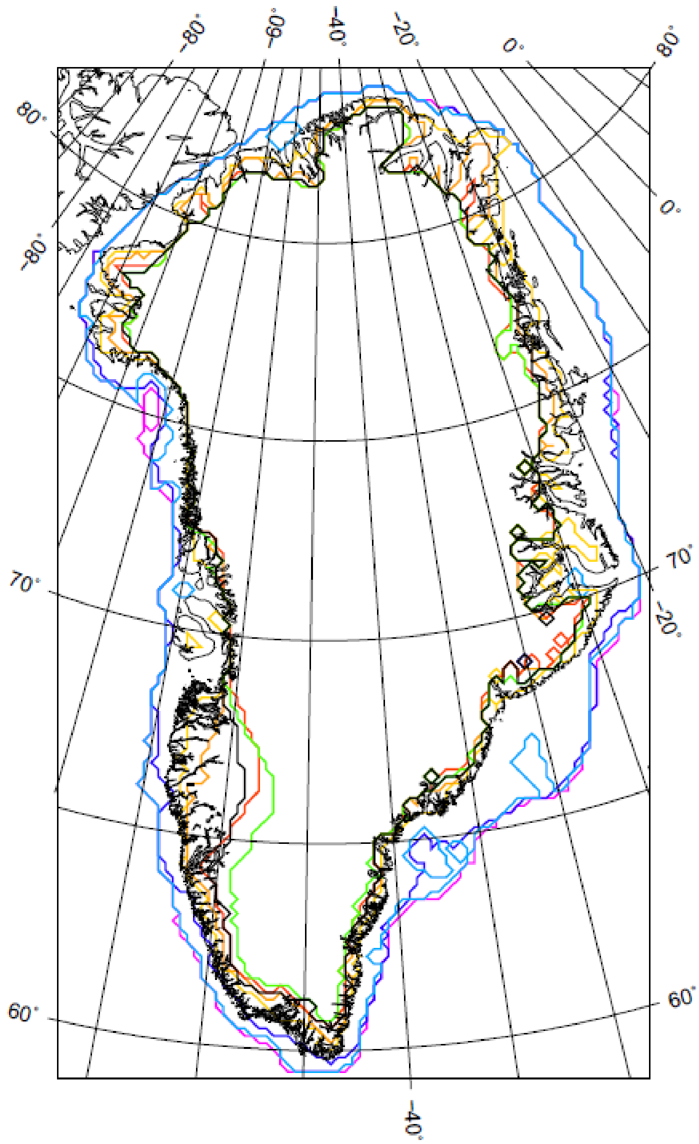

Figure 3.3 The chronology of lateral ice extent for the Huy2 model (16 ka BP – pink; 14 ka BP – dark blue; 12 ka BP – light blue; 10 ka BP – yellow; 9 ka BP – orange; 6 ka BP – red; 4 ka BP – green; present-day - black).

The Huy2 RSL predictions are shown in comparison to another widely used Greenland reconstruction – the GrB model (Tarasov & Peltier 2002) – in Figure 3.4. The GrB model is the Greenland component in the global ICE-5G model (Peltier, 2004). The RSL predictions for this model were generated using the Earth model it was developed with – the so-called “viscosity model 2” or VM2, which comprises a density structure defined by PREM (Dziewonski & Anderson, 1981) and a viscosity profile with an average upper mantle viscosity of ~$5x10^{20}$ Pas and lower mantle of ~$2x10^{21}$ Pas (See Fig 1 from Peltier, 2004). The GrB (ICE-5G Greenland component) model predictions are shown for comparison in Figure 3.4 by the grey curve and not surprisingly it demonstrate a significant misfit to the majority of the observations. The GrB model exhibits these discrepancies due to the assumption of a single viscosity model in the calibration process and the scarcity of available field data at the time.

We begin by focusing our attention on the Huy2 RSL predictions denoted by the black curves in Figure 3.4. Data-model discrepancies will be discussed for all of Greenland, starting in west Greenland and working anti-clockwise. Around Disko Bugt, many isolation basin studies have demonstrated that after a rapid early Holocene fall, RSL fell below PD values by 5-4 ka BP to reach a lowstand at ~2 ka BP before rising back to PD values (Long et al., 1999, 2003, 2006). Generally, the western Huy2 RSL predictions reproduce the RSL observations well with the exception of a notable misfit in the rate of RSL fall and lowstand at Kangerlusuaq (1), Pakitsoq (3), Upernivik (4), Orpisook (5), Qeqertarsiatsuaq (7), Sisimiut(8), and Sondre (9). For example, the Huy2 prediction for Sisimiut suggests a RSL fall that is too gradual with a Late Holocene lowstand that does not sufficiently capture the data.

In the Nuuk region, the Huy2 model fails to produce the shape and amplitude required to fit the RSL limiting dates and index points. Continuing southwards along the southwest coast there is a transition away from the characteristic type of RSL curve found in the west (e.g. Disko Bugt) starting at Paamiut (Fig. 3.4b) where present sea level is reached at 10-9 ka BP. In southern Greenland, sea levels reached the PD value at 10-8 ka BP and continued to fall reaching a lowstand sometime during the Mid Holocene. The Huy2 model does not capture well the constraints on RSL (the ML; time at which PD sea-level is first reached; lowstand amplitude) at a number of locations in this region, including Paamiut, Qaqortoq, Tasiusaq, and Nanortalik (Fig. 3.4b). The earliest sea-level index points are seldom reached by the model predictions. Simpson et al. noted the poor model fits in this region as they cannot be explained by model parameter uncertainties in the Earth structure. A similar result was obtained by Fleming & Lambeck (2004) with their GREEN1 Greenland model. Given that the Huy2 model reached the shelf edge

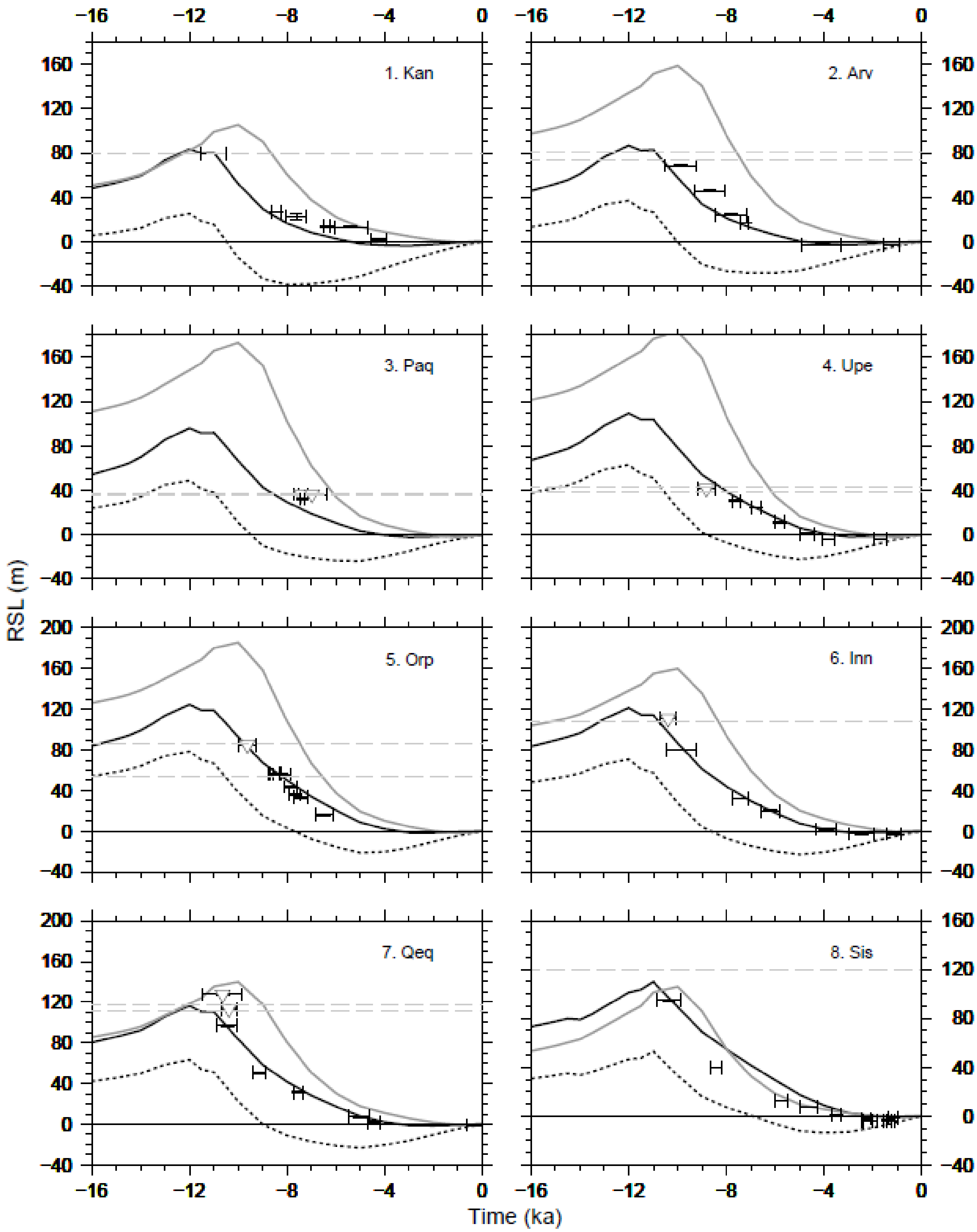
1. Kan
2. Arv
3. Paq
4. Upe
5. Orp
6. Inn
7. Qeq
8. Sis
RSL (m)
Time (ka)

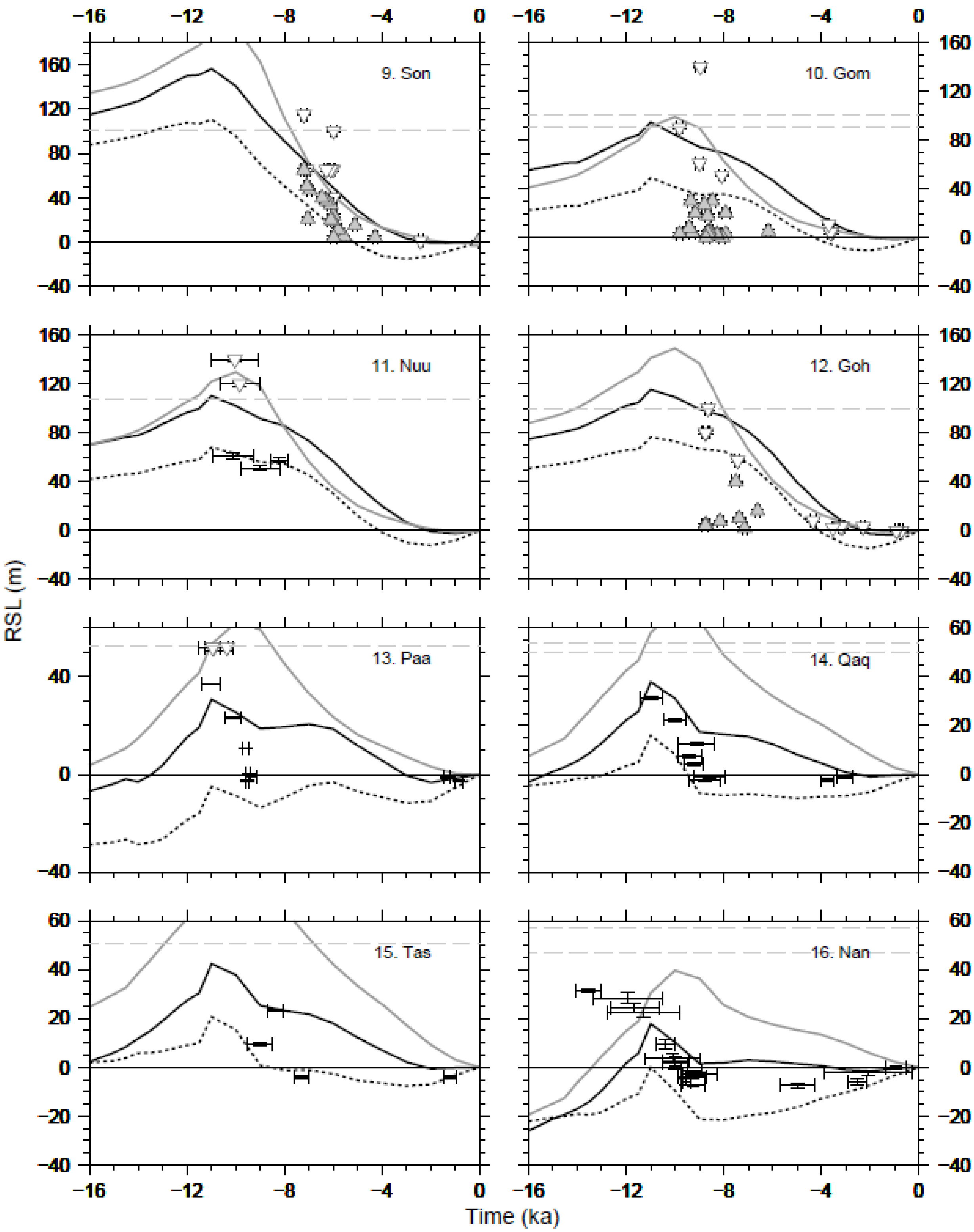
9. Son
10. Gom
11. Nuu
12. Goh
13. Paa
14. Qaq
15. Tas
16. Nan
RSL (m)
Time (ka)

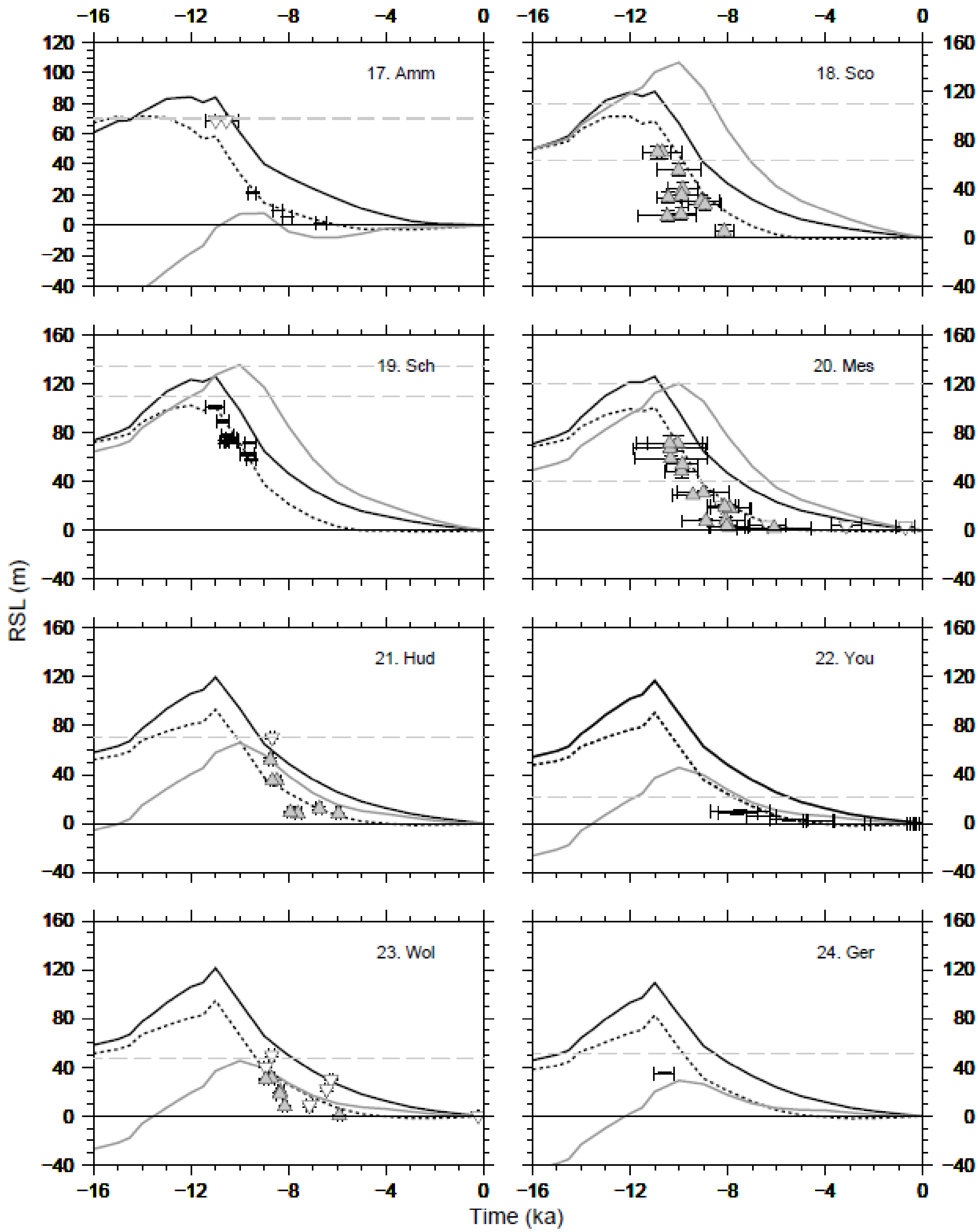

17. Amm
18. Sco
19. Sch
20. Mes
21. Hud
22. You
23. Wol
24. Ger
RSL (m)
Time (ka)

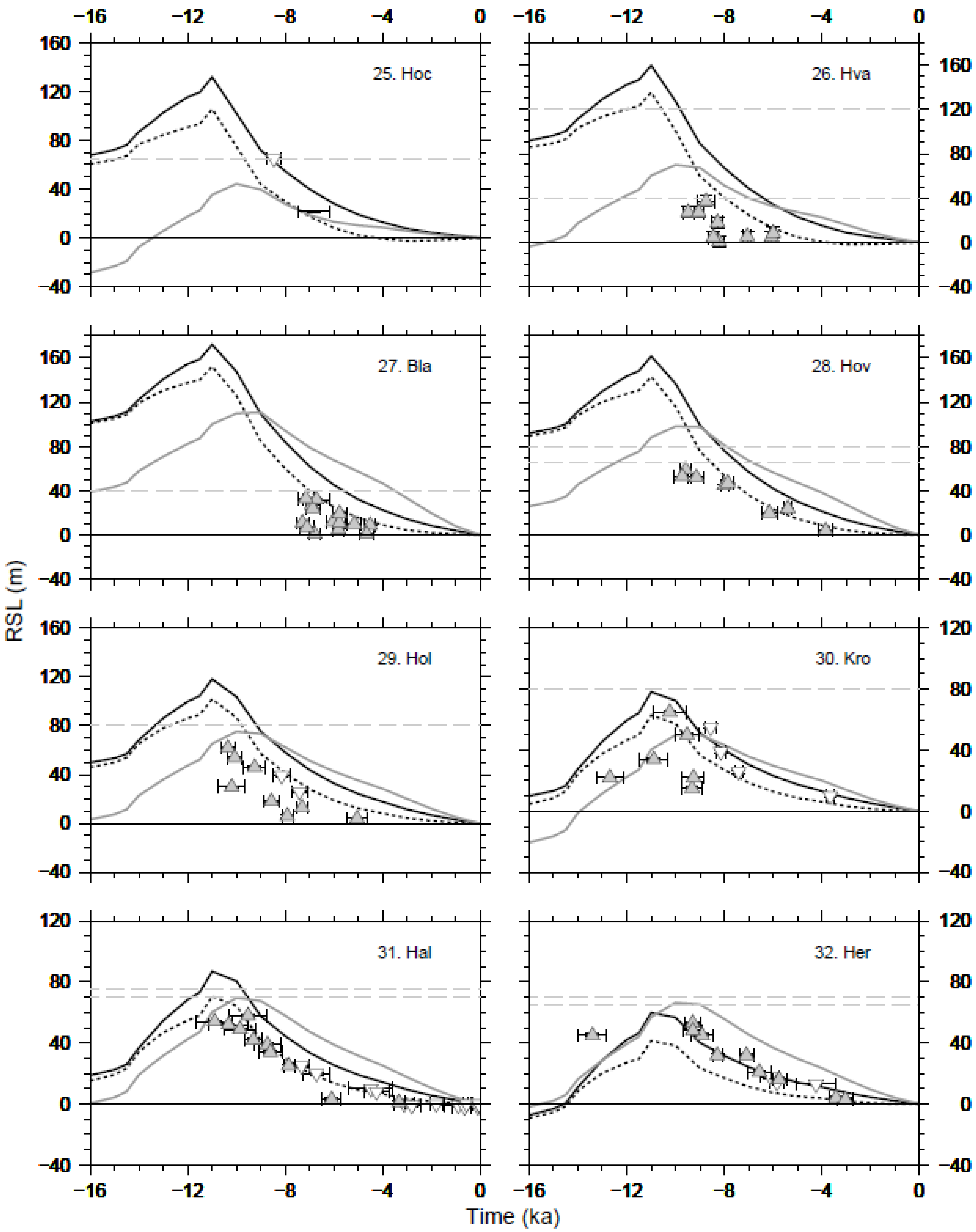
25. Hoc
26. Hva
27. Bla
28. Hov
29. Hol
30. Kro
31. Hal
32. Her
RSL (m)
Time (ka)

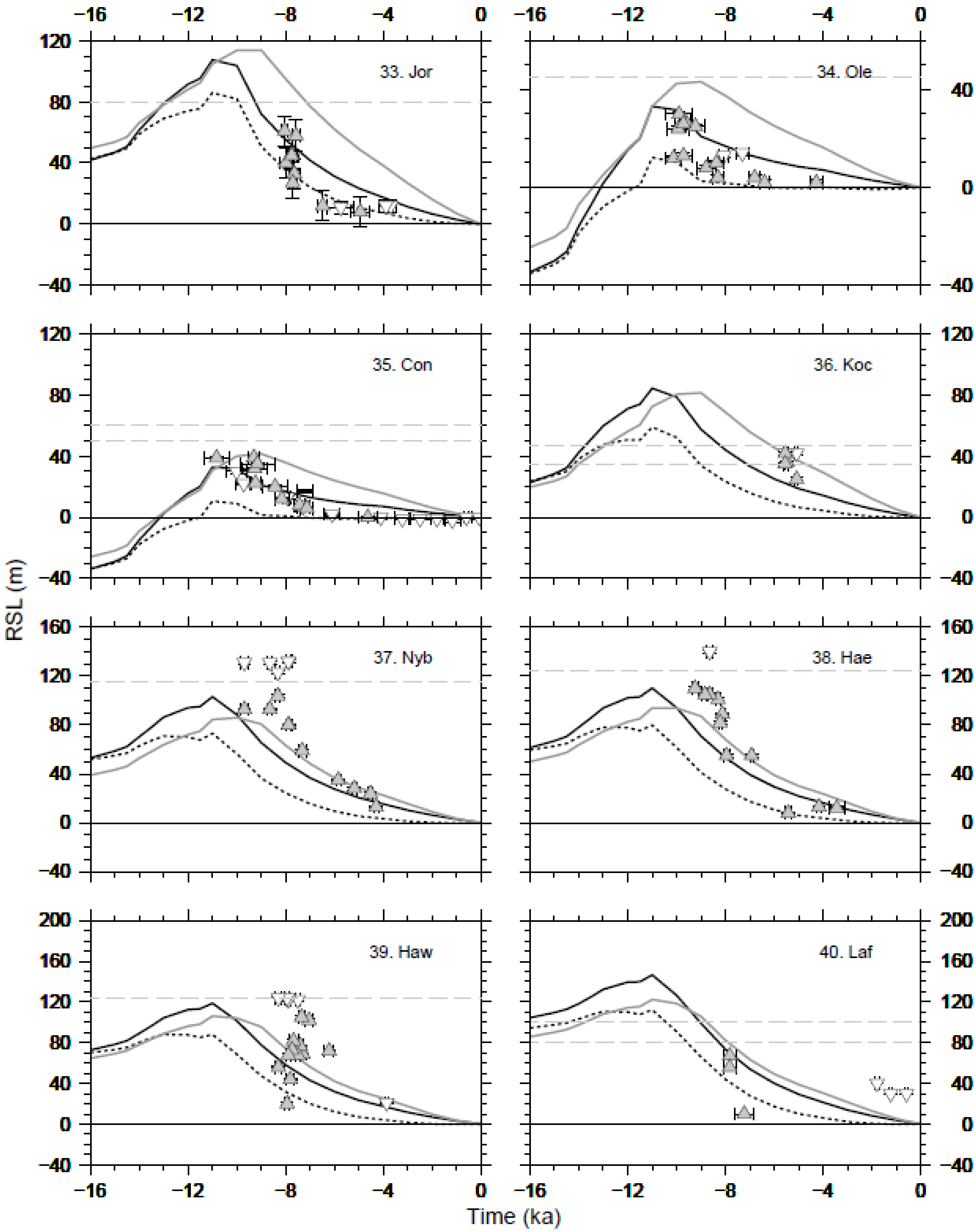
33. Jor
34. Ole
35. Con
36. Koc
37. Nyb
38. Hae
39. Haw
40. Laf
RSL (m)
Time (ka)

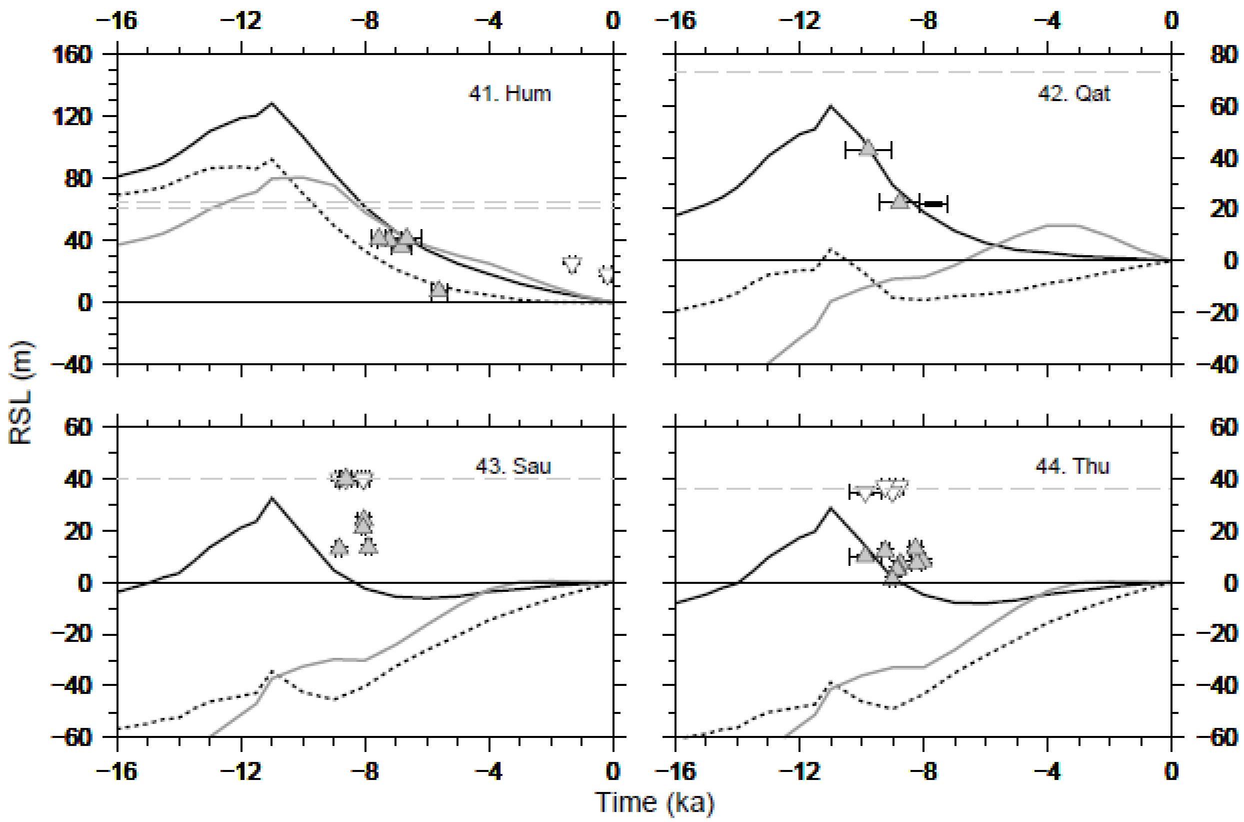

Figure 3.4 RSL predictions for the Huy2 and GrB ice models with their respective optimal Earth model(s). The Huy2 model predictions are generated using its two optimal Earth model where the black curves denotes the optimal viscosity structure obtained using the entire regional RSL data set (120 km lithosphere, upper mantle viscosity of $0.5x10^{21}$Pas, and lower mantle viscosity of 10^{21} Pas) and the dashed black curve represents the alternate viscosity structure obtained by considering data from the East coast only (120 km lithosphere, upper mantle viscosity of $0.3x10^{21}$Pas, and lower mantle viscosity of $50x10^{21}$ Pas). In contrast, the Greenland ice model of ICE5G (GrB; Tarasov & Peltier, 2002) is applied with the VM2 Earth model to produce RSL predictions (grey curves). Sea-level index points are shown as crosses with both time and height error bars. Lower limiting dates are denoted by grey upward pointing triangles, while upper limiting dates are shown by white downward pointing triangles. The black horizontal line highlights present-day sea-level. The grey dashed horizontal line represents the marine limit which marks the highest point reached by sea-level during ice-free conditions at each location. Data locations are shown in Fig. 3.1a (site 1-8, 9-16, 17-24, 25-32, 33-40, 41-44 constitute Fig. 3.4 a,b,c,d,e, and f, respectively).

at the LGM and had retreated to the PD margin by 9 ka BP, as suggested by Weidick et al. (2004), the data-model misfit is most likely due to either insufficient local unloading or the contribution from non-local effects, such as the influence of North American ice.

In the southeast (Ammassalik), the timing of retreat from the shelf (12 ka BP) was too late compared to the geological evidence (Jennings et al., 2006; Andrews, 2008). Additionally, the Huy2 model predicts relatively high RSL values and the rate of sea-level fall is too late and rapid (site 17. Amm; Figure 3.4c). Similar misfits are evident in the East and Northeast where the model fails to produce a low enough amplitude of sea-level change to fit the limiting dates (Fig. 3.4c). As mentioned above, rather than revise the ice model, Simpson et al. chose to invoke a different viscosity structure to better fit the observations along the east coast. The alternate viscosity structure produces an excellent fit to observations in the Scoreby Sund area; however, discrepancies are evident at Hudson and Wollaston where the initial timing of sea-level fall fails to capture the limiting dates (Fig. 3.4c). In northeast Greenland the Huy2 RSL predictions do fit the observations with the east coast Earth model from Hvalroso to Ingelbord Halvo (Fig. 3.4d), however, we note that these sites consist mainly of limiting dates and so the observational constraints are not precise.

In north Greenland the RSL observations are largely comprised of limiting dates and so the constraints are relatively weak. However, predictions based on the Huy2 model (using the west coast viscosity model in this case) do not fit the observations well. The Huy2 model does not capture the initial RSL fall indicated by the data (Fig. 3.4e). The initial timing of RSL fall is insensitive to variations in the adopted Earth structure which suggests that the misfit is due to the regional deglacial history. At the LGM the Innuitian and Greenland ice sheets were dynamically connected; during the Early Holocene there was a saddle collapse which opened up the Nares Strait (Blake, 1999, England, 1999). Final deglaciation of the Strait by 10 ka BP (Zreda et al., 1999) is reproduced by the Huy2 model. The Huy2 model does not simulate this coalesce with the Innuitian ice sheet; therefore, it is not surprising to find that it does not produce well the sea-level response inferred from the ML and limiting dates from Nyboe to Thule (Fig. 3.4e and f).

The RSL observations more effectively constrain the margins of the ice sheet while the ice-core derived thinning curves provide complementary constraints in the interior of the GrIS. Thinning curves for the Huy2 model which consist of both ice thinning and vertical land motion (based on the regional-wide optimal viscosity model) are shown in Figure 3.13. These results suggest that the model misrepresents the chronology by over-responding to the HTM at the DYE-3 site and, conversely, not responding enough at Camp Century. At the more central NGRIP ice-core sites, the Huy2 model captures the inferred thinning within the observational uncertainty (Lecavalier et al., 2013), however the summit of the ice sheet (GRIP) does not thin sufficiently at ~8 ka BP.

The discrepancies noted above are primary targets used to guide the calibration of a new and improved deglaciation model for Greenland. As described above, these discrepancies can be attributed to specific aspects of the model (e.g. uncertainties in Earth viscosity structure; the influence of non-Greenland ice loads; and modelled ice surface elevation). These aspects will be investigated and discussed in the following sections.

3.5.2 HUY3 CALIBRATION

All the changes introduced below are sequentially incorporated and added to the original Huy2 model. Firstly, the LGM ice extent is evaluated and a sensitivity analysis is conducted to arrive at a revised LGM ice mask. Subsequently, the climate and SLFs are discussed and a sensitivity analysis focusing on these model aspects is presented. We then investigate the impact of the North American ice complex on near-field Greenland RSL predictions by considering a suite of ice histories for this region. Finally, using our constraint database and the results of the sensitivity analyses we select optimal model parameters, highlight key parameter trade-offs and model weaknesses.

3.5.2.1 LGM MASK

The Simpson study experimented with three different LGM ice extent scenarios; (1) the original Huy1 LGM extent which acted as the minimum extent case, (2) a maximum extent mask which extended to the shelf edge around the periphery of Greenland, and (3) a hybrid extent which combined elements from both the minimum and maximum case. The LGM mask acts as a direct boundary condition in the glaciological model, if the ice sheet experiences positive mass balance the ice sheet can grow only to the maximal extent defined by the LGM mask. Based on the literature of the time, it was determined that the hybrid LGM ice extent mask was most appropriate for the Huy2 model as it also produced the best fits to RSL observations. The use of indirect constraints such as RSL is necessary since the existing direct evidence is insufficient to define the LGM position of the GrIS margin in many locations.

As discussed in section 3.3.1, new geological and geomorphological evidence has made a compelling case to re-evaluate Greenland ice extent at the LGM. Several recent studies have advocated for an extent which differs than the one used in Simpson et al. (2009) (e.g. O'Cofaigh et al., 2012). In Figure 3.5, the Huy2 hybrid LGM extent contour is plotted in red. Recently Funder et al. (2011) reviewed the literature and proposed an LGM ice extent shown in green (henceforth called the Funder extent) that more or less coincides with the Huy2 hybrid LGM extent. The differences between these two reconstructions are generally found in East and Northeast Greenland where Funder et al. (2011) propose an inner-mid shelf LGM extent as opposed to outer shelf in the Huy2 hybrid model (see Section 3.3.1). The accuracy of the two extent scenarios can be tested by comparing model predictions and observations for the ML as this quantity is highly sensitive to the magnitude of ice unloading and therefore the LGM extent. Figure 3.S1a shows the location of relevant ML observations used to test which of the two extent scenarios is more accurate in the northeast of Greenland. The Huy2 RSL sea-level predictions produce MLs which are substantially too high (Figure 3.S1b) even when parametric uncertainties in the SLF and the Earth's viscosity structure are considered. In contrast, the Funder extent scenario results in lower RSL values which fall within the ML data (Fig. 3.S1b). We note that while there remain ML data-model discrepancies for the Funder extent scenario, the residuals are within parametric uncertainties (e.g. SLF).

The Huy2 extent model was also revised in the West and Northwest of Greenland (compare blue and red contours in Fig. 3.5). Along the west coast, between approximately 67 and 75 degrees North, we push the LGM margin out towards the shelf break in order to capture the constraints of O'Cofaigh et al. (2012) (see Section 3.3.1). Since the O'Cofaigh et al. data only constrain the margin position adjacent to the Jakobshaven Isbrae outlet glacier (approx. 68 degrees North), we use ML data to test the accuracy of a more extensive LGM margin north of this location (Figure 3.S2 a & b).

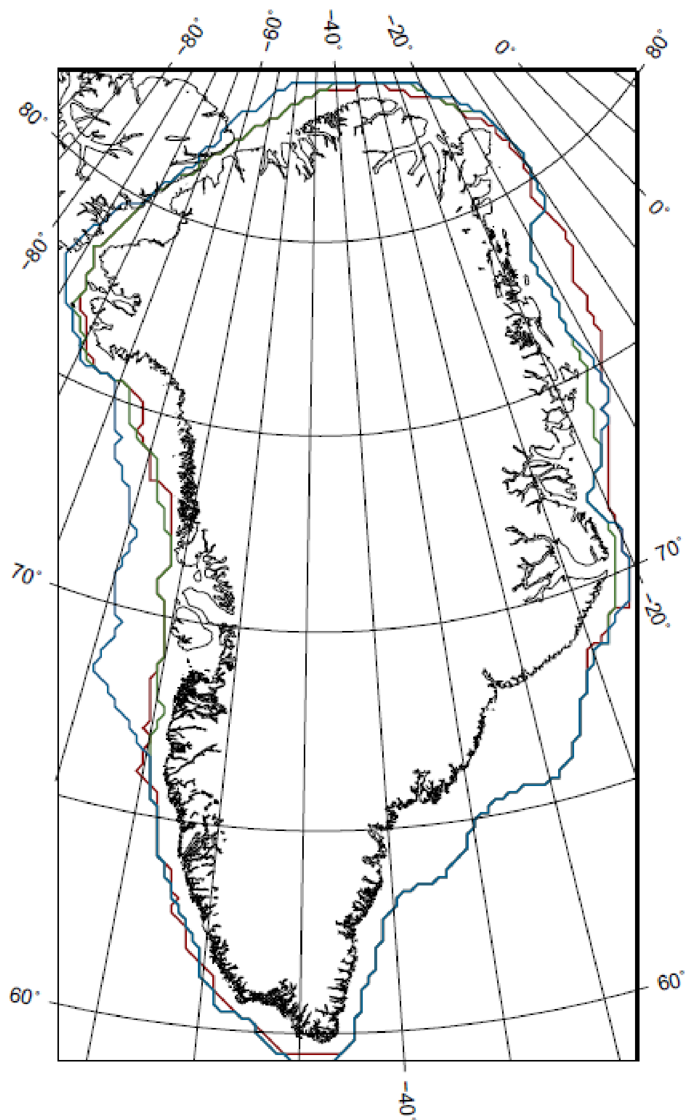

Figure 3.5 The three LGM ice mask extents which are discussed in this study: the original Huy2 LGM extent (red), the Funder extent (green) (Funder et al., 2011), and the revised Huy3 LGM ice mask (blue).

In contrast to the results for the Northeast region, the Huy2 optimal LGM mask predicts ML values that are, in general, too low in the Northwest (even when considering parametric uncertainty) thus supporting the more extensive LGM margin scenario. We note that this revision is not inconsistent with the Funder reconstruction as it was intended to represent a minimum plausible scenario in regions that remain unconstrained by direct observations. In the far Northwest, the LGM margin limit was also pushed father out. While there are no RSL data to support this revision, it was made to compensate for the lack of a dynamically connected Greenland and Innuitian ice sheet as well as the neglect of sea ice buttressing in the model.

Numerous other LGM extent scenarios were investigated in addition to the final revised scenario (blue line in Fig. 3.5) to map out the degree of parametric trade-off between ice extent and SLF (Section 3.5.2.3) on the resulting RSL predictions. Based on this sensitivity analysis and results described above, we adopt the blue line in Fig. 3.5 as the LGM mask for our new model since it is consistent with the majority of direct geological observations of ice extent and optimises the fit to the RSL data.

3.5.2.2 TEMPERATURE FORCING

The surface runoff is calculated using a positive degree day (PDD) algorithm (e.g. Braithwaite, 1995). The surface air temperature is derived from the revised GRIP temperature profile which is applied to generate a Gaussian distribution for monthly temperatures. These derived temperatures are then correlated to the number of positive degrees days to produce melt rates which uses the recalibrated runoff model of Janssens and Huybrechts (2000). Degree day factors (DDFs) behave as another unknown in the climate forcing of the model since they calculate the amount of meltwater which will eventually runoff after saturation of the snowpack. These DDFs act uniformly across the ice sheet and are, respectively, for snow and ice, 3 and 8 mm/day/degree C (water equivalent) (Braithwaite, 1995; Janssens & Huybrechts, 2000; Hock, 2003). In the original Huy1 and Huy2 studies, the DDFs were 3 and 8 mm/day/degree C, respectively and had to be tuned over the Holocene period and subsequently reset so that the model reproduced the PD ice sheet geometry. A sensitivity analysis was conducted on the DDFs (Hock, 2003) and it was determined that few permutations could simultaneously reproduce PD ice volume and compare relatively well against the constraint database.

The temperature reconstruction based on the GRIP $\delta^{18}O$ record (Dansgaard et al., 1993) is used to generate a temperature profile across Greenland to force the ice model (as described in Simpson et al., 2009). The GRIP $\delta^{18}O$ record is converted to temperature using a conversion factor (Cuffey, 2000) and corrected for latitude and elevation changes. However the conversion does not consider the influence of elevation changes on the sensitivity of this isotope to climate which can be non-negligible over periods of small temperature change (Huybrechts, 2002). This is one explanation for the lack of a clearly defined HTM in this temperature reconstruction compared to those reconstructed from other ice cores and other archives in the northern hemisphere (Dansgaard et al., 1971; Cuffey et al., 1995; Dahl Jensen et al., 1998; Koerner & Fisher, 1990; Bennike & Weidick, 2001; Kaufman et al., 2004; Lecavalier et al., 2013). This is accounted for in the Simpson et al. study by superimposing a parabolic function to incorporate a pronounced HTM in the temperature forcing. We adopt their revised GRIP temperature record but consider departures from it by scaling the HTM amplitude to investigate the sensitivity of the model to uncertainty in this forcing component and find the forcing that optimises the fit to observations. Figure 3.6 illustrates the GRIP temperature record and Huy2 and Huy3 HTM scaling from which a temperature profile is derived across Greenland.

The standard deviation of the Gaussian distribution generated from the GRIP temperature record is traditionally held constant in a PDD algorithm. Recently, weather station observations have been used to define a relationship between the standard deviation and temperature (Wake et al., 2013). This relationship was adopted in the glaciological model. It had the effect of removing the need to apply the somewhat unphysical tuning of DDFs to reproduce the PD ice sheet geometry (Figure 3.S3). This result suggests that the revision to the PDD parameterisation is more accurate.

The amplitude of the HTM parabola in the revised GRIP record is adjusted to maximize the fit to observations that suggest a response of the ice sheet to the HTM. Previous studies have found that the southwest region is the most sensitive to this forcing (Tarasov and Peltier, 2002; Simpson et al., 2009).

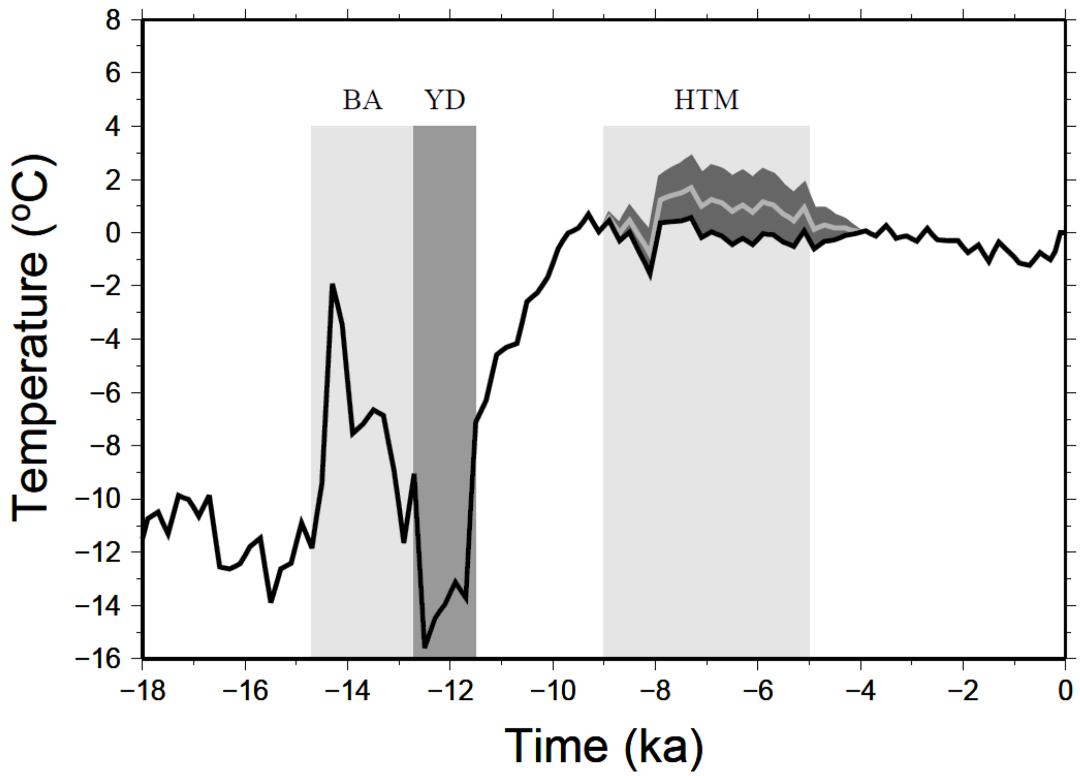

Figure 3.6 The GRIP temperature record prescribed in the model is represented by the black curve alongside the Huy2 revised HTM temperature forcing (upper bound of dark grey envelop). The Huy3 model HTM was parameterized within the grey envelop with an optimal imposed HTM scaling shown in light grey. The following climatic events are annotated: Bolling-Allerod (BA), Younger Dryas (YD), and Holocene Thermal Maximum (HTM).

The imposed HTM causes a margin retreat past its PD location and a subsequent re-growth which causes a change from RSL fall to rise in the southwest of Greenland during the late Holocene. RSL along the west and southwest coasts is well constrained during the Holocene suggesting that it might be possible to infer a minimum ice margin configuration and, therefore, an optimal HTM scaling.

3.5.2.3 SEA LEVEL FORCING

As discussed in Section 3.4.1, the interaction of sea-level and marine-based ice is expressed by parametric equations which reproduce to first-order large-scale ice margin changes (Zweck and Huybrechts, 2003, 2005) by correlating sea-level to ice flux past the grounding line through an empirical formulation which defines a maximum grounding depth beyond which the ice calves. The empirical relationship produces periods of ice advance over the continental shelf during moments of low eustatic sea-level, which allows for the expansion of the ice sheet to its LGM ice extent. Conversely, as sea-level rises the ice sheet migrates landward.

As discussed in Simpson et al., the position of the grounding line is parameterised as a function of eustatic sea level which is taken from the SPECMAP stack of marine oxygen-isotope values (Imbrie et al., 1984). However, as shown in Figure 17 of Simpson et al. (2009), using the more complex treatment of ocean depth in the GIA model, it was found to vary spatially by over 100 m at the LGM relative to present and by 40 m during the Mid to Late Holocene transition. Therefore, a significant error is incurred when adopting eustatic sea-level to force the ice model. In Section 3.3.1, several geological records indicate a spatially and temporally varying retreat of marine-based ice from the continental shelf. Even though the spatial coverage of these data is low and the timing at which the retreat occurs is poorly constrained in many areas, there is enough information to demonstrate the limitation of this aspect of the Huy2 model, which results in a similar timing of retreat around the entire margin (mild variations in the timing of the marine retreat in the Huy2 model reflect ocean bathymetry rather than spatial differences in RSL and ocean temperatures).

In the Simpson et al. study, a total of three different SLFs were applied that were based on parametric equations composed of linear and quadratic expressions (see their equations 3, 4 & 5). The three retreat scenarios are generalized to represent early, mid, and late cases (initial retreat by 16, 14, and 12 ka BP; respectively). The rate at which the ice retreats varies substantially; the late case produces an abrupt and rapid retreat while the early case yields a more gradual withdrawal from the shelf. The SLF was shown to be a strong control on the resulting RSL predictions, affecting the amplitude and timing of the initial RSL fall. Simpson et al. chose their late retreat equation since it optimised the fit to the highest quality data in the Disko Bugt area; however, it was clear that RSL data from the East and Northeast favoured an earlier retreat. RSL and other data suggest a range of different times for the onset of retreat around Greenland and these cannot be captured by applying the same SLF across the entire ice sheet. Therefore, a spatially variable SLF was implemented for the development of Huy3 by allowing regional variation in the applied parametric equations to capture the timing of initial retreat and rate of retreat suggested by geomorphological and geological evidence, and to maximize the fit to the RSL data (Figure 3.S4). Even though this approach is relatively crude in the sense that the underlying physical processes that cause marine grounding line retreat are not modelled (Cornford et al., 2013), it presents the opportunity to match the growing field evidence and produce a more accurate deglaciation history. Even though the retreat criteria is parameterised as a function of eustatic sea level (or, more accurately global ice volume), it is likely that changes in ocean temperature were the dominant driver in some areas at certain times (Holland et al., 2008).

In west Greenland, the ice extended out to the shelf edge during the LGM and initially retreated around ~14 ka BP to reach the PD coastline by ~10 ka BP (O'Cofaigh et al., 2012). This chronology is in good agreement with an intermediate SLF scenario which also happens to achieve the strongest fit to the RSL observations, similar to the original Huy1 forcing. Southern Greenland experiences a better fit to the RSL observations with an intermediate-like SLF which produces an initial retreat ~16 ka BP and reaches the PD coastline by ~10 ka BP as suggested by Bennike et al. (2002) and Sparrenbom et al. (2006a,b). Margin retreat in Southeast Greenland is constrained by a small collection of RSL observations at Ammassalik (south of the Helheim glacier) as well as ice-rafted debris, both of which suggest a rapid retreat shortly after 16 ka BP (Nam et al., 1995; Kuijpers et al., 2003). An intermediate SLF (black curve from Figure 3.S4), similar to that adopted for West Greenland, best fit the geological record and RSL observations in this region. Observations from East Greenland suggest a rapid and relatively late retreat and so favour a SLF that lies between the original Huy1 “intermediate” and Huy2 “late” parameter values (Figure 3.S4). This East Greenland sea-level parameterization results in the deglaciation of Scoresby Sund outer fjord basins by 12 ka BP and all basins by 10 ka BP, exactly as suggested by Funder et al. (1998). Northeast Greenland marine-based ice initially retreated by 10 ka BP (Evans et al., 2009; Winkelmann et al., 2010) while in North Greenland the retreat started sometime during 16 to 10.3 ka BP (Larsen et al., 2010). Furthermore, given the high amplitude of RSL observations in northern Greenland it proposes a late retreat which is best encapsulated by the lower bound SLF parametric equation found in Figure 3.S4. The Nare Strait in northwest Greenland was fully glaciated and began to recede at ~12.5 ka BP (Blake, 1999, England, 1999). It became ice free at ~10 ka BP (Kelly and Bennike, 1992; Zreda et al., 1999). This deglaciation of the Nare Strait is captured by a similarly late SLF scenario.

The ability to apply different SLF parameterisations across Greenland to better match the field constraints has led to an important result: optimal fits to RSL data from both the East and West coasts can be achieved using a single viscosity model. That is, there is no need to invoke lateral variations in Earth viscosity structure to fit the RSL data as done in Simpson et al. We believe this is one of the more significant contributions of this study. In certain regions of Greenland there is either a lack of data or relatively poor constraints making it difficult to discriminate between the different SLF parameterisations (see Section 3.3.1). Also, it is important to note that, even given the broad range of parameters considered, the marine retreat does not occur before 16 ka BP or after 12 ka BP which simply reflects the fact that the input eustatic curve does not change significantly before or after this time interval.

In the following sections, the revised ice extent mask from Section 3.5.2.1 is applied and the advances in the climate (Section 3.5.2.2) and SLF (Section 3.5.2.3) are adopted with their optimal parameterizations. The resulting GrIS reconstruction defines the Huy3 model with the chronology of ice extent shown in Figure 3.7.

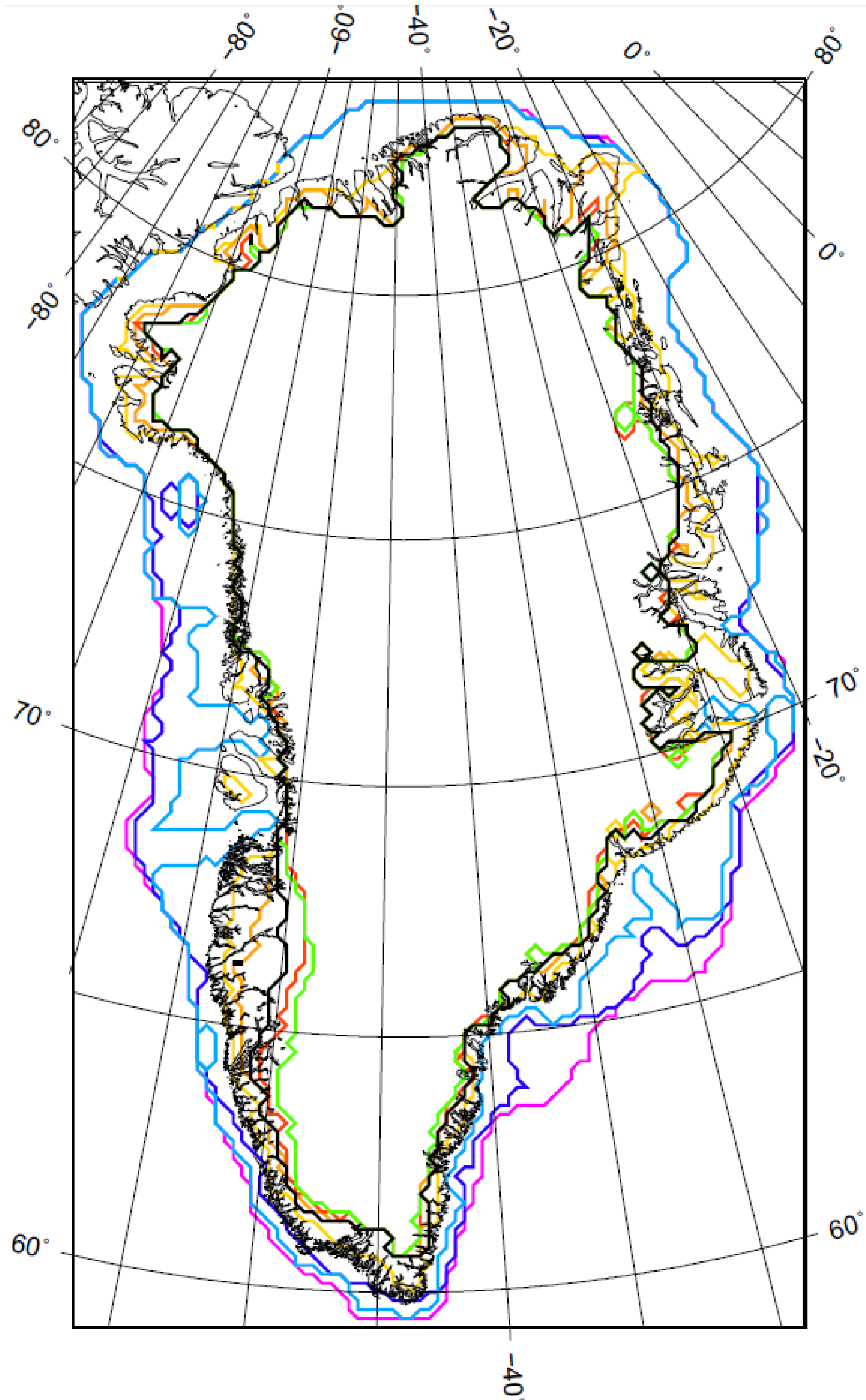

Figure 3.7 The chronology of lateral ice extent for the Huy3 model (16 ka BP – pink; 14 ka BP – dark blue; 12 ka BP – light blue; 10 ka BP – yellow; 9 ka BP – orange; 6 ka BP – red; 4 ka BP – green; present-day - black).

3.5.2.4 NORTH AMERICAN ICE SHEET

As described above, previous studies have demonstrated the influence of the North American ice complex (NAIC) on RSLs around Greenland (Fleming and Lambeck, 2005; Simpson et al., 2009). Therefore, to accurately reconstruct the evolution of the GrIS, it is necessary to at least consider the influence of this adjacent body of ice. By incorporating our GrIS reconstruction within the ICE-5G global model, the influence of the NAIC is implicitly considered. However, all ice model reconstructions have inherent uncertainty and so to account for this we adopt a series of alternate NAIC models. Specifcally, we consider a high variance subset of NAIC deglacial histories from the Bayesian calibration of a glaciologically self-consistent and dynamical ice sheet model (Tarasov et al., 2012). The model calibration procedure applied by Tarasov et al. produces estimates of model uncertainty which we used to select a subset of high variance NAIC models to include within the global ICE-5G model (into which our GrIS model is added).

Figure 3.8 shows the differences between ICE-5G (Peltier, 2004) and the optimal solution from Tarasov et al. (2012). It illustrates the proximity of the NAIC to the GrIS and its relevance to Greenland near-field RSL. The two alternate NAIC models shown in Figure 3.8 demonstrate clear differences in grid resolution, where ICE-5G suffers from significant discontinuities between grid cells resulting in glaciologically unphysical slops. For example, at 16 ka BP the ICE-5G NAIC has neighbouring grid points with differences in ice thickness of 3000 metres. Additionally, the NAIC models exhibit drastically different ice volumes, thicknesses, and chronologies. At 16 ka BP, both models cover a comparable areal extent, however, their respective ice thickness differ in many places by over one kilometre with the ICE-5G component being the larger model. At 12 ka BP, the optimal Tarasov et al. (2012) model exhibits a larger ice volume and extent with the Cordilleran ice sheet remaining in comparison to the ICE-5G NAIC. By 8 ka BP, the ICE-5G NAIC is all but gone while the Tarasov et al. (2012) optimal model has large ice

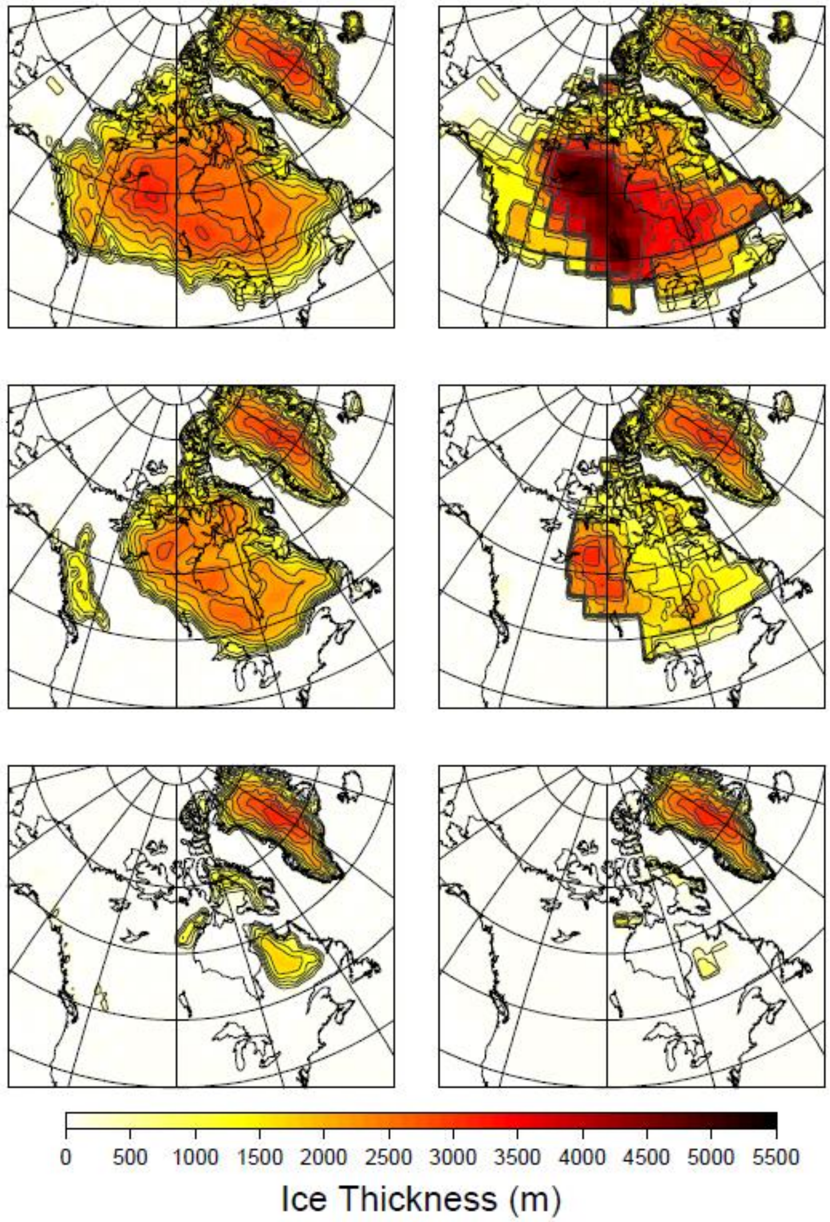

Figure 3.8 The left panes show the glaciologically self-consistent Tarasov et al. (2012) optimal NAIC model while the right panes show the ICE-5G NAIC component (Peltier, 2004). The two panes at the top, middle and bottom represent the 16, 12, and 8 ka BP time slices, respectively. In all panes, the Greenland component shown is the Huy3 model. There are clearly significant differences in the grid resolution, ice volume, thickness, and chronology between the two reconstructions.

caps scattered across eastern and northern Canada. Figure 3.8 clearly illustrates the resulting methodological differences in chronology between a loading model (Peltier 2004) and glaciologically self-consistent model (Tarasov et al., 2012). Figure 3.9 compares the non-Greenland RSL contribution from ICE-5G and the optimal NAIC model from the Bayesian calibration of Tarasov et al. (2012). The difference of these two NAIC RSL contributions around the periphery of Greenland is shown in Fig. 3.9c which illustrates the impact from uncertainties in the NAIC chronology on our Greenland reconstruction.

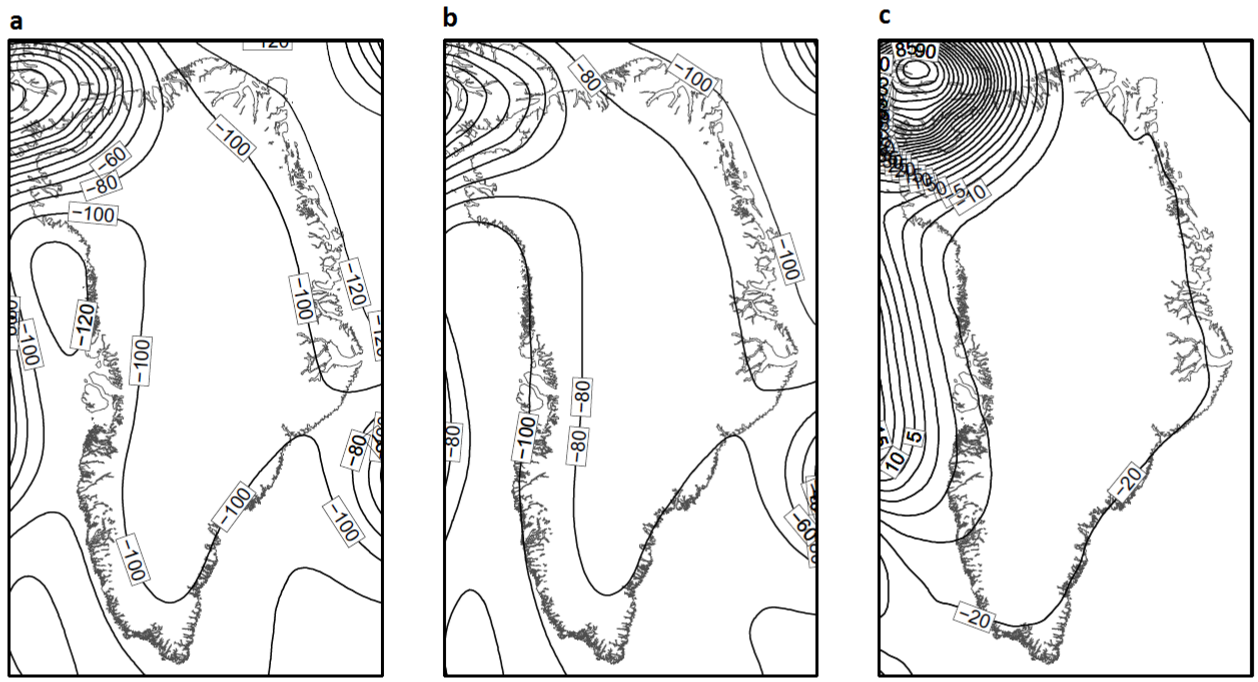

Figure 3.9 A spatial plot of RSL predictions from non-Greenland ice at 16 ka BP from the (a) ICE-5G model and (b) ICE-5G with the NAIC component from the optimal Tarasov et al. (2012) reconstruction. (c) The difference between the RSL contribution from ICE-5G and the Tarasov et al. (2012) optimal model is shown to illustrate the propagating impact on Greenland RSL predictions considering uncertainties in the NAIC.

The uncertainty in Greenland near-field RSL due to the inherent uncertainties in NAIC reconstructions is shown in Figure 3.S5 using a high variance of NAIC reconstructions from Tarasov et al. (2012) and ICE-5G. This uncertainty is a highly spatial signal which introduces large uncertainty in Northwest and South Greenland up to 60 m and 15 m at 16 ka BP (Figure 3.S5 b and e), respectively. In comparison there are regions such as East Greenland where RSLs are relatively unaffected by the NAIC during deglaciation. Northwest Greenland RSL predictions are highly sensitive to the Innuitian ice sheet while South Greenland is most sensitive to the Laurentide ice sheet. Given the limited North American model constraints, the Bayesian calibration yields a wide range of reconstructions which fit the observations.

The envelope of uncertainty on Greenland RSL resulting from these reconstructions (Figure 3.S5) should be considered when gauging the accuracy of our GrIS reconstruction based on fits to these data.

3.5.2.5 RSL PREDICTION

In this section, the revised ice model resulting from the previous sections (3.5.2.1-3.5.2.3; referred to as Huy3) is applied to generate RSL predictions with the Tarasov et al. (2012) optimal NAIC model. Using a suite of 243 Earth viscosity models we compute RSL model predictions for the Huy3 model. The data-model discrepancies are encapsulated within the χ^2 values shown in Figure 3.10. A direct comparison of both the Huy2 (Fig. 15 in Simpson et al., 2009) and Huy3 χ^2 results indicates an improved data-model fit for the Huy3 model. The optimal Huy3 Earth model was found to have a 120 km lithosphere with an upper mantle viscosity of $0.5\text{x}10^{21}$ Pas and lower mantle viscosity of $2\text{x}10^{21}$ Pas. This study investigated a broader range of viscosity models than the Simpson analysis, however the general pattern in the χ^2 results remains similar even when considering this study has many more degrees of freedom. An F-test is performed which considers the variability of the χ^2 values by decomposing the sums of squares from the χ^2 analysis. This suggests a number of Earth models which produces comparable fits to the observations (95% confidence interval). We cannot discriminate between these Earth models; therefore they represent the uncertainty in Earth viscosity structure on the RSL predictions. It should be noted that the optimal Earth model found by the Simpson et al. (2009) study falls within the 95% confidence interval of the Huy3 χ^2 result (Table 3.3).

In Figure 3.11 we compare optimal RSL predictions for the Huy3 model (dark grey curve) against our RSL database. We show the envelope of predictions due to uncertainties in the NAIC deglacial history (Supplementary Section Figure 3.S5) along with the Earth viscosity model uncertainty defined above. The Huy3 predictions are shown with the Huy2 optimal East and West predictions in dotted and solid black, respectively. In the remainder of this sub-section we discuss the data-model fits with a focus on the Huy3 results and the implications for the ice chronology. It is well known that constraining a regional GIA model is a non-unique inversion problem; therefore, we discuss parameter trade-offs and highlight, when possible, independent observational evidence that reduces the possible solution parameter space.

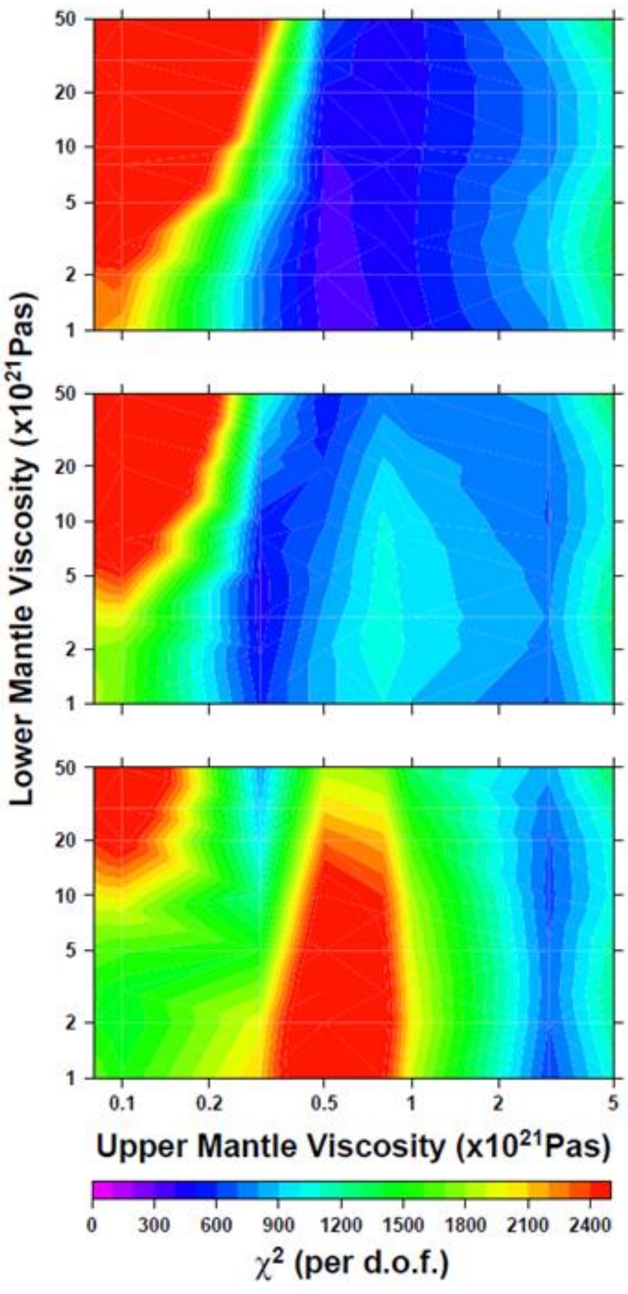

Figure 3.10 The χ^2 result for the Huy3 model with each frame shows results for a fixed value of lithospheric thickness (120 km (top), 96 km (middle), 71 km (bottom). The optimal fit was achieved with a lithospheric thickness of 120 km, upper mantle viscosity of 0.5x10^{21} Pas and lower mantle viscosity of 2x10^{21} Pas. A subset of best-fitting models (95% confidence) is listed in Table 3.3.

Starting in West Greenland and working anti-clockwise we discuss data-model discrepancies. The best-fitting Huy3 predictions produce an excellent fit to the western sites 1-6 (Fig 3.11a); this is not surprising since the χ^2 results are heavily weighted to this region due to the high density of precise sea-level index point data. This could be avoided in future studies by performing an inverse areal density weighting scheme as in Tarasov et al, (2012). Compared to the Huy2 RSL predictions, the Huy3 model achieves a better fit to the sea-level lowstand (e.g. site 4. Upe, Fig 3.S5a) and rate of RSL fall (e.g. site 5. Orp, Fig 3.11a), especially when taking into consideration the uncertainty in Earth structure and non-Greenland ice. There remain two persistent data-model discrepancies at Kangerlusuaq (1) and Pakitsoq (3) where Mid-Holocene RSL observations are under predicted. Overall, the west Greenland Huy3 RSL predictions have much higher amplitude; however they remain consistent with the ML observations since the relevant sites became ice-free sometime between 12 to 9 ka BP (Funder et al., 2011). At Sisimiut (8) and Sondre (9) the Huy3 predictions improve upon the Huy2 model in most respects: capturing the ML, rate of RSL fall and the Late Holocene lowstand. The western coast of Greenland is centered on Disko Bugt where the Jakobshavn Isbrae ice stream drains ~7% of the ice sheet (Bindschadler, 1984). The western shelf and Disko Bugt was covered at the LGM and was probably the site of a Jakobshavn Isbrae predecessor which extended out to the shelf edge (Funder & Hansen, 1996; Weidick & Bennike, 2007; O'Cofaigh et al., 2012). In contrast to the Huy2 reconstruction which adopts an inner shelf LGM extent, we found a more extensive LGM extent better fit the geomorphology observations while maintaining an excellent fit to RSL observations. Furthermore, the Huy2 model has a late deglaciation in West Greenland starting at 12 ka BP leaving the shelf ice free by 10 ka BP. Recent marine geophysical and geological data (O'Cofaigh et al., 2012) have suggested an earlier deglaciation, which is consistent with the western LGM extent and retreat timing in the Huy3 model. This consistency between multiple lines of evidence gives a high level of confidence in the accuracy of the Huy3 model in this region.

LT (km)	UMV (10^{21} Pas)	LMV(10^{21} Pas)
120	0.5	1
120	**0.5**	**2**
120	0.5	3
120	0.5	5
120	0.5	8
120	0.5	10

Table 3.3 The sub-set of Earth structures considered in this study that are within the 95% confidence interval of the χ^2 minimum (based on an F-test). Values in bold face represent the optimal parameters.

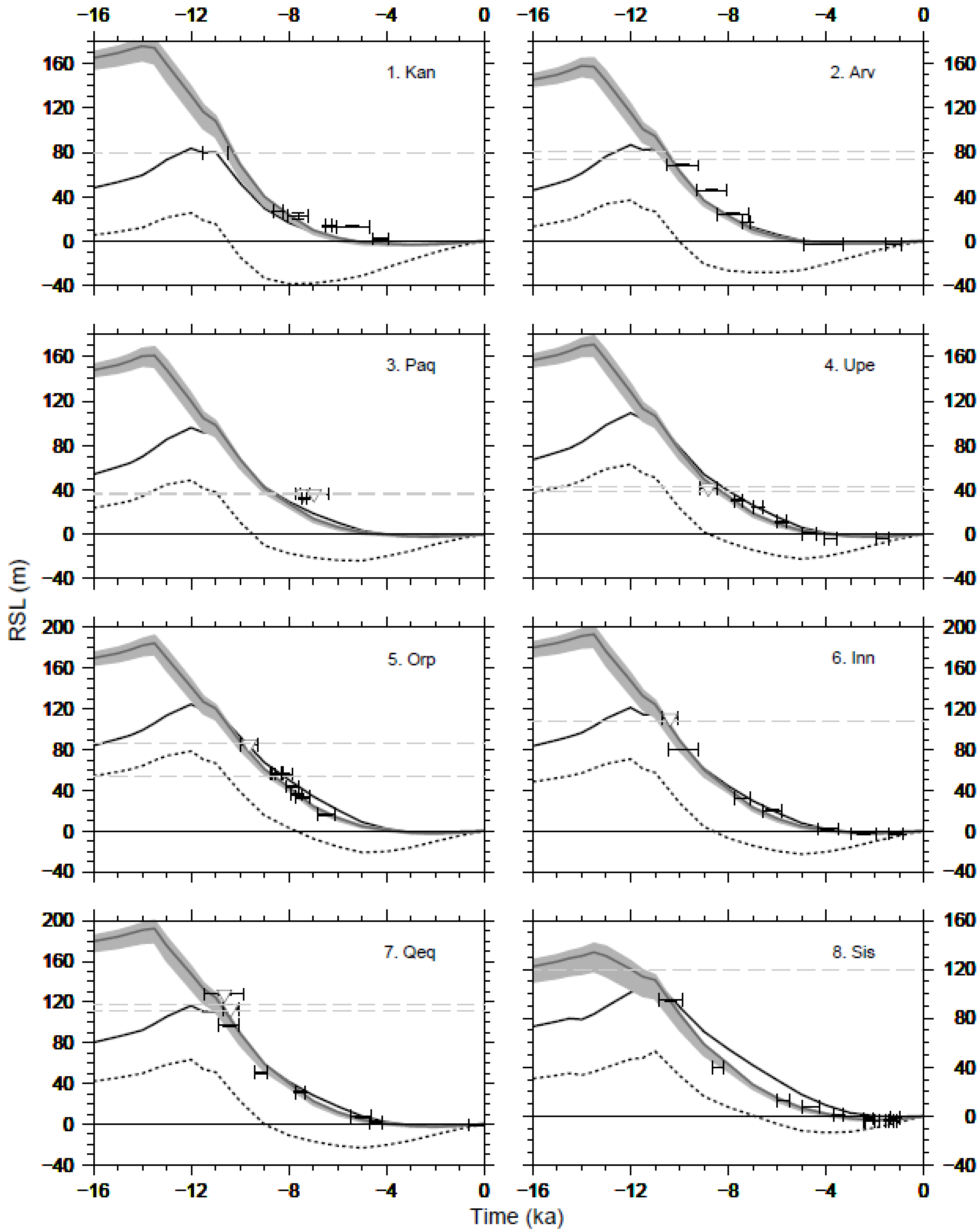
1. Kan
2. Arv
3. Paq
4. Upe
5. Orp
6. Inn
7. Qeq
8. Sis
RSL (m)
Time (ka)

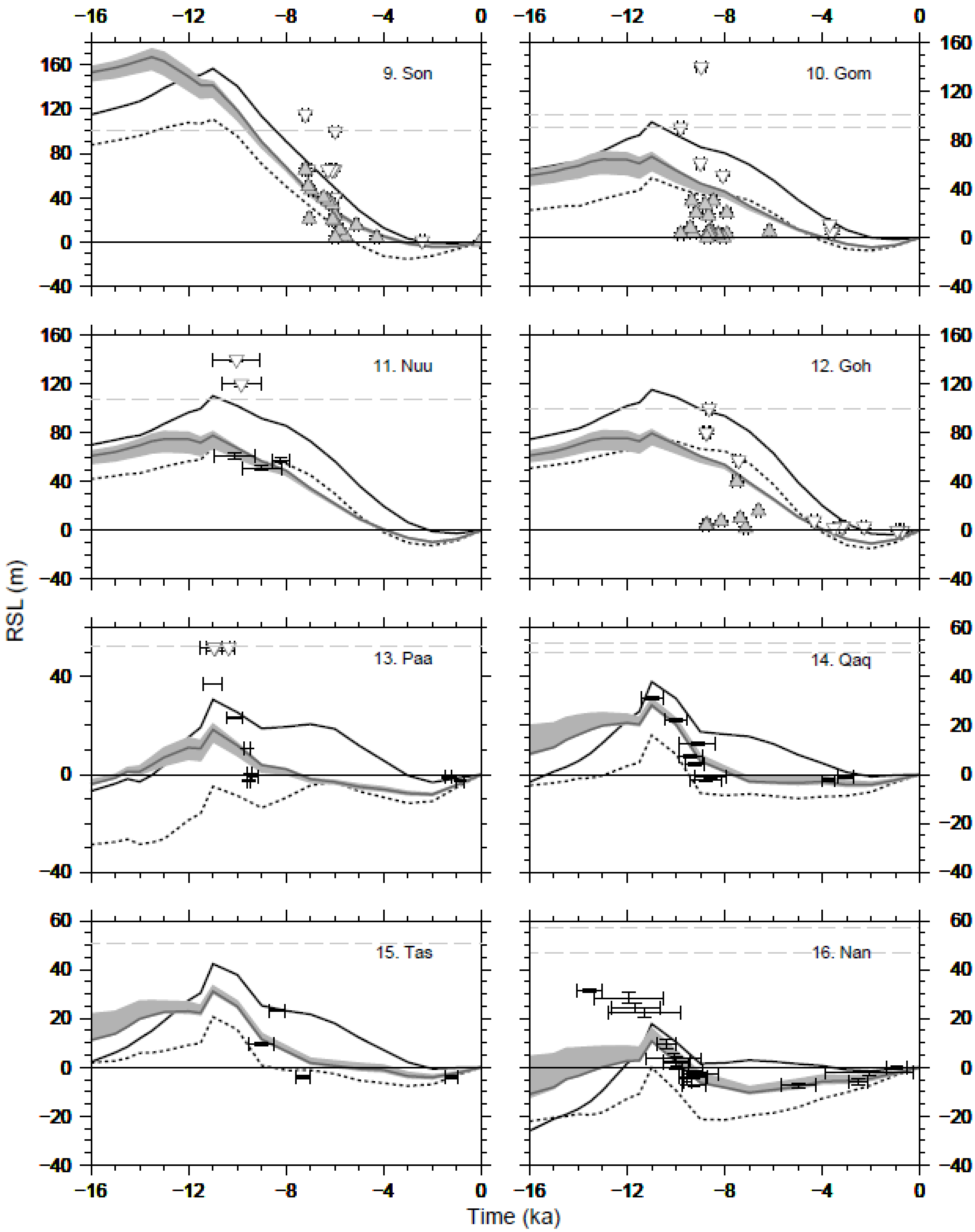
9. Son
10. Gom
11. Nuu
12. Goh
13. Paa
14. Qaq
15. Tas
16. Nan
RSL (m)
Time (ka)
−16
−12
−8
−4
0
160
120
80
40
0
−40
60
20
−20

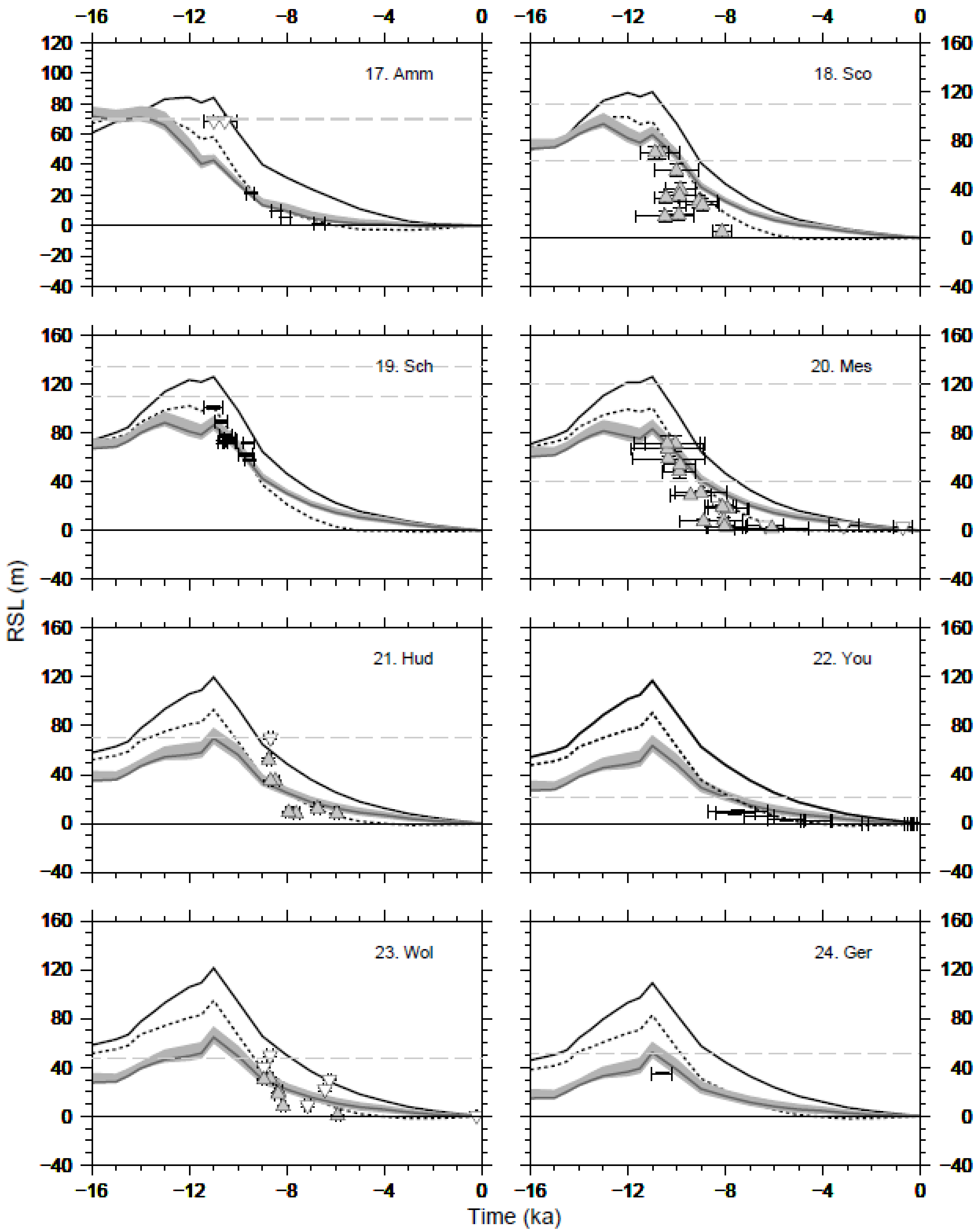
17. Amm
18. Sco
19. Sch
20. Mes
21. Hud
22. You
23. Wol
24. Ger
RSL (m)
Time (ka)
−16
−12
−8
−4
0
120
100
80
60
40
20
0
−20
−40
160

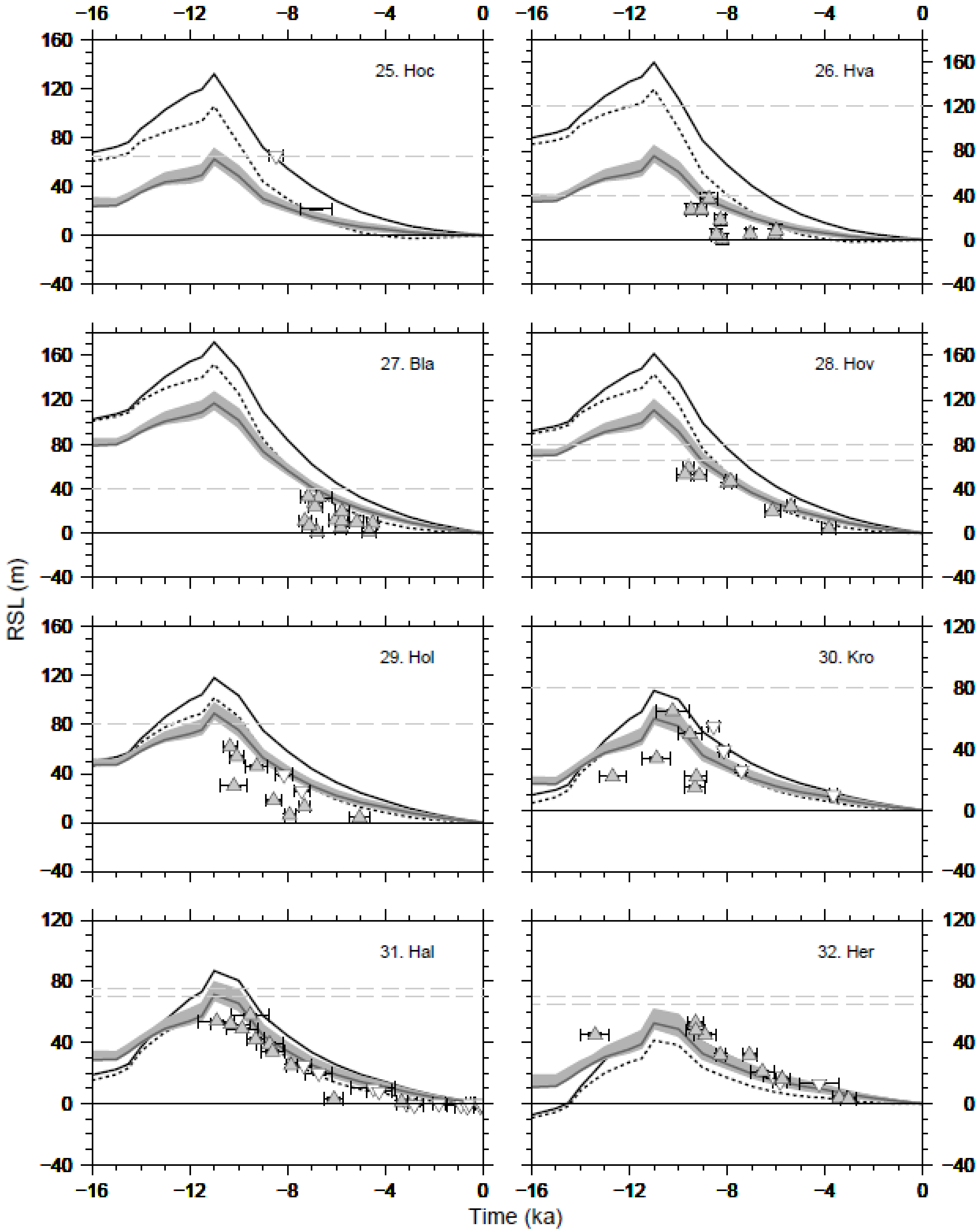
25. Hoc
26. Hva
27. Bla
28. Hov
29. Hol
30. Kro
31. Hal
32. Her
RSL (m)
Time (ka)

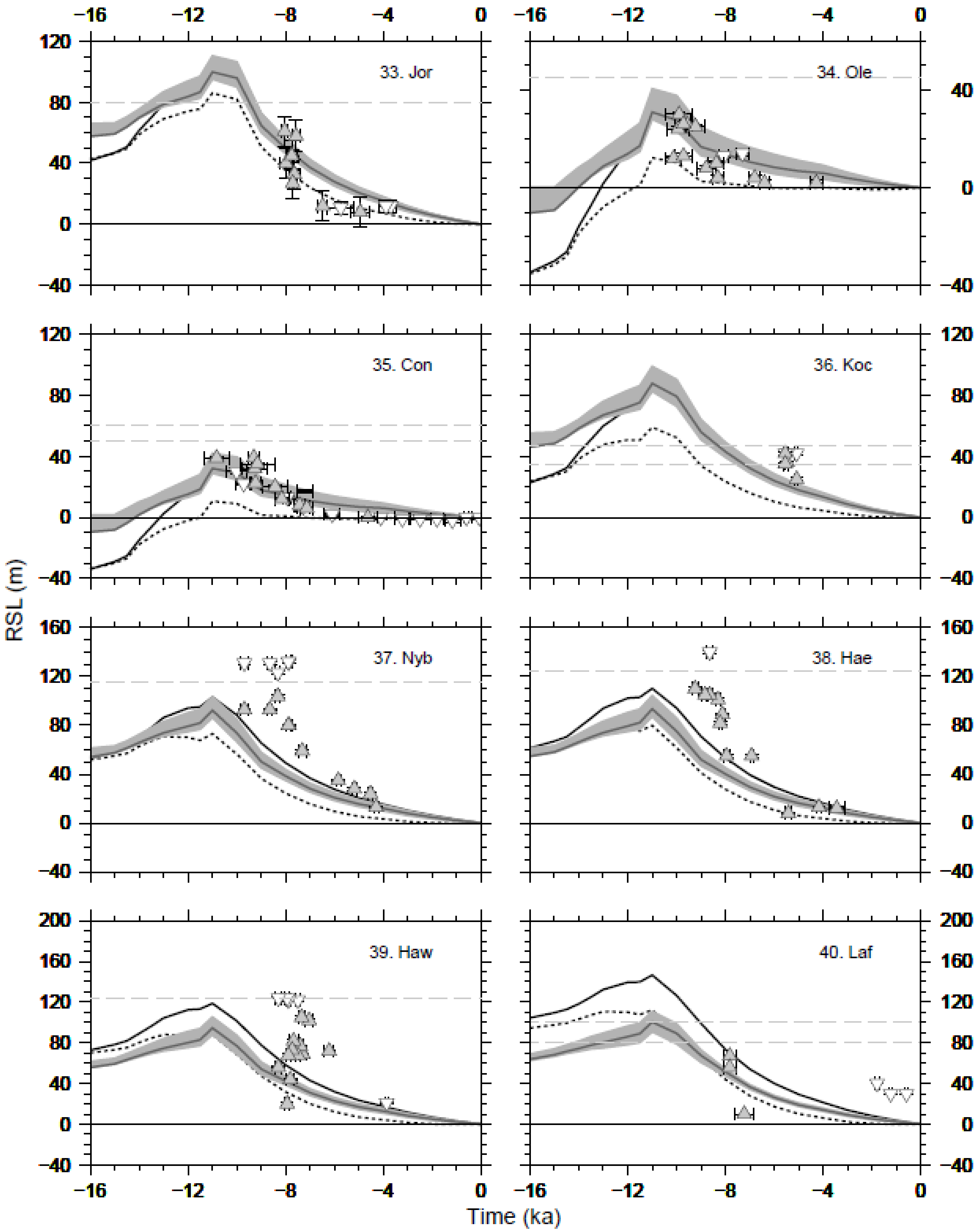
33. Jor
34. Ole
35. Con
36. Koc
37. Nyb
38. Hae
39. Haw
40. Laf
RSL (m)
Time (ka)

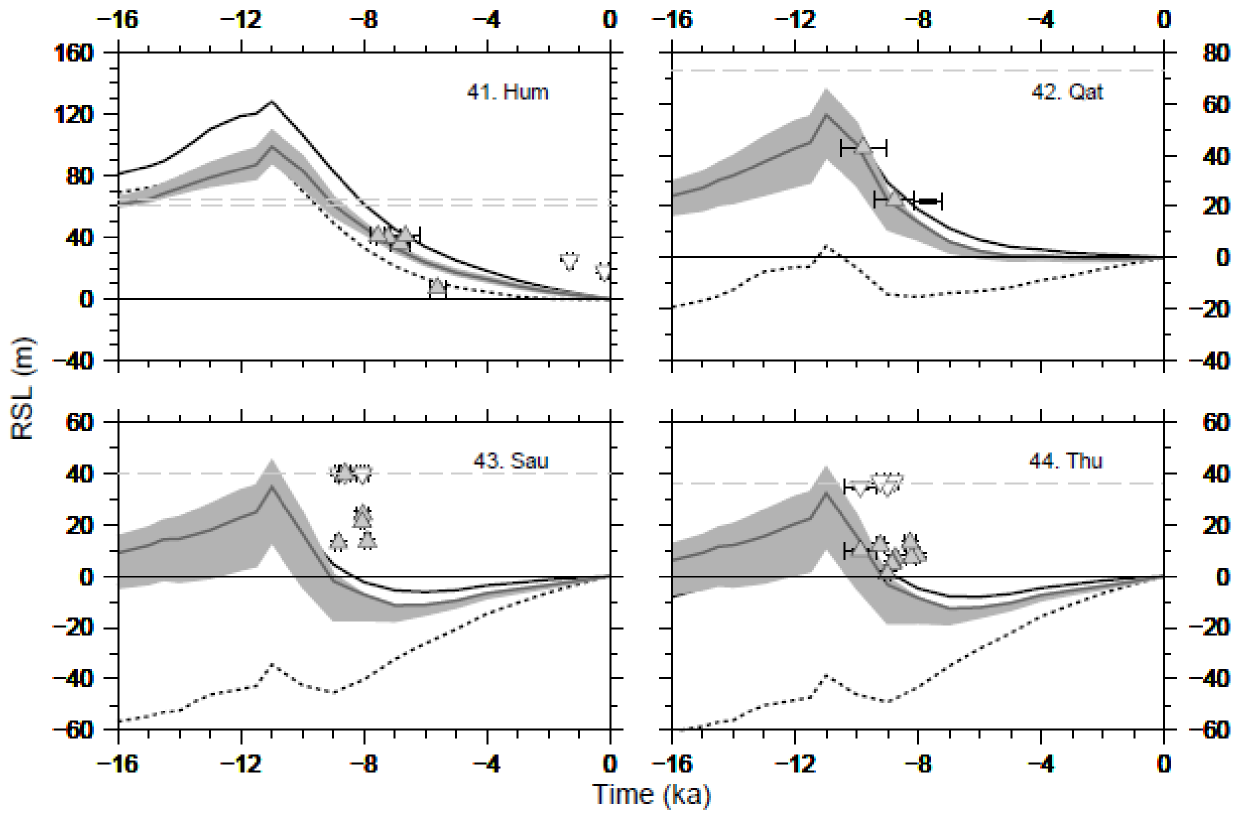

Figure 3.11 RSL predictions generated by the Huy2 reconstruction with the optimal Earth model (black curves) and alternate eastern Earth model (dashed black curves). The Huy3 RSL predictions were generated using the optimal Earth model (LT120, UMV0.5, LMV2; see Figure 11) and are shown by the dark grey curves with the light grey envelop representing the range in RSL predicted using Earth structures within the 95% confidence interval of the χ^2 analysis (Table 3.3). Sea-level index points are shown as crosses with both time and height error bars. Lower limiting dates are denoted by grey upward pointing triangles, while upper limiting dates are shown by white downward pointing triangles. The black horizontal line highlights present day sea-level. The grey dashed horizontal line represents the marine limit which marks the highest point reached by sea-level during ice-free conditions at each locality (site 1-8, 9-16, 17-24, 25-32, 33-40, 41-44 constitute Fig. 3.4 a,b,c,d,e, and f, respectively).

South of Disko Bugt in the Nuuk area, the Huy2 model fails to fit the RSL observations with its optimal Earth model. The Huy3 reconstruction remains consistent with its Earth model and produces an adequate fit to the observations, falling within the limiting dates and capturing a good number of the sea-level index points; however the predicted RSL amplitudes fall short of the ML observations (Fig 3.11b, S5b). At present the southwest margin is the largest ice-free land area in Greenland where observational evidence of the Holocene retreat is well documented with recessional moraine systems and threshold lake data (e.g. Van Tatenhove et al., 1995; Larsen et al., 2013). These features suggest a retreat past the PD margin after 6 ka BP (Van Tatenhove et al., 1996) which remains consistent with both the Huy2 and Huy3 models (orange contour in Figure 3.3 and 3.7 is the 6 ka BP ice extent).

Southwest and South Greenland are areas of high quality data where the largest Huy2 and Huy3 RSL data-model discrepancies exist (Figure 3.11b). Compared to the Huy2 model, the Huy3 RSL predictions achieve an improved fit to the observations at all four sites, Paamiut, Qaqortoq, Tasiusaq, and Nanortalik, especially when considering uncertainties in non-Greenland ice (Figure 3.S5b). The Huy3 RSL predictions capture the Mid to Late Holocene lowstand, reaching PD values of sea-level between 10 to 8 ka BP. However, the MLs are not reached at any of the southern sites and the amplitude of rapid RSL fall from 12 to 10 ka BP is not captured at Paamiut, Tasiusaq and Nanortalik. Several sensitivity analyses were conducted in this region varying the sea-level and climate forcing. The results indicated that a late retreat of marine-based ice would not sufficiently increase the amplitude of RSL change given that it produces a very rapid unloading of ice from the narrow continental shelf which limits the overall magnitude of unloading (Woodroffe et al., 2013). In addition, several parameters in the climate forcing were tuned to examine the impact of a Younger Dryas readvance. We inspected a spectrum of scenarios ranging from there being no readvance to a pronounce regrowth back to the continental edge. This was found to influence the characteristic shape of the RSL prediction in terms of initial fall in RSL but the overall amplitude was left relatively unaffected. As shown by the grey band in Fig. 3.S5b, the NAIC has a significant impact on South Greenland RSL and it has the ability to improve the fit to the Holocene sea-level index points, though it does not sufficiently increase RSL predictions by 12 ka BP. Though a weak viscosity structure under South Greenland could account for some of the discrepancies, we chose to avoid considering models outside of the 95% range of the χ^2 minimum given that there is currently no evidence to support the existence of low viscosities in this part of Greenland (Yakolev et al., 2010).

In the southeast, the Ammassalik sea-level observations are predicted accurately with the Huy3 reconstruction within uncertainties of the Earth viscosity structure and NAIC (Figure 3.11c, 3.S5c).

Furthermore, we emphasise that this result is achieved using an Earth model which is consistent Greenland-wide. This dramatically improved fit for a single Earth model persists for the remaining eastern and northeastern sites, suggesting that the inferred eastern viscosity structure in Simpson et al. (2009) was masking inaccuracies in the ice chronology – as discussed above, a very late retreat (~12 ka BP) is not compatible with emerging field constraints (Jennings et al., 2006; Andrews, 2008). We note, however, that there are a few sites where the Huy2 model and its alternate (East) Earth structure produce a better fit to the observations such as Mesters Vig. A few sea-level upper limits are not reached by the Huy3 predictions since the persistent rapid RSL fall is not maintained reaching PD RSL by ~7 to 6 ka BP. In East Greenland, the PD margin was reached by approximately 8 to 7.5 ka BP (Funder, 1987) with the outer fjord basin being ice free by 12 to 10 ka BP (Funder et al., 1998), this is represented well by the Huy3 chronology suggesting that it has a certain level of accuracy. North of Scoresby Sund, the Huy3 RSL predictions produce a better fit to observations compared to the Huy2 model, especially considering our consistent Earth structure. Some data-model discrepancies remain, however, even when taking uncertainties in Earth structure into account. At site 21 (Hudson; Figure 3.11c) the ML is reached; however the timing and rate of RSL fall is inaccurate causing predicted RSL to fall significantly below the highest marine limiting date at ~60 m.

The Huy3 RSL predictions fit the majority of observations in Northeast Greenland within uncertainty of the Earth structure (Figure 3.11d). In contrast, North Greenland has a number of significant data-model misfits. The data is of low precision but they generally indicate a late and rapid fall in RSL (Figure 3.11e). Results for Northwest Greenland indicate a similar data-model discrepancy where the model fails to produce a sufficiently late RSL fall (Figure 3.11f). Neither the Huy2 nor Huy3 models satisfactorily fit the observations in these regions, even though both adopt a late SLF parameterisation. However, as previously stated, the model can only produce a retreat of marine-based ice as late as ~12 ka BP. Furthermore, the ice model applied to reconstruct the GrIS does not account for the buttressing effect of multiyear sea-ice nor the dynamic connection to the Innuitian ice sheet, both of which would act to produce a thicker ice sheet in north and northwest Greenland.

3.5.3 ICE SHEET INTERIOR

A valuable boundary condition which has significant constraining power, particularly in the ice-sheet interior is the state of the PD ice sheet. Bamber et al. (2001) applied ice thickness data from ice-penetrating radar measurements to derive the PD ice geometry with a volume of 7 m IESL. Additionally, Rignot & Mouginot (2012) used satellite radar interferometry data to generate surface profiles of the GrIS, specifically of the surface velocity (Figure 2 in Rignot & Mouginot, 2012). The PD Huy3 surface velocity and ice thickness is shown in Figure 3.12 along with a comparison to the Bamber et al. (2001) PD ice thickness. The Huy3 model broadly captures the Rignot & Mouginot (2012) surface velocities with the exception of rapid ice streams which are not properly resolved in the model which can explain in part the discrepancies between modelled and observed PD ice thickness. The misfits shown in Figure 3.12c and their potential sources are discussed in greater detail in Section 3.6.2.

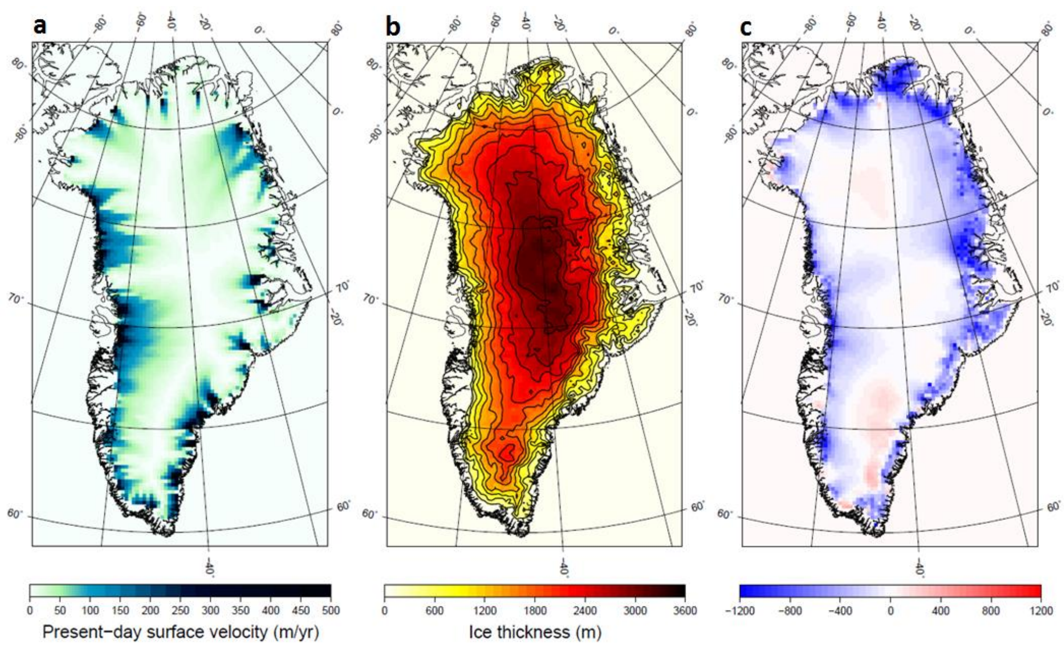

Figure 3.12 The Huy3 present-day (a) surface velocity, (b) ice thickness, and (c) the observed (Bamber et al., 2001) minus modelled (Huy3) ice thickness in metres.

Another of the few constraints in the interior of the ice sheet is the ice-core derived thinning curves at GRIP, NGRIP, Camp Century, and DYE-3 (Lecavalier et al., 2013). The Huy3 thinning curve predictions (dashed black curve) are found in Figure 3.13. The evolution of the surface elevation is generated using the Huy3 ice thickness chronology and model predictions for vertical land motion from the 95% confidence interval from the χ^2 analysis (grey envelop; Figure 3.13). Given the uncertainty to signal ratio of the thinning curves, the model predictions generally remain within error. The exceptions are at Camp Century where the Huy3 model fails to capture the rapid thinning which occurs at 8 to 6 ka BP and the subsequent maximum response to interglacial conditions. As previously discussed, the Greenland ice sheet was dynamically connected to the Innuitian ice sheet. This aspect is not represented

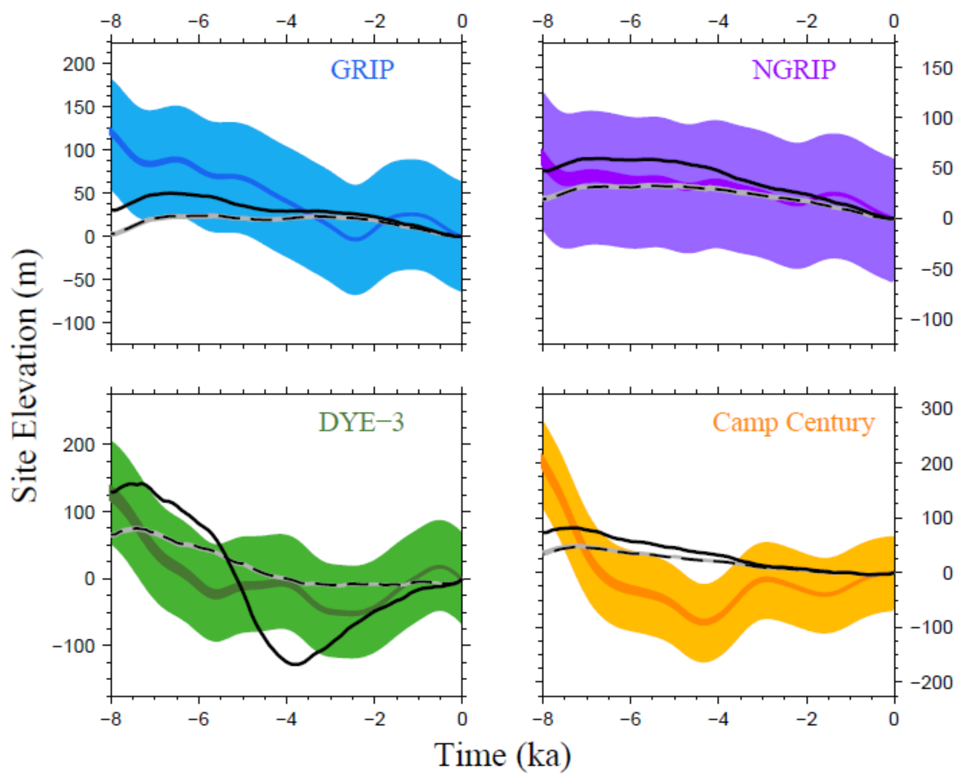

Figure 3.13 The ice-core derived thinning curves compared to the Huy3 model predictions (dashed black curves) at GRIP, NGRIP, DYE-3, and Camp Century. The predictions consist of ice thinning at each core site along with vertical land motion due to glacial isostatic adjustment using the optimal Earth model (LT120, UMV0.5, LMV2). The subset of optimum Earth models that partner the Huy3 ice model (Table 3.3) were also used but make very little difference to the model curves (grey band). Results for the Huy2 ice model and its partnering Earth model (LT120, UMV0.5, LMV1) are shown by the solid black curves.

in the Huy3 model and it is believe that this would produce thicker ice across northeast Greenland and rapid thinning after the disintegration of the Nares strait which could account for the remaining discrepancy at the Camp Century thinning curve. Additionally, it is possible that we misrepresent the timing and magnitude of the HTM in North Greenland where it is poorly constrained. This could consequently explain remaining RSL data-model misfits. Furthermore, at the GRIP site the thinning curve is marginally under predicted at 8 ka BP, similar to the Huy2 prediction. This could be due to poorly constrained boundary conditions at the bedrock allowing for quick transport of ice permitting the PD summit to thin quickly during the Holocene. Additionally, as suggested by the Camp Century thinning curve and misrepresented by Huy3 model, significant thinning in North Greenland could propagate to the interior of the ice sheet, thinning the summit.

3.6 DISCUSSION

The Huy3 model builds upon the work of Simpson et al. (2009) who calibrated an ice sheet model in series with a GIA and RSL model. The Huy3 calibration includes several noteworthy advances over its predecessor: (1) a larger constraint database of RSL and ice extent, (2) model improvements to the climate and SLF, and (3) the inclusion of a suite of glaciologically-consistent NAIC models. Some of these advances were chosen to address specific data-model misfits and model weaknesses. The Simpson study presented a single solution to a non-unique problem, while the Huy3 ice model being another better constrained and better fitting solution. In this study a sensitivity analysis of key model parameters was conducted to target those that were effective at improving the fit to our constraint database, similar to the dominant key parameters described in Zweck & Huybrechts (2005).

3.6.1 GRIS EVOLUTION

3.6.1.1 ICE VOLUME AND MARINE RETREAT

The Huy3 model features a number of distinct large scale characteristics. Figure 3.14 illustrates the evolution of the ice volume and areal extent of the Huy3 model deglaciation. Additionally, Figure 3.15 and 3.16 demonstrate ice thickness and relative sea-level at the times 16, 12, 8 and 4 ka BP. The Huy3 model has a relatively large LGM volume (4.5 m excess IESL) and areal extent. Clark & Mix (2002) estimated a Greenland LGM volume of 2-3m excess IESL. The Huy1 model of Huybrechts (2002) produced a value of 2.7 m excess IESL, although parametric uncertainties yielded a range of 1.9 to 3.5 m. The Huy2 reconstruction contains an LGM volume of 4.1 m excess IESL. The general trend to a larger Greenland LGM volume is consistent with recent findings of moraines on the continental shelf which have suggested a much larger LGM extent than previously thought (e.g. O'Cofaigh et al., 2012). As for the Huy2 model, Huy3 reaches a maximum volume after the LGM at 16.5 ka BP with 5.0 m excess IESL compared to 4.6 m for Huy2. The timing of this volume maximum occurs due to the outpacing of accumulation by ablation (Cuffey & Clow, 1997). Post maximum extent at 16.5 ka BP, the Huy3 model undergoes a spatially variable retreat from the continental shelf; the southern half of Greenland underwent

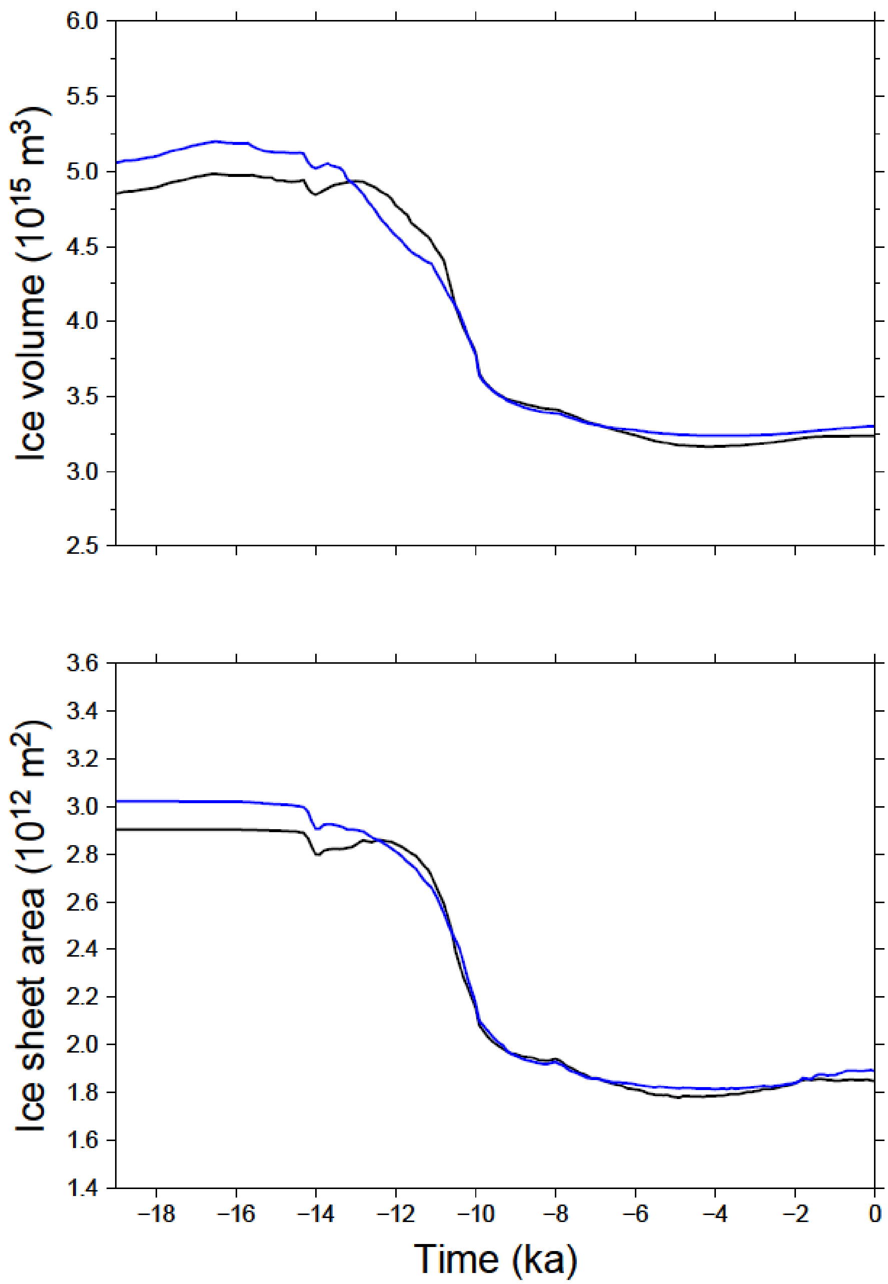

Figure 3.14 The Huy3 model predictions (blue curves) for ice sheet volume (top) and areal extent (bottom) compared to the Huy2 predictions (black curves).

a slow gradual retreat from ~16 to 10 ka BP while in the far north, retreat is rapid and late starting at ~12 ka BP. In comparison, the GREEN1 model begins to retreat from the continental shelf at 16.3 ka BP while the GrB and Huy2 models do so at 12 ka BP. By 10 ka BP the Nares Strait opens up and, regardless of region, the Huy3 ice extent has retreated to reach the PD coast line, as supported by the field observations (Funder et al., 2011). By incorporating a spatially variable SLF in the development of Huy3, the resulting marine retreat history better encapsulates the variability proposed by the observations compared to the Huy2 reconstruction.

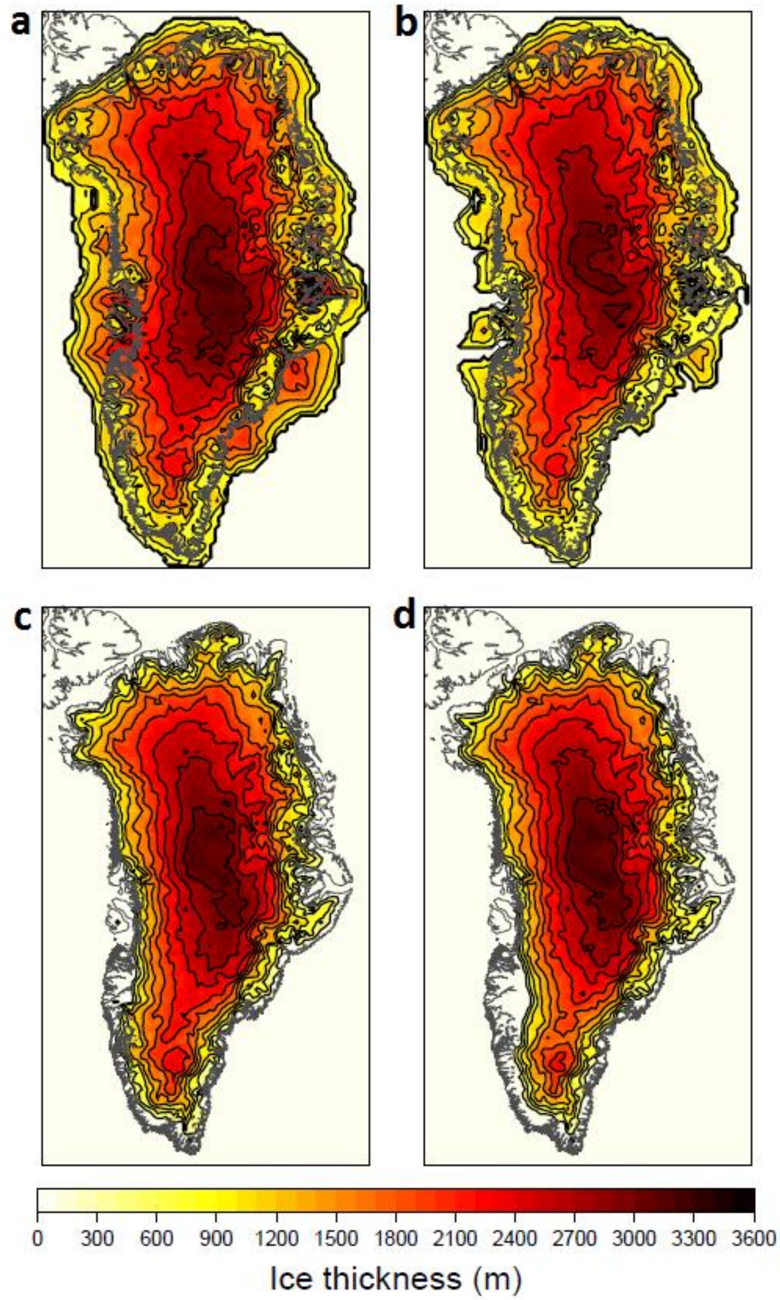

Figure 3.15 Huy3 ice thickness for the time slices: (a) 16 ka BP, (b) 12 ka BP, (c) 8 ka BP, and (d) 4 ka BP.

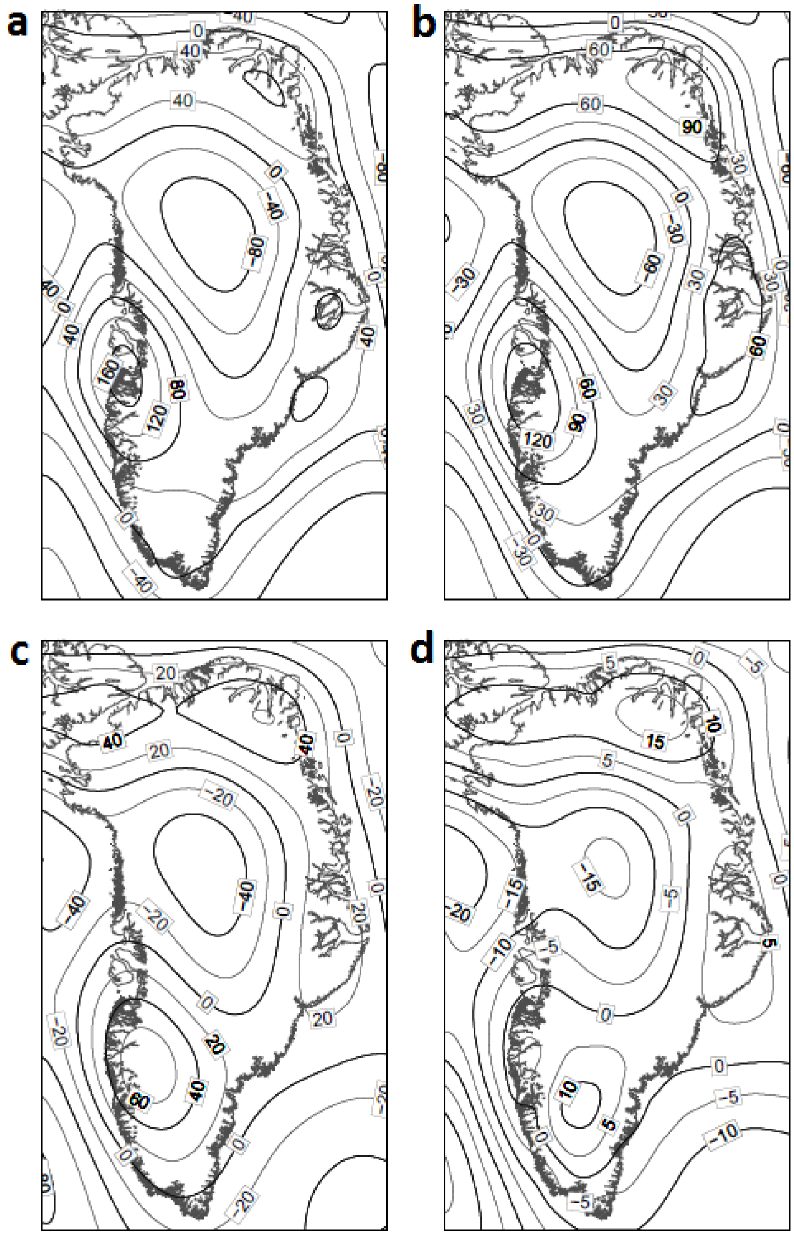

Figure 3.16 Spatial plots of RSL predictions (in metres) from the Huy3 reconstruction using the optimal Earth model for the time slices: (a) 16 ka BP, (b) 12 ka BP, (c) 8 ka BP, and (d) 4 ka BP.

3.6.1.2 LAND-BASED RETREAT AND REGROWTH

In response to the HTM, the margin of Huy3 in some areas retreated past the PD margin between 9 to 6 ka BP (see Figure 3.7). As in the Huy2 model, the Southwest Greenland margin responded most dramatically to the HTM and had receded beyond the PD margin location by 8 to 6 ka BP which is in agreement with deglaciation dates for this location (Bennike, 2008; Larsen et al., 2013). While there are some discrepancies between Huy3 and observed deglaciation dates, these are mostly related to the model resolution (20x20km) which limits the accuracy of margin predictions (Larsen et al., 2013). The minimum areal extent of Huy3 is reached between 5 to 3.5 ka BP with the greatest volume deficit of 0.17 m IESL ocurring at 3.8 ka BP (Figure 3.15d). While the Huy2 model produced the same ice volume deficit at minimum extent, it had too great of a response to the HTM; particularly in the southwest as suggested by the DYE-3 thinning curve (Figure 3.13). In the Huy2 reconstruction, the southwest margin responded by receding 60 to 100 km past the PD margin position; in comparison the Huy3 model produces a more modest retreat of 20 to 60 km. The Huy3 model exhibits more widespread thinning in the Southwest compared to Huy2 which compensates for the more modest margin response and results in similar IESL deficits in the two models. The Huy3 HTM response is more consistent with observational evidence at the ice front which suggest that the western margin was up to 20km inland of the PD extent (Weidick et al., 1990). Earlier ice modelling studies compared model output to recessional moraine systems and proposed a retreat up to 50 km behind the current southwest margin (Van Tatenhove et al., 1995, 1996). In comparison, the GrB model (Tarasov & Peltier, 2002) reached an extent minimum considerably earlier at 8 ka BP with a significant and widespread retreat past the present margin by 80 to 120 km in the Southwest. In the GREEN1 model (Fleming & Lambeck, 2004) a retreat of 40km in the southwest was imposed in order to fit RSL observations in this region. In general, the Huy3 model is more consistent with the observational evidence compared to other modelling studies. Based on the sensitivity tests performed in generating Huy3, we agree with the conclusions arrived at in previous studies, that a neoglacial regrowth of the GrIS facilitates a fit to RSL observation from West Greenland (Tarasov and Peltier, 2002; Fleming and Lambeck, 2004; Simpson et al., 2009).

3.6.2 DATA-MODEL MISFIT

While the Huy3 GrIS reconstruction does account for a number of data-model misfits shown by the Huy2 model (Figures 3.11 and 3.13), there remain a number of outstanding discrepancies (e.g. Figure

3.11e). Here we discuss these discrepancies in the context of parameter trade-off, model limitations and model uncertainty.

The Earth model applied here is spherically symmetric and so cannot accurately account for heterogeneity in the Earth structure. This model limitation is undoubtedly a source of data-model discrepancies due to the likely existence of lateral Earth structure beneath Greenland (e.g. Darbyshire et al., 2004; Yakovlev et al., 2011). In the Simpson study, the existence of lateral Earth structure was proposed as one possible source of the data-model discrepancies with the Huy2 model. Three-dimensional Earth modelling studies of GIA and RSL applying the Huy2 model indicate that lateral structure does impact RSL computations, particularly those associated with spatial variations in lithospheric thickness which amplified Huy2 data-model discrepancies (G. Milne; personal communication). Simpson et al. also proposed that the poorer fits along the East coast could have been due to the limitation of a spatially uniform SLF resulting in synchronous marine retreat when, in reality, this might not have been the case. Subsequent studies have supported this idea (e.g. Funder et al., 2011) and so an important element of this study was the implementation of a regionally variable SLF to test this hypothesis further. Our results show that the West-East data-model residuals can be accounted for with this model extension, thus providing further support for this hypothesis. However, this does not rule out the likely influence of lateral Earth structure in some areas of Greenland and so an important avenue for future work entails applying our Huy3 reconstruction with a 3D Earth model to investigate the potential impact of lateral structure on RSL predictions.

The non-Greenland ice with greatest implications for Greenland RSL is the NAIC. As outlined in Section 3.5.2.4, the Huy2 model was amalgamated with the global loading model ICE-5G. In this study, the NAIC in ICE-5G was replaced with a more recent reconstruction based on a glaciological model (Tarasov et al., 2012). These two NAIC reconstructions are compared in Figure 3.8. Figure 3.9 shows the RSL contribution around Greenland from two alternate NAIC which produces a RSL gradient across

Greenland on the order of 10s of metres. During deglaciation of the NAIC, the net effect on Greenland sea levels was a fall due to the influence of gravitational changes (acting to lower the ocean surface (Figure 3.9). By 8 ka BP, North American ice was mostly gone and thus the prevailing contribution to sea-level was vertical land motion related with subsidence of the peripheral forebulge causing a rise in RSL. Due to Northwest Greenland's proximity to Ellesmere Island and the Innuitian ice sheet, postglacial rebound due to deglaciation of ice in this area dominates over the collapse of the Laurentide forebulge leading to a sea-level fall in this part of Greenland (see Fig. 3.9). As previously stated in Simpson et al. (2009), once the GrIS was predominantly land-based, the contribution to local RSL from changes in non-Greenland ice can be equal or opposite to changes driven by the Greenland ice sheet. Thus RSL predictions around Greenland can be highly sensitive to the adopted NAIC model as illustrated in Figure 3.S5 where we plot predictions for the ICE-5G North American component and a high variance subset of NAIC models from Tarasov et al. (2012). This figure illustrates that some previous model discrepancies can be accounted for given uncertainties in the NAIC reconstructions.

The Huy3 ice model is compared to the PD ice sheet extent from Bamber et al. (2001). The differences are shown in Figure 3.12. Calculating the root mean square of the differences between the modelled and observed ice thicknesses gives values 214.1 m. This is comparable to the Huy2 value of 239.3 m. When comparing the Huy3 model to the PD geometry, negligible discrepancies are noticed over the interior of the ice sheet but large differences are evident at the margins. Fig. 3.12 indicates that the Huy3 model over predicts ice thickness at the margins. This is not surprising given that the shallow ice approximation adopted in the ice model applied here is least accurate when ice surface gradients are high (Huybrechts et al., 1996; Van den Berg et al., 2006). Also, ice streams are not well resolved due to the grid spacing adopted and so the discharge of ice at the margins is under-estimated (Fig. 3.12), which will also lead to an overestimate of ice thickness at the margins. These model limitations are common to a number of recent analyses (e.g. Tarasov et al., 2012; Whitehouse et al., 2012), and can be overcome by the application of more sophisticated ice models (e.g. Pollard and Deconto, 2009; Cornford et al., 2012) but the cost in computation time is somewhat prohibitive for the large ensemble and long-time integrations required for paleo reconstructions.

The climate forcing was found to be the dominant control on ice sheet evolution and given how past climate is poorly constrained; it remains the largest source of uncertainty on the chronology of the ice sheet over the deglaciation, especially since it is poorly constrained. In this study we present an optimal model (Huy3) while a qualitative assessment of alternate reconstruction was conducted, a robust quantitative assessment of chronology uncertainties is lacking and would be better conducted by a data-constrained Bayesian calibration (e.g. Tarasov et al., 2012). Even though parameter variations in the treatment of ice flow, isostasy, marine calving and basal processes have a considerable impact on the resulting reconstruction, there remain data-model discrepancies inexplicable by parametric uncertainties, particularly in North and South Greenland. This suggests limitations in our adopted glaciological, RSL and GIA model. As previously outlined in Section 3.4.1, some physical processes are not represented in our ice model. The model lacks higher-order stresses and the grid spacing prevents a physical representation of ice stream dynamics (e.g. Saito et al., 2003). With regards to marine-based ice, there lacks a proper ice calving law and since it is not fully understood our ice model applies a series of parametric equations to simulate ice flux past the grounding line. Finally, given that a full-stokes solution to simulate ice dynamics over the deglaciation is too computationally intensive (Gillet-Chaulet et al., 2012; Larour et al., 2012), a shallow ice approximation is used. Even though the approximation is less accurate at the margins where bedrock and surface slope are steep (Baral et al., 2001), it has been used countless times to successfully simulate the large-scale evolution of an ice sheet over the deglaciation (Van de Wal. 1999; Huybrechts, 2002; Tarasov et al., 2012). At present, the above mentioned model developments are a focus of intense research. However, most of these recent advances are computationally intensive and target studies of the past and future 100 years, therefore they could not be used effectively to simulate 100 ka time intervals. Furthermore, this study involved a total of 250,000 sets of model predictions compared to our constraint database to properly sample the parametric phase-space to assess the issue of non-uniqueness.

3.7 CONCLUSION

1. A new deglacial model of the GrIS which builds upon the work of Simpson et al. (2009) is presented. It incorporates several model developments and a larger constraint database and produces better agreement to a number of sea-level data and ice extent observations.

2. The Huy3 model exhibits an excess IESL of 4.5 m at the LGM and reaches a maximum volume of 5.0 m by 16.5 ka BP. These larger values are a product of revisions to the lateral extent of the LGM ice sheet.

3. By implementing a spatially variable ocean forcing (encapsulating both ocean warming and sea level rise), we considered a variety of marine margin retreat scenarios that were consistent with the somewhat limited extent and retreat information. An optimum fit to the extent and RSL data was achieved with the following chronology. In Southwest and Southeast Greenland, initial retreat of the model occurs between 16 to 14 ka BP with some regions experiencing a re-advance during the Younger Dryas period. In contrast, the northern half of Greenland experienced a rapid and late retreat at ~12 ka BP. The PD coastline was reached across Greenland by 10 ka BP. Implementation of this chronology negates the requirement to invoke a strong East-West gradient in mantle viscosity structure.

4. The model response to the HTM is characterised by a minimum in ice sheet volume (0.17 m IESL) around 4 ka BP and a 40 to 60 km retreat of the ice margin past its PD position in Southwest Greenland. In comparison to the Huy2 model, the optimal response was achieved using a decreased temperature forcing resulting in a reduced margin retreat in Southwest Greenland but increased marginal thinning to produce the same IESL deficit of 0.17 m. Thus, the Huy3 reconstruction exhibits greater climate sensitivity to the HTM than Huy2. Finally, in response to the HTM, our optimal model reconstruction lost mass at a maximum rate of 103.7 Gt/a, which is 27% less than that inferred for the period 1992 to 2011 (Shepherd et al., 2012).

5. The isostatic response of the solid Earth to past changes in ice and ocean loading is required to correct geodetic satellite observations to obtain the PD mass balance of the GrIS. Using the Huy3 reconstruction

with its optimal Earth model, PD uplift rates were calculated and exhibit considerable spatial variability with a range in values of 3.5 to -7 mm/a around Greenland (Figure 3.17).

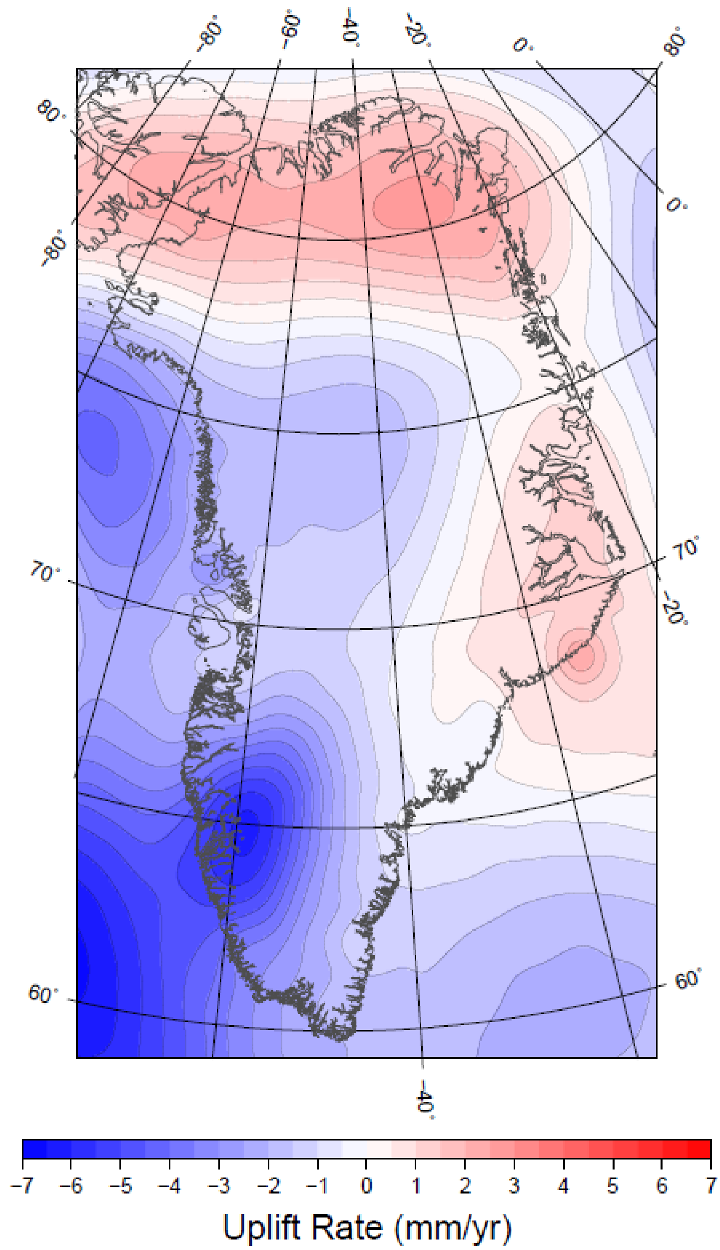

Figure 3.17 Present-day uplift rates as predicted by the Huy3 reconstruction and its optimal Earth model. The Earth structure uncertainty (upper and lower bound) on present-day uplift rates was generated using the 95% confidence interval of the χ^2 analysis and shown in Figure 3.S6.

6. With regard to the influence of North American ice on Greenland RSL, we expanded upon previous studies (Fleming and Lambeck, 2004; Simpson et al., 2009) by considering a high variance set of 8 model

reconstructions for the NAIC. Our results show that this source of uncertainty is largest in North West, West, and South Greenland and can account for some of the data-model misfits in these areas.

7. The Huy3 model achieves an improved fit to the constraint database, particularly when considering a single Earth model. There remain significant discrepancies between the modelled and observed RSLs in the far South and North of Greenland. The former are most likely associated with the influence of lateral Earth structure and/or non-Greenland ice; the latter are most likely related to the buttressing of sea ice and not incorporating an Innuition ice sheet in the model. Improving these aspects of the model are clear targets for future research.

3.8 REFERENCES

Andrews, J., Thang, P., Smith, I.M., Preston, R., Cooper, T., Jennings, A.E., 1997. Spatial and temporal patterns of iceberg rafting (IRD) along the East Greenland margin, ca. 68_N, over the last 14 cal. ka. Journal of Quaternary Science 12, 1–13.

Andrews, J.T., Cooper, T.A., Jennings, A.E., Stein, A.B., Erlenkeuser, H.,1998. Late Quaternary iceberg-rafted detritus events on the Denmark Strait-Southeast Greenland continental slope (c. 65N) related to North Atlantic Heinrich events? Marine Geology 149, 211–228.

Andrews, J.T., 2008. The role of the Iceland ice sheet in the north Atlantic during the late Quaternary: a review and evidence from Denmark Strait. Journal of Quaternary Science 23 (1), 3–20.

Bamber, J.L., Layberry, R.L., Gogineni, S., 2001. A new ice thickness and bed data set for the Greenland ice sheet 1. Measurement, data reduction, and errors. Journal of Geophysical Research – Atmospheres 106 (D24), 33773–33780.

Baral, D.R., Hutter, K., Greve, R., 2001. Asymptotic theories of large-scale motion, temperature, and moisture distribution in land-based polythermal ice sheets: a critical review and new developments. Applied Mechanics Reviews 54 (3), 215–256.

Bennike, O., 1995. Paleoecology of 2 lake basins from Disko, west Greenland. Journal of Quaternary Science 10 (2), 149–155.

Bennike, O., Weidick, A., 2001. Late Quaternary history around Nioghalvfjerdsfjorden and Jokelbugten, north-east Greenland. Boreas 30 (3), 205–227.

Bennike, O., 2002. Late Quaternary history of Washington Land, north Greenland. Boreas 31 (3), 260–272.

Bennike, O., Bjo¨ rck, S., 2002. Chronology of the last recession of the Greenland ice sheet. Journal of Quaternary Science 17 (3), 211–219.

Bennike, O., Bjo¨ rck, S., Lambeck, K., 2002. Estimates of south Greenland late-glacial ice limits from a new relative sea level curve. Earth and Planetary Science Letters 197 (3–4), 171–186.

Bennike, O., 2008. An early Holocene Greenland whale from Melville Bugt, Greenland. Quaternary Research 69 (1), 72–76.

Bennike, O., Anderson, N.J., McGowan, S., 2010. Holocene palaeoecology of southwest Greenland inferred from macrofossils in sediments of an oligosaline lake. Journal of Paleolimnology 43, 787–798.

Bennike, O., Wagner, B., Richter, A., 2011. Relative sea level changes during the Holocene in the Sisimiut area, south-western Greenland. Journal of Quaternary Science 26 (4), 353-361.

Bennike, O., Wagner, B., 2012. Deglaciation chronology, sea-level changes and environmental changes from Holocene lake sediments of Germania Havn Sø, Sabine Ø, northeast Greenland. Quaternary Research 78, 103-109.

Berglund, M.H., 2003. The architecture at three Saqqaq sites in the Nuuk Fjord, Greenland. Études/Inuit/Studies 27 (1-2), 329-346.

Bindschadler, R.A., 1984. Jakobshavn Glacier Drainage-Basin – a balance assessment. Journal of Geophysical Research – Oceans 89 (NC2), 2066–2072.

Blake, W., 1999. Glaciated landscapes along Smith Sund, Ellesmere Island, Canada and Greenland. Annals of Glaciology 28, 40–46.

Braithwaite, R.J., 1995. Positive degree-day factors for ablation on the Greenland ice-sheet studied by energy-balance modeling. Journal of Glaciology 41 (137), 153–160.

Briner, J.P., Stewart, H.A.M., Young, N.E., Philipps, W., Losee, S., 2010. Using proglacial-threshold lakes to constrain fluctuations of the Jakobshavn Isbrae ice margin, western Greenland, during the Holocene. Quaternary Science Reviews 29, 3861-3874.

Clark, J. A., Farrell, W. E., Peltier, W. R., 1978. Global changes in postglacial sea level: a numerical calculation. Quaternary Research, 9(3), 265-287.

Clark, P.U., Mix, A.C., 2002. Ice sheets and sea level of the Last Glacial Maximum. Quaternary Science Reviews 21 (1–3), 1–7.

Cornford, S.L., Martin, D.F., Graves, D.T., Ranken, D.F., Le Brocq, A.M., Gladstone, R.M., Payne, A.J., Ng, E.G., Lipscomb, W.H., 2013. Adaptive mesh, finite volume modeling of marine ice sheets. Journal of Computational Physics 232, 529-549.

Cuffey, K.M., Clow, G.D., Alley, R.B., Stuiver, M., Waddington, E.D., Saltus, R.W., 1995. Large arctic temperature-change at the Wisconsin-Holocene glacial transition. Science 270 (5235), 455–458.

Cuffey, K.M., Clow, G.D., 1997. Temperature, accumulation, and ice sheet elevation in central Greenland through the last deglacial transition. Journal of Geophysical Research – Oceans 102 (C12), 26383–26396.

Cuffey, K.M., 2000. Methodology for use of isotopic climate forcings in ice sheet models. Geophysical Research Letters 27 (19), 3065–3068.

Dahl Jensen, D., Mosegaard, K., Gundestrup, N., Clow, G.D., Johnsen, S.J., Hansen, A.W., Balling, N., 1998. Past temperatures directly from the Greenland ice sheet. Science 282 (5387), 268–271.

Dahl-Jensen, D., Albert, M. R., Aldahan, A., Azuma, N., Balslev-Clausen, D., Baumgartner, M., et al., 2013. Eemian interglacial reconstructed from a Greenland folded ice core. Nature 493, 489-494.

Dansgaard, W., Johnsen, S.J., Clausen, H.B., Langway Jr., C.C., 1971. Climatic record revealed by the Camp Century ice core. In: Turekian, K.K. (Ed.), The Late Cenozoic Glacial Ages. Yale University Press, New Haven, CT, pp. 37–56.

Dansgaard, W., Johnsen, S.J., Clausen, H.B., Dahl Jensen, D., Gundestrup, N.S., Hammer, C.U., Hvidberg, C.S., Steffensen, J.P., Sveinbjornsdottir, A.E., Jouzel, J., Bond, G., 1993. Evidence for general instability of past climate from a 250-Kyr ice-core record. Nature 364 (6434), 218–220.

Dowdeswell, J.A., Evans, J., O'Cofaigh, C., 2010. Submarine landforms and shallow acoustic stratigraphy of a 400 km-long fjord-shelf-slope transect, Kangerlussuaq margin, East Greenland. Quaternary Science Reviews 29, 3359–3369.

Dyke, A.S., Prest, V.K., 1987. Late Wisconsinan and Holocene Retreat of the Laurentide Ice Sheet. Scale 1:5,000,000. Map 1702A. In: Geological Survey of Canada, Ottawa, Ontario, Canada.

Dziewonski, A.M., Anderson, D.L., 1981. Preliminary reference Earth model. Physics of the Earth and Planetary Interiors 25 (4), 297–356.

England, J., 1985. The late Quaternary history of Hall Land, northwest Greenland. Canadian Journal of Earth Sciences 22(10), 1394-1408.

England, J., 1999. Coalescent Greenland and Innuitian ice during the Last Glacial Maximum: revising the Quaternary of the Canadian High Arctic. Quaternary Science Reviews 18 (3), 421–456.

England, J., 1999. Coalescent Greenland and Innuitian ice during the Last Glacial Maximum: revising the Quaternary of the Canadian High Arctic. Quaternary Science Reviews 18 (3), 421–456.

Evans, J., Dowdeswell, J.A., Grobe, H., Niessen, F., Stein, R., Hubberten, H.W., Whittington, R.J., 2002. Late Quaternary sedimentation in Kejser Franz Joseph Fjord and the continental margin of east Greenland. In: Dowdeswell, J.A., O'Cofaigh, C. (Eds.), Glacier-Influenced Sedimentation on High-Latitude Continental Margins. Geological Society of London, London, United Kingdom.

Evans, J., O´Cofaigh, C.A., Dowdeswell, J.A., Wadhams, P., 2009. Marine geophysical evidence for former expansion and flow of the Greenland Ice Sheet across the north-east Greenland continental shelf. Journal of Quaternary Science 24, 279–293.

Farrell, W.E., Clark, J.A., 1976. Postglacial sea-level. Geophysical Journal of the Royal Astronomical Society 46 (3), 647–667.

Fisher, D.A., Koerner, R.M., Reeh, N., 1995. Holocene climatic records from Agassiz Ice Caps, Ellesmere Island, NWT, Canada. The Holocene 5(1), 19-24.

Fleming, K., Lambeck, K., 2004. Constraints on the Greenland ice sheet since the Last Glacial Maximum from sea-level observations and glacial-rebound models. Quaternary Science Reviews 23 (9–10), 1053–1077.

Fredh, D., 2008. Holocene Relative Sea-level Changes in the Tasiusaq Area, Southern Greenland, with Focus on the Ta4 Basin. Examensarbeten i geologivid Lunds universitet, (221).

Fredskild, B., 1972. Palynological evidence for Holocene climatic changes in Greenland. In Vasari, Y., Hyvarinen, H., and Hicks, S. (eds.), Climatic Changes in Arctic Areas During the Last Ten Thousand Years, Acta Universitatis Ouluensis Series. A., No. 3, Geol. No. 1: 277-305.

Fredskild, B., 1983. The Holocene vegetational development of the Godtha°bsfjord area, West Greenland. Meddelelser om Grønland Geoscience 10, 28.

Fredskild, B., 1985. The Holocene vegetational development of Tugtuligssuaq and Qeqertat, Northwest Greenland. Meddelelser om Grønland Geoscience 14, 20.

Funder, S., 1987. Quaternary Geology and Landforms of the Coast of Jameson Land, East Greenland. In: Geological Survey of Greenland, Copenhagen (map sheet).

Funder, S., Abrahamsen, N., 1988. Palynology in a polar desert, eastern north Greenland. Boreas 17 (2), 195–207.

Funder, S., 1989. Quaternary geology of the ice-free areas and adjacent shelves of Greenland. In: Fulton, R.J. (Ed.), Quaternary Geology of Canada and Greenland. Geological Survey of Canada, pp. 741–792.

Funder, S. 1990. Late Quaternary stratigraphy and glaciology in the Thule area, Northwest Greenland (22). Kommissionen for videnskabelige undersøgelser i Grønland.

Funder, S., Hansen, L., 1996. The Greenland ice sheet – a model for its culmination and decay during and after the Last Glacial Maximum. Bulletin of the Geological Society of Denmark 42, 137–152.

Funder, S., Hjort, C., Landvik, J.Y., Nam, S.I., Reeh, N., Stein, R., 1998. History of a stable ice margin east Greenland during the Middle and Upper Pleistocene. Quaternary Science Reviews 17 (1–3), 77–123.

Funder, S., Jennings, A., Kelly, M., 2004. Middle and Late Quaternary glacial limits in Greenland. In: Ehlers, J., Gibbard, P. (Eds.), Quaternary Glaciations. Extent and Chronology II. Elsevier, Amsterdam, pp. 425–430.

Funder, S., Goosse, Hugues, Jepsen, H., Kaas, E., Kjaer, K.H., Korsgaard, N.J., Larsen, N.K., Linderson, H., Lysa, A., Moller, P., Olsen, J., Willerslev, E., 2011. A 10,000-year record of arctic ocean sea-ice variability – view from the beach. Science 333 (6043), 747-750.

Funder, S., Kjeldsen, K.K., Kjaer, K.H., O'Cofaigh, C., 2011. The Greenland ice sheet during the past 300,000 years: A review. In: Ehlers, J., Gibbard, P.L., Hughes, P.D. (Eds.), Quaternary Glaciations. Extent and Chronology. Elsevier, Amsterdam, Developments in Quaternary Science 15, 699-713.

Gillet-Chaulet, F., Gagliardini, O., Seddik, H., Nodet, M., Durand, G., Ritz, C., Zwinger, T., Greve, R., Vaughan. D.G., 2012. Greenland Ice Sheet contribution to sea-level rise from a new-generation ice-sheet model. The Cryosphere 6, 1561-1576.

Glen, J.W., 1955. The creep of polycrystalline ice. Proceedings of the Royal Society of London Series A, 228 (1175), 519-538.

Grachev, A.M., Severinghaus, J.P., 2005. A revised þ10_ 4 degrees C magnitude of the abrupt change in Greenland temperature at the Younger Dryas termination using published GISP2 gas isotope data and air thermal diffusion constants. Quaternary Science Reviews 24 (5–6), 513–519.

Håkansson, L., Briner, J., Alexanderson, H., Aldahan, A., Possnert, G., 2007b. Be-10 ages from central east Greenland constrain the extent of the Greenland ice sheet during the Last Glacial Maximum. Quaternary Science Reviews 26 (19–21), 2316–2321.

Håkansson, L., Alexanderson, H., Hjort, C., Mo¨ller, P., Briner, J.P., Aldahan, A., Possnert, G., 2009. Late Pleistocene glacial history of Jameson Land, central East Greenland, derived from cosmogenic 10Be and 26Al exposure dating. Boreas 38, 244–260.

Hall, B., Baroni, C., Denton, G., Kelly, M.A., Lowell, T., 2008. Relative sea-level change, Kjove Land, Scoresby Sund, East Greenland: implications for seasonality in Younger Dryas time. Quaternary Science Reviews 27, 2283–2291.

Hall, B., Baroni, C., Denton, G., 2010. Relative sea-level changes, Schuchert Dal, East Greenland, with implications for ice extent in late-glacial and Holocene times. Quaternary Science Reviews 29, 3370–3378.

Hjort, C., Funder, S., 1974. The subfossil occurrence of Mytilus edulis L. in central East Greenland. Boreas. 3 (1), 23-33.

Hjort, C., 1979. Glaciation in northern East Greenland during the late Weichselian and Early Flandrian. Boreas. 8 (3), 281-296.

Hjort, C., 1981. A glacial chronology for northern East Greenland. Boreas, 10 (3), 259-274.

Hjort, C., 1997. Glaciation, climate history, changing marine levels and the evolution of the northeast Water Polynya. Journal of Marine Systems 10 (1–4), 23–33.

Holland, D.M., Thomas, R.H., deYoung, B., Ribergaard, M.H., Lyberth. B., 2008. Acceleration of Jakobshavn Isbrae triggered by warm subsurface ocean waters. Nature Geoscience, 1 (10), 659-664.

Hutter, K., 1983. Theoretical Glaciology: Material Science of Ice and the Mechanics of Glaciers and Ice Sheets. Kluwer Academic, Norwell, Massachusetts.

Huybrechts, P., 1996. Basal temperature conditions of the Greenland ice sheet during the glacial cycles. Annals of Glaciology 23, 226–236.

Huybrechts, P., de Wolde, J., 1999. The dynamic response of the Greenland andAntarctic ice sheets to multiple-century climatic warming. Journal of Climate 12 (8), 2169–2188.

Huybrechts, P., 2002. Sea-level changes at the LGM from ice-dynamic reconstructions of the Greenland and Antarctic ice sheets during the glacial cycles. Quaternary Science Reviews 21 (1–3), 203–231.

Ingolfsson, O., Frich, P., Funder, S., Humlum, O., 1990. Paleoclimatic implications of an early Holocene glacier advance on Disko-Island, west Greenland. Boreas 19 (4), 297–311.

Imbrie, J.Z., Hays, J.D., Martinson, D.G., MacIntyre, A., Mix, A.C., Morley, J.J., Pisias, N.G., Prell, W.L., Shackleton, N.J., 1984. The orbital theory of Pleistocene climate: support from a revised chronology of the marine d18O record. In: Berger, A., Imbrie, J.Z., Hays, J.D., Kukla, G., Saltzman, B. (Eds.). Milankovitch and Climate. D. Reidel, Dordrecht, pp. 269–305.

Jakobsen, B.H., Fredskild, B., Pedersen, J.B.T., 2008. Holocene changes in climate and vegetation in the Ammassalik area, East Greenland, recorded in lake sediments and soil profiles. Danish Journal of Geography 108, 21–50.

Janssens, I., Huybrechts, P., 2000. The treatment of meltwater retention in massbalance parameterizations of the Greenland ice sheet. Annals of Glaciology 31, 133–140.

Jennings, A.E., Hald, M., Smith, M., Andrews, J.T., 2006. Freshwater forcing from the Greenland ice sheet during the Younger Dryas: evidence from southeastern Greenland shelf cores. Quaternary Science Reviews 25 (3–4), 282–298.

Johnsen, S.J., Clausen, H.B., Dansgaard, W., Gundestrup, N.S.,Hansson, M., Jonsson, P., et al., 1992. A ‘deep’ ice core from East Greenland. Meddelelser om Grønland. Geoscience 29, 22 pp.

Kaufman, D.S., Ager, T.A., Anderson, N.J., Anderson, P.M., Andrews, J.T., Bartlein, P.J., Brubaker, L.B., Coats, L.L., Cwynar, L.C., Duvall, M.L., Dyke, A.S., Edwards, M.E., Eisner, W.R., Gajewski, K., Geirsdottir, A., Hu, F.S., Jennings, A.E., Kaplan, M.R., Kerwin, M.N., Lozhkin, A.V., MacDonald, G.M., Miller, G.H., Mock, C.J., Oswald, W.W., Otto-Bliesner, B.L., Porinchu, D.F., Ruhland, K., Smol, J.P., Steig, E.J., Wolfe, B.B., 2004. Holocene thermal maximum in the western Arctic (0–180 degrees W). Quaternary Science Reviews 23 (5–6), 529–560.

Kelly, M., 1980. The status of the neoglacial in western Greenland. Rapport Grønlands Geologiske Undersøgelse 96, 24.

Kelly, M., Bennike, O., 1992. Quaternary geology of western and central North Greenland. Rapport Grønlands Geologiske Undersøgelse 153, 34.

Kelly, M., Funder, S., Houmark-Nielsen, M., Knudsen, K.L., Kronborg, C., Landvik, J.Y., Sorby, L., 1999. Quaternary glacial and marine environmental history of north-west Greenland: a review and reappraisal. Quaternary Science Reviews 18, 373–392.

Kelly, M.A., Lowell, T.V., 2009. Fluctuations of local glaciers in Greenlandduring latest Pleistocene and Holocene time. Quaternary Science Reviews 28, 2088–2106.

Kendall, R.A., Mitroviva, J.X., Milne, G.A., 2005. On post-glacial sea level: II. Numerical formulation and comparative results on spherically symmetric models. Geophysical Journal International 161 (3), 679–706.

Khan, S.A., Wahr, J., Leuliette, E., van Dam, T., Larson, K.M., Francis, O., 2008. Geodetic measurements of postglacial adjustments in Greenland. Journal of Geophysical Research – Solid Earth 113, B02402.

Klug, M., Bennike, O., Wagner, B., 2009. Repeated short-term bioproductivity changes in a coastal lake on Store Koldewey, northeast Greenland: an indicator of varying sea-ice coverage? Holocene 19, 653–663.

Koerner, R.M., Fisher, D.A., 1990. A record of Holocene summer climate from a Canadian High-Arctic Ice Core. Nature 343 (6259), 630–631.

Kuijpers, A., Troelstra, S.R., Prins, M.A., Linthout, K., Akhmetzhanov, A., Bouryak, S., Bachmann, M.F., Lassen, S., Rasmussen, S., Jensen, J.B., 2003. Late Quaternary sedimentary processes and ocean circulation changes at the southeast Greenland margin. Marine Geology 195 (1–4), 109–129.

Kuijpers, A., Dalhoff, F., Brandt, M.P., Hu¨mbs, P., Schot, T., Zotova, A., 2007. Giant iceberg plow marks at more than 1 km water depth offshore West Greenland. Marine Geology 246, 60–64.

Lambeck, K., Smither, C., Johnston, P. 1998. Sea-level change, glacial rebound and mantle viscosity for northern Europe. Geophysical Journal International, 134 (1), 102-144.

Landvik, J.Y., 1994. The last glaciation of Germania-land and adjacent areas, northeast Greenland. Journal of Quaternary Science 9 (1), 81–92.

Landvik, J. Y., Weidick, A., Hansen, A. 2001. The glacial history of the Hans Tausen Iskappe and the last glaciation of Peary Land, North Greenland. Meddelelser om Grønland Geoscience 39, 27-44.

Larour, E., Seroussi, H., Morlighem, M., Rignot, E. 2012. Continental scale, high order, high spatial resolution, ice sheet modeling using the Ice Sheet System Model (ISSM). Journal of Geophysical Research: Earth Surface (2003–2012), 117(F1).

Larsen, N.K., Kjær, K.H., Funder, S., Mo¨ller, P., van der Meer, J., Schomacker, A., Linge, H., Darby, D., 2010. Extensive ice shelf glaciation in northern Greenland during the Last Glacial Maximum. Quaternary Science Reviews 29, 3399–3414.

Larsen, N. K., Funder, S., Kjær, K. H., Kjeldsen, K. K., Knudsen, M. F., Linge, H., 2013. Rapid early Holocene ice retreat in West Greenland.Quaternary Science Reviews. In Press.

Lecavalier, B. S., Milne, G. A., Vinther, B. M., Fisher, D. A., Dyke, A. S., Simpson, M. J., 2013. Revised estimates of Greenland ice sheet thinning histories based on ice-core records. Quaternary Science Reviews, 63, 73-82.

Letre´ guilly,A., Reeh, N., Huybrechts, P.,1991. The Greenland ice-sheet through the Last Glacial interglacial cycle. Global and Planetary Change 90 (4), 385–394.

Lloyd, J.M., Park, L.A., Kuijpers, B., Moros, M., 2005. Early Holocene palaeoceanography and deglacial chronology of Disko Bugt, west Greenland. Quaternary Science Reviews 24 (14–15), 1741–1755.

Long, A.J., Roberts, D.H., Wright, M.R., 1999. Isolation basin stratigraphy and Holocene relative sea-level change on Arveprinsen Ejland, Disko Bugt, west Greenland. Journal of Quaternary Science 14 (4), 323–345.

Long, A.J., Roberts, D.H., 2002. A revised chronology for the ‘Fjord Stade’ moraine in Disko Bugt, west Greenland. Journal of Quaternary Science 17 (5–6), 561–579.

Long, A.J., Roberts, D.H., 2003. LateWeichselian deglacial history of Disko Bugt, west Greenland, and the dynamics of the Jakobshavns Isbrae ice stream. Boreas 32 (1), 208–226.

Long, A.J., Roberts, D.H., Rasch, M., 2003. New observations on the relative sea level and deglacial history of Greenland from Innaarsuit, Disko Bug. Quaternary Research 60 (2), 162–171.

Long, A.J., Roberts, D.H., Dawson, S., 2006. Early Holocene history of the west Greenland ice sheet and the GH-8.2 event. Quaternary Science Reviews 25 (9–10), 904–922.

Long, A.J., Roberts, D.H., Simpson, M.J.R., Dawson, S., Milne, G.A., Huybrechts, P., 2008a. Late Weichselian relative sea-level changes and ice sheet history in southeast Greenland. Earth and Planetary Science Letters 272 (1–2), 8–18.

Long, A., Woodroffe, S., Dawson, S., Roberts, D.H., Bryant, C., 2008b. Late Holocene relative sea level rise and the Neoglacial history of the Greenland ice sheet. Journal of Quaternary Science 24, 345-359.

Long, A.J., Woodroffe, S.A., Roberts, D.H., Dawson, S., 2011. Isolation basins, sea-level changes and the Holocene history of the Greenland ice sheet. Quaternary Science Reviews 30 (27-28), 3748-3768.

Milne, G. A., Davis, J. L., Mitrovica, J. X., Scherneck, H. G., Johansson, J. M., Vermeer, M., Koivula, H., 2001. Space-geodetic constraints on glacial isostatic adjustment in Fennoscandia. Science, 291 (5512), 2381-2385.

Milne, G. A., Mitrovica, J.X., 1998. Postglacial sea-level change on a rotating Earth. Geophysical Journal International, 133(1), 1-19.

Mitrovica, J.X., Milne, G.A., 2003. On post-glacial sea level: I. General theory. Geophysical Journal International 154 (2), 253–267.

Mitrovica, J.X., Wahr, J., Matsuyama, I., Paulson, A., 2005. The rotational stability of an ice-age earth. Geophysical Journal International, 161 (2), 491-506.

Möller, P., Larsen, N.K., Kjær, K., Funder, S., Schomacker, A., Linge, H., 2010. Early to middle Holocene valley glaciations on northernmost Greenland. Quaternary Science Reviews 29, 3379–3398.

Nam, S.I., Stein, R., Grobe, H., Hubberten, H., 1995. Late Quaternary glacial interglacial changes in sediment composition at the east Greenland continental margin and their paleoceanographic implications. Marine Geology 122 (3), 243–262.

Nghiem, S.V., Hall, D.K., Mote, T.L., Tedesco, M., Albert, M.R., Keegan, K., Shuman, C.A., DiGirolamo, N.E., Neumann, G., 2012. The extreme melt across the Greenland ice sheet in 2012. Geophysical Research Letters 39, L20502.

Nörgaard-Pedersen, N., Mikkelsen, N., 2009. 8000 year marine record of climate variability and fjord dynamics from Southern Greenland. Marine Geology 264, 177–189.

O'Cofaigh, C., Dowdeswell, J.A., Evans, J., Kenyon, N.H., Taylor, J., Mienert, A., Wilken, M., 2004. Timing and significance of glacially influenced mass-wasting in the submarine channels of the Greenland Basin. Marine Geology 207 (1–4), 39–54.

O'Cofaigh, C., Dowdeswell, J.A., Jennings, A.E., Hogan, K.A., Kilfeather, A., Hiemstra, J.F., Noormets, R., Evans, J., McCarthy, D.J., Andrews, J.T., Lloyd, J.M., Moros, M., 2012. An extensive and dynamic ice sheet on the west Greenland shelf during the last glacial cycle. Geology 41 (2), 219-222.

Pedersen, J. B. T., Kroon, A., & Jakobsen, B. H., 2011. Holocene sea-level reconstruction in the Young Sound region, Northeast Greenland. Journal of Quaternary Science 26 (2), 219-226.

Peltier,W.R., 1974. The impulse response of a Maxwell Earth. Reviews of Geophysics and Space Physics 12, 649–669.

Peltier, W.R., 2004. Global glacial isostasy and the surface of the ice-age earth: the ICE-5G (VM2) model and grace. Annual Review of Earth and Planetary Sciences 32, 111–149.

Peltier, W.R., Andrews, J.T., 1976. Glacial-Isostatic Adjustment—I. The Forward Problem. Geophysical Journal of the Royal Astronomical Society 46 (3), 605-646.

Pollard, D., DeConto, R.M., 2009. Modelling West Antarctic ice sheet growth and collapse through the past five million years. Nature, 458 (7236), 329-332.

Ren, J., Jiang, H., Seidenkrantz, M.S., Kuijpers, A., 2009. A diatom-based reconstruction of Early Holocene hydrographic and climatic change in a southwest Greenland fjord. Marine Micropaleontology 70, 166–176.

Rignot, E., Mouginot, J., 2012. Ice flow in Greenland for the International Polar Year 2008-2009. Geophysical Research Letters 39, L11501.

Roberts, D. H., Long, A. J., Schnabel, C., Davies, B. J., Xu, S., Simpson, M. J., & Huybrechts, P., 2009. Ice sheet extent and early deglacial history of the southwestern sector of the Greenland Ice Sheet. Quaternary Science Reviews 28 (25), 2760-2773.

Saito, F., Abe-Ouchi, A., Blatter, H., 2003. Effects of first-order stress gradients in an ice sheet evaluated by a three-dimensional thermomechanical coupled model. Annals of Glaciology 37, 166–172.

Schmidt, S., Wagner, B., Heiri, O., Klug, M., Bennike, O., Melles, M., 2010. Chironomids as indicators of the Holocene climatic and environmental history of two lakes in Northeast Greenland. Boreas 40, 116-130.

Seidenkrantz, M.-S., Roncaglia, L., Fischel, A., Heilmann-Clausen, C., Kuijpers, A., Moros, M., 2008. Variable North Atlantic climate seesaw patterns documented by a late Holocene marine record from Disko Bugt, West Greenland. Marine Micropaleontology 68, 66–83.

Shepherd, A., Ivins, E.R., Geruo, A., Barletta, V.R., Bentley, M.J., Bettadpur, S., Briggs, K.H., Bromwich, D.H., Forsberg, R., Galin, N., Horwath, M., Jacobs, S., Joughin,I., King, M.A., Lenaerts, J.T.M., Li, J., Ligtenberg, S.R.M., Luckman, A., Luthcke, S.B., McMillan, M., Meister, R., Milne, G.A., Mouginot, J., Muir, A., Nicolas, J.P., Paden, J., Payne, A.J., Pritchard, H., Rignot, E., Rott, H., Sørensen, L.S., Scambos, T.A., Scheuchl, B., Schrama, E.J.O., Smith, B., Sundal, A.V., van Angelen, J.H., van de Berg, W.J., van den Broeke, M.R., Vaughan, D.G., Velicogna, I., Wahr, J., Whitehouse, P.L., Wingham, D.J., Yi, D., Young, D., Zwally H.J., 2012. Science 338 (6111), 1183-1189

Simpson, M.J.R., Milne, G.A., Huybrechts, P., Long, A.J., 2009. Calibrating a glaciological model of the Greenland ice sheet from the Last Glacial Maximum to present-day using field observations of relative sea level and ice extent. Quaternary Science Reviews 28, 1631–1657.

Simpson, M.J.R., Wake, L., Milne, G.A., Huybrechts, P., 2011. The influence of decadal to millennial-scale ice mass changes on present-day vertical land motion in Greenland: Implications for the interpretation of GPS observations. Journal of Geophysical Research 116, B02406.

Sommerhoff, G., 1981. Geomorphologische Prozesse in der Labrador – und Imingersee. Ein Beitrag zur submarinen Geomorphologie einer subpolaren Meeresregion. Polarforschung 51, 175–191.

Sparrenbom, C.J., 2006. Constraining the Southern Part of the Greenland Ice Sheet since the Last Glacial Maximum from Relative Sea-Level Changes, Cosmogenic Dates and Glacial-Isostatic Adjustment Models. Ph.D. thesis. Centre for Geo- Biosphere Science, Lund University.

Sparrenbom, C.J., Bennike, O., Bjorck, S., Lambeck, K., 2006a. Relative sea-level changes since 15 000 cal. yr BP in the Nanortalik area, southern Greenland. Journal of Quaternary Science 21 (1), 29–48.

Sparrenbom, C.J., Bennike, O., Bjorck, S., Lambeck, K., 2006b. Holocene relative sealevel changes in the Qaqortoq area, southern Greenland. Boreas 35 (2), 171–187.

Steffensen, J.P., Andersen, K.K., Bigler, M., Clausen, H.B., Dahl-Jensen, D., Fischer, H., Goto-Azuma, K., Hansson, M., Johnsen, S.J., Jouzel, J., Masson-Delmotte, V., Popp, T., Rasmussen, S.O., Rothlisberger, R., Ruth, U., Stauffer, B., Siggaard-Andersen, M-L., Sveinbjornsdottir, A.E., Svensson, A., White, J.W.C., 2008. High-resolution Greenland ice core data show abrupt climate change happens in few years. Science 321, 680–684.

Stein, R., Nam, S., Grobe, H., Hubberten, H., 1996. Late Quaternary glacial history and short-termice-rafted debris fluctuations along the east Greenland Continental Margin. In: Andrews, et al., (Ed.), Late Quaternary Paleoceanography of the North Atlantic Margins, Geological Society
Special Publication, 111, 135–151.

Tarasov, L., Peltier, W.R., 2002. Greenland glacial history and local geodynamic consequences. Geophysical Journal International 150 (1), 198–229.

Tarasov, L., Dyke, A.S., Neal, R.M., Peltier, W.R., 2012. A data-calibrated distribution of deglacial chronologies for the North American ice complex from glaciological modeling. Earth and Planetary Science Letters 315-316, 30-40.

Ten Brink, N.W., Weidick, A., 1974. Greenland ice sheet history since the last glaciation. Quaternary Research 4, 429–440.

Trautman, M.A., Willis, E.H., 1963. Isotopes, Inc., radiocarbon measurements III. Radiocarbon 5, 62–79.

Van deWal, R.S.W.,1999. The importance of thermodynamics for modeling the volume of the Greenland ice sheet. Journal of Geophysical Research 104, 3887-3898.

Van den Berg, J., van de Wal, R.S.W., Oerlemans, J., 2006. Effects of spatial discretization in ice-sheet modelling using the shallow-ice approximation. Journal of Glaciology 52, 89–98.

Van Tatenhove, F.G.M., van der Meer, J.J.M., Huybrechts, P., 1995. Glacial–geological geomorphological research in west Greenland used to test an ice-sheet. Quaternary Research 44 (3), 317–327.

Van Tatenhove, F.G.M., van der Meer, J.J.M., Koster, E.A., 1996. Implications for deglaciation chronology from new AMS age determinations in central west Greenland. Quaternary Research 45 (3), 245–253.

Van Tatenhove, F. G., van der Meer, J. J., & Koster, E. A., 1996. Implications for deglaciation chronology from new AMS age determinations in central West Greenland. Quaternary Research, 45(3), 245-253.
Vinther, B.M., Buchardt, S.L., Clausen, H.B., Dahl-Jensen,D., Johnsen, S.J., Fisher, D.A., Koerner, R.M., Raynaud, D., Lipenkov, V., Andersen, K.K., Blunier, T., Rasmussen, S.O., Steffensen, J.P., Svensson, A.M., 2009. Holocene thinning of the Greenland ice sheet. Nature 461, 385–388.

Wagner, B., Bennike, O., Cremer, H., Klug, M., 2010. Late Quaternary history of the Kap Mackenzie area, northeast Greenland. Boreas 39, 492–504.

Walker, M., Johnsen, S., Rasmussen, S.O., Popp, T., Steffensen, J-P., Gibbard, P., Hoek, W., Lowe, J., Andrews, J., Bjorck, S., Cwynar, L.C., Hughen, K., Kershaw, P., Kromer, B., Litt, T., Lowe, D.J., Nakagawa, T., Newnham, R., Schwander, J., 2009. Formal definition and dating of the GSSP (Global Stratotype Section and Point) for the base of the Holocene using the Greenland NGRIP ice core, and selected auxiliary records. Journal of Quaternary Science 24, 3–17.

Washburn, A.L., Stuiver, M., 1962. Radiocarbon-dated post-glacial deleveling in northeast Greenland and its implications. Arctic 15, 66–73.

Weidick, A., 1972. Holocene shore-lines and glacial stages in Greenland – an attempt at correlation. Rapport Grønlands Geologiske Undersøgelse 41, 1–39.

Weidick, A., 1976. Glaciation and the Quaternary of Greenland. In: Escher, A., Watt, W.S. (Eds.), Geology of Greenland. Geological Survey of Greenland, Copenhagen, pp. 405–458.

Weidick, A., Oerter, H., Reeh, N., Thomsen, H.H., Thorning, L.S., 1990. The recession of the Inland Ice margin during the Holocene climatic optimum in the Jakobshavn Isfjord area of West Greenland. Palaeogeography, Palaeoclimatology, Palaeoecology 82, 389–399.

Weidick, A., Kelly, M., Bennike, O., 2004. Late Quaternary development of the southern sector of the Greenland ice sheet, with particular reference to the Qassimiut lobe. Boreas 33 (4), 284–299.

Weidick, A., Bennike, O., 2007. Quaternary glaciation history and glaciology of Jakobshavn Isbrae and the Disko Bugt region, west Greenland: a review. Geological Survey of Denmark and Greenland Bulletin 14.

Wilken, M., Mienert, J., 2006. Submarine glacigenic debris flows, deep-sea channels and past ice-stream behaviour of the east Greenland continental margin. Quaternary Science Reviews 25 (7–8), 784–810.

Winkelmann, D., Jokat, W., Jensen, L., Schenke, H-W., 2010. Submarine end moraines on the continental shelf off NE Greenland—implications for Lateglacial dynamics. Quaternary Science Review 29, 1069–1077.

Whitehouse, P.L., Bentley, M.J., Le Brocq, A.M., 2012. A deglacial model for Antarctica: geological constraints and glaciological modelling as a basis for a new model of Antarctic glacial isostatic adjustment. Quaternary Science Reviews 32, 1-24.

Woodroffe, S.A., Long, A.J., Lecavalier, B.L., Milne, G.A., 2013. Using relative sea-level data to constrain the deglacial and Holocene history of southern Greenland. Quaternary Science Reviews xxx, 1-12.

Yokoyama, Y., Lambeck, K., De Dekker, P., Johnston, P., Fifield, L.K., 2000. Timing of the Last Glacial Maximum from observed sea-level minima. Nature 406 (6797), 713–716.

Zreda, M., England, J., Phillips, F., Elmore, D., Sharma, P., 1999. Unblocking of the Nares Strait by Greenland and Ellesmere ice-sheet retreat 10,000 years ago. Nature 398 (6723), 139–142.

Zweck, C., Huybrechts, P., 2003. Modeling the marine extent of northern Hemisphere ice sheets during the last glacial cycle. Annals of Glaciology 37,173–180.

Zweck, C., Huybrechts, P., 2005. Northern hemisphere ice sheet modeling of the last glacial cycle and glaciological sensitivity. Journal of Geophysical Research 110, D07103.

3.9 SUPPLEMENTARY MATERIAL

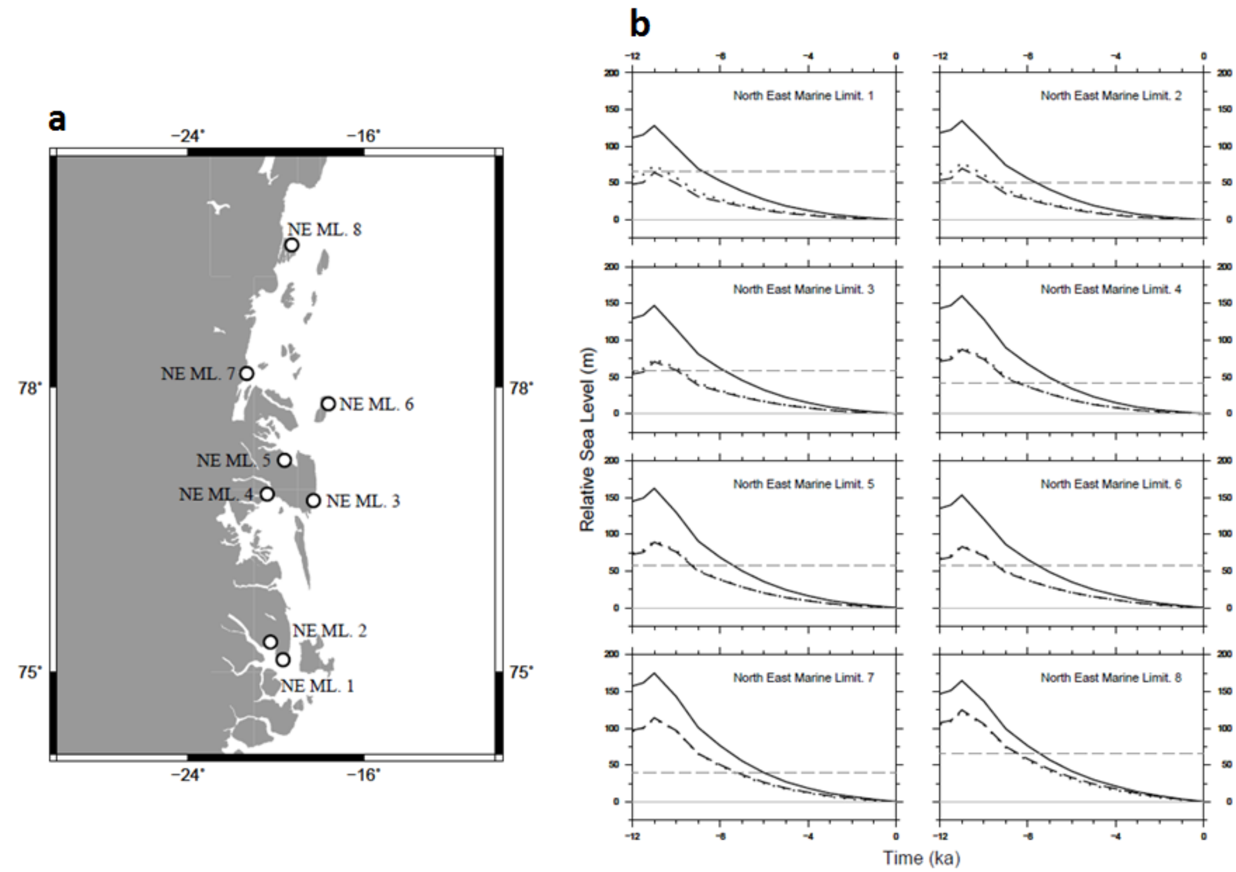

Figure 3.S1 (a) The distribution of marine limit observations along northeast Greenland which can indirectly constrain the LGM ice extent by bounding the amplitude of sea-level change. The marine limit is shown by the grey horizontal line in (b) along with the optimal RSL predictions from the Huy2 model (black curve), the Funder et al. (2011) LGM extent (dashed black curve), and the O'Cofaigh et al. (2012) revised extent (dotted black curve). These results are based on the optimum Earth model for Huy2 (LT120, UMV0.5, LMV1).

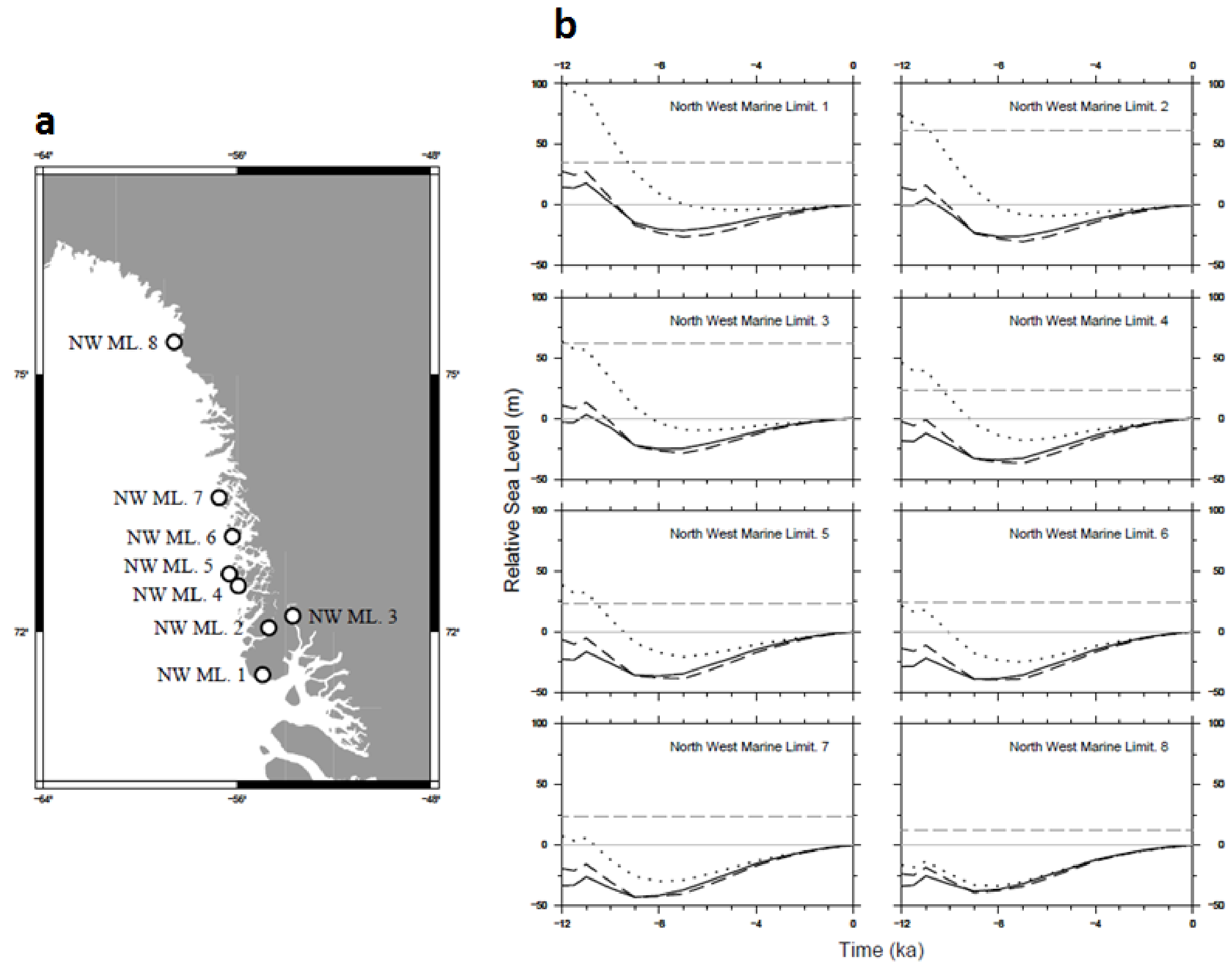

Figure 3.S2 (a) The distribution of ML observations along northwest Greenland which can indirectly constrain the LGM ice extent by bounding the amplitude of sea-level change. The marine limit is shown by the grey horizontal lines in (b) along with the optimal RSL predictions from the Huy2 model (black curve), the Funder et al. (2011) LGM extent (dashed black curve), and the O'Cofaigh et al. (2012) revised extent (dotted black curve).

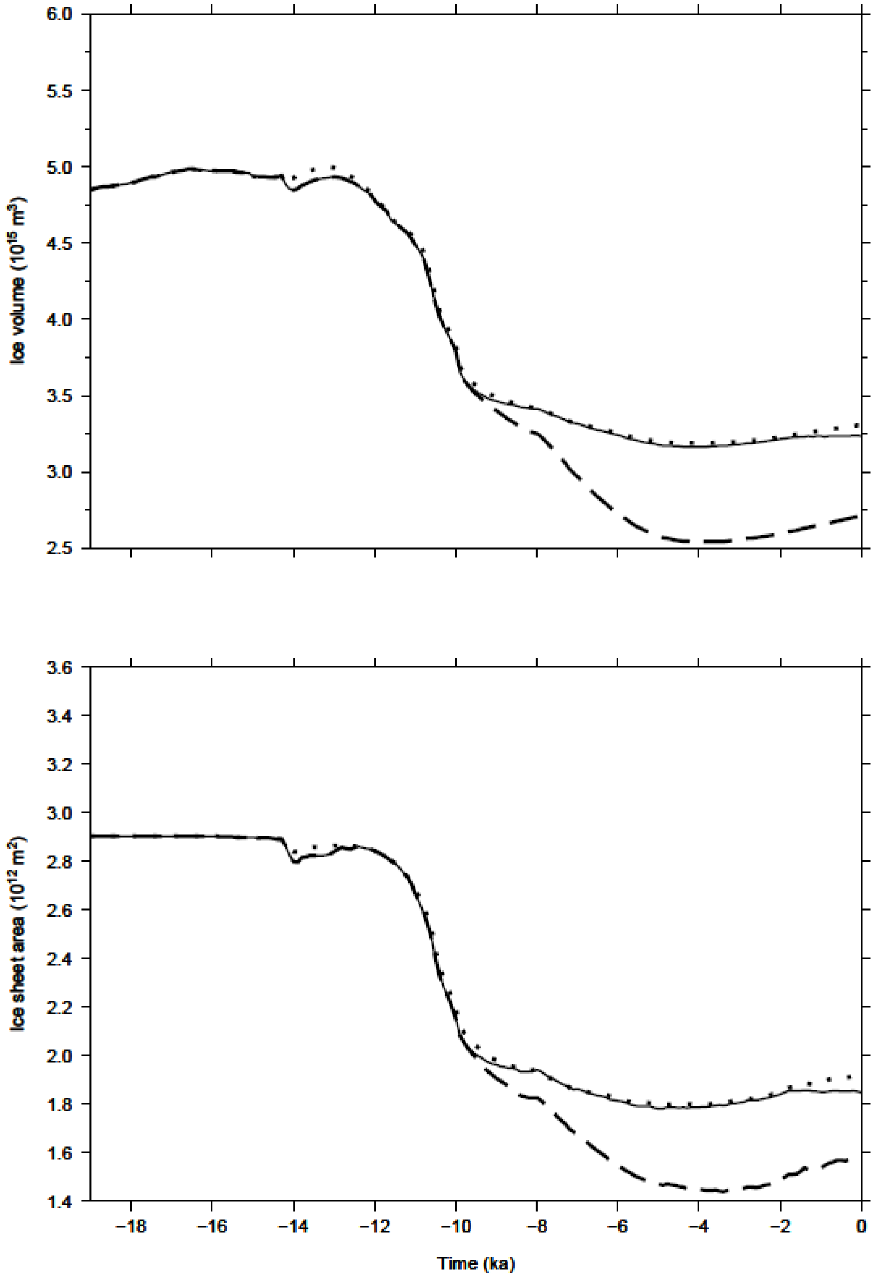

Figure 3.S3 Predictions of ice sheet volume (top) and area (bottom) for the original Huy2 model with its DDF tuning of minus 30% (black curves) and with zero scaling (dashed black curves) which produces a massive volume and extent deficit. The revised PDD algorithm incorporated in this study is shown by the dotted curves which reached PD geometries without the unphysical tuning of the DDFs.

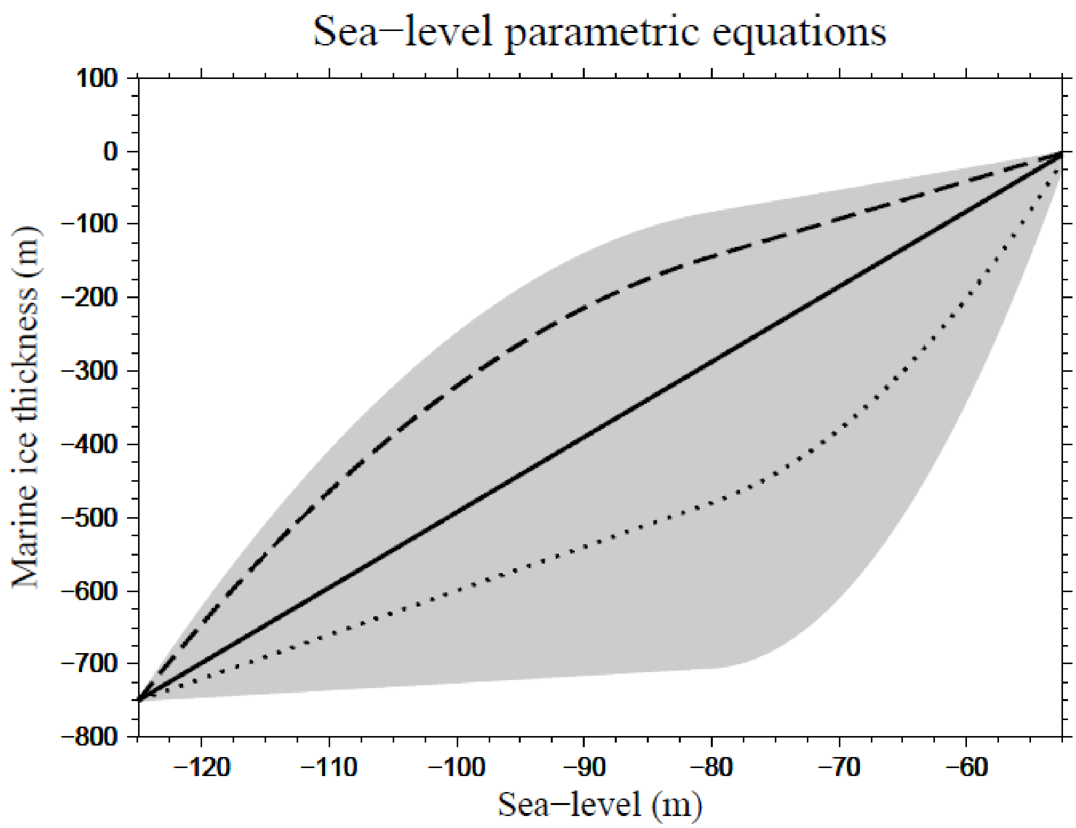

Figure 3.S4 The sea-level forcing is dealt with using parametric equations to define at what depth ice can remain grounded. In Simpson et al. (2009), a total of three different SLFs were investigated that resulted in early (dashed curve), intermediate (black line), and late (dotted curve) retreat histories. In this study we not only vary this parameterization spatially across Greenland but also sample a continuous range of parametric equations (grey envelop) which share the same characteristic quadratic form as those used by Simpson et al. (2009).

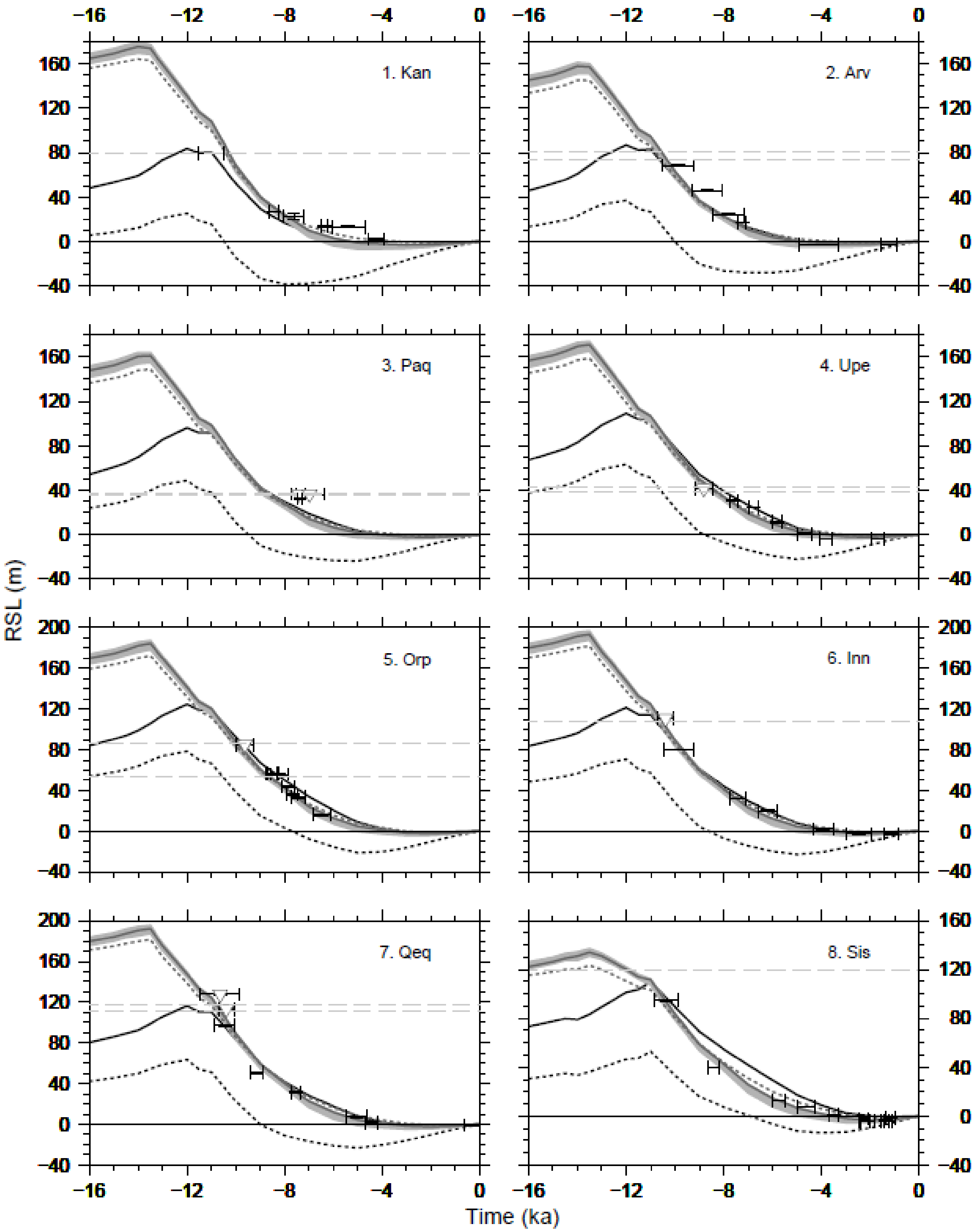
1. Kan
2. Arv
3. Paq
4. Upe
5. Orp
6. Inn
7. Qeq
8. Sis
RSL (m)
Time (ka)

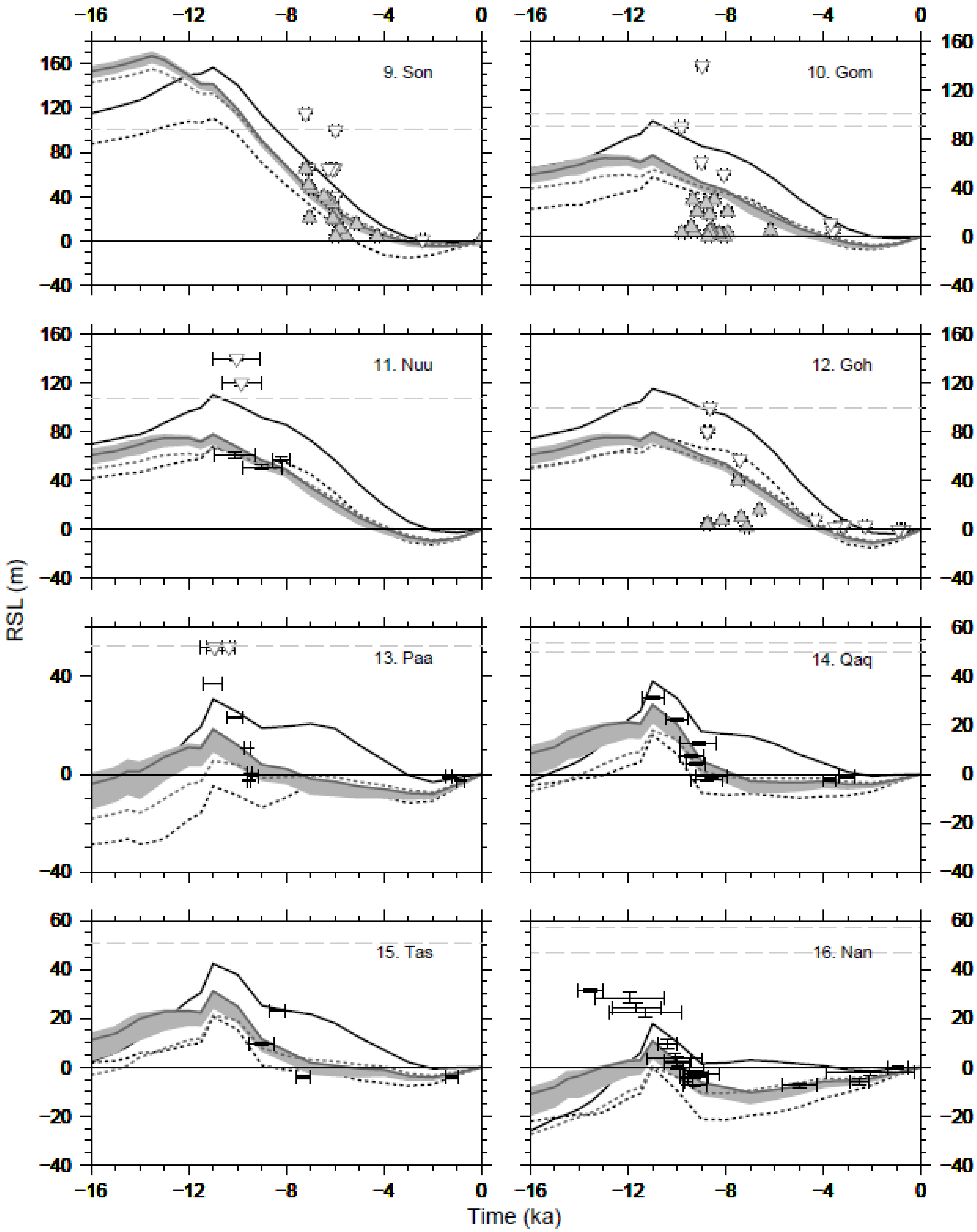
9. Son
10. Gom
11. Nuu
12. Goh
13. Paa
14. Qaq
15. Tas
16. Nan
RSL (m)
Time (ka)

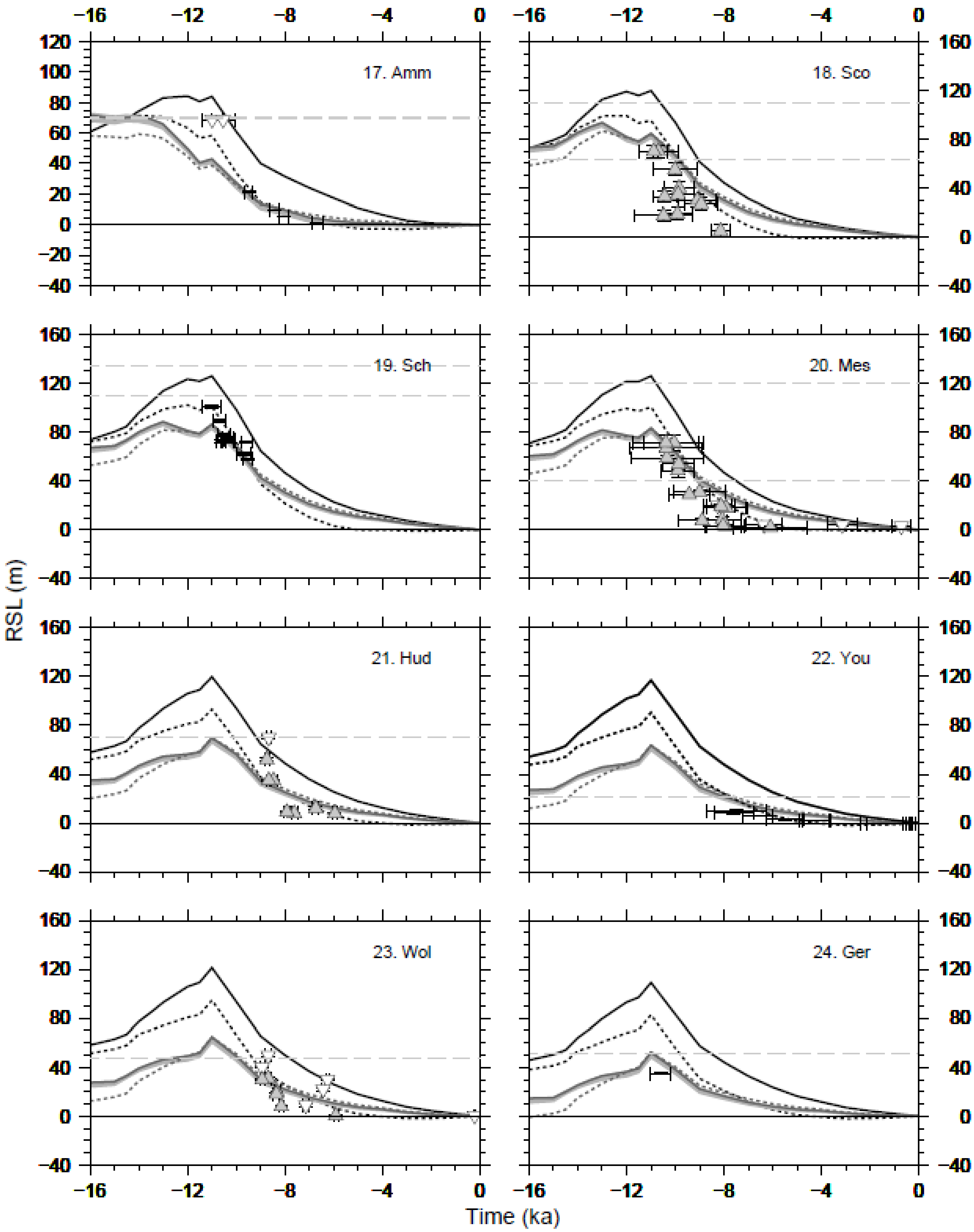
17. Amm
18. Sco
19. Sch
20. Mes
21. Hud
22. You
23. Wol
24. Ger
RSL (m)
Time (ka)

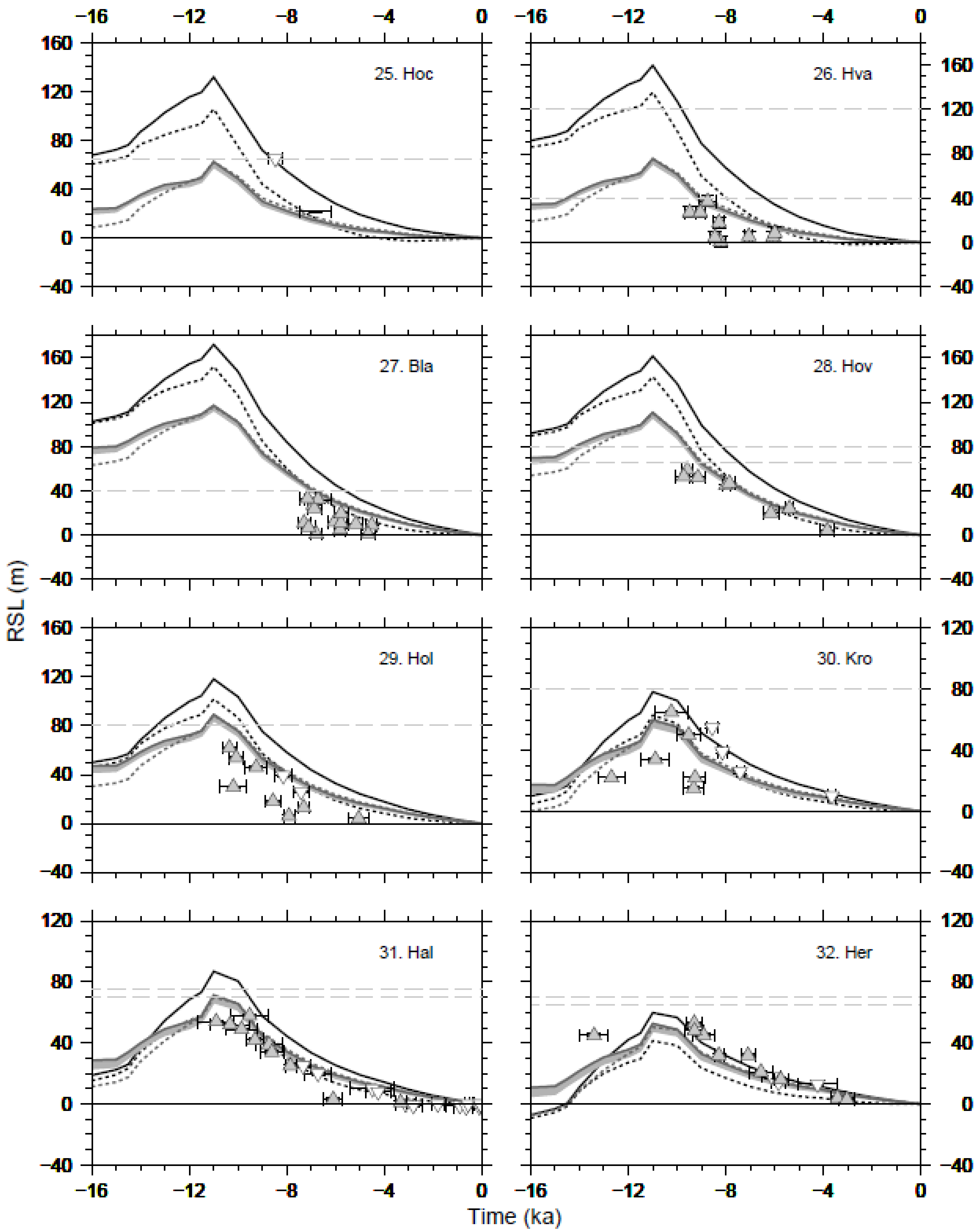
25. Hoc
26. Hva
27. Bla
28. Hov
29. Hol
30. Kro
31. Hal
32. Her
RSL (m)
Time (ka)

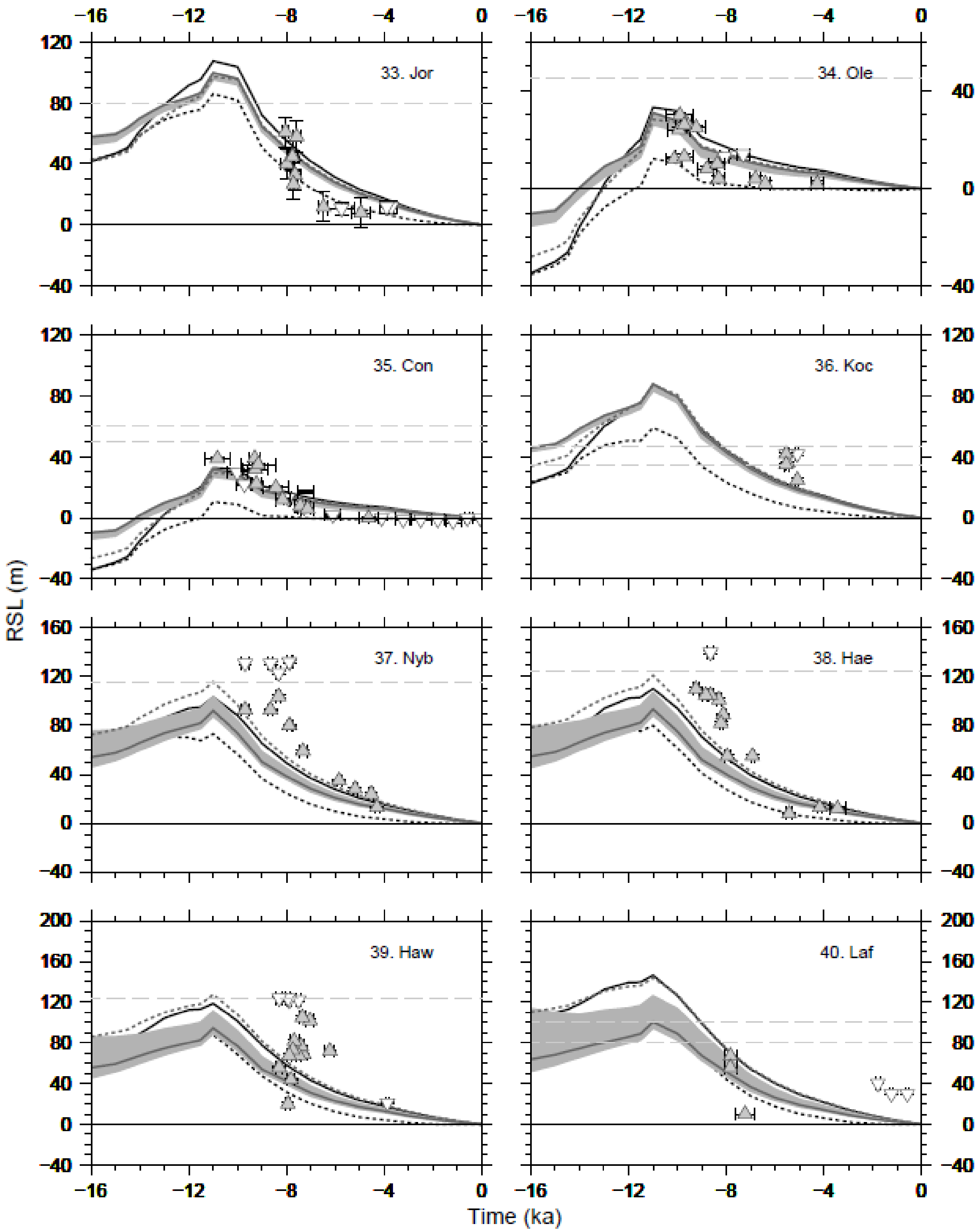
33. Jor
34. Ole
35. Con
36. Koc
37. Nyb
38. Hae
39. Haw
40. Laf
RSL (m)
Time (ka)
−16
−12
−8
−4
0
120
80
40
0
−40
160
200

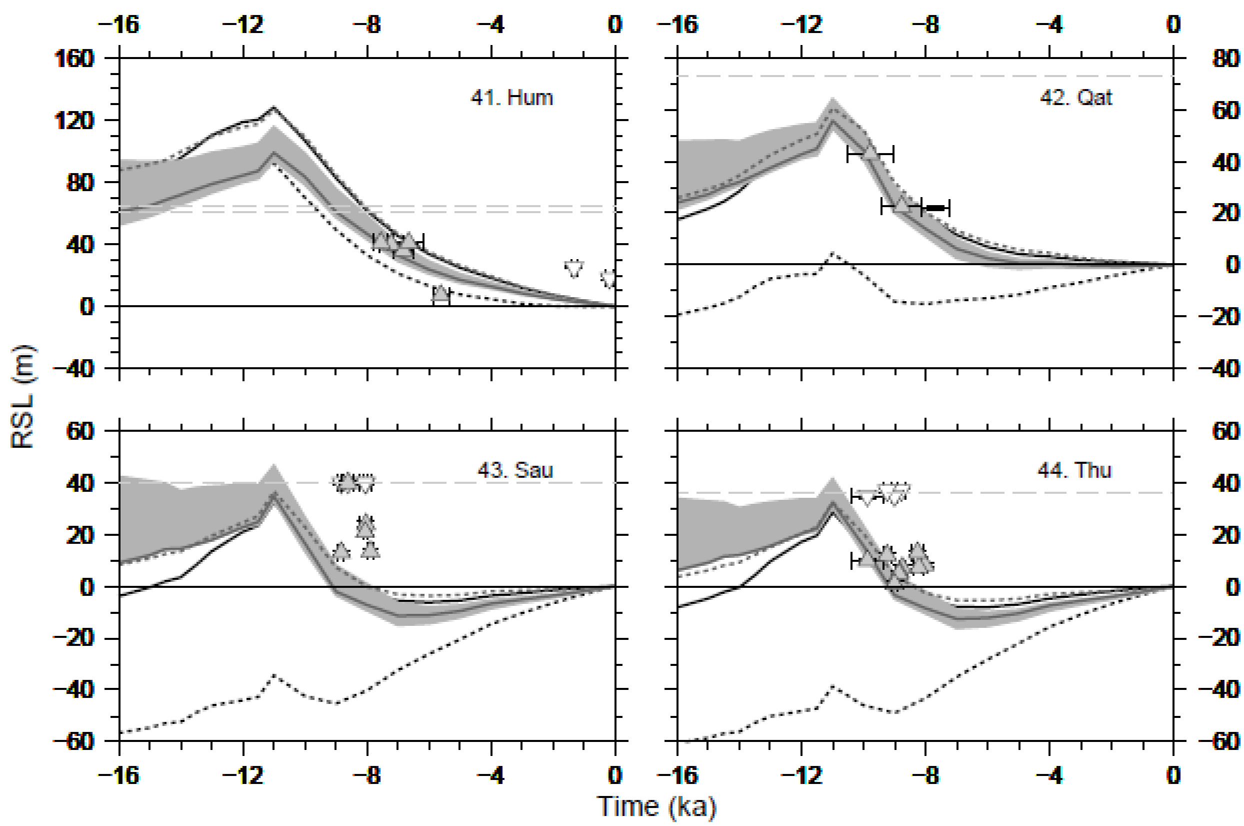

Figure 3.S5 RSL predictions generated by the Huy2 reconstruction with its optimal Earth model (black curves) and alternate Eastern Earth model (dashed black curves). The Huy3 RSL predictions are also shown based on its optimal Earth model (LT120, UMV0.5, LMV2; dark grey curves) and the light grey envelop around these results represents the range in predictions when a series of alternate NAIC components from a high-variance subset were adopted within the non-Greenland ice model (Tarasov et al., 2012). The dark grey dashed curve represents the Huy3 model predictions as in the non-dashed counterpart except with the original ICE-5G NAIC component in place. Sea-level index points are shown as crosses with both time and height error bars. Lower limiting dates are denoted by grey upward pointing triangles, while upper limiting dates are shown by white downward pointing triangles. The black horizontal line highlights present day sea-level. The grey dashed horizontal line represents the marine limit which marks the highest point reached by sea-level during ice-free conditions at each location (site 1-8, 9-16, 17-24, 25-32, 33-40, 41-44 constitute Fig. 3.4 a,b,c,d,e, and f, respectively).

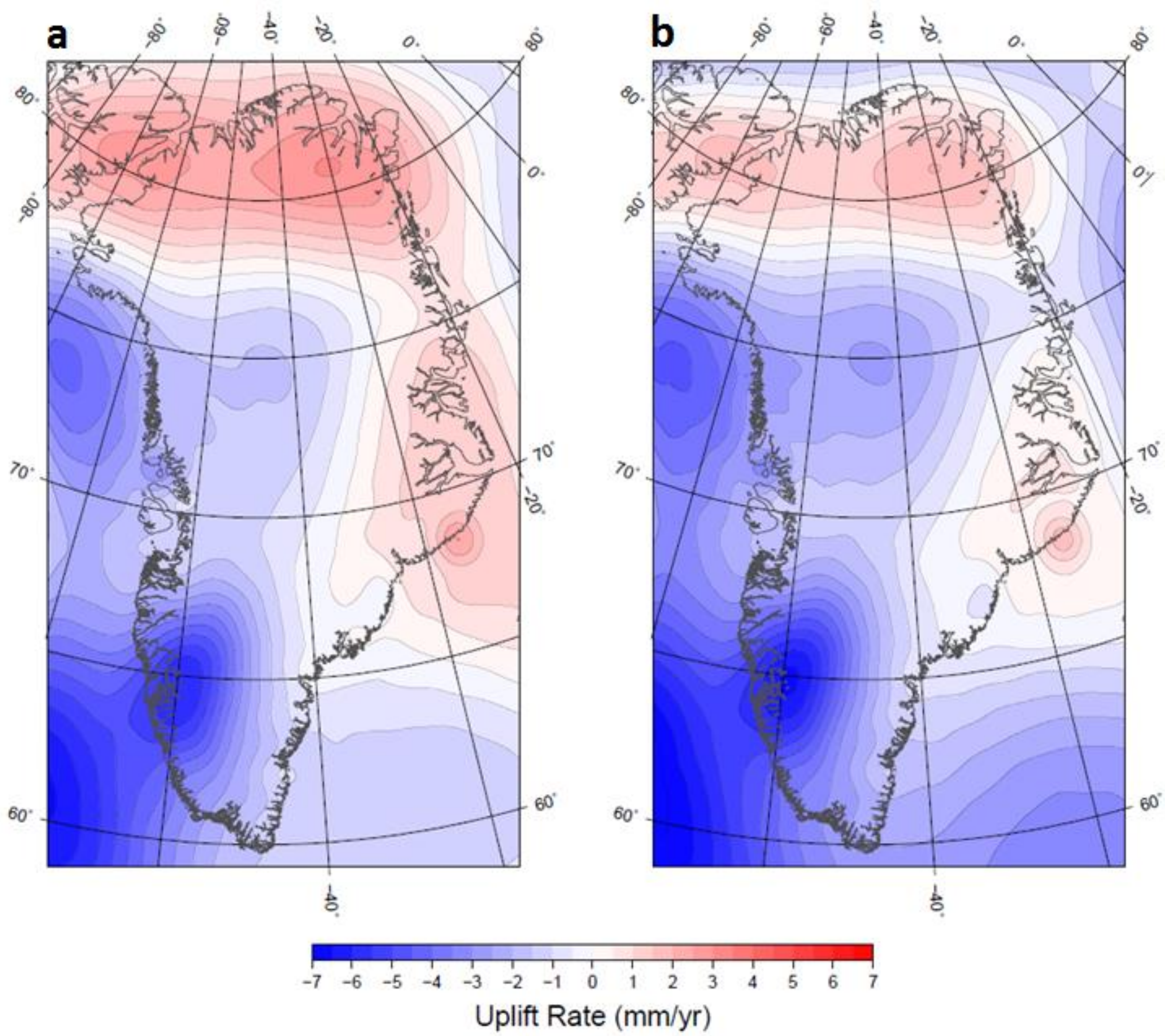

Figure 3.S6 The (a) upper and (b) lower bound present-day uplift rates given uncertainties in Earth structure generated using the 95% confidence interval of the χ^2 analysis and the Huy3 ice model reconstruction.

4. CONCLUSIONS

The research presented in this thesis made use of glaciological, GIA and RSL models to investigate the evolution of the Greenland ice sheet during the more recent deglaciation (LGM to present). This final section reviews the methodology applied in this project, specifically with regard to producing the Huy3 model. Moreover, I revisit the motivations and implications of this work and summarize the main findings. Finally, I conclude by discussing possible avenues of future research.

4.1 OVERVIEW

The goal of this research was to improve our understanding of the Greenland ice sheet and how it responds to climate change. The first research project involved deriving the thinning of the Greenland ice sheet using ice-core records collected across Greenland and the Canadian Arctic (Section 2). This work was conducted by isolating background δ^{18}O values at the Renland and Agassiz ice cap (near the GrIS). This was achieved by the calibration of a GIA model to sea-level observations to yield the deformation of the solid Earth due to changes in ice and ocean loading. The subsequent uplift predictions were applied to correct the ice-core δ^{18}O records from the Renland and Agassiz ice caps for elevation changes and thus infer a background δ^{18}O (temperature) profile across Greenland. This was then used to isolate elevation changes from Greenland ice-core δ^{18}O records, which show thinning of the GrIS at the GRIP, NGRIP, DYE-3, and Camp Century ice-core sites in response to climate change during the Holocene. These results are incorporated in the main project of this thesis which aimed to better constrain the evolution of the ice sheet.

The bulk of this thesis focuses on reconstructing the deglacial evolution of the GrIS using inferences of past ice extent and RSL. This is performed by building upon the work initially conducted by Simpson et al. (2009). The adopted methodology involves calibrating, in series, a glaciological model with a GIA and RSL model. This study extended the Simpson et al. work in several respects: (1) a larger observational database was compiled to constrain the model; (2) the glaciological model was modified through its ensemble parameters to explore the parameter space; (3) a sensitivity analysis of key model parameters was conducted to target those that were effective at improving the fit to our constraint database; (4) model developments were performed on the glaciological model, specifically to the climate and sea-level forcing component which further improved the fits to the observations.

A total of ~250,000 sets of model predictions were directly compared to the observational database to assess the model quality. To increase our level of confidence in our optimal GrIS reconstruction (Huy3), uncertainties with regards to the Earth structure and non-local ice were explicitly evaluated. As for the remaining data-model discrepancies, they can attributed to weaknesses with the glaciological model in terms of resolving sub-grid features and processes, and the Earth model component of the GIA model for not being able to incorporate lateral Earth structure.

4.2 GRIS DEGLACIATION

During the deglaciation the world transitioned from glacial to interglacial conditions. However, this was punctuated by abrupt climate events and sea-level rise (see Figure 4.1). The response of the GrIS to climate change, particular to warmer climate relative to present and abrupt events, sheds light on the behaviour of the ice sheet to contemporary warming. As suggested by the research conducted in this thesis, the GrIS underwent large-scale changes during the deglaciation.

Our new model, termed Huy3, fits the majority of ice extent and RSL observations and is characterised by a number of defining features as shown in Figure 4.1. Initially, the ice sheet responded to ocean forcing, particularly by the calving of icebergs from the marine based ice. As the ice sheet receded and became predominantly land-based by ~10 ka BP, mass balance was dictated by surface melting. For instance, during the LGM, the ice sheet had an excess of 4.5 m ice-equivalent SL (IESL) and reached a maximum volume of 5.0 m IESL at 16.5 ka BP, which is larger than previously thought [Clark & Mix, 2002; Tarasov & Peltier, 2002; Fleming & Lambeck, 2004; Simpson et al., 2009]. The ice sheet retreated from the continental shelf to the present coast lines through a succession of spatially varying retreats and advances. Southwest and Southeast Greenland began to retreat from the shelf by ~16 to

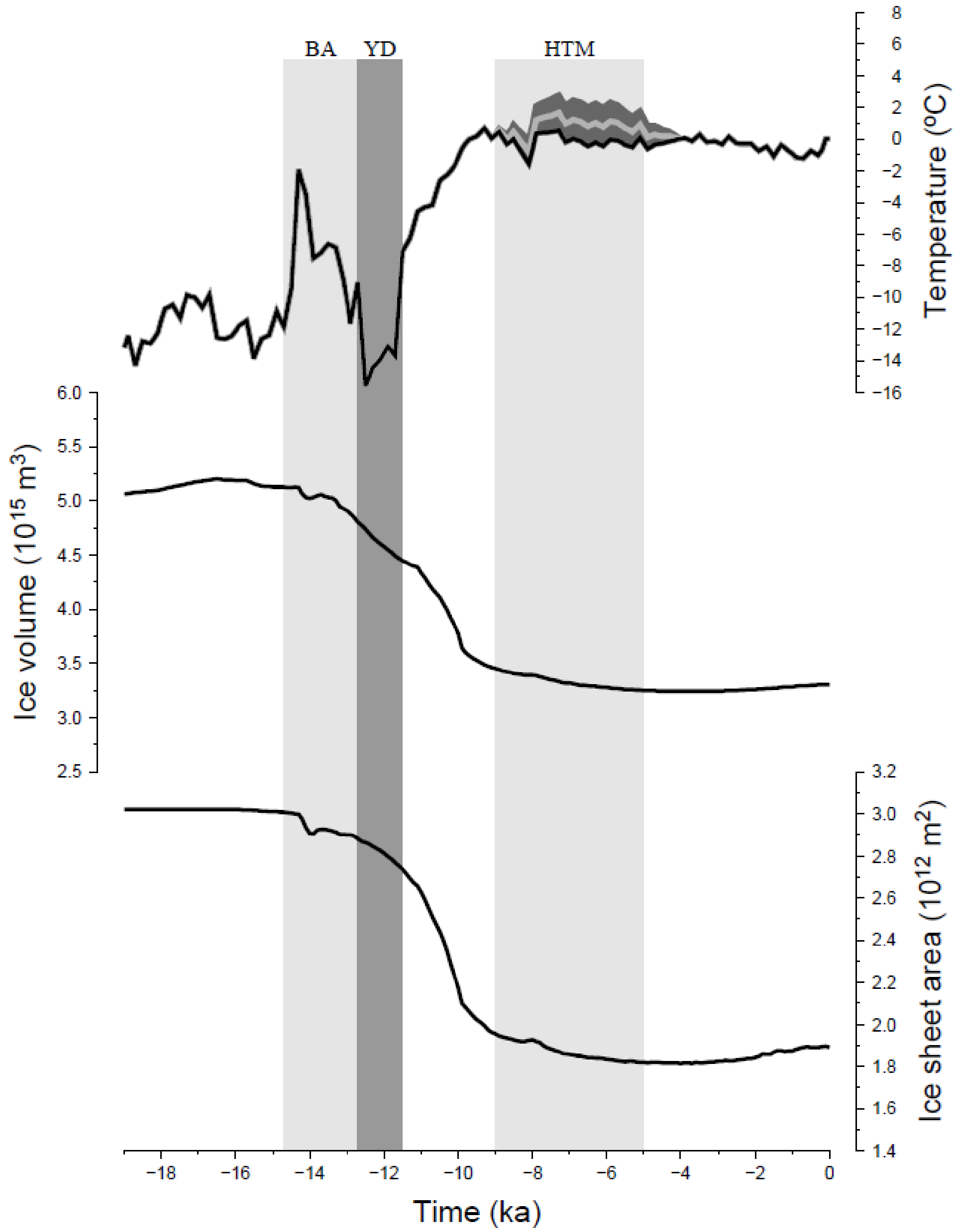

Figure 4.1 From top to bottom we have the GRIP temperature record prescribed in the glaciological model as represented by the black curve including the envelop of values considered for the HTM temperature forcing (dark grey envelop). The light grey curve indicates the optimal forcing used in the Huy3 reconstruction. The following climatic events are annotated: Bolling-Allerod (BA, ~14 ka BP), Younger Dryas (YD, ~12 ka BP), and Holocene Thermal Maximum (HTM, 9-5 ka BP). The Huy3 model predictions for ice sheet volume and extent are illustrated in the middle and bottom frame by the black curve.

14 ka BP, substantially responding to the Bolling-Allerod warm event (14 ka BP); subsequently the Southern tip readvanced during the cold climatic event at ~12 ka BP (Younger Dryas). North Greenland retreated rapidly from the continental shelf (12-10 ka BP) upon the climatic recovery out of the Younger Dryas and into the current interglacial conditions. Shortly after the beginning of the Holocene at 11.7 ka BP, the ice sheet became land-based. During the HTM, temperatures across Greenland were higher than they are at present; therefore, the response of the GrIS to this past climate forcing is an analogue that can be used to inform and assess estimates of future GrIS mass balance. The Huy3 reconstruction responds most dramatically to the HTM in the southwest region of the ice sheet. Given that the model fits the majority of observations along West and South Greenland, there is high confidence that the large-scale response of the southwestern part of the GrIS to the HTM is accurately captured. The Greenland ice sheet retreated past its present-day southwest position by 40 to 60 km at 4 ka BP which produced a deficit volume of 0.17 m IESL relative to present, in response to the HTM warming of 1.6 ± 0.8 ^{o}C above pre-industrial levels [Kaufman et al., 2004]. During the HTM, the Greenland ice sheet was losing mass at a maximum rate of 103.7 Gt/a at 7.8 ka BP, which is 27% less than that inferred for the period 1992 to 2011 [Shepherd et al., 2012]. This defines a long term (millennial scale) sensitivity of the ice sheet than can be compared to results from studies that project future changes based on specified climate scenarios.

4.3 FUTURE WORK

4.3.1 PRESENT-DAY VERTICAL LAND MOTION

Geodetic satellite observations track ice surface and gravitational changes across Greenland. Prior to inferring contemporary mass balance for the ice sheet using these observations, it is first necessary to correct the data for the vertical motion of the solid Earth due to past ice sheet changes [Shepherd et al., 2012]. The isostatic response of the solid Earth to past changes in ice and ocean loading is understood through the relaxation of a visco-elastic Earth model. The Huy3 Greenland reconstruction is applied with our optimal Earth model to generate present-day uplift rates (Figure 4.2). The heavily data-calibrated

Huy3 model is the most sophisticated reconstruction of the GrIS over the deglaciation. By applying the Huy3 Greenland reconstruction with our optimal Earth model I generate present-day uplift rates across Greenland due to past changes in the ocean and ice loading with explicit error bars due to uncertainties in the Earth structure (Fig. 4.2). Given the magnitude of present-day uplift rates due to past changes, and the strong spatial variation in this signal, it is crucial to correct for this vertical land motion before interpreting the geodetic observations. In a follow-up study, the predicted present-day uplift rates are going to be applied to correct geodetic observations to more accurately estimate the contemporary mass loss of the GrIS.

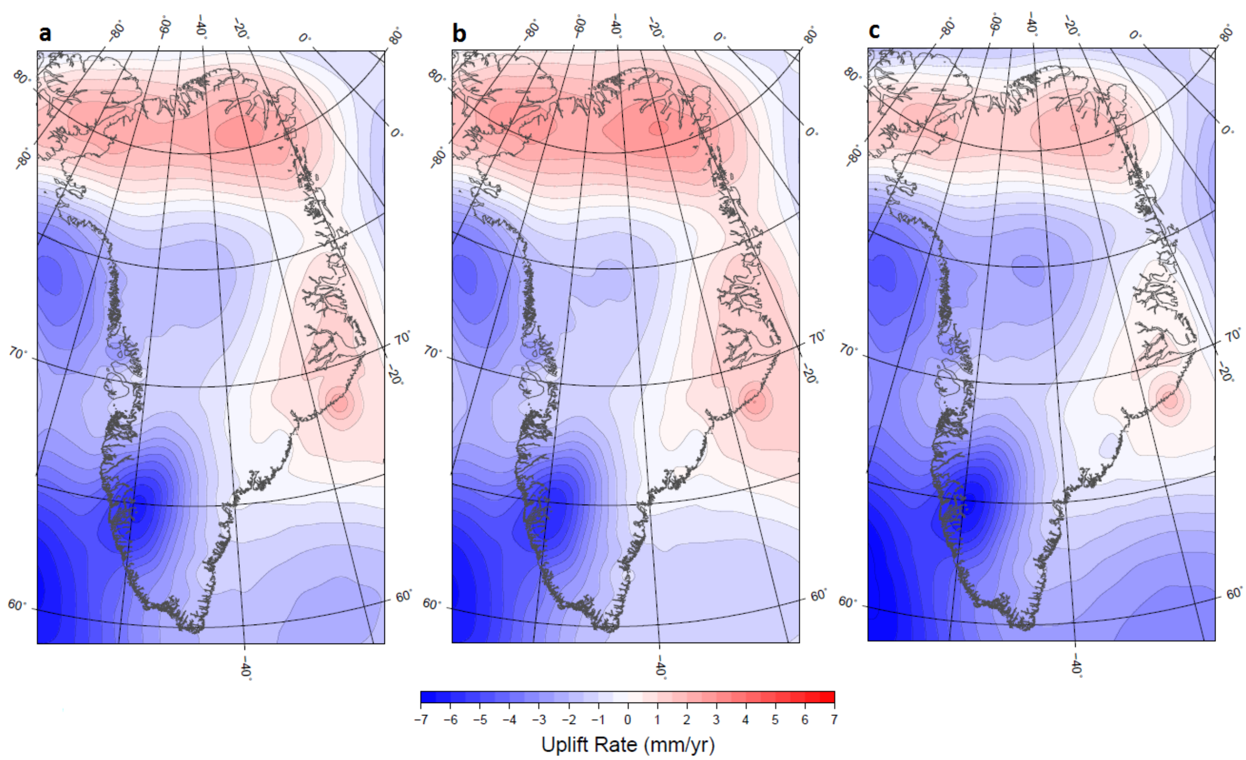

Figure 4.2 (a) The Huy3 GrIS reconstruction with its optimal Earth model is applied to generate present-day uplift rates across Greenland due to past changes in the ocean and ice loading. Uncertainties in the Earth structure are considered with the Huy3 model to calculate upper (b) and lower (c) bounds on the predicted present-day uplift rates.

4.3.2 MODEL WEAKNESSES

As previously stated, the Huy3 Greenland reconstruction fits the majority of observations. However there remain data-model discrepancies which can be affiliated with missing physics and sub-grid processes of the glaciological model and uncertainties in lateral Earth structure which has implications for the ice chronology and present-day geometry. Specifically, up-scaling the ice sheet model grid resolution would help resolve fjords, ice streams, and outlet glaciers which would facilitate drainage at the margin where ice thickness is over-predicted. To represent particular features such as fast-flowing ice streams, ice shelves and iceberg calving requires the inclusion of additional physical processes through a shallow-shelf approximation and a physical ground-line parameterization [Pollard and DeConto, 2009; Gomez et al., 2012]. Unfortunately, these model developments are at the expense of computational time and they introduce numerous additional parameters. Given that I conduct large-ensemble data-constrained calibrations, this has to be taken into consideration since the model needs to remain computationally efficient. Additional sources of uncertainty which have implications on the data-model misfits are poorly known boundary conditions, such as the past climate, bedrock topography, lateral Earth structure and a number of loosely constrained parameters (e.g. flow law coefficient and exponent, DDFs).

5. REFERENCES

The references listed are those for Section 1 and 4.

Adams, J., Maslin, M., Thomas, E., 1999. Sudden climate transitions during the Quaternary. Progress in Physical Geography 23, 1, 1-36.

Alley, R. B., Clark, P. U., Huybrechts, P. & Joughin, I., 2005. Ice-sheet and sea-level change. Science 310, 456–460.

Andrews, T., Gregory, J.M., Webb, M.J., Taylor, K.E., 2012. Forcing, feedbacks and climate sensitivity in CMIP5 coupled atmosphere–ocean climate models. Geophysical Research Letter 39, L09712.

Amiot, R., Lécuyer, C., Buffetaut, E., Escarguel, G., Fluteau, F., Martineau, F., 2006. Oxygen isotopes from biogenic apatites suggest widespread endothermy in Cretaceous dinosaurs. Earth and Planetary Science Letters 246 (1-2), 41-54.

Andrews, J.T., Cooper, T.A., Jennings, A.E., Stein, A.B., Erlenkeuser, H.,1998. Late Quaternary iceberg-rafted detritus events on the Denmark Strait-Southeast Greenland continental slope (c. 65_N) related to North Atlantic Heinrich events? Marine Geology 149, 211–228.

Bamber, J.L., Layberry, R.L., Gogineni, S., 2001. A new ice thickness and bed data set for the Greenland ice sheet 1. Measurement, data reduction, and errors. Journal of Geophysical Research – Atmospheres 106 (D24), 33773–33780.

Beerling, D.J., Berner, R.A., 2000. Impact of a permo-carboniferous high O2 event on the terrestrial carbon cycle. Proceedings of the National Academy of Sciences 97 (23), 12428-12432.

Bertrand, P., 2005. Chapitre ‘‘Vers une régulation planétaire’’ Des atomes aux planètes habitables de Gargaud, M., Claeys, P., Martin, H. P.U., Bordeaux. Collection: L’origine de la vie

Bintanja, R., van de Wal, R.S.W., 2008. North American ice-sheet dynamics and the onset of 100,000-year glacial cycles. Nature 454, 869-872.

Box, J.E., Steffen, K., 2012. Sublimation on the Greenland ice sheet from automated weather station observations. Journal of Geophysical Research: Atmospheres 106 (D24), 33965-33981.

Brown, R.D., Mote, P.W., 2009. The response of northern hemisphere snow cover to a changing climate. Journal of Climate 22, 2124-2145.

Budd, W.F., 1970. Ice flow over bedrock perturbations. Department of Supply Melbourne Antarctic DIV. No. ANARE-Reprint-GL/71.

Budyko, M.I., 1969. The effect of solar radiation variations on the climate of the Earth. Tellus 21 (5), 611-619.

Catling, D.C., Claire, M.W., 2005. How Earth’s atmosphere evolved to an oxic state: a status report. Earth and Planetary Science Letter 237, 1–20.

Charbit, S., Paillard, D., Ramstein, G., 2008. Amount of CO_2 emissions irreversibly leading to the total melting of Greenland. Geophysical Research Letters 35, L12503.

Clark, P.U., Mix, A.C., 2002. Ice sheets and sea level of the Last Glacial Maximum. Quaternary Science Reviews 21 (1–3), 1–7.

Cuffey, K.M., Marshall, S.J., 2000. Substantial contribution to sea-level rise during the last interglacial from the Greenland ice sheet. Nature 404, 591-594.

Cuffey, K.M., Paterson, W.B.S., 2010. The physics of glaciers. 4^{th} ed., Academic, Amsterdam.

Dahl Jensen, D., Mosegaard, K., Gundestrup, N., Clow, G.D., Johnsen, S.J., Hansen, A.W., Balling, N., 1998. Past temperatures directly from the Greenland ice sheet. Science 282 (5387), 268–271.

Dahl-Jensen et al., 2013 Eemian interglacial reconstructed from a Greenland folded ice core. Nature 493, 489-494.

Dansgaard, W., 1961. The isotopic composition of natural waters. Meddelelser Om Grjnland 165, 2.

DeConto, R., Pollard, D., 2003. Rapid Cenozoic glaciation of Antarctica induced by declining atmospheric CO_2. Nature 421, 245–249

Donnadieu, Y., Godderis, Y., Pierrehumbert, R., Dromart, G., Fluteau, F., Jacob, R., 2006. A GEOCLIM simulation of climatic and biogeochemical consequences of Pangea breakup. Geochemistry Geophysics Geosystems 7(Q11019), 21.

Dorado, G., Rey Fraile, I., Morales, A., Hernandez, P., Vasquez, V.F., 2010. Biological mass extinctions on planet Earth. Arqueovios 4(1), 53-64.

Dziewonski, A.M., Anderson, D.L., 1981. Preliminary reference Earth model. Physics of the Earth and Planetary Interiors 25 (4), 297–356.

Farrell, W.E., Clark, J.A., 1976. Postglacial sea-level. Geophysical Journal of the Royal Astronomical Society 46 (3), 647–667.

Flanner, M.G., Shell, K.M., Barlage, M., Perovich, D.K., Tschudi, M.A., 2011. Radiative forcing and albedo feedback from the northern hemisphere cryosphere between 1979 and 2008. Nature Geoscience 4, 151-155.

Fleming, K., Lambeck, K., 2004. Constraints on the Greenland ice sheet since the Last Glacial Maximum from sea-level observations and glacial-rebound models. Quaternary Science Reviews 23 (9–10), 1053–1077.

Frakes, L.A., Francis, J.E., Syktus, J.I., 1992. Climate modes of the phanerozoic: the history of the earth’s climate over the past 600 million years. Cambridge University Press, 274 pp.

Funder, S., Kjeldsen, K.K., Kjaer, K.H., O’Cofaigh, C., 2011. The Greenland ice sheet during the past 300,000 years: A review. In: Ehlers, J., Gibbard, P.L., Hughes, P.D. (Eds.), Quaternary Glaciations. Extent and Chronology. Elsevier, Amsterdam, Developments in Quaternary Science 15, 699-713.

Funder, S., Goosse, Hugues, Jepsen, H., Kaas, E., Kjaer, K.H., Korsgaard, N.J., Larsen, N.K., Linderson, H., Lysa, A., Moller, P., Olsen, J., Willerslev, E., 2011. A 10,000-year record of arctic ocean sea-ice variability – view from the beach. Science 333 (6043), 747-750.

Glen, J.W., 1955. The creep of polycrystalline ice. Proceedings of the Royal Society of London Series A, 228 (1175), 519-538.

Gomez, N., Mitrovica, J. X., Huybers, P., Clark, P. U., 2010. Sea level as a stabilizing factor for marine-ice-sheet grounding lines. Nature Geoscience 3 (12), 850-853.

Gregory, J.M., Huybrechts, P., 2006. Ice-sheet contributions to future sea-level change. Philiosophical transactions of the Royal Society A-Mathematical Physical and Engineering Sciences 364 (1844), 1709-1731.

Hansen, J.E., Sato, M., 2012 Paleoclimate implications for human-made climate change. Climate Change. Springer Vienna, 21-47.

Hays, J.D., Imbrie, J., Shackleton, N.J., 1976. Variations in the Earth's Orbit: Pacemaker of the Ice Ages. Science, 194(4270), 1121-1132.

Hoffman, P.F., Schrag, D.P., 2002 The snowball Earth hypothesis: testing the limits of global change. Terra Nova 14,129–155.

Hoffman, P.F., Kaufman, A.J., Halverson, G.P., Schrag, D.P., 1998. A Neoproterozoic snowball Earth. Science 281(5381), 1342–1346.

Huybrechts, P., 1986. A three-dimensional time-dependent numerical model for polar ice sheets: some basic testing with a stable and efficient finite difference scheme. VUB Geografisch Instituut Report 86-1, 39.

Huybrechts, P., 2002. Sea-level changes at the LGM from ice-dynamic reconstructions of the Greenland and Antarctic ice sheets during the glacial cycles. Quaternary Science Reviews 21 (1–3), 203–231.

Imbrie, J.Z., Hays, J.D., Martinson, D.G., MacIntyre, A., Mix, A.C., Morley, J.J., Pisias, N.G., Prell, W.L., Shackleton, N.J., 1984. The orbital theory of Pleistocene climate: support from a revised chronology of the marine d18O record. In: Berger, A., Imbrie, J.Z., Hays, J.D., Kukla, G., Saltzman, B. (Eds.). Milankovitch and Climate. D. Reidel, Dordrecht, pp. 269–305.

Imbrie, J., Boyle, E.A., Clemens, S.C., Duffy, A., Howard, W.R., Kukla, G., Kutzbach, J., Martinson, D.G., McIntyre, A., Mix, A.C., Molfino, B., Morley, J.J., Peterson, L.C., Pisias, N.G., Prell, W.L., Raymo, M.E., Shackleton, N.J., Toggweiler, J.R., 1992. On the structure and origin of major glaciation cycles 1. Linear reponses to Milankovitch forcing. Paleoceanography 7 (6), 701-738.

Johnsen, S.J., White, J.W.C., 1989. The origin of Arctic precipitation under present and glacial conditions. Tellus 41B, 452-468.

Johnsen, S.J., Dahl-Jensen, D., Gundestrup, N., Steffensen, J.P., Clausen, H.B., Miller, H., Masson-Delmotte, V., Sveinbjornsdottir, A.E., White, J., 2001. Oxygen isotope and palaeotemperature records from six Greenland ice-core stations: Camp Century, Dye-3, GRIP, GISP2, Renland and NorthGRIP. Journal of Quaternary Science 16 (4), 299-307.

Kasting, J.F., 2005. Methane and climate during the Precambrian era. Precambrian Research 137 (3-4), 119-129.

Kaufman, D.S., Ager, T.A., Anderson, N.J., Anderson, P.M., Andrews, J.T., Bartlein, P.J., Brubaker, L.B., Coats, L.L., Cwynar, L.C., Duvall, M.L., Dyke, A.S., Edwards, M.E., Eisner, W.R., Gajewski, K., Geirsdottir, A., Hu, F.S., Jennings, A.E., Kaplan, M.R., Kerwin, M.N., Lozhkin, A.V., MacDonald, G.M., Miller, G.H., Mock, C.J., Oswald, W.W., Otto-Bliesner, B.L., Porinchu, D.F., Ruhland, K., Smol, J.P., Steig, E.J., Wolfe, B.B., 2004. Holocene thermal maximum in the western Arctic (0–180 degrees W). Quaternary Science Reviews 23 (5–6), 529–560.

Kendall, R.A., Mitroviva, J.X., Milne, G.A., 2005. On post-glacial sea level: II. Numerical formulation and comparative results on spherically symmetric models. Geophysical Journal International 161 (3), 679–706.

King, M.A., Bingham, R.J., Moore, P., Whitehouse, P.L., Bentley, M.J., Milne, G.A., 2012. Lower satellite-gravimetry estimates of Antarctic sea-level contribution. Nature 491, 586-589.

Kirschvink, J.L., 1992. Late proterozoic low-latitude global glaciation: the snowball earth. Section 2.3, In: Schopf, J.W., Klein, C., Des Maris, D., (eds), The proterozoic biosphere: a multidisciplinary study. Cambridge University Press, 51–52.

Koenig, S.J., DeConto, R.M., Pollard, D., 2011. Late Pliocene to Pleistocene sensitivity of the Greenland ice sheet in response to external forcing and internal feedbacks. Climate Dynamics 37 (5-6), 1247-1268.

Kopp, R. E., Simons, F. J., Mitrovica, J. X., Maloof, A. C., Oppenheimer, M., 2013. A probabilistic assessment of sea level variations within the last interglacial stage. Geophysical Journal International, 193 (2), 711-716.

Lemke, P., Ren, J., Alley, R.B., Allison, I., Carrasco, J., Flato, G., Fujii, Y., Kaser, G., Mote, P., Thomas, R.H., Zhang, T., 2007. Observations: changes in snow, ice and frozen ground. In: Solomon, S., Qin, D., Manning, M., Chen, Z., Marquis, M., Averyt, K.B., Tignor, M., Miller, H.L. (Eds.), Climate Change 2007: The Physical Science Basis. Contribution of Working Group 1 to the Fourth Assessment Report of the Intergovernmental Panel on Climate Change. Cambridge University Press, Cambridge, United Kingdom and New York, NY, USA.

Letréguilly, A., Reeh, N., Huybrechts, P.,1991. The Greenland ice-sheet through the Last Glacial interglacial cycle. Global and Planetary Change 90 (4), 385–394.

Long, A.J., Woodroffe, S.A., Roberts, D.H., Dawson, S., 2011. Isolation basins, sea-level changes and the Holocene history of the Greenland ice sheet. Quaternary Science Reviews 30 (27-28), 3748-3768.

Lunt, D.J., Foster, G.L., Haywood, A.M., Stone, E.J., 2008. Late Pliocene Greenland glaciation controlled by a decline in atmospheric CO2 levels. Nature 252, 1102-1105.

Meehl, G.A., Stocker, T.F., Collins, W.D., Friedlingstein, P., Gaye, A.T., Gregory, J.M., Kitoh, A., Knutti, R., Murphy, J.M., Noda, A., Raper, S.C.B., Watterson, I.G., Weaver, A.J., Zhao, Z.-C., 2007. Global Climate Projections. In: Solomon, S., Qin, D., Manning, M., Chen, Z., Marquis, M., Averyt, K.B., Tignor, M., Miller, H.L. (Eds.), Climate Change 2007: The Physical Science Basis. Contribution of

Working Group 1 to the Fourth Assessment Report of the Intergovernmental Panel on Climate Change. Cambridge University Press, Cambridge, United Kingdom and New York, NY, USA.

Meier, M.F., Dyurgerov, M.B., Rick, U.K., O'Neel, S., Pfeffer, W.T., Anderson, R.S., Anderson, S.P., Glazovsky, A.F.,l., 2007. Glaciers dominate eustatic sea-level rise in the 21st century. Science 317 (5841), 1064-1067.

Milne, G.A. & Mitrovica, J.X. Postglacial sea-level change on a rotating Earth, Geophys. J. Int., 133, 1-19, 1998.

Milne, G.A. Refining models of the glacial isostatic adjustment process, PhD Thesis, 1998.

Milne, G.A., How the climate drive, Bullerwell lecture. 2008.

Mitrovica, J.X., 1996. Haskell [1935] revisited. Journal of Geophysical Research 101, 555-569.

Mitrovica, J.X., Forte, A.M., 1997. Radial profile of mantle viscosity: results from the joint inversion of convection and postglacial rebound observables. Journal of Geophysical Research – Solid Earth 102 (B2), 2751–2769.

Mitrovica, J.X., Milne, G.A., 2003. On post-glacial sea level: I. General theory. Geophysical Journal International 154 (2), 253–267.

Mound J.E., Mitrovica, J.X., 1998. True polar wander as a mechanism for second-order sea-level variations. Science 279 (5350), 534-537.

Muscheler, R., Heikkila, U., 2011. Constraints on long-term changes in solar activity from the range of variability of cosmogenic radionuclide records. Astrophysics and Space Sciences Transactions, 7(3), 355-364.

Nick, F.M., Vieli, A., Howat, I.M., Joughin, I., 2009. Large-scale changes in Greenland outlet glacier dynamics triggered at the terminus. Nature Geoscience 2, 110-114.

Nghiem, S.V., Hall, D.K., Mote, T.L., Tedesco, M., Albert, M.R., Keegan, K., Shuman, C.A., DiGirolamo, N.E., Neumann, G., 2012. The extreme melt across the Greenland ice sheet in 2012. Geophysical Research Letters 39, L20502.

Nye, J.F., 1969. A calculation on the sliding of ice over a wavy surface using a Newtonian viscous approximation. Proceedings of the Royal Society of London 311 (1506), 445-467.

O'Cofaigh, C., Dowdeswell, J.A., Jennings, A.E., Hogan, K.A., Kilfeather, A., Hiemstra, J.F., Noormets, R., Evans, J., McCarthy, D.J., Andrews, J.T., Lloyd, J.M., Moros, M., 2012. An extensive and dynamic ice sheet on the west Greenland shelf during the last glacial cycle. Geology 41 (2), 219-222.

Oerlemans, J., 1981. Some basic experiemnts with a vertically-integrated ice sheet model. Tellus 33 (1), 1-11.

Pagani, M., Zachos, J.C., Freeman, K.H., Tipple, B., Bohaty, S., 2005. Marked decline in atmospheric carbon dioxide concentrations during the Paleogene. Science 309 (5734), 600–603.

Peltier, W.R., Fairbanks, R.G., 2006. Global glacial ice volume and last glacial maximum duration from an extended Barbados sea level record. Quaternary Science Reviews 25 (23-24), 3322-3337.

Peltier, W.R., 2004. Global glacial isostasy and the surface of the ice-age earth: the ICE-5G (VM2) model and grace. Annual Review of Earth and Planetary Sciences 32, 111–149.

Petit, J.R., Jouzel, J., Raynaud, D., Barkov, N.I., Barnola, J.M., Basile, I., Bender, M., Chappellaz, J., Davis, J., Delaygue, G., Delmotte, M., Kotlyakov, V.M., Legrand, M., Lipenkov, V., Lorius, C., Pépin, L., Ritz, C., Saltzman, E., Stievenard, M., 1999. Climate and Atmospheric History of the Past 420,000 years from the Vostok Ice Core, Antarctica. Nature 399(6735), 429-436.

Pollard, D., Deconto, R., 2009. Modelling West Antarctic ice sheet growth and collapse through the past five million years. Nature 458 (7236), 329-332.

Ramstein, G., Donnadieu ,Y., Goddéris, Y., 2004a. Proterozoic glaciations. Comptes Rendus Geoscience 336 (7–8), 639–646.

Ramstein, G., Khodri, M., Donnadieu, Y., Goddéris, Y., 2004b. Impact of the hydrological cycle on past climate changes: three illustrations at different time scales. Comptes Rendus Geoscience 337 (1-2), 125–137.

Ramstein, G., 2011. Climates of the Earth and Cryosphere Evolution. Surveys in Geophysics 32, 329-350.
Raymo, M.E., Huybers, P., 2008. Unlocking the mysteries of the ice ages. Nature 451, 284-285.

Ridley, J., Gregory, J., Huybrechts, P., Lowe, J., 2010. Thresholds for irreversible decline of the Greenland ice sheet. Climate Dynamics, 35, 1049-1057.

Ritz, C., Fabre, A., Letréguilly, A., 1997. Sensitivity of a Greenland ice sheet model to ice flow and ablation parameters: consequences for the evolution through the last climatic cycle. Climate Dynamics 13, 11–24.

Shepherd, A., Ivins, E.R., Geruo, A., Barletta, V.R., Bentley, M.J., Bettadpur, S., Briggs, K.H., Bromwich, D.H., Forsberg, R., Galin, N., Horwath, M., Jacobs, S., Joughin,I., King, M.A., Lenaerts, J.T.M., Li, J., Ligtenberg, S.R.M., Luckman, A., Luthcke, S.B., McMillan, M., Meister, R., Milne, G.A., Mouginot, J., Muir, A., Nicolas, J.P., Paden, J., Payne, A.J., Pritchard, H., Rignot, E., Rott, H., Sørensen, L.S., Scambos, T.A., Scheuchl, B., Schrama, E.J.O., Smith, B., Sundal, A.V., van Angelen, J.H., van de Berg, W.J., van den Broeke, M.R., Vaughan, D.G., Velicogna, I., Wahr, J., Whitehouse, P.L., Wingham, D.J., Yi, D., Young, D., Zwally H.J., 2012. Science 338 (6111), 1183-1189.

Simpson, M.J.R., Milne, G.A., Huybrechts, P., Long, A.J., 2009. Calibrating a glaciological model of the Greenland ice sheet from the Last Glacial Maximum to present-day using field observations of relative sea level and ice extent. Quaternary Science Reviews 28, 1631–1657.

Sleep, N.H., Zahnle, K., 2001. Carbon dioxide cycling and implications for climate on ancient Earth. Journal of Geophysical Research: Planets 106, 1373-1399.

Stone, E. J., Lunt, D. J., Annan, J. D., Hargreaves, J. C., 2013. Quantification of the Greenland ice sheet contribution to Last Interglacial sea level rise. Climate of the Past, 9 (2), 621-639.

Tarasov, L., Peltier, W.R., 2002. Greenland glacial history and local geodynamic consequences. Geophysical Journal International 150 (1), 198–229.

UNEP/GRID-Arendal Global Outlook for Ice and Snow, 2007

van Angelen, J.H., Lenaerts, J.T.M., Lhermitte, S., Fettweis, X., Kuipers Munneke, P., van den Broeke, M.R., van Meijgaard, E., Smeets, C.J.P.P., 2012. Sensitivity of Greenland ice sheet surface mass balance to surface albedo parameterization: a study with a regional climate model. The Cryosphere 6, 1175-1186.
Vaughan, D. G. & Arthern, R. 2007. Why is it so hard to predict the future of ice sheets. Science 315, 1508–1510.

Vinther, B.M., Buchardt, S.L., Clausen, H.B., Dahl-Jensen, D., Johnsen, S., Fisher, D.A., Koerner, R.M., Raynaud, D., Lipenkov, V., Andersen, K.K., Blunier, T., Rasmussen, S.O., Steffensen, J.P., Svensson, A.M., 2009. Holocene thinning of the Greenland ice sheet. Nature 461, 385-388.

Wake, L. & Huybrechts, P. & Box, J. & Hanna, E. & Janssens, I & Milne, G., 2009. Surface mass-balance changes of the Greenland ice sheet since 1866, Annals of Glaciology, 50.

Weertman, J., 1961. Mechanism for the formation of inner moraines found near the edge of cold ice caps and ice sheets. Journal of Glaciology 3 (30), 965-978.

Whitehouse, P.L., Bentley, M.J., Le Brocq, A.M., 2012. A deglacial model for Antarctica: geological constraints and glaciological modelling as a basis for a new model of Antarctic glacial isostatic adjustment. Quaternary Science Reviews 32, 1-24.

Winkelmann, D., Jokat, W., Jensen, L., Schenke, H-W., 2010. Submarine end moraines on the continental shelf off NE Greenland—implications for Lateglacial dynamics. Quaternary Science Review 29, 1069–1077.

Wiscombe, W.J., Warren, S.G., 1980. A model for the spectral albedo of snow. I: pure snow. Journal of Atmospheric Science 37, 2712-2733.

Woodroffe, S.A., Long, A.J., Lecavalier, B.L., Milne, G.A., 2013. Using relative sea-level data to constrain the deglacial and Holocene history of southern Greenland. Quaternary Science Reviews xxx, 1-12.

Yuen, D.A., Sabadini, R., Boschi, E.V., 1982. Viscosity of the lower mantle as inferred from rotational data. Journal of Geophysical Research 87 (B13), 10745-10762.